Studies on Metal Hydride Based Hydrogen Storage Device

A thesis submitted in partial fulfillment of the requirements for the degree of

Doctor of Philosophy

by

S. Anbarasu

Department of Mechanical Engineering

Indian Institute of Technology Guwahati

Guwahati – 781039, India

December 2014

Department of Mechanical Engineering
Indian Institute of Technology Guwahati
Guwahati – 781039, India

THESIS CERTIFICATE

This is to certify that the work contained in the thesis entitled **Studies on Metal Hydride Based Hydrogen Storage Device** by **S. Anbarasu**, a student of the Department of Mechanical Engineering, Indian Institute of Technology Guwahati, for the award of the degree of **Doctor of Philosophy** has been carried out under our supervision and that this work has not been submitted elsewhere for any degree.

Dr. P. Muthukumar
Associate Professor
Department of Mechanical Engineering
Indian Institute of Technology Guwahati
Guwahati – 781039, India

Dr. Subhash C. Mishra
Professor
Department of Mechanical Engineering
Indian Institute of Technology Guwahati
Guwahati – 781039, India

Dedicated to

My Family

Acknowledgement

I express my deepest gratitude and hearty thanks to my supervisors Dr. P. Muthukumar and Dr. Subhash C. Mishra, for their invaluable guidance and constant encouragement. I am deeply inspired by not only their rich experience and knowledge but also by the way of approaching a problem, immense patience and utmost care. I am highly indebted to them for their untiring devotion and willingness. During my project work, they provided me with the most invaluable ideas, books and journals that played a vital role in completing the thesis successfully. I enjoyed each and every moment working under their supervision and learnt a lot of things from them, which will be an asset for my future research.

I would like to thank Ministry of New and Renewable Energy (MNRE), Government of India, for their financial support (Project No: 103/63/2006-NT). I express my heartfelt thanks to Dr. -Ing. Manfred Groll, IKE, University of Stuttgart, Germany for providing valuable technical suggestions and ideas during the initial stage of my research work. I am very grateful to Dr. M. R. Nouni, Scientist-F, Director, NT Group, MNRE for providing insightful comments and valuable suggestions during my research work.

I am thankful to my doctoral committee members Dr. P. Mahanta, Dr. N. Sahoo and Dr. V. S. Moholkar for giving their valuable suggestions and encouragement which helped to shape myself to meet the requirement of a successful researcher. I would like to express my

sincere thanks to Dr. D. Chakraborty and Dr. P. Mahanta (ex. HOD) and Dr. A. K. Dass (HOD) for providing all the facilities needed during my research work and financial support extended by the Mechanical Engineering Department. I take this opportunity to thank all the faculty members for valuable suggestions and cooperation during my course work.

I specially thank Mr. D. Chetri, Mr. J. Basumatary, Mr. Nip Borah and Mr. R. Saikia for their help during the course of fabrication of the reactor and also their assistance when needed during my experimental studies, and also I would like to thank Mr. S. Srinivasan, Mr. Dass and Mr. Raja Ganesan (M/s Shakunth Aqua Products, Chennai) for their sincere help and workmanship rendered throughout my fabrication work.

I should take this opportunity to thank my mentor Dr. M. Siva Sankar who insisted me to apply for Ph.D in IIT Guwahati.

I would like to express my sincere thanks to Dr. A. Satheesh and Dr. D. Santhosh Kumar for teaching the basic of metal hydrides and C language, and valuable discussions and suggestions throughout my research work. I would like to thank Dr. S. Murugavelh, with whom I had academic discussions, shared my personal feelings and he provided constant encouragement and continuous help during my entire stay in IIT Guwahati.

I am thankful to Dr. V. K. Pantangi, Mr. C. Shravankumar, Dr. B. Satya Sekhar, Mr. Bibin John, Mr. Shyamkumar, Mr. P. Suresh, Mr. S. Sajith, Mr. Sujit Roy, Mr. N. K. Mishra, Mr. Hakeem Niyas, Mr. L. G. Kirankumar, Mr. M. S. Aravinda Kumar, Mr. Rupesh Singh, Mr. Koushik Das,

Mr. & Mrs. A. Ghatak, Dr. B. K. Debnath, Mr. J. Sardar, Mr. L. Prasad, Mr. P. Pritish, Mr. A. Ganesh, Mr. Vivek Selvan, Mr. Kiran, Mr. Atul, Mr. Chandrasekhar, Mr. S. Sharma for their constant support and valuable friendship. I express my thanks to Mr. Chilaka Ravi Chandra Rao and family for their affection and made my stay at IIT Guwahati a memorable experience.

I would like to thank Mr. & Mrs. V. Anand, Mr. & Mrs. R. Samuel Povas, Mr. P. Anandan, Dr. D. Karthik, Mr. & Mrs. M. Karthik, Mr. Mahendran, Dr. Balasubramainan, Mr. Hariharan, Mr. U. Kannan, Mr. Chandran, Shri. & Smt. Narayanasami whose continuous support gave me motivation to complete the thesis work.

I would like to express my sincere gratitude to my parents Mr. M. Subramanian and Mrs. S. Maheswari, my brother Dr. S. Rajkumar, Mrs. R. Senthil Vadivu, R. Arjun, my parents-in-law Mr. V. Krishna Kumar and Mrs. S. Sivakozhunthu, Dr. K. Jayachandran, Ms. Priyanka, Dr. A. Varadharajan and his family whose blessings, prayers and never ending support is the real impetus that continuously motivates me to produce my best. Last but not the least, my deepest gratitude goes to my wife Mrs. Mogana Priya for her constant encouragement, unlimited sacrifices, patience, continuous support and motivation for the completion of this thesis work.

S. ANBARASU

Abstract

Demand for energy is continuously increasing with time, and till date, the fossil fuels remain the major source of energy. Reserves of fossil fuels are, on one hand limited, and on the other, its usages result in environmental pollution and ecological imbalance. Both these badly affect all living beings on the earth. Thus, to meet the energy demand with minimal pollution, for decades researchers throughout the globe have been endeavoring for an alternative to the fossil fuels. Hydrogen, which is abundant in nature and produces zero pollution, is one of the best alternatives. While hydrogen production and conversion do not pose any technical challenge, its storage and delivery remain a serious challenge. Developing safe, reliable, compact and versatile hydrogen storage system is one of the most important aspects to the widespread use of hydrogen as an energy carrier. Hydrogen storage devices have potential applications in automobiles, fuel cell, heat pump, heat transformer, etc. In recent years, researchers have been exploring the various ways of safe storage of hydrogen that can be refilled fast and when needed, can supply hydrogen with ease.

Storage of hydrogen is a critical issue due to its low density and wide range of flammability. Conventional methods such as pressurized gas storage and cryogenic liquefaction system require special maintenance, safety precautions, high operating cost and effort. Hence, these options are not practical for the day-to-day usage. Among these storage options, metal hydrides (MH) based hydrogen storage systems have stood ahead of the other hydrogen storage technologies. This method uses a hydrogen absorbing alloy that absorbs and stores large amount of hydrogen by chemical bonding. MH based hydrogen storage systems deserve attention as they possess higher volumetric storage capacity and also store hydrogen at near ambient condition over a longer period of time. Hence, MH provides a platform for hydrogen storage with a high standard of safety for both mobile and stationary applications. Absorption/desorption of hydrogen to/from the hydride bed are exothermic/endothermic reactions, respectively. The performance of metal hydride based hydrogen storage device (MHHSD) depends on the rate at which the heat is removed/supplied from/to the hydride bed during hydriding/dehydriding process. Development

of an efficient and economic design of MHHSD requires a mathematical model. Hence it is very essential to carry out the numerical simulations before conducting the expensive experiments.

The major objectives of the present work are (i) to study the absorption and desorption characteristics of lab-scale prototype MHHSD considering the volumetric radiation effect in the energy equation, (ii) to develop a 2-D mathematical model for optimizing the number of embedded cooling tubes (ECT) and their arrangements in a metal hydride based hydrogen storage device (MHHSD), (iii) to develop a 3-D mathematical model for predicting the absorption and desorption characteristics of MHHSD with optimized configuration of ECT at different operating conditions and (iv) to test the performances of the MHHSD with ECT at various operating conditions.

A numerical study of coupled heat and hydrogen transfer processes in an annular cylindrical hydrogen storage reactor filled with Mg_2Ni is presented. An unsteady, 2-D mathematical model of a lab-scale prototype MHHSD is developed for predicting the hydriding and dehydriding characteristics during hydrogen absorption and desorption processes. The effect of volumetric radiation is accounted in the thermal model. Both energy equation and divergence of radiative heat flux are solved using finite volume method. Effects of hydride bed thickness, initial absorption temperature, hydride bed thermal conductivity and hydrogen supply pressure on the hydrogen storage capacity and the average bed temperature are studied during the hydriding process. Effect of desorption temperature and overall heat transfer coefficients on the amount of hydrogen desorbed and the average bed temperature are studied during dehydriding process. Thinner hydride bed is found to enhance the hydriding rate accomplishing a rapid reaction. At absorption conditions of 20 bar supply pressure and 300 °C initial absorption temperature, Mg_2Ni stores about 36.7 g of hydrogen per kg of alloy. At desorption conditions of 350 °C desorption temperature and 1 bar desorption pressure, the optimum values of overall heat transfer coefficient and effective thermal conductivity are 1000 $W/m^2 \cdot K$ and 2.5 $W/m \cdot K$, respectively. The maximum amount of hydrogen desorbed at the above said condition is about 36.2 g of hydrogen per kg of alloy. The numerical results are compared with the experimental data reported in the literature, and a good agreement is observed.

To study the transient behavior of heat and hydrogen transfer characteristics of 2.75 kg of $LmNi_{4.91}Sn_{0.15}$ based hydrogen storage device, a 2-D mathematical model in cylindrical co-ordinates is developed by varying the arrangement of embedded cooling tubes (24 – 70 ECT) using COMSOL Multiphysics 4.3. The number of ECT is optimized on the basis of hydriding/dehydriding time. Further, this computational study is extended to a 3-D mathematical model by employing a cylindering MHHSD with 60 ECT filled with 2.75 kg of $LmNi_{4.91}Sn_{0.15}$. Hydriding and dehydriding characteristics are investigated at different hydrogen supply pressures (10 – 35 bar), heat transfer fluid (HTF) temperatures (30 – 60 °C) and effective thermal conductivity of the hydride bed (0.2 – 2.5 W/m·K). It is observed that the rate of hydriding is rapid for higher supply pressures (above 30 bar) and lower absorption temperatures (below 30 °C). The rate of dehydriding is prompt at a higher HTF temperature of about 60 °C. At a given operating condition, increasing the hydride bed effective thermal conductivity up to 2.5 W/m·K reduces the absorption/desorption time significantly. The numerical and experimental results have been found to have a good agreement.

Based on the numerical investigations, two MHHSDs with 36 and 60 ECT filled with 2.75 kg of $LmNi_{4.91}Sn_{0.15}$ are fabricated. Performances of these devices in terms of hydrogen absorption rate and amount of hydrogen absorbed are reported for different supply pressures (10 – 35 bar), absorption temperatures (20 – 30 °C) and cooling fluid flow rates (2.2 – 30 l/min). At any given absorption temperature, the rate of hydrogen absorption and the amount of hydrogen absorbed (wt%) are found to increase with hydrogen supply pressure up to about 35 bar. At the supply condition of 35 bar, hydrogen pressure and 30 °C absorption temperature, with oil as a HTF at a flow rate of 3.2 l/min, the maximum amount of hydrogen absorbed are ≈ 1.18 wt% in 10 min for 36 ECT, and 8 min for 60 ECT. At the absorption condition of 25 bar supply pressure, 30 l/min water flow rate and 30 °C absorption temperature, the absorption time of the reactor with 60 ECT is reduced to 5 min.

For both reactors, the desorption characteristics of the hydrogen storage devices are also studied varying the hot fluid temperature (30 – 60 °C), and the HTF flow rate (2.2 – 30 l/min). In the reactor with 36 ECT and 60 ECT, with oil flow rate as 3.2 l/min, at 60°C hot fluid temperature, the desorption rate of hydrogen is found to be rapid. With the same reactor configuration

(60 ECT), water as HTF at a flow rate of 30 l/min and at 50 °C, the maximum amount of hydrogen desorbed is ≈ 1.08 wt% within 8 min. The desorption time is decreased by 46.7% when the flow rate is increased from 5 l/min to 30 l/min. For a given flow rate, the reactor with 36 ECT is having more pressure drop in comparison with 60 ECT reactor. The reason for higher pressure drop in the reactor with 36 ECT is more flow resistance and higher flow velocity.

Based on the above discussions one can conclude that the MHHSD with ECT can be effectively used as a safe storage medium of hydrogen storage. Further, the results presented in thesis will be beneficial for developing the commercial hydrogen storage device for on-board and industrial applications. Employing the developed thermal models, one can predict the performances of MHHSD with ECT filled with different hydrogen absorbing alloys without performing the expensive experimental studies.

Nomenclature

C	:	Reaction rate constant (1/s)
C_p	:	Heat capacity (J/kg·K)
E	:	Activation energy of the reaction (J/mol)
G	:	Incident radiation
K	:	Permeability (m^2)
m	:	Mass (g)
M	:	Molecular weight of hydrogen (kg/mol)
N_a	:	Number of hydrogen atoms in the metal hydride
N_{H_2}	:	Number of hydrogen moles absorbed/desorbed (mol)
P	:	Pressure (bar)
q	:	Heat flux (W/m^2)
R_u	:	Ideal gas constant (J/mol·K)
t	:	Time (s)
T	:	Temperature (K)
U	:	Overall heat transfer coefficient ($W/m^2 \cdot K$)
V	:	Velocity (m/s)
x	:	Fraction of absorbed/desorbed hydrogen
ρ	:	Alloy or gas density (kg/m^3)

ε	:	Porosity
λ	:	Thermal conductivity (W/m·K)
ζ	:	Mass of hydrogen absorbed/desorbed (kg/m^3·s)
μ	:	Dynamic viscosity (kg/m^2·s)
ΔH	:	Enthalpy of formation (J/mol)
ΔS	:	Entropy of formation (J/mol·K)
φ_s	:	Slope factor
φ_o	:	Constant
β	:	Hysteresis factor, extinction coefficient
σ	:	Coefficient (radiative property)
ω	:	Scattering albedo

Subscripts

a	:	Absorption, alloy
d	:	Desorption
e	:	Effective
eq	:	Equilibrium, equation
f	:	Fluid, final
g	:	Gas
i	:	Inner
ini	:	Initial
m	:	Metal
0	:	Initial

o	:	Outer
R	:	Radiation
s	:	Supply, scattering
ss	:	Saturation state

Abbreviations used

ECT	:	Embedded cooling tubes
FDM	:	Finite difference method
FVM	:	Finite volume method
HFT	:	Hot fluid temperature
HPMH	:	High pressure metal hydride
HSC	:	Hydrogen storage capacity
HTF	:	Heat transfer fluid
MH	:	Metal hydride
MHHSD	:	Metal hydride based hydrogen storage device
PCT	:	Pressure-Concentration-Temperature

Contents

List of Figures

List of Tables

Chapter 1

Introduction

1.1 Preface

Increase in worldwide energy demand and global warming are the major issues growing at an alarming rate. The energy demand is being met in large-scale by fossil fuel reserves that emit carbon dioxide (CO_2) and other pollutants. The fossil fuel reserves are limited in nature and if the world's energy supply from fossil fuels continues at the present rate, oil and gas reserves will run out of stock within few decades. The shortage of conventional energy resources, rising demand for energy and environmental pollution indicate that there is a need to search for alternate sources of energy to ensure the long-term security of energy supply with low carbon emissions. The criteria such as mobility, storability, versatility, utilization efficiency, eco-friendly, safety and economy are essential in considering an energy source. Failure to meet these criteria will

have significant negative impact on the economy and the environment. A number of renewable energy sources such as solar energy, wind energy, geothermal energy, tidal energy, etc. are generating significant wattage, making off-peak generation important but most of these resources are intermittent power sources that researchers must find ways to store for on – demand use.

1.2 Hydrogen as an alternative energy

Hydrogen as an alternative to conventional energy sources which satisfy most of the criteria has been the focus of this research. It is indispensable to solve world's energy demand and energy security. Hydrogen is the simplest element of all and exerts advantages such as wide availability, eco – friendly, high power density, etc. Hydrogen is not a primary energy source like coal and gas, it is a secondary energy carrier and it is a convenient, safe, and versatile fuel source which can be easily and efficiently converted to desirable forms of energy. The amount of energy per unit mass produced by hydrogen (high gravimetric energy density) is about three times higher than that generated from gasoline and almost seven times higher than the energy obtained from coal in an equal mass. Hydrogen storage a critical issue as it is less dense and hence, several options are being devised to store hydrogen effectively.

Hydrogen is a light gas, and in a given volume, to increase its mass, it has to be compressed to a very high pressure (> 300 bar). Increasing the pressure of the storage device leads to an increase in the weight of the storage tank in one hand, and the possibility of leaks on the other. In the liquid form, at atmospheric pressure, hydrogen needs to be stored at 20 K. If the insulation of the storage tank is not proper, with heat transfer through the wall of the tank, hydrogen will start boiling at ~21 K which will further lead to the raise of pressure in the tank and finally resulting

in boil-off loss. This is not at all a concern with the fuel tanks of petroleum – or diesel – based storage devices. Hydrogen storage in the form of metal hydride (MH) is one of the safest hydrogen storage methods which does not require any special attention in comparison with conventional methods such as high pressure gas storage and liquid hydrogen at 20 K. In metal hydrides (MH), hydrogen is stored in the form of solid solution and so there is no issue of leakage. Further, metal hydride based hydrogen storage requires only low-grade thermal inputs for the gas delivery. For optimum hydrogen storage, the metal should have following desirable properties:

- High hydrogen storage capacity per unit mass and unit volume.
- Low dissociation temperature and moderate dissociation pressure.
- Moderate heat of formation to minimize the energy necessary for hydrogen release and moderate heat dissipation during the exothermic hydride formation.
- Reversibility for limited energy loss during charge and discharge of hydrogen.
- Fast reaction kinetics.
- High stability against O_2 and moisture for a long life cycle.
- Low cost of recycling and charging infrastructures.
- High safety.

1.3 Metal hydrides and thermodynamics of hydride formation

Hydrogen has the ability to interact and form chemical compounds with most of the elements in the Periodic table (metals, non–metal and metalloids). MH is formed spontaneously on exposure of metals to hydrogen at near ambient conditions and with help of catalyst to ease the reaction. Initially, the hydrogen molecules dissolve in the metal to form a solid solution of hydrogen in the

metal (α – phase) which, after reaching a steady state, undergoes transition to the metal hydride, or β – phase, by a chemical reaction with hydrogen. The formation of metal hydride and the desorption process may be written as the following equations,

In general,

$$\text{Metal} + \text{Hydrogen} \underset{\text{desorption}}{\overset{\text{absorption}}{\rightleftharpoons}} \text{Metal hydride} + \text{Heat} \tag{1.1}$$

In chemical form,

$$M + \frac{Y}{2} H_2 \Leftrightarrow MH_Y \left(\alpha - \text{phase}\right) \tag{1.2}$$

$$MH_Y + \frac{X - Y}{2} H_2 \Leftrightarrow MH_X \left(\beta - \text{phase}\right) \tag{1.3}$$

The different steps involved during the hydriding and dehydriding processes are shown in Fig. 1.1 (Muthukumar *et al.*, 2009b). In the hydriding process, more amount of heat is liberated due to exothermic reaction. The sequence of steps leading to the formation of MH consist of,

i. Physisorption of hydrogen molecules on the surface of the metal.
ii. Chemisorption and dissociation of hydrogen molecules.
iii. Surface penetration of the atomic hydrogen into bulk and formation of α – solid solution.
iv. Diffusion of hydrogen atoms through the layer of α – solid solution, involving interstitial and vacancy mechanism.
v. Hydride formation at the interface of the metal (nucleation and growth).

To retrieve the hydrogen from the metal hydride, the heat transfer fluid is supplied to hydride bed at desired desorption temperature. This process is an endothermic one. The order of the process will be reverse.

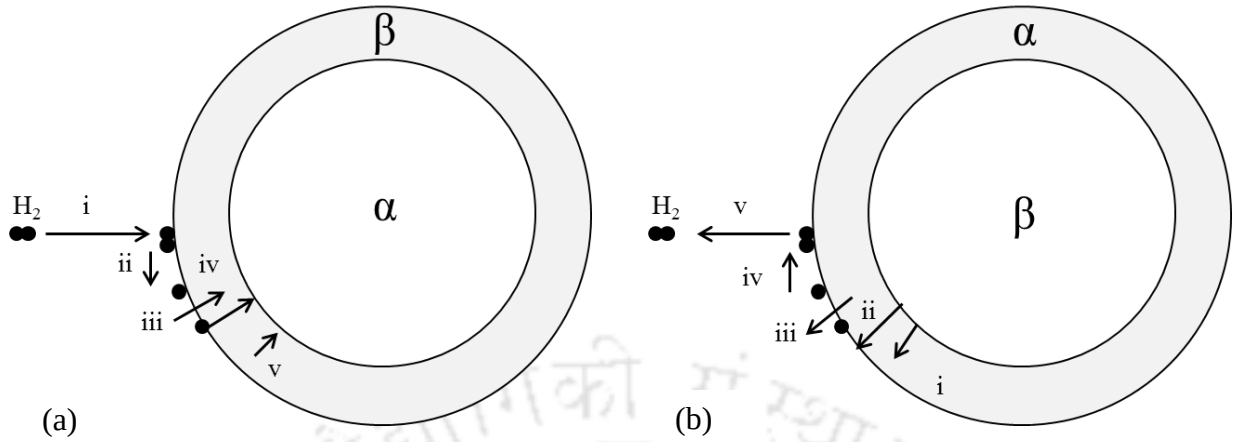

Fig. 1.1 – Different steps involved during (a) hydriding process and (b) dehydriding process.

The hydrogen – metal interaction is well understood by use of phase diagram. The Pressure – Composition – Temperature (PCT) curve relates the hydriding and dehydriding with equilibrium pressure, temperature and hydrogen concentration. The ideal PCT diagram is shown in Fig. 1.2(a). The PCT curve has three distinct phases such as α – phase, (α+β) – phase and β – phase. The α – phase represents an initial steep slope in which hydrogen molecules dissociate into atoms and penetrate into the metal surface, then diffuse through the metal lattice. As the hydrogen supply pressure increases, a small amount of hydrogen is absorbed by the metal to form a solid solution. The correlation between the pressure and the amount of hydrogen absorbed obeys the Sievert's law given by

$$x_{H_2} \alpha \sqrt{p_{H_2}} \tag{1.4}$$

According to Eq. 1.4, in α – phase, the increase in hydrogen supply pressure leads to a small amount of hydrogen dissolution. Here, the two components (metal and hydrogen) and two phases (solid and gaseous) exist at the same time. Thus, based on the Gibb's phase rule (Eq. 1.5), the degree of freedom is two, viz. temperature and pressure. At an isothermal condition (absorption temperature), the amount of hydrogen absorbed is only associated with the hydrogen supply

pressure. After reaching the steady state, formation of the metal hydride starts and the α – phase undergoes a transition phase (α + β) – phase. In the (α + β) – phase three phases exist namely a gaseous (hydrogen) phase and two solid phases (metal and metal hydride).

$$f = C - P + 2 \tag{1.5}$$

From Eq. 1.5, the degree of the freedom is one. The temperature is considered as an independent variable, the other variables are calculated as a function of temperature under equilibrium conditions. With isothermal thermal conditions, the formation of MH will occur at a constant equilibrium pressure. After all the hydride is converted to β – phase, the pressure starts raising steeply as more hydrogen is added to the system. The flat plateau region where the two phases, α – phase and β – phase coexist represents the (α+β) – phase. This flat (α+β) – region is the most important part of the PCT diagram as most of the hydrogen is absorbed in this region under a constant pressure. The slope and length of the equilibrium plateau is of particular importance for hydrogen storage application. The length of the flat region represents the amount of hydrogen that can be stored reversibly with small pressure variation. Hence, the MH with wide plateau region is advantageous for hydrogen storage applications (higher hydrogen storage capacity). It is observed from the Fig. 1.2 that the increase in temperature reduces the width of the plateau pressure. Beyond the critical temperature T_c, plateau region disappears and α – phase converts to β – phase directly and then no metal hydride will be formed. The transformation from α – phase to (α+β) – phase and from (α+β) – phase to β – phase adapts the Sieverts law. At a given temperature, the value of plateau pressure is the direct indication of thermal stability of the MH. Stability of the metal and intermetallic hydrides can be evaluated from the van't Hoff equation. It is the function of the equilibrium pressure and the absolute temperature $\left(1/T\right)$ and it's shown in Fig. 1.2.

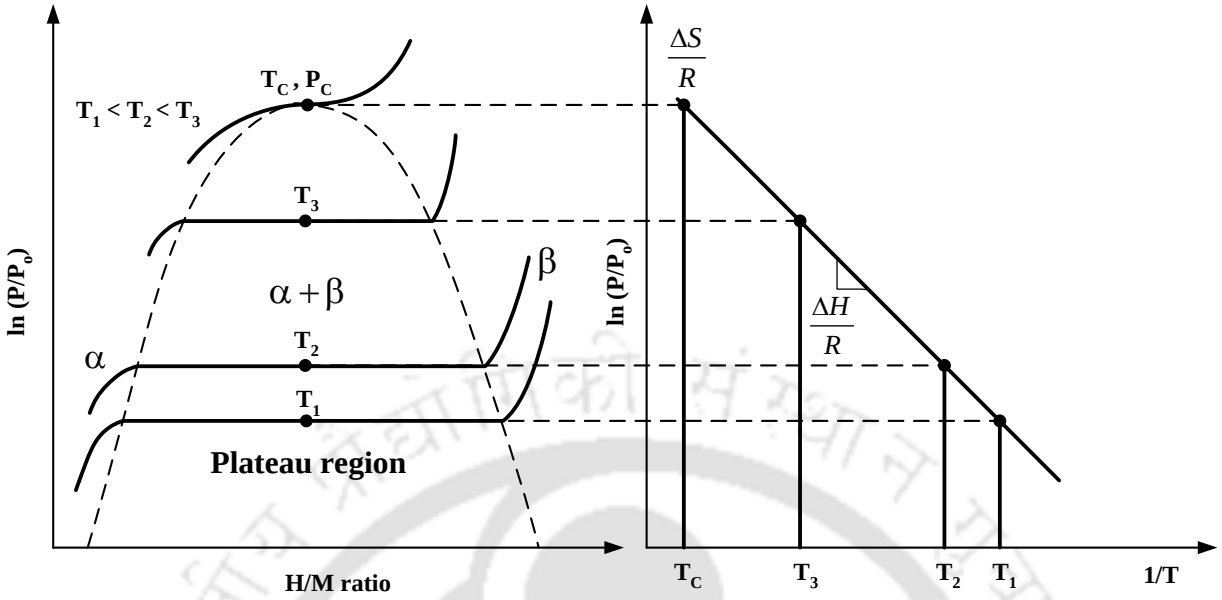

Fig. 1.2(a) - Ideal pressure-concentration-temperature diagram.

Fig. 1.2(b) - Ideal van't Hoff plot.

The negative slope and the intercept from the plot denote the enthalpy of formation (ΔH) and entropy of formation (ΔS), respectively. The real PCT i.e. Plateau slope and hysteresis have significant impact on the performance of the MH systems as shown in the Fig.1.3. The hysteresis effect is not desirable in the practical applications as at the same temperature, hydrogen is released at a pressure slightly lower during desorption than that of the absorption. Apart from the hysteresis, another factor that reduces the system efficiency is the plateau slope. In actual systems all the hydrides possess slopped plateau, the magnitude of which varies from material to material. Because of the plateau slope, the equilibrium pressure in the α+β region increases with concentration during absorption, and decrease with concentration during desorption. This reduces the usable hydrogen storage capacity, the heat and mass transfer rates also reduce with plateau slope, and resulting in poorer system performance. These irreversibility can be reduced by the substitutions of metals such as Ni, Al, Mn, etc. in the host alloy.

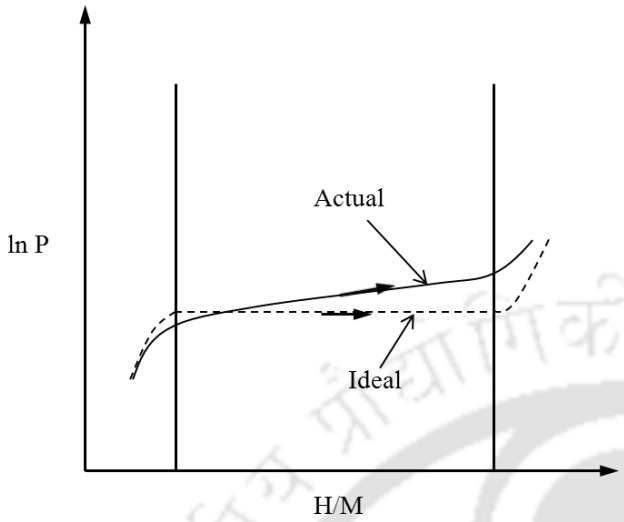

Fig. 1.3(a) - Plateau slope.

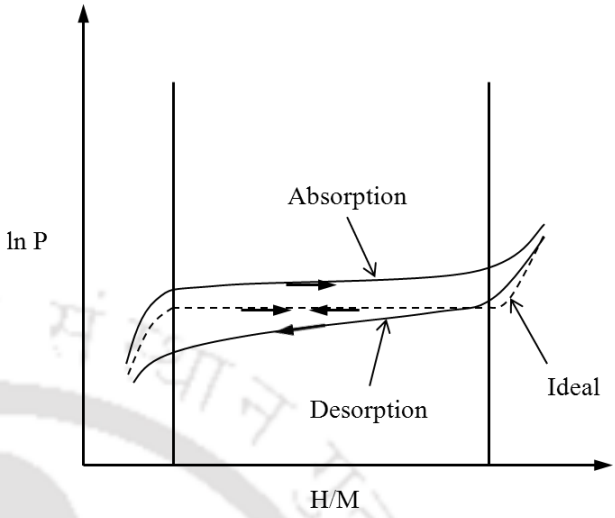

Fig. 1.3(b) - Hysteresis effect.

The hydrogen storage capacity (HSC) of MH in terms of weight percentage (wt%) can be calculated as follows:

$$wt\% = \frac{m_{H_2}}{m_a} = \frac{N_a \times \left(x_f - x_{ini}\right) \times M_{H_2}}{2 \times M_a} \times 100 \tag{1.6}$$

where N_a is the number of hydrogen atoms in the metal hydride, M_{H_2} is the molecular weight of hydrogen and M_a is the molecular weight of the metal hydride.

In other words, the hydrogen storage capacity can be written as (Sekhar *et al*., 2013):

$$HSC\left(wt\%\right) = \frac{\text{Weight of the hydrogen absorbed}}{\text{Weight of the metal hydride}} \times 100 \tag{1.7}$$

1.4 Classification of metal hydrides

Based on the strength and type of bond between the metal and hydrogen, MH have been broadly classified into three different types. They differ in their thermo – physical properties and absorption and desorption characteristics.

i. Metallic hydrides
   - Formed mainly by transition and rare earth or lanthanide group of metals.
   - It has ease hydriding and dehydriding processes.

ii. Ionic or saline hydrides
   - Ca and Mg – based hydrogen storage system and/or related applications.

iii. Covalent hydrides
   - Formed mostly by metals and metalloids of group IB to VB of the Periodic table.
   - They are low melting solids, low boiling liquids and gases with poor stability and high toxicity.
   - It is not suitable for hydrogen storage application due to its thermo – physical properties.

Among these hydrides, the metallic hydrides possess more attention for hydrogen storage application. The recent developments have been concentrated on improving the reaction kinetics of intermetallic compounds, hydrogen storage capacity and also economic feasibility. The number of intermetallic compounds has been characterized based on their enthalpy and entropy of formation and so this can be used in many engineering applications. In general, the intermetallic compounds have one or more than one elements such as A and B element. Here element A is a strong hydrogen absorber and B is a week absorber that act as a catalyst to facilitate the reaction. Based on these elements, the MH have been characterized into four

different types such as A_2B (Mg_2Ni, Zr_2Cu), AB (MgNi, TiFe), AB_2 ($TiMn_2$, $ZrMn_2$) and AB_5 ($LaNi_5$, $CaNi_5$).

1.5 Applications of metal hydrides

Several MH have been synthesized and characterized by the numerous researchers. On basis of their thermo – physical properties, MH are categorized for various engineering applications. The important properties such as enthalpy and entropy formations during the hydriding and dehydriding process are considered as the major deciding factors for selecting the MH for a specific application. The applications of MH, their required characteristics and examples of metal hydride are shown in Table 1.1. In addition, for all the applications, metal hydrides should have good cycling stability and durability.

1.6 Motivation of thesis

Hydrogen energy is a secondary energy carrier which is being considered as a replacement of fossil fuels in on-board applications. Therefore, methods to store H_2 with appropriate weight and volume are important. The development of a hydrogen storage device having light weight and high storage capacity is necessary to enable the fuel cell vehicles to replace the fossil fuel vehicles. More importantly, the developed vehicle should be operated at temperatures of 30 – 120 °C and pressures of 5 – 20 bar. The vehicle should also have a fast recharge/discharge cycle. The high gravimetric and volumetric capacities of MH make them appealing for reversible H_2 storage in on-board applications. A typical metal hydride based hydrogen storage device comprises the reactor (reaction bed) as a core component.

Table 1.1 – List of applications of MH, required characteristics and types of alloys used for the specific application

Application	**Required MH attributes**	**Examples (alloys)**
Hydrogen storage	• Desorption at low or moderate pressure and temperature. • Low enthalpy formation.	AB (ZrMoCr), AB_2 ($ZrCr_{0.4}Fe_{1.4}$), AB_5 ($MmNi_{4.5}Mn_{0.5}$)
Hydrogen storage for stationary fuel cell	• Delivery pressure range (P_d ~ 1 – 10 bar). • Low cost. • HSC > 2 wt%	TiFe, V – alloys, Mg – alloys, AB_2 alloys
Vehicular fuel storage (fuel cell and IC Engines)	• HSC > 5 wt%. • Low cost. • Rapid reaction kinetics. • P_d ~ 1 – 10 bar at ambient temperature • Low and moderate desorption temperatures.	AB_2 alloys, alanates, Mg – alloys
Heat pump/heat transformer and refrigerator	• High enthalpy formation. • Less pressure variation with increase in temperature. • Fast kinetics. • Low cost and P_d ~ 1 – 5 bar at ambient temperature • Utilization of waste heat.	AB_5 ($LaNi_5$), AB ($TiFe_{0.9}Ni_{0.1}$) based alloys
Compressor (up to ~ 500 bar)	• A high desorption pressure at moderate temperature ranges. • High thermal efficiency (i.e., high $\Delta P/\Delta T$ ratio). • Less enthalpy formation. • High pressure rise with less temperature.	$LaNi_5$, $LaNi_{4.7}Al_{0.3}$, TiFe, $TiCr_{1.8}$, $MmNi_{4.6}Al_{0.4}$
Energy storage	• Large amount of energy to be stored at low pressure without exceeding higher temperature.	Mg, MgNi, Mg_2Ni, $LaNi_{4.25}Al_{0.75}$
Electrodes/Ni – MH batteries	• P_d < 1 bar. • Reversible energy capacity. • High power density. • Low activation energy. • Economically low cost.	AB_5, AB_2, AB – based alloys
Purification, chemical separation & isotope separation	• Fast kinetics. • Low activation energy. • Low impurity and contamination. • High reaction efficiency.	Pd, V – alloys, Zr – alloys (AB_2, AB)
Sorption cryocoolers (space flight application)	• Fast kinetics. • Constant absorption plateau. • Power and reliability.	$LaNi_{4.8}Sm_{0.2}$, V-alloys, AB_5, AB_2

The design of the reactor especially considering the heat and hydrogen transfer characteristics and the selection of suitable metal hydride alloys are extremely important. In the present thesis, the performances of metal hydride based hydrogen storage device with embedded cooling system are studied. A major importance is given to the heat and mass transfer processes associated with the reaction beds.

1.7 Thesis structure

As stated earlier, the performance of MHHSD depends on the selection of metal hydride alloys and the heat and hydrogen transfer aspects of MH reaction bed at different operating conditions. The objective of the present thesis is to study the performance of the metal hydride based hydrogen storage devices at different operating conditions. This thesis is organized in 6 chapters. A brief description of the content of each of the chapters is provided below:

Chapter 1 starts with brief introduction of MH and its thermodynamic formation. The classification of MH, various engineering applications and motivation of the present work are presented in sequence.

Chapter 2 is devoted for the state-of-the-art of literature which are focused on the coupled heat and mass transfer characteristics of MHHSD during absorption and desorption processes and design and development of MHHSD. In this chapter, several experimental and numerical investigations on hydriding and dehydriding characteristics of MHHSD with various influencing parameters are discussed. Numerous thermal models, design and optimization of MHHSD, various heat transfer enhancement techniques to improve the performance of the hydrogen storage device are also reviewed. Based on the conclusions of the literature survey, objectives of the present thesis work are framed.

In chapter 3, formulation of the thermal model for predicting the coupled heat and hydrogen transfer characteristics of the hydride during both hydriding and dehydriding processes are presented.

Based on the numerical investigations, the reactors with 36 and 60 ECT's are chosen for the experimental study. Employing 2.75 kg of $LmNi_{4.91}Sn_{0.15}$, two reactors with different embedded cooling tubes (ECT) arrangements are fabricated. The details of design and activation procedure for alloys are discussed in chapter 4.

Chapter 5 described the results obtained from the numerical and experimental investigations on the hydriding and dehydriding processes of Mg_2Ni based lab-scale hydrogen storage device and $LmNi_{4.91}Sn_{0.15}$ based MHHSD with ECT at different operating conditions.

Major conclusions arrived from the present research work are presented in Chapter 6. Scope for future work and recommendations are also given in this chapter.

1.8 Summary

This chapter starts with the brief introduction of MH and its thermodynamic formation and also reports the classification of MH. The different engineering applications of MH and required important characteristics of MH and types of MH alloys used for the specific application are listed in Table 1.1. The motivation of the thesis is discussed and finally the thesis structure is also clearly explained in sequence.

Chapter 2

State-of-the-Art

2.1 Preface

Over the last three decades worldwide interest in the use of hydrogen has led to more research focus on its storage and usage. Several experimental and numerical works have been carried out on metal hydride based hydrogen storage devices (MHHSD) focusing on the improvement in heat and mass transfer characteristics of metal hydride bed during the hydriding and dehydriding processes. Simultaneous heat and mass transfer takes place with chemical reaction therefore hydriding or dehydriding process is quite complicated. The gas motion and change in physical properties add difficulties to the problem. So a lot of experimental and numerical works are stated on diverse viewpoints of the metal hydrides. Most of the reported numerical studies presume that the hydriding or dehydriding (absorption or desorption) techniques are a transient

heat conduction problem with an interior heat source and variable physical parameters. Recent developments in metal hydride technology also show that the metal hydrides provide opportunity for hydrogen storage to a high standard of safety for both mobile and stationary applications.

In this chapter, a detailed state-of-the-art on reaction kinetics of metal hydrides, coupled heat and mass transfer characteristics during the hydrogen charging/discharging processes are presented. Further, a detailed literature survey on numerical and experimental investigations of lab-scale prototype MHHSD and MHHSD with heat transfer augmentation techniques are also discussed.

2.2 The reaction kinetics on hydriding and dehydriding characteristics

In this section, the reaction kinetics on hydrogen absorption and desorption processes at various operating parameters are described. Several literatures are reported for improving the hydriding/dehydriding kinetics of a particular metal hydride.

Reilly and Wiswall (1973) experimentally studied the dehydriding kinetics of FeTi at 1 bar desorption pressure and 0 °C. They reported the hysteresis effect, the absorption and desorption isotherms at different operating temperatures. For a slight excess of Ti in the equiatomic proportion, the pressure – composition isotherms no longer exhibit the plateaus. Van Mal *et al*. (1974) reported the experimental results for the change in equilibrium pressure during hydrogen absorption and desorption processes employing $LaNi_5$. They studied the change in hydrogen sorption properties affected by replacing La or Ni in $LaNi_5$ by other metals. They also examined the desorption isotherms at 40 °C for $LaNi_4M$, where M represents Pd, Co, Fe, Cr, Ag or Cu, and for $La_{0.8}R_{0.2}N_5$, where R represents Nd, Gd, Y and Er, also Th and Zr. They

reported that the more stable was binary compound whereas the less stable was ternary hydride. Later, the similar study was carried out by Goodell *et al*. (1980). They tested the dynamic response in terms of dynamic reaction kinetics and also compared the dynamic and conventional pressure-concentration-temperature of $LaNi_5$. They reported that the reaction kinetics was reduced by substituting Co and Al in place of Ni. Employing three different alloys viz., AB, AB_5 and A_2B, the similar study was carried out by Huston and Sandrock (1980). They reported the properties of plateau pressure – temperature, hysteresis, plateau slope and hydrogen storage capacity.

Suda *et al*. (1980) studied the hydriding and dehydriding reaction rates of $LaNi_5$, $MmNi_5$, Al substituted mischmetal nickel, $TiMn_{1.5}$ and $Ti_{0.8}Zr_{0.2}Cr_{0.8}Mn_{1.2}$. They found that the addition of a small amount of more reactive hydride to a less reactive hydride was effective in improving the hydriding properties of the less reactive metal hydride. Goodell and Rudman (1983) studied the intrinsic reaction rates during hydriding and dehydriding of $LaNi_5$ at various operating pressure and absorption temperature (60 – 65 °C). Miyamoto *et al*. (1983) experimentally investigated the reaction kinetics of well activated $LaNi_5$ at constant pressure and the absorption temperatures range of 15 – 80 °C. They obtained the activation energy of 7.7 kcal/mol from the Arrhenius plot. They reported that the rate was controlled in the plateau region by the chemical reaction at an interface between unreacted core particle and the hydride. Hirata *et al*. (1983) attempted to increase the hydrogen dissociation pressure of the hydride Mg_2NiH_4 by partially substituting other alloys for Mg or Ni in Mg_2Ni. They characterized the intermetallic compounds with their hydrogen storage capacities and thermodynamic properties by a volumetric method. They found that the stability of the hydride was reduced by substituting some of the Mg by Al. They

measured the dehydriding kinetics of $Mg_{1.92}Al_{0.08}Ni$ by monitoring the change in hydrogen pressure as a function of time in a constant volume and the temperature range 200 – 300 °C. The activation energy determined by them for the dehydriding process was 84 kJ/mol.

To improve hydrogen flow and heat transfer enhancement in the reaction bed, Supper *et al*. (1984) presented an experimental study on the reaction kinetics of various AB_5 alloys for different bed thicknesses (1 – 4 mm) at different absorption temperatures (20 – 50 °C). They examined the influences of the parameters such as bed thickness, porosity and temperature which are needed for the design of fast reaction beds required in thermodynamic machines. They observed the faster reaction for 1 mm bed thickness with high porosity. Han and Lee (1987) studied the hydriding reaction kinetics of Mg_2Ni at various temperatures viz., 250 °C, 260 °C, 280 °C and 300 °C. At the initial stage of the reaction, they reported that the rate of controlling step was the forced flow. The activation energy at the later stage was ~ 19.6 kJ/mol.

Koh *et al*. (1989) compared the hydriding and dehydriding reactions of $LaNi_5$ alloy in the plateau region. They used various pressure ratios (the equilibrium pressure to supply pressure) viz., 2, 3, 4 and 5, and the sample was maintained at isothermal condition. It was revealed that the hydriding and dehydriding rates were controlled in the phase transmission region $(\alpha+\beta)$. They found the activation energy at the given supply conditions as 27 and 37 kJ/mol for the absorption and desorption processes respectively, at the pressure ratio of 2.

With the consideration of thermal effects on reaction kinetics for the design of a reactor, Wang and Suda (1990a; 1990b; 1990c) extensively reviewed both experimental and theoretical studies

on the reaction kinetics of hydriding/dehydriding processes. They proposed the hydriding and dehydriding reaction rate equation as a function of pressure of the system and the hydrogen concentration in the metal hydride. Later, employing $LaNi_{4.7}Al_{0.3}$ alloy and the step-wise method, same authors reported the hydriding and dehydriding kinetics under isochoric, variable pressure and isothermal conditions. They found that the rate constants were independent of hydrogen concentration and hydrogen pressure in $(\alpha+\beta)$ phase. Jung *et al*. (1990) investigated the reaction kinetics of Mg_2Ni in the $(\alpha+\beta)$ region. They performed the experiments in the temperature range of 280 °C - 340 °C at the pressure difference (P_O+P_{eq}) range from 1.5 to 3.0 bar. They also proposed the reaction rate equation and from their experimental study they observed that the reaction rate was controlled by the chemical reaction and the diffusion of hydrogen atom in the $(\alpha+\beta)$ region.

Employing $LaNi_5$, Nahm *et al*. (1992) experimentally estimated the reaction rate at different temperature range (20 – 60 °C) and supply pressure (5 – 20 bar). They observed that the reaction rate was linearly proportional to the reaction time at a constant temperature and pressure. They also found that the dissociate chemisorption of hydrogen molecule on the surface of $LaNi_5$ alloy was a controlled step and the activation energy of the reaction was found to be 20 kJ/mol. Martin *et al*. (1996) presented the absorption kinetics of $LaNi_{4.7}Al_{0.3}$ hydride with different pressures i.e. 4.7, 6.2 and 7.8 bar at 70 °C, for Mg hydride with different pressures viz., 3.8, 4.8, 5.6 and 11.2 bar at 320 °C. The desorption kinetics was measured for $LaNi_{4.7}Al_{0.3}$ hydride at 25 °C, 33 °C and 55 °C, for Mg hydride at 272 °C, 292 °C and 361 °C. They reported that the absorption process for $LaNi_{4.7}Al_{0.3}$ was controlled by surface reaction. Employing $MmNi_{4.2}Al_{0.8}$, Mungole and Balasubramaniam (1998) investigated the hydrogen desorption

kinetics. They studied the pressure – concentration isotherms for hydriding and dehydriding at 15 °C, 25 °C and 35 °C. With the help of Arrhenius equation, the activation energy for desorption reaction was found to be 48.09 kJ/mol.

Inomata *et al*. (1998) experimentally measured the hydriding and dehydriding reaction rates of $LaNi_5H_x$ under various temperatures (10 – 60 °C) and the supply pressures (1.2 – 7 bar). They proposed the reaction rate equation on the basis of experimental results and stated that the rate controlled step was changed from nucleation and growth process to hydrogen diffusion through the hydriding phase during hydriding process. With the isochoric measurement method, Kapischke and Hapke (1998) determined the pressure concentration isotherms, reaction enthalpies and reaction entropies of five metal hydrides (low and high temperature alloys) at desired operating parameters. With similar measurements in a closed volumetric system, Skripnyuk and Ron (2003) studied the desorption kinetics of commercially available metal hydrides (C_2, $C5_1$ and $C5_2$) within the temperature range between -20 °C and 20 °C. They applied the normalized pressure dependence method for interpreting the experimental data and to compare each other. They reported the activation energy in the above said temperature range to be 33, 40 and 30 kJ/mol for C2, $C5_1$ and $C5_2$, respectively. Paya *et al*. (2009) experimentally investigated the Pressure – Concentration isotherms for hydriding and dehydriding processes of $LmNi_{4.91}Sn_{0.15}$ and $Ti_{0.99}Zr_{0.01}V_{0.43}Fe_{0.09}Cr_{0.05}Mn_{1.5}$ at 27 °C, 42 °C and 60 °C. They compared their results with other models available in the literature such as the Zhou model, Lacher – Lototsky model and the polynomial fitting method. They developed the Zhou model in order to account for smooth transition between different phase regions. They obtained the best fit for the Zhou model and the polynomial fitting method.

With consideration of two kinetics models namely Johnson – Mehl – Avrami (JMA) and Jander diffusion model (JDM), Muthukumar *et al*. (2009a) carried out experimental investigations for predicting the hydriding kinetics of $LaNi_5$, $LaNi_{4.7}Al_{0.3}$ and $LmNi_{4.91}Sn_{0.15}$ at isothermal conditions. They found that the rate controlled mechanism in the $(\alpha+\beta)$ phase region was the diffusion of hydride atom into the metal hydride. With JDM, using Arrhenius plot, they obtained the activation energy of $LaNi_5$, $LaNi_{4.7}Al_{0.3}$ and $LmNi_{4.91}Sn_{0.15}$ alloys as 27.7, 29.1 and 28 kJ/mol, respectively. Employing $LaNi_5$, $LaNi_{4.7}Al_{0.3}$, $LmNi_{4.91}Sn_{0.15}$, $Ti_{0.99}Zr_{0.01}V_{0.43}Fe_{0.09}Cr_{0.05}Mn_{1.5}$ and $MmCo_{0.72}Al_{0.87}Fe_{0.04}Ni_{3.91}$, Muthukumar *et al*. (2009b) experimentally measured the Pressure – Concentration – Temperature (PCT) characteristics at isothermal condition during hydriding and dehydriding processes. They observed that the effect of hydrogen concentration on reaction enthalpies was more significant for the alloys having larger plateau slopes.

Recently, with consideration of 3 Titanium (Ti), 5 Misch metal (Mm) and 8 Lanthanum (La) based metal hydride alloys, Selvam *et al*. (2013) estimated the thermochemical properties (enthalpy of formation, entropy of formation) during hydriding and dehydriding reactions at different operating temperatures. From the PCT characteristics, van't Hoff plots during hydriding and dehydriding processes was constructed for different hydrogen concentrations. They reported that the average ΔH_d for Ti and La based alloys was ~ 3 – 18% higher than their respective hydriding enthalpies. The difference in reaction enthalpies during the initial and final stages of hydriding process of Ti based alloys was in the range of 7 – 9%, while the respective ranges for Mm and La based alloys were about 3 – 7.5% and 2.1 – 8.5%, respectively.

2.3 Studies on coupled heat and hydrogen transfer characteristics in lab–scale

Extensive research works have been reported on the coupled heat and hydrogen transfer characteristics of lab–scale metal hydride based hydrogen storage devices (MHHSD) at different operating conditions. Several experimental investigations and numerical simulations that were performed to evaluate the absorption/desorption (hydriding/dehydriding) characteristics of La, Lm, Mm and Mg based hydrogen storage device at desired operating conditions are reported in this section.

2.3.1 Numerical investigations on hydriding/dehydriding characteristics of MHHSD

Some of the thermal models applied for predicting the hydrogen transfer characteristics of lab-scale MHHSD are discussed in this sub-section.

During last three decades, various researchers [Lucas and Richard, 1984; Mayer *et al*., 1987; Groll *et al*., 1987; Sun and Deng, 1988; Gopal and Murthy, 1992; 1993; 1999; Gambini, 1994; Donald and Rowe, 2006b; Forde *et al*., 2009; Melnichuk *et al*., 2009] focused on the development 1-D mathematical model for predicting the heat and mass transfer characteristics of MHHSD. Mayer *et al*. (1987) developed a 1-D mathematical model for evaluating heat and mass transfer characteristics of $LaNi_{4.7}Al_{0.3}$ and $LmNi_5$ based MHHSD during hydriding process at different temperatures. The same research group (1987) also described the importance of metal hydrides properties and its requirement in metal hydride applications. They reported that the enhanced heat and mass transfer inside the hydride bed, high external heat transfer coefficient and good thermal contact between hydrides to the reactor wall increased the reaction rate.

Sun and Deng (1988) developed a transient 1-D mathematical model for predicting the heat and mass transfer characteristics of $TiMn_{1.5}$ based MHHSD during both hydriding and dehydriding processes at different temperatures (30 °C, 40 °C, 50 °C). The importance of enhanced metal hydride heat transfer and optimum design of metal hydride reactors such as rapid reaction rate and short reaction time were discussed. Gopal and Murthy (1992; 1993; 1999) presented a 1-D mathematical model for evaluating the heat and mass transfer in $LaNi_{4.7}Al_{0.3}$ based MHHSD of cylindrical configuration at desired operating conditions. Their results were obtained in non-dimensionless form. They concluded that to achieve better heat and mass transfer rates in MHHSD the hydride bed thickness should be as small as possible and the thermal conductivity of hydride bed should be improved. Later, the same authors developed a 1-D heat and mass transfer analysis of metal hydride beds of rectangular configuration. They investigated the effects of bed parameters such as bed thickness and effective thermal conductivity, and operating parameters such as cooling and heating temperatures, supply and delivery pressures on hydriding and dehydriding rates of same $LaNi_{4.7}Al_{0.3}$. They reported that the metal hydrides with smaller activation energies and higher reaction rate constants have offered shorter cycle time. Gambini (1994) presented a 1-D numerical model for predicting the transient behavior of heat and mass transfer characteristics of $MmNi_{4.5}Al_{0.5}$ and $MmNi_{4.2}Al_{0.1}Fe_{0.7}$ based MHHSD during hydriding and dehydriding processes at different operating conditions.

Several studies also reported on the development of 2-D mathematical model for predicting the transient heat and mass transfer characteristics of MHHSD during hydriding/dehydriding process. Jemni and Nasrallah (1995a, 1995b) developed a 2-D mathematical model for predicting the transient heat and mass transfer characteristics within the metal hydride bed ($LaNi_5$) during

both absorption and desorption processes at different supply pressures and temperatures. They accounted the effect of difference between the solid and gas temperature, as well as that of the variation of gas pressure in the numerical model. They used finite domain method for solving their model. The reported that the thermal equilibrium assumption was not valid in the whole reactor, the term of heat transport by convection was neglected and an increase in the effective thermal conductivity of the solid lead to significant improvement of performance for the reactor. Isselhorst (1995) numerically investigated the heat and mass transfer characteristics of $LmNi_{4.49}Co_{0.1}Al_{0.21}Mn_{0.21}$ and $LmNi_{4.85}Sn_{0.15}$ during both absorption and desorption processes. The discretization of time dependent equations was done by Crank-Nicolson scheme. They reported the transient behavior of hydrogen volume flow rate, the pressures in and between the coupled reaction beds and the temperature distributions inside the reaction bed. Their numerical results showed good agreement with the experimental results.

Nasrallah and Jemni (1997) numerically investigated the heat and mass transfer in $LaNi_5$ based MHHSD with and without three hypotheses such as both solid and gas at same temperature, effect of pressure variation in the reactor was negligible and the effect of hydrogen concentration on the equilibrium pressure was negligible. They compared the numerical results of both cases and found that these hypotheses were valid under almost all conditions. Guo and Sung (1999) developed a 2-D mathematical model to determine the conjugate heat and mass transfer of $LaNi_{4.7}Al_{0.3}$ based MHHSD. They studied the effect of heat transfer enhancement on the hydriding reaction rate by inserting Al sheets into the hydride bed. They found that the insertion of Al sheets into the bed significantly improved the reaction rate. They concluded that the thickness of hydride bed also play a significant role in the heat transfer of metal hydride bed.

Nakagawa *et al*. (2000) presented a 2-D mathematical model for evaluating the transient heat and hydrogen transfer in a $LaNi_5$ based MHHSD during hydriding and dehydriding processes at desired operating parameters. For validating the model, they assumed that the local gas temperature was equal to the bed temperature and the convection term in an energy equation for gas phase was negligible. They reported the results on velocity, temperature and composition distribution within the hydride bed.

Mat and Kaplan (2001) numerically studied a continuum mathematical model of $LmNi_5$ during hydriding process at 10 °C absorption temperature. The presented results were with isotherms and iso – concentration contours, temperature and concentration at various locations. The numerical results were compared with the experimental data reported in Mayer *et al*. (1987). Askri *et al*. (2003) studied the importance of considering the radiation effect in the mathematical model for predicting the hydriding characteristics of $LaNi_5$ and Mg based MH alloys. They have studied the time – space variations of temperature, hydride density in the reactor and determined sensitivity of some parameters (absorption coefficient, scattering coefficient, reactor wall emissivity). They observed that the effect of radiative heat transfer was significant for high temperature alloy i.e. Mg based alloys while for $LaNi_5$ alloy, it is negligible. Dogan *et al*. (2004) developed a 2-D mathematical model for investigating the complex heat and mass transfer characteristics during hydriding process at 10 °C. Using finite volume method (FVM), they solved the governing equations with fully implicit numerical scheme embodied in PHOENIC code. The numerical results showed that the hydriding performance depends on the temperature distribution in the hydride bed. They found that hydrogen must be supplied radially from both sides for a rapid filling of hydrogen.

Askri *et al*. (2004a) studied the heat and mass transfer characteristics of $LaNi_5$ based MHHSD and used a 2-D mathematical model for investigating the transient transport process of hydrogen in the two domains of a closed cylinder during hydriding process. They solved the equation numerically by the control volume based finite element method. They reported the effect of operating conditions such as dimensions of the expansion volume, height to the reactor radius ratio, and the initial hydrogen to metal atomic ratio, on the evolution of the pressure, fluid flow, temperature and the hydrogen mass. The same research group (2004b) studied a dynamic behavior of $LaNi_5$ based MHHSD during hydriding process. They described the hydrogen flow by general momentum conservation equations instead of Darcy's law. They evaluated the temperature, hydrogen concentration and hydrogen flow velocity. They also determined the effects of the reactor dimensions, the inlet diameter, the volume of the expansion part, the tank volume, the initial pressure and the amount of hydrogen in the tank on the heat and hydrogen transfer.

Ha *et al*. (2004) presented a 2-D mathematical model for predicting an unsteady heat and mass transfer characteristics of $LaNi_5$ based MHHSD during the hydriding process. They solved the mass, momentum and energy conservation equations to investigate the physical mechanism of the hydriding process using a FVM. They observed that the whole hydriding process occurred in the bed was governed and controlled by heat transfer from the hydride bed to the surrounding heat transfer fluid (HTF). They concluded that the higher thermal conductivity, smaller bed diameter and the presence of fins in the bed gave more enhanced heat transfer rate from the bed. Bilgili *et al*. (2005) numerically analyzed a 2-D mathematical model of cylindrical MHHSD filled with $LaNi_5$ which had been cooled both on internal and external surfaces. They presented

the temperature distribution and hydrogen/metal atomic ratio at different radial and axial locations. They observed that the hydride formation was occurred near the cold boundaries. For the proposed geometry, they optimized the cooling fluid rate. They extended this work to obtain the effect of porosity, mass flow rate of coolant and magnitude of the heat transfer coefficients. They stated that the high hydrogen absorption rate was obtained by the porous metal bed that has high thermal conductivity and specific heat, and by the geometry with high cooling rate as proposed in this work.

Marty *et al*. (2006) presented a 2-D numerical model for predicting the heat and mass transfer characteristics of $LaNi_5$ and Mg based MHHSD during hydriding process at 10 bar supply pressure and 27 °C. They showed the importance of 3-D modeling and also proposed the design of an industrial tank for hydrogen storage systems. Phate *et al*. (2007) reported a numerical analysis of heat and mass transfer in a cylindrical MHHSD during hydrogen sorption process using FLUENT 6.2. The effect of bulk diffusion was considered for the mass transfer in the solid phase and not considered the plateau slope and hysteresis effects of the alloy in their model. They plotted the temporal and spatial variations of temperature and concentration of hydride bed, also studied the effect of L/D ratio and porosity. They reported that the radial variations in temperature and concentration of bed were more significant than the variations along the axial direction. Gambini *et al*. (2008) developed a lumped numerical model to simulate the dynamic characteristics of $MmNi_{4.6}Fe_{0.4}$ based MHHSD during hydrogen charging and discharging processes at different supply pressures and different HTF temperatures. They reported that the time evaluation of several key parameters such as hydrogen mass flow, temperature and pressure. They compared the numerical results to the experimental data

[Muthukumar *et al*. (2005)] and found a good accord between them. They proposed the lumped model applied as a reliable prediction tool in the prototype phases of an energy system including a MHHSD.

Muthukumar's research group did few numerical investigations (Muthukumar *et al*., 2007; 2009a; 2012; Muthukumar and Ramana, 2009; 2010) and experimental studies (Sekhar *et al*., 2012; 2013) on the hydriding and dehydriding characteristics of lab–scale prototype MHHSD at IIT Guwahati. Muthukumar *et al*. (2007) developed a 2-D mathematical model for investigating the heat and mass transfer characteristics of $MmNi_{4.6}Al_{0.4}$ based MHHSD during hydrogen absorption process at different supply pressures and absorption temperatures using FLUENT 6.1.22. They reported that at the supply conditions of 30 bar and 298 K, $MmNi_{4.6}Al_{0.4}$ stored ~ 13.1 g hydrogen per kg alloy and overall heat transfer coefficient beyond 1250 $W/m^2 \cdot K$ was not beneficial. Muthukumar *et al*. (2009a) developed a 2-D numerical model for evaluation of coupled heat and mass transfer processes of $MmNi_{4.6}Fe_{0.4}$ and $MmNi_{4.6}Al_{0.4}$ during dehydriding process at various desorption temperatures (30 – 50 °C) and bed thicknesses (5 – 15 mm) using FLUENT 6.1.22. They reported the temperature and concentration profile at different radial locations, average hydride bed temperature and amount of hydrogen desorbed at different hot fluid temperatures and different bed thicknesses. They validated both the computed results with the experimental data reported in the literature Muthukumar *et al.* (2005).

The importance of employing variable wall convective boundary condition in the thermal modeling of $MmNi_{4.6}Al_{0.4}$ based MHHSD was first reported by Muthukumar and Ramana (2009, 2010). They developed a 2-D mathematical model for investigation of heat and hydrogen transfer

characteristics during hydriding and dehydriding processes at different supply pressures and HTF temperatures. They presented the changes in hydride concentration, hydride equilibrium pressure and average hydride bed temperature at various axial locations for both cases. They also reported the effect of variable wall temperature on hydrogen absorption rate for different supply pressures and hydride bed thicknesses. With 17.5 mm thickness of MH bed, they found that the maximum difference in hydriding time between the variable wall and constant wall temperature boundary conditions was ~ 300 s at 20 bar supply pressure (absorption process) and for the desorption case was about 375 s at 30 °C.

Chung and Ho (2009) investigated the influence of expansion volume (domain of pure hydrogen) and heat convection in a $LaNi_5$ based MHHSD during hydriding and dehydriding processes at various supply pressures and HTF temperatures. They accounted the concept of mass and energy conservation equation in their model. They reported that an expansion volume reduced the reaction rate by increasing thermal resistance to the heat transfer from the outside cooling/heating bath. Ye *et al*. (2010) numerically developed a 2-D mathematical model to investigate the heat and mass transfer characteristics of $Ti_{0.98}Zr_{0.02}V_{0.43}Fe_{0.09}Cr_{0.05}Mn_{1.5}$ based MHHSD during hydriding process using finite difference method (FDM). They studied the effects of supply pressure, cooling fluid temperatures, overall heat transfer coefficient and height to radius ratio on the hydrogen storage capacity. They found that hydride formation initially took place uniformly all over the hydride bed and the hydriding rate was lesser at the core region and enhanced near the boundary wall. They reported that the higher supply pressure, lower cooling fluid temperature and larger overall heat transfer coefficient, the rate of hydride formation was higher.

Few researchers have developed 3-D mathematical model for evaluating the hydriding and dehydriding characteristics of MHHSD at various operating conditions [Aldas *et al*. 2002; Askri *et al*. 2009; Krokos *et al*. 2009; Wang *et al*. 2009, Nam *et al*., 2012]. Aldas *et al*. (2002) numerically developed a 3-D mathematical model for evaluating heat and mass transfer characteristics, fluid flow and chemical reaction of $LaNi_5$ based MHHSD during hydriding process at 20 °C absorption temperature using PHOENICS code. They reported that the rate of hydride formation was a strong function of temperature. Their results showed that the fluid flow significantly influenced the temperature profile in the system; however the hydride formation was not affected by fluid flow. They also found that the hydriding process was uniform all over the bed initially, later it was slower at the core region and it was more near the boundary walls. Wang *et al*. (2009) presented a 3-D mathematical model for investigating the mass and heat transport in $LaNi_5$ based MHHSD during hydrogen absorption process at 10 bar supply pressure and 20 °C. Nam *et al*. (2012) developed a 3-D mathematical model to predict the heat and mass transport phenomena in $LaNi_5$ based MHHSD during hydriding process at the supply conditions of 10 bar and 20 °C. They reported an efficient design of the storage vessel and observed that the cooling system was critical to achieve rapid hydrogen charging performance.

Employing AX-21 super-activated carbon and sodium alanates, Kumar *et al*. (2012) developed a system simulation models for automotive on-board MHHSD, i.e. cryo – adsorption system and MHHSD. They tested the storage system ability to meet the fuel cell demand for different drives cycle and various operating conditions. They solved the mass, energy balance and absorption kinetics to compute the temperature, pressure and adsorbate concentration. They also evaluated the gravimetric and volumetric capacities of both the systems and also presented the relative

merits and demerits of the systems. Melnichuk and Silin (2012) presented the guidelines for thermal management design of MHHSD. Container heat management was one among the most relevant aspects of study in the hydrogen storage system, a limiting factor for charging and discharging rate of hydrogen. The authors proposed the general design guidelines using non–dimensional parameters to evaluate the thermodynamic and kinetic behavior in order to predict the hydriding time.

2.3.2 Heat transfer augmentation techniques

Heat exchanger provides an ample heat transfer area which aids in improving the rate of heat transfer significantly. Therefore, in the recent time, metal hydride reactors have been made similar to the heat exchangers and external fins (Donald and Rowe, 2006a; 2006b; Chung and Lin, 2009; Visaria *et al*., 2011a; 2012a), embedded filters (Mohan *et al*. 2007), embedded cooling tubes (Mohan *et al*. 2007; Freni *et al*. 2009; Krokos *et al*. 2009; Muthukumar *et al*. 2012), Al foam heat exchanger (Mellouli *et al*. 2009), circular fins and finned spiral heat exchangers (Mellouli *et al*. 2010), MHHSD with inner fins (Melnichuk *et al*. 2009), concentric tube equipped with fins (Askri *et al*. 2009) and shell and tube heat exchanger and helical coil heat exchanger (Raju and Kumar, 2012).

The ability of three different MHHSD to satisfy the minimum hydrogen delivery pressure were simulated and compared. Donald and Rowe (2006a) developed a 2-D mathematical model to investigate the heat and hydrogen transfer enhancement of $Ti_{0.98}Zr_{0.02}V_{0.43}Fe_{0.09}Cr_{0.05}Mn_{1.5}$ based MHHSD with different types of configurations viz., without heat transfer enhancements, with external fins attached to the outside of the storage tank and an annular tank designs. They found

that both the finned and annular cases were able to meet the demands. They reported that the finned case yielded higher pressures and occupies more space, while the annular case yielded acceptable pressures and required less space. The same research group (2006b) numerically investigated a 1-D resistive analysis and a 2-D transient model used to determine the impact of external fins on the ability of $LaNi_5$ based MHHSD during hydrogen desorption process at specific flow rate. They found that the fins had a large impact on the pressure of hydrogen within the container when a periodic hydrogen demand was imposed.

Employing three different heat exchanger configurations Chung and Lin (2009) numerically simulated a 2-D mathematical model for predicting the dehydriding characteristics of Mg_2Ni based MHHSD at the supply conditions of 300 °C desorption temperature and 1 bar desorption pressure. They found that the canister equipped with the concentric heat exchanger pipe and fins completed the desorption process within 1.7 hours than the other heat exchanger model. Visaria *et al*. (2011a; 2012a) presented a systematic heat exchanger design methodology for $Ti_{1.1}CrMn$ based MHHSD employing high pressure metal hydride (HPMH) and developed a design to meet the 5 min hydriding time requirement corresponding to minimum heat exchanger mass, supported by a 2-D computation model of the heat exchanger's thermal and kinetic response. They concluded that an enhancement in the thermal performance of the heat exchanger was achieved with the aid of tapered collets that helped in eliminating contact resistance between the coolant tube and the heat exchanger parts. Their computational model provided a detailed understanding of the spatial and temporal response of the hydride bed temperature, hydriding rate and heat generation rate. The same research group developed a prototype MHHSD heat exchanger filled with 4 kg of $Ti_{1.1}CrMn$ for supplying hydrogen to a fuel cell of an automobile

application. They reported that the hydrogen absorption time was ~ 5 min at the supply condition of ~ 330 bar hydrogen pressure and 0.5 °C cooling fluid temperature with a fluid flow rate of 17 l/min. They validated obtained experimental data with numerical results and found a good agreement between these results.

Mohan *et al*. (2007) simulated a 2-D model for predicting the performance of hydrogen absorption on $LaNi_5$ based MHHSD with embedded filters and embedded cooling tubes (ECT) using COMSOL Multiphysics. They studied the influencing parameter which includes hydrogen supply pressure, coolant temperature and tube side heat transfer coefficient at different operating conditions. Freni *et al*. (2009) numerically developed a 3-D mathematical model to investigate the heat and mass transfer resistance through a non-uniform pressure and temperature of $LaNi_5$ based MHHSD with ECT using COMSOL Multiphysics. They obtained the shortest absorption time of 15 min for a reactor with 12 ECT and outer cooling jackets. They also reported that the effective thermal conductivity of hydride bed improved the rate of hydrogen absorption significantly.

Krokos *et al*. (2009) presented a novel systematic approach for the optimum design to increase the heat transfer in the hydride bed and thus minimize the storage time of $LaNi_5$ based MHHSD with 9 ECT for fuel cell application at 10 bar and 17 °C. They developed a 3-D Cartesian mathematical model to predict the hydriding characteristics and validated against a 2-D cylindrical model developed by Kikkinides *et al*. (2006). They optimized the storage tank design and revealed that 90% improvement of storage time was achieved, over the case where the tank was not optimized.

Employing $MmNi_{4.6}Al_{0.4}$ based MHHSD with different configuration of embedded cooling tubes (ECT), Muthukumar *et al*. (2012) developed a 2-D thermal model to evaluate the hydriding characteristics at various operating conditions (supply pressure, HTF temperatures and overall heat transfer coefficients) using COMSOL Multiphysics. In an industrial scale MHHSD reactor with 48 ECT, they also modeled the capacity ranged between 120 – 150 kg of alloy and reported that the hydriding time significantly reduced. With Al foam heat exchanger, Mellouli *et al*. (2009) developed a 2-D mathematical model to estimate the transient heat and hydrogen transfer characteristics in $LaNi_5$ based MHHSD during hydriding process at different geometric and operating parameters. They revealed that the use of Al foam enhanced the heat transfer rate and consequently 60% improvement of the time required for 90% storage was achieved in comparison to the case without metal foam.

Employing MHHSD equipped with finned spiral tube heat exchanger, Mellouli *et al*. (2010) presented a 2-D mathematical model to optimize the heat and mass transfer characteristics of $LaNi_5$ based MHHSD for fuel cell application. They also studied the effect of the pitch, length, thickness and arrangement of fins on the hydriding performance of MHHSD. They revealed that the use of circular fins enhanced the heat transfer and consequently 66% improvement of the time required for 90% storage was achieved while compared to the case without fins. Melnichuk *et al*. (2009) developed a 1-D mathematical model to evaluate the heat and mass characteristics of a $LaNi_5$ based MHHSD with inner fins during hydriding process at the supply conditions of 12.6 bar supply pressure and 50 °C. The governing equations were simulated using FDM. The heat transfer fin design was optimized for different absorption times and container diameters applying the gradient method.

Askri *et al*. (2009) developed a 3-D computational model for investigating the coupled heat and mass transfer characteristics of $MmNi_{4.6}Al_{0.4}$ based MHHSD equipped with fins. They studied the bed parameters such as length, thickness and thermal conductivity of the fins and overall heat transfer coefficient on hydrogen storage performance of the MHHSD. They validated their computational results with the experimental data and found a good agreement between them. They also observed that the use of fins enhanced the heat transfer within hydride bed and thus 40% improvement of time required for 90% of storage was achieved. Raju *et al*. (2010) developed a Mat lab-Simulink based system model for a high pressure $Ti_{1.1}CrMn$ based MHHSD with shell and tube heat exchanger. They analyzed the both refueling and drive cycle simulations. They revealed that the heat transfer played a major influence in both refueling and drive cycle. They found that for a full-scale automotive application, a coolant flow rate of 360 l/min at 0 °C was required to charge the tank in 5 min. During drive cycle, radiator fluid flow rate of 12 l/min at 65 °C was sufficient to supply the necessary heat for complete discharge of hydrogen during driving cycle.

Visaria *et al*. (2010) studied the heat transfer and kinetics parameters influencing the design of heat exchangers for MHHSD in high pressure metal hydrides using fuel cell vehicle. They developed a new parameter called non-dimensional conductance that served as a characteristic parameter to estimate the effects of various parameters on the reaction rate. They reported that the hydrogen fill time was sensitive mostly for the effect thermal conductivity of high pressure metal hydride and coolant's temperature, followed by the contact resistance between the powder and cooling surface. Employing three different shell and tube heat exchanger design with sodium alanates as storage material, Raju and Kumar (2012) presented a systematic study to optimize the

heat exchanger design using COMSOL – MATLAB computational tool. They reported that the design of the MHHSD heat exchanger had influence on the hydrogen storage capacity, the gravimetric hydrogen storage density and the refueling time for automotive on-board MHHSD. They found that the helical coil heat exchanger was a useful design for metal hydrides with higher storage capacity, faster rate of absorption and effective in designing a feasible MHHSD.

The detailed summary of the above described literatures on the numerical investigations of coupled heat and mass transfer characteristics are presented in Table 2.1.

2.4 Experimental studies on lab-scale prototype metal hydride based hydrogen storage device

In this section, the detailed literature survey on the experimental aspects of MHHSD during hydriding and dehydriding processes are discussed.

Suda *et al*. (1983) experimentally studied the heat transfer characteristics of $MmNi_{4.54}Al_{0.51}$ based MHHSD during hydriding and dehydriding reactions at 1 bar, 40 °C desorption temperature and 4 l/min HTF rate. They solved the differential heat balance equation to predict the temperature profiles of metal hydride bed, hydrogen transfer. They compared the computed results with their experimental data and found good agreement between them. Lucas and Richards (1984) did both experimental and numerical studies on Mg based MHHSD. With consideration of heat conduction alone in energy equation, they developed a 1-D mathematical model for predicting the time taken to absorb/release of hydrogen during hydriding/dehydriding process. Due to non-availability of data on thermal conductivity and thermal diffusivity of metal

hydrides, there was a large disagreement between their predicted numerical results and experimental data. Employing $MmNi_{4.5}Al_{0.5}$, Gopal and Murthy (1995) experimentally studied the performance of the MHHSD during both absorption and desorption processes at different HTF temperatures. The results highlighted the poor performances of hydride bed and the need for enhancing the effective thermal conductivity of hydride bed. There was a good agreement between the experimental and numerically predicted heat and mass transfer rates despite some discrepancy in the hydride temperature. The discrepancy in the hydride bed temperature was due to the thermal mass of the reactor and the pressure drop through the hydride bed.

Jemni *et al*. (1999) presented the both experimental and theoretical studies of $LaNi_5$ based MHHSD. They determined the effective thermal conductivity of the hydride bed, conductance between hydride bed and fluid around the reactor, equilibrium pressure and an expression of reaction kinetics and also accounted the initial condition, the temperature and the temporal evolution of the applied hydrogen pressure. They validated the theoretical model with experimental results and found a good agreement between them.

The similar study performed by Demircan *et al*. (2005) presented the both experimental and theoretical investigation on $LaNi_5$ based MHHSD during hydrogen absorption process. They reported the temperature variations in the hydride bed. For theoretical study, they developed a 2-D mathematical model which considered complex heat and mass transfer and fluid flow. They obtained a reasonable agreement between the numerical results and experimental data.

Muthukumar *et al*. (2005) tested the performance of AB_5 alloys namely $MmNi_{4.6}Fe_{0.4}$ and $MmNi_{4.6}Al_{0.4}$ based MHHSD during hydrogen absorption and desorption processes at different supply pressures, absorption temperatures and overall heat transfer coefficients. They observed that pressure at given absorption temperature, the absorption rate and storage capacity were found to increase with supply. At 35 bar supply pressure and absorption temperature of 15 °C, $MmNi_{4.6}Fe_{0.4}$ alloy stored about 1.6 wt%, while $MmNi_{4.6}Al_{0.4}$ stored ~1.3 wt%. Higher values of heat transfer coefficient yielded better hydrogen transferred rates during absorption and desorption processes. They also studied desorption characteristics of both the alloys and the desorption rate was found to be faster at higher hot fluid temperatures. They reported the desorption time to complete the desorption process for $MmNi_{4.6}Fe_{0.4}$ alloy as ~ 75 s and for $MmNi_{4.6}Al_{0.4}$ alloy as ~ 250 s at 50 °C. The same research group (2008) tested the Mg_2Ni based MHHSD during absorption and desorption processes at different HTF temperatures and supply pressures. They found that the maximum storage capacity (3.67 wt%) was attained at 20 bar supply pressure and 300 °C absorption temperature. They also studied the hydriding and dehydriding characteristics of small sample of 5g (Mg_2Ni) alloy at desired supply conditions and found that the rate of absorption was faster than the desorption rate.

Dhaou *et al*. (2007) studied both experimental and numerical investigations of heat and mass transfer characteristics of $LaNi_5$ during hydrogen desorption process at different HTF temperatures. They concluded that the heating fluid temperature was found to have a significant effect on the hydrogen desorption rate. They also validated their numerical results with the experimental data and found a reasonable agreement between them. With same base dimensions, employing three different cylindrical reactors, at different charging pressures and

cooling techniques, Kaplan (2009) investigated the effects of heat transfer augmentation during charging process of $LaNi_5$ based MHHSD. They revealed that the lowest hydride bed temperature and the fastest rate of hydrogen absorption were obtained for the reactor with water cooled spirally. They showed that the charging of hydride reactors was mainly heat transfer rate dependent and the reactor with better cooling exhibited the fastest charging characteristics. Forde *et al*. (2009) presented both experimental and numerical investigations on the thermal behavior of $La_{0.83}Ce_{0.10}Pr_{0.04}Nd_{0.03}Ni_{4.40}Al_{0.60}$ based MHHSD. They reported that the absorption and desorption times for the reactor were dependent on both charging and discharging pressure and also on HTF temperature. Melnichuk *et al*. (2010) experimentally and numerically evaluated the performance of MHHSD during discharging process at different discharge flow rates and discharge pressures. They also developed a 1-D numerical model for predicting the heat transfer at radial direction using FDM. They compared both numerical and experimental results for validation of their numerical model and found a good agreement.

Sekhar *et al*. (2012; 2013) tested the performance of Mg + 30 % $MmNi_5$ based thermal energy storage device at various supply pressures and temperatures. They reported the maximum amount of heat stored was 0.714 MJ/kg at T_a = 150 °C and P_s = 20 bar. Recently, the same research group has performed the experimental study on the Mg + 30% $MmNi_5$ and $MmNi_{4.08}Co_{0.2}Mn_{0.62}Al_{0.1}$ based hydrogen storage device at different absorption/desorption temperature. They reported that the maximum hydrogen storage capacities of Mg + 30% $MmNi_5$ at P_s = 20 bar and T_a = 150 °C and $MmNi_{4.08}Co_{0.2}Mn_{0.62}Al_{0.1}$ at P_s = 30 bar, and T_a = 30 °C are 2.5 wt% and 1.2 wt%, respectively.

2.4.1 Experimental studies on MHHSD with heat transfer enhancement techniques

To reduce the charging/discharging time (absorption/desorption time) of MHHSD, more attention has been paid to the design of MH reactors. In this section, some of the important literatures about the development of MHHSD with various heat transfer augmentation techniques such as capillary bundle heat exchanger (Linder *et al*., 2010), Cu finned spiral heat exchanger (Dhaou *et al*., 2011), coiled – tube and modular tube fin heat exchanger (Visaria and Mudawar, 2011b; 2012b; 2012c), spiral finned and finned tube heat exchanger (Souahlia *et al*., 2011), heat exchanger (Johnson *et al*., 2012) are described. With capillary tube bundle heat exchanger, Linder *et al*. (2010) experimentally studied the influencing parameters on the dynamic characteristic of $LmNi_{4.91}Sn_{0.15}$ based MHHSD during dehydriding process at different HTF temperatures and different HTF flow rates. They reported that the intrinsic desorption kinetics of the metal hydride would limit the reaction bed dynamics of fast reaction metal hydride bed. Employing MHHSD with Cu finned spiral heat exchanger, Dhaou *et al*. (2011) experimentally investigated the hydriding/dehydriding characteristics of $LaNi_5$ based MHHSD during hydriding and dehydriding processes at various HTF temperatures and HTF flow rates. For low HTF/high temperatures and HTF flow rates, they reported that the absorption/desorption time of MHHSD was reduced significantly. With two different heat exchangers (spiral finned and finned tube) of $LaNi_5$ based MHHSD, Souahlia *et al*. (2011) tested the hydriding characteristics at different HTF temperatures and hydrogen supply pressures. They found that the hydriding rate was more in spiral finned heat exchanger than in finned tube heat exchanger.

Employing 4 kg of $Ti_{1.1}CrMn$ (high pressure alloy), Visaria and Mudawar (2011b; 2012b) experimentally studied the development and thermal performance of a coiled–tube heat

exchanger for a fuel cell integrated MHHSD during hydriding process. Experimental study was performed to evaluate the influence of different operating conditions on the heat removal rate during hydriding process. They showed that the distance of metal hydride particles from the coolant tube had the most dominant influence on the hydriding rate. They achieved the shortest hydriding time at low coolant temperature (2.5 °C) and higher hydrogen pressure (270 bar). By comparing tests with and without coolant flow, they observed that the heat exchanger reduces hydriding time by 75% that occupied only 7% of the storage pressure vessel volume. The same research group has developed a 3-D numerical model for solving the coupled heat diffusion and hydriding reaction equations of $Ti_{1.1}CrMn$ based MHHSD. Their numerical model proved that coolant temperature had the greatest influence on the time needed to complete the hydriding reaction.

Visaria and Mudawar (2012c) presented both experimental and theoretical investigations of dehydriding performances of $Ti_{1.1}CrMn$ based MHHSD with modular tube fin and simpler coiled tube design. The performance test was carried out to investigate the influence of heating fluid flow rate and fluid temperature on the desorption rate. They observed that dehydriding rate was accelerated by increasing the fluid temperature and/or rate of pressure drop. They found that the higher heat transfer rates enabled the modular tube fin design to achieve faster rate of hydrogen desorption. They also developed 2-D and 3-D models using FLUENT to predict the spatial and temporal variations of hydride bed temperature.

Johnson *et al*. (2012) designed, fabricated and examined a vehicle-scale hydrogen storage system using sodium alanates. They developed a computational model of the system to investigate the

coupled heat and mass transfer characteristics. Module heat exchange systems were optimized using multi-dimensional models of coupled fluid dynamics and heat transfer. They reported that the fluid flow distribution was a key aspect of the design for hydrogen storage modules and numerical simulations were used to balance heat transfer with fluid pressure requirements.

The detailed summary of the above described literatures on experimental investigations of hydriding and dehydriding characteristics are reported in Table 2.2.

Table 2.1 – Summary on numerical investigations of heat and hydrogen transfer characteristics in lab-scale MHHSD

Author(s) and Year	Contributions
Mayer *et al*. (1987)	• Developed a 1-D mathematical model for evaluating heat and mass transfer characteristics of $LaNi_{4.7}Al_{0.3}$ and $LmNi_5$ based MHHSD during hydriding process at different temperatures.
Sun and Deng (1988)	• Developed an unsteady 1-D mathematical model for predicting the heat and mass transfer characteristics of $TiMn_{1.5}$ based MHHSD during both hydriding and dehydriding processes • Reported the importance of enhanced metal hydride heat transfer and optimum design of metal hydride reactors to enhance the hydriding rate.
Gopal and Murthy (1992; 1993; 1999)	• Presented a 1-D mathematical model for evaluating the heat and mass transfer in $LaNi_{4.7}Al_{0.3}$ based MHHSD of cylindrical configuration at desired operating conditions. • Reported that the metal hydrides with smaller activation energies and higher reaction rate constants have offered shorter cycle time.
Gambini (1994)	• Presented a 1-D numerical model for the transient behavior of heat and mass transfer characteristics of $MmNi_{4.5}Al_{0.5}$ and $MmNi_{4.2}Al_{0.1}Fe_{0.7}$ based MHHSD during hydriding and dehydriding processes at different operating conditions.
Jemni and Nasrallah (1995a; 1995b)	• Developed a 2-D mathematical model for predicting the transient heat and mass transfer characteristics within the metal hydride bed ($LaNi_5$) during both absorption and desorption processes at different supply pressures and temperatures.
Isselhorst (1995)	• Numerically investigated the heat and mass transfer characteristics of $LmNi_{4.49}Co_{0.1}Al_{0.21}Mn_{0.21}$ and $LmNi_{4.85}Sn_{0.15}$ during both absorption and desorption processes.
Nasrallah and Jemni (1997)	• Numerically investigated the heat and mass transfer in $LaNi_5$ based MHHSD with and without three hypotheses such as both solid and

Author(s) and Year	Contributions
	gas at same temperature, effect of pressure variation in the reactor was negligible and the effect of hydrogen concentration on the equilibrium pressure was negligible.
Guo and Sung (1999)	• Developed a 2-D mathematical model to determine the conjugate heat and mass transfer of $LaNi_{4.7}Al_{0.3}$ based MHHSD. • Studied the effect of heat transfer enhancement on the hydriding reaction rate by inserting Al sheets into the hydride bed.
Mat and Kaplan (2001)	• Numerically studied a continuum mathematical model of $LmNi_5$ during hydriding process at 10 °C absorption temperature.
Askri *et al*. (2003)	• Studied the importance of considering the radiation effect in the mathematical model for predicting the hydriding characteristics of $LaNi_5$ and Mg based MH alloys.
Askri *et al*. (2004a; 2004b)	• Studied a dynamic behavior of $LaNi_5$ based MHHSD during hydriding process. • Darcy law has been accounted in the mathematical model.
Dogan *et al*. (2004)	• Developed a 2-D mathematical model for investigating the complex heat and mass transfer characteristics during hydriding process at 10 °C.
Ha *et al*. (2004)	• Numerically studied a 2-D mathematical model for unsteady heat and mass transfer characteristics of $LaNi_5$ based MHHSD during the hydriding process. • Concluded that the higher thermal conductivity, smaller bed diameter and also the presence of fins in the bed provide better heat transfer rate from the bed.
Bilgili *et al*. (2005)	• Numerically analyzed a 2-D mathematical model of cylindrical MHHSD filled with $LaNi_5$ which had been cooled both on internal and external surfaces. • Higher the thermal conductivity and specific heat of the hydride bed and thus it increases the hydriding rate.

Author(s) and Year	**Contributions**
Gambini *et al*. (2008)	• Developed a lumped numerical model to simulate the dynamic characteristics of $MmNi_{4.6}Fe_{0.4}$ based MHHSD during hydrogen charging and discharging processes at different supply pressures and different HTF temperatures.
Muthukumar *et al*. (2007; 2009a)	• Developed a 2-D mathematical model for investigating the heat and mass transfer characteristics of $MmNi_{4.6}Al_{0.4}$ based MHHSD during hydriding and dehydriding processes at different supply pressures and absorption temperatures using FLUENT 6.1.22.
Muthukumar and Ramana (2009; 2010)	• Reported the importance of employing variable wall convective boundary condition in the thermal modeling of $MmNi_{4.6}Al_{0.4}$ based MHHSD during hydriding and dehydriding processes.
Chung and Ho (2009)	• Investigated the influence of expansion volume (domain of pure hydrogen) and heat convection in a $LaNi_5$ based MHHSD during hydriding and dehydriding processes at various supply pressures and HTF temperatures.
Ye *et al*. (2010)	• Numerically developed a 2-D mathematical model to investigate the heat and mass transfer characteristics of $Ti_{0.98}Zr_{0.02}V_{0.43}Fe_{0.09}Cr_{0.05}Mn_{1.5}$ based MHHSD during hydriding process using finite difference method. • For the higher supply pressure, lower cooling fluid temperature and larger overall heat transfer coefficient, the rate of hydride formation was higher.
Aldas *et al*. (2002)	• Numerically investigated a 3-D mathematical model for evaluating heat and mass transfer characteristics, fluid flow and chemical reaction of $LaNi_5$ based MHHSD during hydriding process at 20 °C absorption temperature using PHOENICS code.
Wang *et al*. (2009)	• Studied a 3-D mathematical model to investigate the mass and heat transport in $LaNi_5$ based MHHSD during hydrogen absorption process at 10 bar supply pressure and 20 °C.

Author(s) and Year	**Contributions**
Nam *et al*. (2012)	• Developed a 3-D mathematical model to predict the heat and mass transport phenomena in $LaNi_5$ based MHHSD during hydriding process at the supply conditions of 10 bar and 20 °C.
Donald and Rowe (2006a)	• Developed a 2-D mathematical model to investigate the heat and hydrogen transfer enhancement of $Ti_{0.98}Zr_{0.02}V_{0.43}Fe_{0.09}Cr_{0.05}Mn_{1.5}$ based MHHSD with different types of configurations viz., without heat transfer enhancements, with external fins attached to the outside of the storage tank and an annular tank designs.
Chung and Lin (2009)	• Numerically simulated a 2-D mathematical model for predicting the dehydriding characteristics of Mg_2Ni based MHHSD with three different heat exchanger configurations at the supply conditions of 300 °C desorption temperature and 1 bar desorption pressure. • The canister equipped with the concentric heat exchanger pipe and fins completed the desorption process within 1.7 hours than the other heat exchanger model.
Visaria *et al*. (2011a; 2012a)	• Presented a systematic heat exchanger design methodology for $Ti_{1.1}CrMn$ based MHHSD employing high pressure metal hydride (HPMH) and developed a design to meet the 5 min hydriding time requirement corresponding to minimum heat exchanger mass, supported by a 2-D computation model of the heat exchanger's thermal and kinetic response.
Mohan *et al*. (2007)	• Simulated a 2-D model for predicting the performance of hydrogen absorption on $LaNi_5$ based MHHSD with embedded filters and ECT using COMSOL Multiphysics.
Freni *et al*. (2009)	• Numerically developed a 3-D mathematical model to investigate the heat and mass transfer resistance through a non-uniform pressure and temperature of $LaNi_5$ based MHHSD with ECT using COMSOL Multiphysics.

Author(s) and Year	**Contributions**
Krokos *et al*. (2009)	• Presented a novel systematic approach for the optimum design to increase the heat transfer in the hydride bed and thus to minimize the storage time of $LaNi_5$ based MHHSD with 9 ECT.
Muthukumar *et al*. (2012)	• Developed a 2-D thermal model to evaluate the hydriding characteristics of $MmNi_{4.6}Al_{0.4}$ based MHHSD with ECT using COMSOL Multiphysics. • Presented a model for an industrial scale MHHSD with capacity of 120 – 150 kg of alloy for the prediction of hydriding performance.
Mellouli *et al*. (2009)	• Developed a 2-D mathematical model to estimate the transient heat and hydrogen transfer characteristics in $LaNi_5$ based MHHSD with Al foam heat exchanger.
Mellouli *et al*. (2010)	• Presented a 2-D mathematical model to optimize the heat and mass transfer characteristics of $LaNi_5$ based MHHSD equipped with finned spiral tube heat exchanger.
Melnichuk *et al*. (2009)	• Developed a 1-D mathematical model to evaluate the heat and mass transfer characteristics of a $LaNi_5$ based MHHSD with inner fins during hydriding process.
Askri *et al*. (2009)	• Developed a 3-D computational model for investigating the coupled heat and mass transfer characteristics of $MmNi_{4.6}Al_{0.4}$ based MHHSD equipped with fins.
Raju *et al*. (2010)	• Developed a Mat lab-Simulink based system model for a high pressure $Ti_{1.1}CrMn$ based MHHSD with shell and tube heat exchanger.
Visaria *et al*. (2010)	• Studied the heat transfer and kinetics parameters influencing the design of heat exchangers for MHHSD in high pressure metal hydrides using fuel cell vehicle.
Raju and Kumar (2012)	• Presented a systematic study to optimize the heat exchanger design using COMSOL – MATLAB computational tool.

Table 2.2 – Summary on experimental investigations of heat and hydrogen transfer characteristics in lab-scale MHHSD

Author(s) and Year	Contributions
Suda *et al*. (1983)	• Experimentally studied the heat transmission analysis of $MmNi_{4.54}Al_{0.51}$ based MHHSD during hydriding and dehydriding reactions at 1 bar, 40 °C desorption temperature and 4 l/min HTF rate.
Gopal and Murthy (1995)	• Experimentally studied the performance of $MmNi_{4.5}Al_{0.5}$ based MHHSD during both absorption and desorption processes at different HTF temperatures.
Jemni *et al*. (1999)	• Presented the both experimental and theoretical studies of $LaNi_5$ based MHHSD during hydriding and dehydriding processes.
Demircan *et al*. (2005)	• Presented both experimental and theoretical investigation on $LaNi_5$ based MHHSD during hydrogen absorption process.
Muthukumar *et al*. (2005; 2008)	• Tested the performance of $MmNi_{4.6}Fe_{0.4}$ and $MmNi_{4.6}Al_{0.4}$ based MHHSD during hydrogen absorption and desorption processes at different supply pressures, absorption temperatures and overall heat transfer coefficients. • At 35 bar absorption pressure and absorption temperature 15 °C, $MmNi_{4.6}Fe_{0.4}$ alloy stored was ~ 1.6 wt%, while $MmNi_{4.6}Al_{0.4}$ stored was ~1.3 wt%. • The desorption time to complete the desorption process for $MmNi_{4.6}Fe_{0.4}$ alloy was ~ 75 s and for $MmNi_{4.6}Al_{0.4}$ alloy was ~ 250 s at 50 °C. • Tested the Mg_2Ni based MHHSD during absorption and desorption processes at different HTF temperatures and supply pressures. • The maximum storage capacity (3.67 wt%) was attained at 20 bar supply pressure and 300 °C absorption temperature.

Author(s) and Year	**Contributions**
Dhaou *et al*. (2007)	• Presented both experimental and numerical investigations on heat and mass transfer aspects of $LaNi_5$ based MHHSD during hydrogen desorption process at different HTF temperatures.
Kaplan (2009)	• Investigated the effects of heat transfer augmentation during charging process of $LaNi_5$ based MHHSD. • Revealed that the lowest hydride bed temperature and the fastest rate of hydrogen absorption were obtained for the reactor with water cooled spirally.
Forde *et al*. (2009)	• Presented both experimental and numerical investigation of the transient hydrogen charging and discharging rates and thermal behavior of $La_{0.83}Ce_{0.10}Pr_{0.04}Nd_{0.03}Ni_{4.40}Al_{0.60}$ based MHHSD.
Melnichuk *et al*. (2010)	• Experimentally and numerically evaluated the performance of MHHSD during discharging process at different discharge flow rates and discharge pressures.
Sekhar *et al*. (2012; 2013)	• Tested the performance of Mg + 30 % $MmNi_5$ based thermal energy storage device at various supply pressures and temperatures. • Performed the experimental study on the Mg + 30% MmNi5 and $MmNi_{4.08}Co_{0.2}Mn_{0.62}Al_{0.1}$ based hydrogen storage device at different absorption/desorption temperature.
Linder *et al*. (2010)	• Experimentally studied the influencing parameters on the dynamic characteristic of $LmNi_{4.91}Sn_{0.15}$ based MHHSD with capillary tube bundle heat exchanger during dehydriding process at different HTF temperatures and different HTF flow rates.
Dhaou *et al*. (2011)	• Experimentally investigated the hydriding/dehydriding characteristics of $LaNi_5$ based MHHSD with Cu finned spiral heat exchanger during hydriding and dehydriding processes at various HTF temperatures and HTF flow rates.
Souahlia *et al*. (2011)	• Tested the hydriding characteristics of $LaNi_5$ based MHHSD with two different heat exchangers (spiral finned and finned tube) at

Author(s) and Year	Contributions
	different HTF temperatures and hydrogen supply pressures. • The hydriding rate was more in spiral finned heat exchanger than in finned tube heat exchanger.
Visaria and Mudawar (2011b; 2012b)	• Experimentally studied the development and thermal performance of 4 kg of $Ti_{1.1}CrMn$ based MHHSD with a coiled–tube heat exchanger during hydriding process. • Reported the shortest hydriding time at low coolant temperature (2.5 °C) and higher hydrogen pressure (270 bar). • Developed a 3-D numerical model for solving the coupled heat diffusion and hydriding reaction equations of $Ti_{1.1}CrMn$ based MHHSD
Visaria and Mudawar (2012c)	• Presented both experimental and theoretical investigations on the dehydriding performances of $Ti_{1.1}CrMn$ based MHHSD with modular tube fin and simpler coiled tube design. • The higher heat transfer rates enabled the modular tube fin design to achieve faster rate of hydrogen desorption.

2.5 Some metal hydride reactor designs reported in the literature

The schematic view of MHHSD designs reported in the literature are given in Fig. 2.1. These lab-scale prototype reactors were used for studying the hydriding and dehydriding characteristics of various MH alloys at different operating conditions. Several heat transfer enhancement techniques viz, capillary bundle heat exchanger (Linder et al., 2010), Cu finned spiral heat exchanger (Dhaou et al., 2011), coiled-tube (Visaria and Mudawar, 2012) and modular tube fine heat exchanger (Shouahlia et al., 2011) proposed in the literature are also shown in. Fig.2.1.

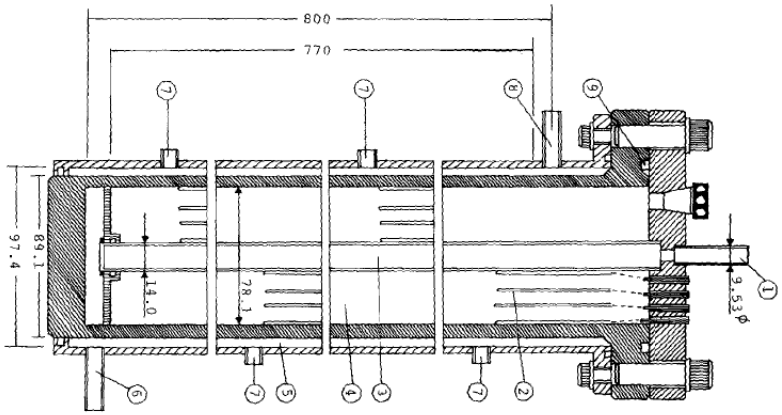

1. Hydrogen gas inlet; 2. Pipes of diameter 1mm for the thermocouple port; 3. Sintered metal filter (2µm); 4. Metal hydride bed; 5. Cooling-heating jacket; 6. Fluid inlet; 7. Pipes for thermocouple ports; 8. Fluid outlet; 9. O-ring seal.

(A) The details of the hydride test bed [Suda *et al*., 1983]

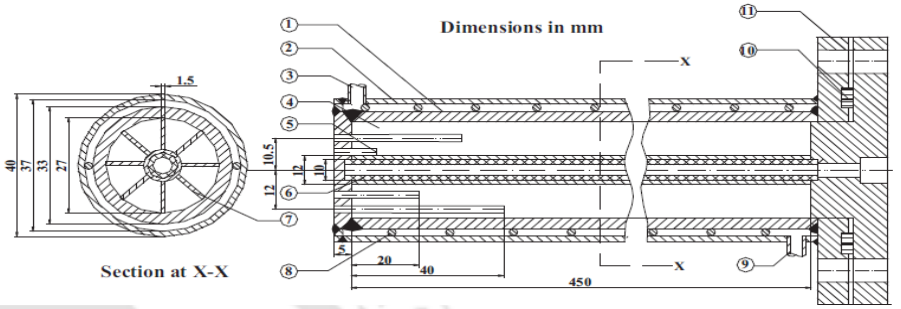

1. Reactor wall; 2. HT fluid jacket; 3. HT fluid inlet; 4. Metal hydride; 5. Thermocouple; 6. Filter; 7. Copper fins; 8. Copper wire; 9. HT fluid outlet; 10. Teflon wahser; 11. Flange (not to scale)

(B) Schematic of the cylindrical reactor [Muthukumar *et al*., 2005]

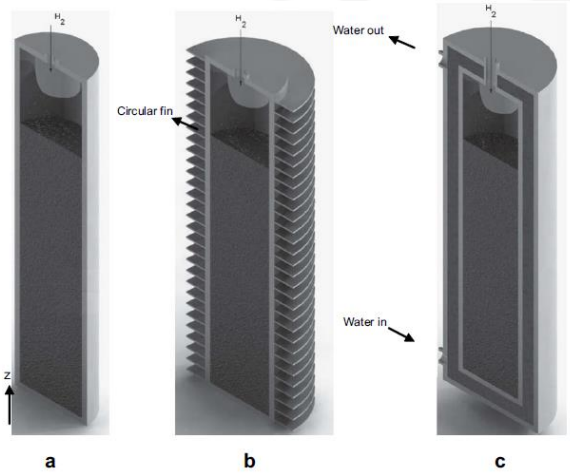

(C) Cross section of three different reactors (a) reactor 1 (b) reactor 2 (c) reactor 3 [Kaplan., 2009]

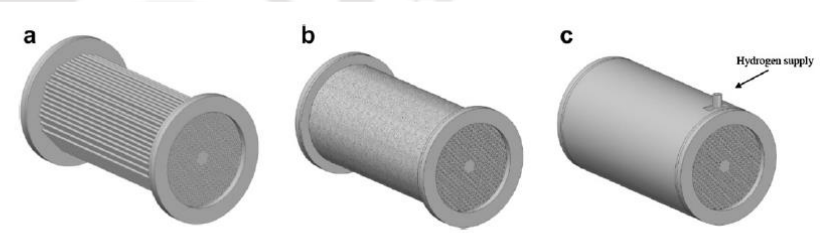

(length:135 mm, diameter 65 mm)

(D) Capillary tube bundle reactor with three different views [Linder *et al*., 2010]

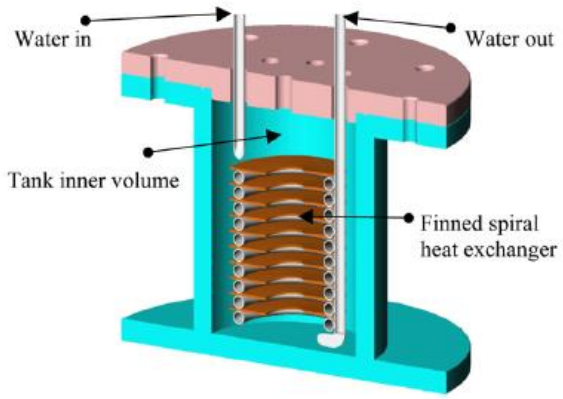

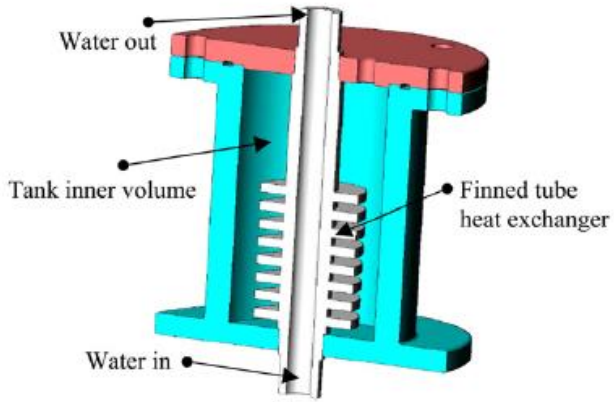

(110 mm height and 80 mm diameter)

(E) Cross section of storage tank designs T_1 and T_2 [Souahlia *et al*., 2011]

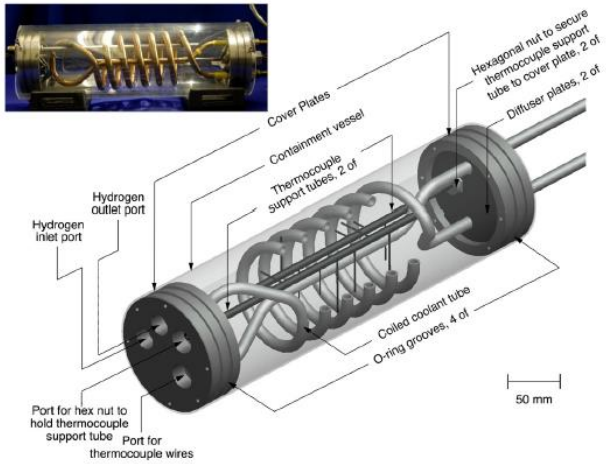

(F) Detailed 3-D modelling of containment vessel/heat exchanger assembly [Visaria and Mudawar., 2012]

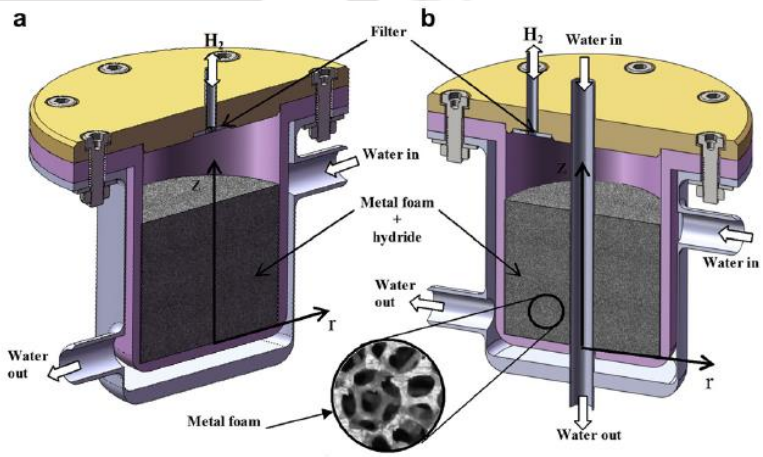

(G) Schematic of metal hydrogen storage tank with foam [Mellouli *et al*., 2009]

Fig. 2.1 – The schematic view of the metal hydride reactor designs reported in the literature

2.6 Literature closure

From the literature survey, the following conclusions are made.

- Many reaction kinetics models and reaction rate equations are available in the literature and these are mostly alloy dependent. Therefore, for the simulation of MHHSD, a generalised reaction kinetics equation which can be applied for variety of MH alloys should be employed.

- Most of the reported heat and mass transfer studies on MHHSD are carried out by considering the constant wall temperature boundary conditions, without considering the effects of hysteresis and plateau slope of the Pressure – Concentration characteristics of metal hydride alloys.

- Earlier studies on hydrogen charging/discharging behavior of MHHSD are mainly concerned with investigating the effects of supply pressure, absorption/desorption temperatures, mass flow rate of cooling/heating fluid (heat transfer fluid) and overall heat transfer coefficient on the hydrogen absorption/desorption rate.

- Few experiments (Linder *et al*., 2010; Dhaou *et al*., 2011; Visaria and Mudawar, 2011b; 2012b; 2012c; Souahlia *et al*., 2011; Johnson *et at*., 2012) and numerical simulations (Donald and Rowe, 2006a; 2006b; Chung and Lin, 2009; Visaria *et al*., 2010; 2011a; 2012a; Mohan *et al*., 2007; Freni *et al*., 2009; Krokos *et al*., 2009; Muthukumar *et al*., 2012; Mellouli *et al*., 2009; 2010; Melnichuk *et al*., 2009; Askri *et al*., 2009; Raju and Kumar, 2012) have been carried out by adopting various heat transfer enhancement

methods to improve the heat transfer in the MH reaction bed. Some of the heat transfer enhancement techniques such as different types of heat exchangers and different configurations of cooling/heating tubes arrangements have been proposed to improve the hydriding/dehydriding rate and to reduce the absorption/desorption time of the MHHSD.

- Few researchers have optimized the design of reactors and cooling tubes arrangement inside the hydride bed. Previous works reported in the literatures enlighten the absorption/desorption characteristics mainly influenced by heat transfer fluid (HTF) temperatures and its fluid flow rates of metal hydride based hydrogen storage devices (MHHSD).

- The reported works are mainly focused on the improvement of the dynamic heat and hydrogen transfer characteristics of MH bed during absorption and desorption processes in order to achieve shorter cycle time for charging/discharging of hydrogen to/from the MHHSD employing a simple reactor geometry.

- Askri *et al*. (2003) studied the importance of considering the radiation effect in the mathematical model for predicting the hydriding characteristics of $LaNi_5$ and Mg based MH alloys. They observed that the effect of radiative heat transfer is significant for high temperature alloy i.e. Mg based alloys while for $LaNi_5$ alloy, it is negligible. However, they have not validated the numerical results and also not presented the effect of various operating parameters on the hydrogen storage performances of the system. For high temperature MH alloys, inclusion of the radiative heat flux term in the energy equation to

predict the temperature in the MH reaction bed is essential. No mathematical model (except Askri *et al*. (2003)) is reported with inclusion of radiative heat flux term in the energy equation.

- Most of the reported studies are limited only to the lab – scale prototype reactors (considered about 1 kg of alloy). However, Visaria *et al*. (2010; 2011a; 2011b; 2012a; 2012b; 2012c) research group studied the hydriding performance of Ti based MHHSD with 4 kg alloy; they tested the MHHSD only at a higher pressure range from 70 to 330 bar. This shows that there is a lack of studies on MHHSD with ECTs at lower supply pressures in the range of 5 – 30 bar and at near ambient temperature.

- From the literature survey, it is observed that there is a lack of profound experimental and numerical studies on MHHSD with embedded cooling tubes (ECT) during absorption and desorption of hydrogen. The performance studies on MHHSD with ECTs at lower supply pressures in the range of 5 – 30 bar and at near ambient temperature (hydriding process), different desorption temperatures and hot fluid (oil, water) flow rates are much needed.

- No 3-D mathematical model on the hydriding and dehydriding performances of MHHSD with ECT is reported in the literature. Hence, a detailed numerical simulation is required to improve the hydriding and dehydriding rates of the MHHSD.

In the view of above closure of literature review, the following aspects are considered in the Ph.D. thesis work:

- To study the absorption and desorption characteristics of lab-scale prototype MHHSD by considering the volumetric radiation effect in the energy equation.
- To develop a 2-D mathematical model for optimizing the number of embedded cooling tubes (ECT) and their arrangements in a metal hydride based hydrogen storage device (MHHSD).
- To develop a 3-D mathematical model for predicting the absorption and desorption characteristics of MHHSD with optimized configuration of ECT at different operating conditions.
- To test the performances of absorption and desorption characteristics of MHHSD with ECT at various operating conditions.
- To validate the numerical results with experimental data.

2.7 Summary

In this chapter, the detailed literature survey on the reaction kinetics of MH, experimental and numerical investigations of coupled heat and hydrogen transfer characteristics of MHHSD during hydriding/dehydriding process are reported. Few studies reported on heat transfer enrichment techniques within MH beds are also reviewed. The detailed summary on both numerical and experimental investigations on hydriding/dehydriding characteristics of lab-scale MHHSD is discussed. The literature closure is reported clearly. Finally the objectives of the Ph.D. thesis work are framed and presented in sequence.

Chapter 3

Heat and Mass Transfer Models

In this chapter, the detailed physical models of the lab-scale metal hydride based hydrogen storage devices (MHHSD) and MHHSD with embedded cooling tubes (ECT) and their respective thermal modeling are discussed.

3.1 Physical model of lab-scale MHHSD

The physical models of the cylindrical reactors used for absorption/desorption of hydrogen to/from the lab-scale metal hydride beds are shown in Figs.3.1 and 3.2, respectively. Heat transfer fluid/cooling fluid (HTF) flows spirally through the space between inner and outer concentric tubes. The Mg_2Ni alloy fills the space between the inner tube and the filter. In order to prevent the heat transfer from the reactor to the surroundings, the reactor is well insulated. The inner tube of the cylindrical reactor is the filter which acts as a passage and distributor of

hydrogen to the metal hydride (MH) bed. In the hydriding (absorption) process, as shown in Fig 3.1, hydrogen flows to the MH bed. Opposite is the case in dehydriding (desorption) process (Fig. 3.2). The porous filter also prevents the hydride particles from being carried away by the hydrogen gas during desorption process. The pressure at the inlet is considered to be constant and does not vary with time. Hydrogen is supplied at a constant pressure throughout the absorption process. In order to validate the numerical model, the experimental conditions from Muthukumar *et al*., (2008) are chosen for the lab-scale MHHSD.

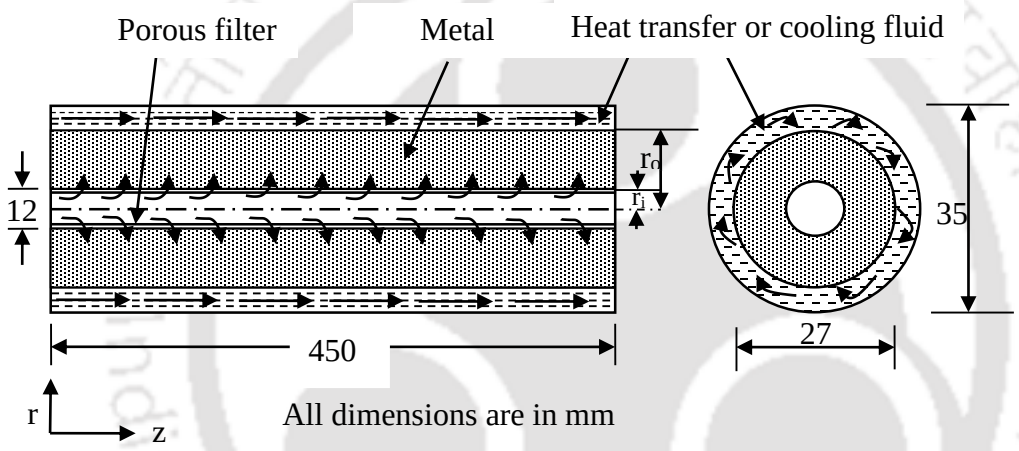

Fig. 3.1 – Schematic of metal hydride based hydrogen storage cylindrical container: absorption process.

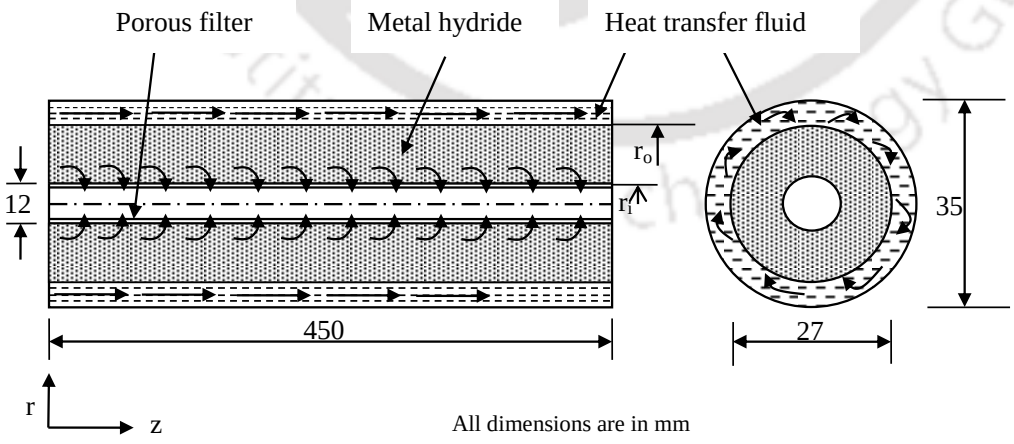

Fig. 3.2 – Schematic of metal hydride based hydrogen storage cylindrical container: desorption process.

3.2 Physical model of MHHSD with ECT

In order to predict the heat and hydrogen transfer characteristics for higher storage capacity MHHSD, 2-D and 3-D cylindrical MHHSD with ECT models employing $LmNi_{4.91}Sn_{0.15}$ are developed using COMSOL Multiphysics 4.3. The inner diameter of the cylindrical reactor is 103.4 mm with a thickness of 6.05 mm. The outer diameter of the embedded cooling tube is 6.35 mm with a thickness of 1 mm. The overall length of the reactor is 160 mm. The schematic view of ECT of different configurations (24, 36, 48, 60 and 70) is shown in Fig. 3.3 and their arrangement detail is given in Table 3.1. The sectional one half view of the thermal model of the reactor with 60 ECT is shown in Fig. 3.4. This study involves the combined transient heat and hydrogen transfer in the porous media, the pressure difference between hydrogen supply pressure and hydride equilibrium pressure, hydrogen flow and diffusion, rate of hydrogen absorption/desorption process and heat transfer between the hydride bed and HTF. These problems are integrated and solved using COMSOL Multiphysics.

In this numerical study, both 2-D and 3-D thermal models are developed for evaluating the hydriding and dehydriding characteristics of $LmNi_{4.91}Sn_{0.15}$ based MHHSD with ECT during hydrogen absorption and desorption processes. The 2-D model is mainly focused on optimizing the arrangements of ECT, while the 3-D model is mainly devoted to the prediction of hydrogen storage performances of MHHSD at different operating conditions. In order to reduce the computational time, the simulation is carried out by considering only half of the reactor (Fig. 3.4).

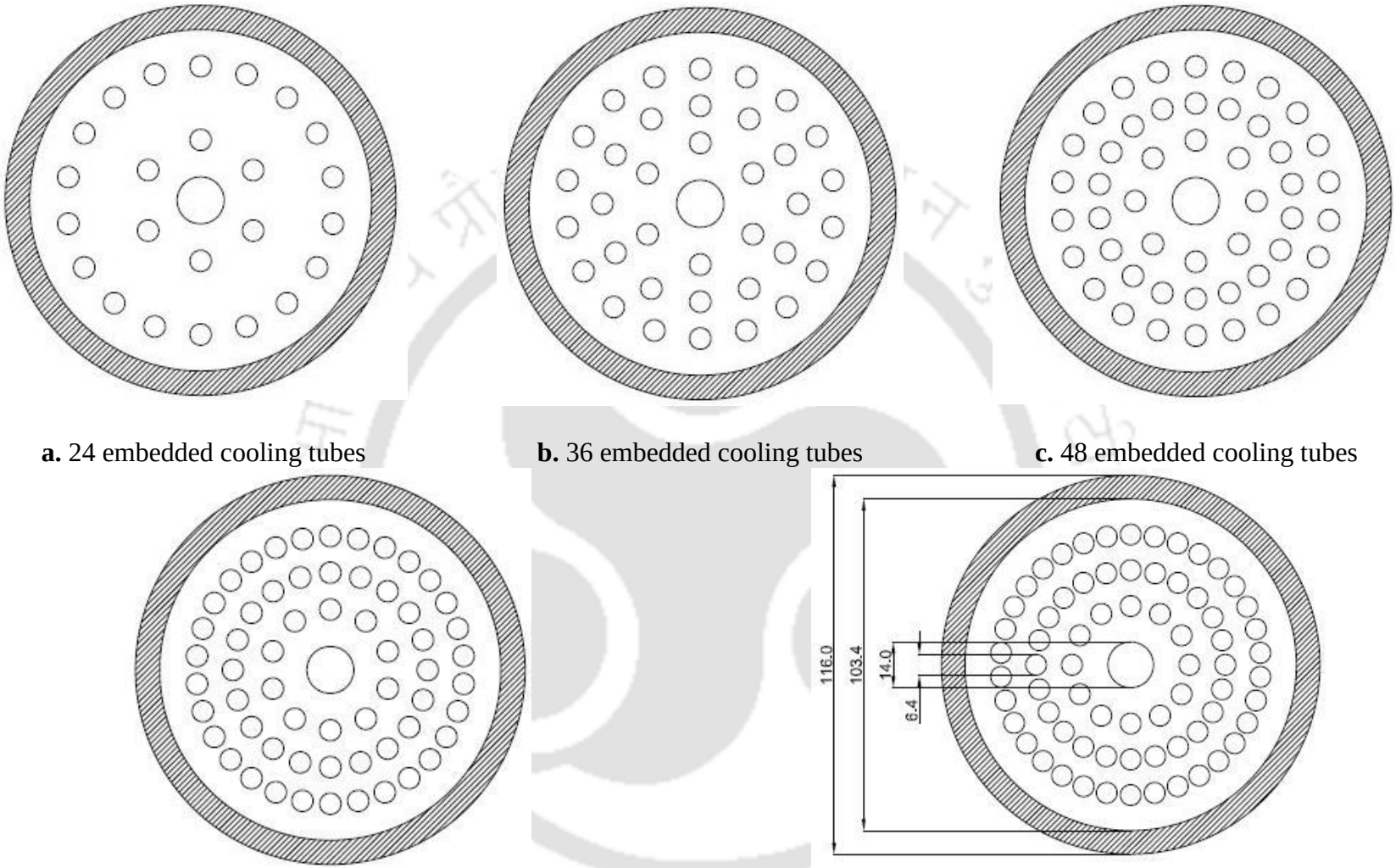

a. 24 embedded cooling tubes **b.** 36 embedded cooling tubes **c.** 48 embedded cooling tubes

d. 60 embedded cooling tubes **e.** 70 embedded cooling tubes

Fig. 3.3 – Schematic view of hydrogen storage device (2-D model) with different configurations of embedded cooling tubes.

Table 3.1 – Number of embedded cooling tubes (ECT) and their arrangements at diameter 36 mm, 58 mm and 80 mm

Total number of ECT	Number of ECT at diameter 36 mm	Angle between two cooling tubes at 36 mm (°)	Number of ECT at diameter 58 mm	Angle between two cooling tubes at 58 mm (°)	Number of ECT at diameter 80 mm	Angle between two cooling tubes at 80 mm (°)
24	6	60	-	-	18	20
36	6	60	12	30	18	20
48	8	45	18	20	22	16
60	10	36	20	18	30	12
70	12	30	24	15	34	11

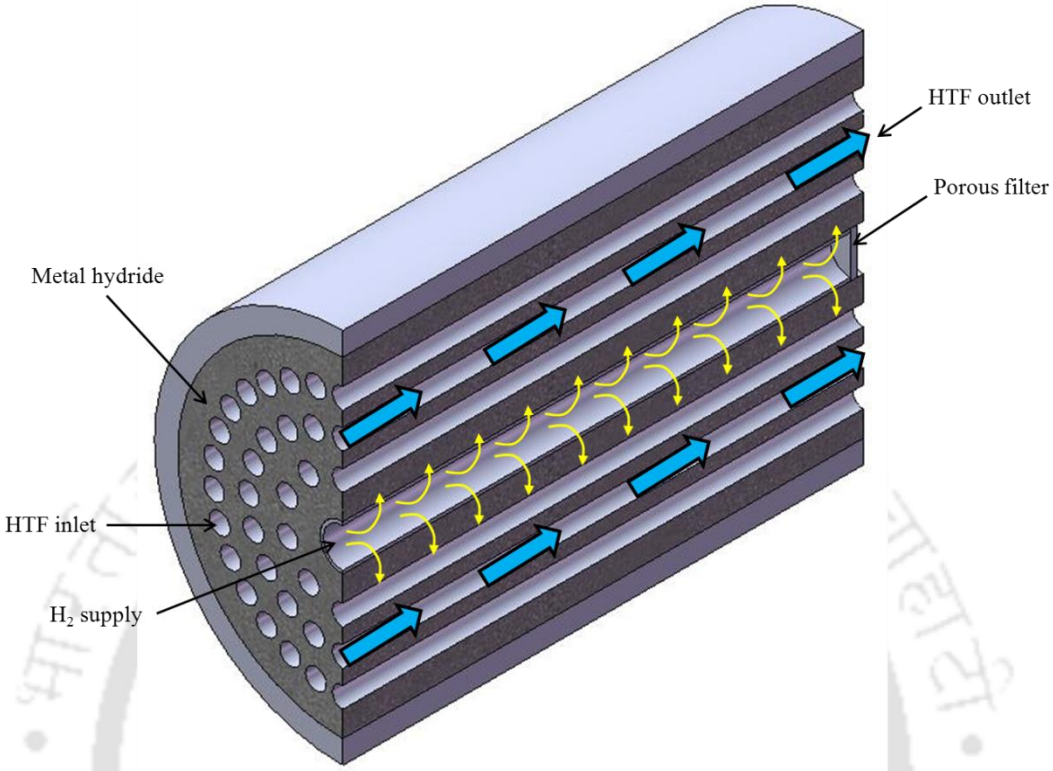

Fig. 3.4 – Sectional one half view of the thermal model of the reactor with 60 ECT.

For the numerical analysis, the following assumptions are made to simplify the governing equations [Jemni and Nasrallah, 1995a; 1995b; Gopal and Murthy, 1995; Askri *et al.*, 2003; 2009; Mellouli *et al.*, 2009; Muthukumar and Ramana, 2009; 2010]:

- The gas phase: hydrogen is treated as ideal gas.
- The solid phase: MH has uniform porosity and isotropic.
- The porous filter is adiabatic (only hydrogen transfer takes place through the filter).
- Inside the hydrogen storage container: both the hydrogen and MH are in local thermal equilibrium.
- The hydrogen storage container is adiabatic (there is no heat transfer between the container and ambient).

- Thermo – physical properties are constant and independent of hydride bed temperature and other operating parameters.
- MH at high temperature (Mg_2Ni), the effect of volumetric radiation is accounted. It absorbs, emits and isotropically scatters the radiative energy.
- MH at low temperature ($LmNi_{4.91}Sn_{0.15}$), the effect of volumetric radiation is negligible.

3.3 Formulations

Lab-scale MHHSD:

For the 2-D geometry under consideration, with incorporation of the volumetric radiation $\nabla \cdot \vec{q}_R$, with reference to the coordinate system shown in Figs. 3.1 and 3.2, the governing energy equation is given by (Muthukumar and Ramana, 2009):

$$\left(\rho C_p\right)_e \frac{\partial T}{\partial t} = \frac{1}{r}\frac{\partial}{\partial r}\left(r\lambda_e \frac{\partial T}{\partial r}\right) + \frac{\partial}{\partial z}\left(\lambda_e \frac{\partial T}{\partial z}\right) - \left(\rho C_p V_{gr}\right)\frac{\partial T}{\partial r} - \left(\rho C_p V_{gz}\right)\frac{\partial T}{\partial z} - m\left[\frac{\Delta H}{M_g} - T\left(C_{pg} - C_{pm}\right)\right] - \nabla \cdot \vec{q}_R \quad (3.1)$$

In Eq. (3.1), the divergence of radiative heat flux given is given by (Mishra and Roy, 2007)

$$\nabla \cdot \vec{q}_R = \beta\left(1-\omega\right)\left(4\pi\frac{\sigma T^4}{\pi} - G\right) \quad (3.2)$$

where β is the extinction coefficient $\left(\beta = \sigma_a + \sigma_s\right)$, ω is the scattering albedo $\left(\omega = \frac{\sigma_s}{\beta}\right)$ and G is the incident radiation.

MHHSD with ECT:

Based on the assumption of local thermal equilibrium between the hydride bed and the hydrogen, the governing energy equation is written as (Muthukumar *et al*., 2012):

$$\left(\rho C_p\right)_e \frac{\partial T}{\partial t} + \left(\rho C_p\right)_g \left(\vec{V}_g \cdot \nabla T\right) = \nabla \cdot \left(\lambda_e \nabla T\right) + S_h \tag{3.1a}$$

where S_h is the source term given by

$$S_h = \zeta \left(\frac{\Delta H}{M_g}\right) \tag{3.2a}$$

In the energy equation, an effective heat capacitance and effective thermal conductivity of the hydride bed is given by

$$\left(\rho C_p\right)_e = \varepsilon \left(\rho C_p\right)_g + \left(1-\varepsilon\right)\left(\rho C_p\right)_m \quad \text{and} \quad \lambda_e = \varepsilon \lambda_g + \left(1-\varepsilon\right)\lambda_m \tag{3.3}$$

The MH bed is assumed as a sink. The amount of hydrogen absorbed/desorbed is calculated using the continuity equation which includes the density (ideal gas equation) and velocity (Darcy's law) of hydrogen inside the container. The continuity equation is written as (Muthukumar *et al*., 2012):

$$\varepsilon \frac{\partial \rho_g}{\partial t} + \nabla \cdot \left(\rho_g \vec{V}_g\right) = -\zeta \tag{3.4}$$

$$\rho_g = \frac{P_g M_{H_2}}{R_u T} \tag{3.5}$$

$$V_g = -\frac{K}{\mu_g} \nabla P_g \tag{3.6}$$

The amount of hydrogen absorbed/desorbed which is directly associated with rate of reaction is given by (Muthukumar *et al*., 2012; Muthukumar and Ramana, 2010):

$$\zeta = C_a \exp\left(\frac{-E_a}{R_u T}\right) \ln\left(\frac{P_s}{P_{eq}}\right)\left(\rho_{ss} - \rho_t\right) \quad \text{(absorption)} \tag{3.7}$$

$$\zeta = C_d \exp\left(\frac{-E_d}{R_u T}\right)\left(\frac{P_{eq} - P_d}{P_{eq}}\right)\left(\rho_s\right) \quad \text{(desorption)} \tag{3.8}$$

The equilibrium pressure of hydride bed during hydriding and dehydriding processes are calculated using van't Hoff equation and it's expressed as (Nishizaki *et al*., 1983):

$$\frac{P_{eq}}{P_0} = \exp\left[\frac{\Delta S}{R_u} - \frac{\Delta H}{R_u T} + \left(\varphi_s \pm \varphi_o\right) \times \tan\left(\pi\left(\frac{x}{x_f} - \frac{1}{2}\right)\right) \pm \frac{\beta}{2}\right] \tag{3.9}$$

where "+" is for absorption process and "-" is for the desorption process, ΔS is the entropy of formation, ΔH is the enthalpy of formation, φ_s is the slope factor, x and x_f are concentration at the given time (t) and the final concentration of H_2.

The number of hydrogen moles absorbed/desorbed to/from the MHHSD is expressed as:

$$N_{H_2} = \frac{1000 \times \left(x - x_{ini}\right) \times m_a \times N_a}{2 \times M_a} \tag{3.10}$$

The mass of hydrogen absorbed/desorbed is given by

$$m_{H_2} = N_{H_2} \times M_{H_2} \tag{3.11}$$

The hydrogen storage capacity and the amount of hydrogen desorbed in (wt%) are calculated from the above Eq. (3.10) and Eq. (3.11)

$$wt\% = \frac{m_{H_2}}{m_a} = \frac{N_{H_2} \times M_{H_2}}{m_a} = \frac{N_a \times \left(x_f - x_{ini}\right) \times M_{H_2}}{2 \times M_a} \times 100\% \tag{3.12}$$

where N_a is the number of hydrogen atoms in the metal hydride, M_{H_2} is the molecular weight of hydrogen and M_a is the molecular weight of the metal hydride.

3.4 Initial conditions and boundary conditions

3.4.1 Lab-scale MHHSD

Initially $(t = 0.0)$, the bed temperature, hydride equilibrium pressure and hydride density are assumed to be uniform throughout the reactor.

$$\rho_m(z,r) = \rho_0;\ \ T_m(z,r) = T_g(z,r) = T_0;\ \ \ P_g(z,r) = P_0. \tag{3.13}$$

and for time $t > 0.0$, the conditions are the following:

Along the porous wall (absorption): $$P_g(z,r_i) = P_s, \frac{\partial T(z,r_i)}{\partial r} = 0.0 \tag{3.14}$$

Along the porous wall (desorption): $$P_g(z,r_i) = P_d, \frac{\partial T(z,r_i)}{\partial r} = 0.0 \tag{3.14a}$$

Along the left face $(z = 0.0)$, the adiabatic and impervious conditions give: $$\frac{\partial T(0,r)}{\partial z} = 0.0, \ \frac{\partial P_g(0,r)}{\partial z} = 0.0 \tag{3.15}$$

Along the right face $(z = Z)$, the adiabatic and impervious conditions give: $$\frac{\partial T(Z,r)}{\partial z} = 0.0, \ \frac{\partial P_g(Z,r)}{\partial z} = 0.0 \tag{3.16}$$

At the top of reactor (Figs.3.1 and 3.2), the convective boundary including the radiation effect is given by

$$-\lambda_e \frac{\partial T(r_o,z)}{\partial r} + \vec{q}_R(r_o,z) = U(T - T_f) \tag{3.17}$$

where U is the overall heat transfer coefficient, T_f is the heat transfer/cooling fluid temperature.

3.4.2 MHHSD with ECT

For the MHHSD with ECT, initially (t = 0.0) the temperature of hydride bed and hydrogen gas, hydride equilibrium pressure, hydride density and hydride concentration are assumed to be constant.

2-D model:

$$\rho_m(r,\theta)=\rho_0;\;\; T_m(r,\theta)=T_g(r,\theta)=T_0;\;\; P_g(r,\theta)=P_0. \tag{3.18}$$

3-D model:

$$\rho_m(r,\theta,z)=\rho_0;\;\; T_m(r,\theta,z)=T_g(r,\theta,z)=T_0;\;\; P_g(r,\theta,z)=P_0. \tag{3.19}$$

When the absorption/desorption time (t > 0.0);

At the porous wall (absorption) is given by

$$P_g\left(r_i,t\right)=P_s,\;\frac{\partial T(r_i)}{\partial r}=0.0 \tag{3.20}$$

At the porous wall (desorption) is given by

$$P_g\left(r_i,t\right)=P_d,\;\frac{\partial T(r_i)}{\partial r}=0.0 \tag{3.21}$$

2-D model: the convective boundary condition at each ECT is written as:

$$-\lambda_e\frac{\partial T\left(r_0,\theta,t\right)}{\partial r}=U\left(T_{r_o,\theta,t}-T_f\right) \tag{3.22}$$

where T_f is the temperature of HTF.

3-D model:

At the left face (z = 0.0), the adiabatic and impermeable conditions are given by

$$\frac{\partial T(r,\theta,0,t)}{\partial z}=0.0,\;\frac{\partial P_g(r,\theta,0,t)}{\partial z}=0.0 \tag{3.23}$$

At the right face (z = Z), the adiabatic and impermeable conditions are given by

$$\frac{\partial T(r,\theta,Z,t)}{\partial z}=0.0,\ \frac{\partial P_g(r,\theta,Z,t)}{\partial z}=0.0 \tag{3.24}$$

Along the ECT, variable wall temperature is given by [Muthukumar and Ramana, 2009; 2010)]:

$$T_{fo}(t)=T_{fi}+\left(T_{r_0,\theta,z,t}-T_{fi}\right)\times\left(1-\exp\left(-\frac{UA}{m_f C_{pf}}\right)\right) \tag{3.25}$$

where A is the surface area of the ECT, C_{pf} is the specific heat of HTF, U is the overall heat transfer coefficient, $T_{r_0,\theta,z,t}$ is the temperature of the hydride bed at interface between the hydride bed and convective wall (outer radius of the ECT), T is the temperature with suffixes *fi* and *fo* for inlet and outlet temperature of HTF, respectively and m_f is the mass flow rate of HTF.

Outer wall of the MHHSD considered as a convective boundary conditions is given by

$$-\lambda_e\frac{\partial T(r_0,\theta,Z,t)}{\partial r}=U\left(T_{r_o,\theta,Z,t}-T_{air}\right) \tag{3.26}$$

3.5 Solution methodology

3.5.1 Lab-scale MHHSD

The governing equations are discretized by using the finite volume method (FVM). The solution methodology is similar to the one presented in Muthukumar and Ramana, 2009. An alternative direction implicit (ADI) scheme with tri-diagonal matrix algorithm (TDMA) is used for solving the governing equations. Velocity terms are controlled using staggered grids to catch the heat transfer across the control volume by convection. Boundary conditions are applied using half control volume method. Values of different thermo-physical parameters are taken from Muthukumar *et al*., 2003; Muthukumar and Ramana, 2009 and Chung and Lin, 2009, and the optical properties such as the extinction coefficient β and the scattering albedo ω are taken

from Askri *et al*., 2003. The radiative information has been calculated as per the FVM outlined in Kim, 2008. The thermo-physical properties of hydriding alloy and various constants used in this thermal model are listed in Table 3.2. For the dimensions of the reactor given in Table 3.2, the effect of sizes of control volumes $(\Delta r \times \Delta z)$ on the average bed temperature with time is studied. There is no change in results beyond 64×90 control volumes. Hence, in the following, all analyses are carried out with 64×90 control volumes.

3.5.2 MHHSD with ECT

The solution procedure and the assumptions to simplify the governing equations are similar to the one presented in Muthukumar *et al*. (2012). The thermo physical properties of $LmNi_{4.91}Sn_{0.15}$ and hydrogen used to compute the present problem are listed in Table. 3.3. The mesh of computational domain considered is free tetrahedral mesh and simulations are also performed using COMSOL Multiphysics 4.3. It effectively solves the energy equation (convection and conduction mode heat transfer) (Eq. 3.1a) and the hydrogen mass (diffusion) (Eq. 3.4) and momentum (Darcy's law) (Eq. 3.6) transport equations in porous media module. User – defined functions are incorporated for calculating the specific parameters such as the rate of hydrogen absorption (Eq. 3.7), rate of hydrogen desorption (Eq. 3.8), hydride concentrations during hydriding and dehydriding processes and equilibrium pressure (Eq. 3.9).

The geometry of MHHSD with 60 ECT and mesh map related to the calculation tolerance are defined first. Fig. 3.4 shows the 3-D computational domains implemented. The first domain simulates the geometry of the above described basic 60 ECT. The second domain describes the MH reaction bed. The outer wall of ECT is introduced by fixing variable wall temperature

boundary condition. Two sub – domains considered are the porous MH bed and the ECT which is used as a heat exchanger for the flow of HTF (i.e. water, oil). To reduce the calculation time and also for symmetry reasons the computational domain simulates a half reactor.

After introducing the MH and gas properties, the boundary conditions and initial values are assigned. The convergence of the solutions determines temperature, pressure and MH density distributions.

Table 3.2 – Thermo – physical properties of Mg_2Ni, hydrogen and constants used in the analysis (Muthukumar *et al*., 2003; Askri *et al*., 2003; Muthukumar and Ramana, 2009; Chung and Lin, 2009)

Reactor geometry			
Length of the geometry		:	450 mm
Inner radius of inner cylinder		:	6 mm
Inner radius of outer cylinder		:	13.5 mm
Thickness of cylinder wall		:	3 mm
Properties of Mg_2Ni			
Density of metal		:	3200 kg/m^3
Specific heat of metal		:	1414 J/kg·K
Effective thermal conductivity of metal (including copper additive)		:	1.4 W/m·K
Porosity		:	0.5
Effective density of solid		:	3200 kg/m^3
Effective density of solid at saturation state		:	3276 kg/m^3
Activation energy	E_a	:	55,000 J/mol
	E_d	:	58,500 J/mol
Entropy of reaction	ΔS_a	:	124.5 J/mol·K
	ΔS_d	:	131.5 J/mol·K
Enthalpy of reaction	ΔH_a	:	64,550 J/mol
	ΔH_d	:	70,776 J/mol
Properties of hydrogen			
Thermal conductivity of hydrogen		:	0.1272 W/m·K
Specific heat hydrogen		:	14,283 J/kg·K
Density of hydrogen		:	0.0838 kg/m^3
Constants used			
Universal gas constant		:	8.314 J/mol·K
Reaction constant	C_a	:	100 1/s
	C_d		40 1/s
Slope factor		:	0.35
Constant		:	0.15
Hysteresis factor		:	0.2
Scattering albedo, ω		:	0.03
Extinction coefficient, β		:	5.0

Table 3.3 – Thermo – physical properties of $LmNi_{4.91}Sn_{0.15}$, hydrogen and constants used in the analysis (Paya *et al*., 2009; Satheesh and Muthukumar, 2010)

Reactor geometry			
Length of the reactor		:	160 mm
Cooling tube outer diameter		:	6.35 mm
Cylinder inner diameter		:	103.4 mm
Thickness of cylinder wall		:	6.05 mm
Properties of **$LmNi_{4.95}Sn_{0.15}$**			
Density of metal		:	8500 kg/m^3
Specific heat of metal		:	500 J/kg·K
Effective thermal conductivity of hydride		:	0.2 W/m·K
Porosity		:	0.5
Effective density of solid		:	4250 kg/m^3
Effective density of solid at saturation state		:	4310 kg/m^3
Activation energy	E_a	:	30,500 J/mol
	E_d	:	28,000 J/mol
Entropy of formation	ΔS_a	:	105.4 J/mol·K
	ΔS_d	:	110.6 J/mol·K
Enthalpy of formation	ΔH_a	:	27,000 J/mol
	ΔH_d	:	32,400 J/mol
Properties of hydrogen			
Thermal conductivity of hydrogen		:	0.1272 W/m·K
Specific heat hydrogen		:	14,283 J/kg·K
Density of hydrogen		:	0.0838 kg/m^3
Constants used			
Universal gas constant		:	8.314 J/mol·K
Reaction constant	C_a	:	80 1/s
	C_d	:	40 1/s
Slope factor		:	0.35
Constant		:	0.15
Hysteresis factor		:	0.2
Mass flow rate of HTF		:	3.2 l/min

3.6 Summary

In this chapter, the detailed physical models of lab-scale MHHSD and MHHSD with ECT and their respective thermal modeling are reported. The formulations of the thermal model for predicting the coupled heat and hydrogen transfer characteristics during hydriding and dehydriding processes, initial conditions and boundary conditions are presented separately for both lab-scale MHHSD and MHHSD with ECT models. For lab-scale MHHSD, the governing equations are numerically solved using FVM and the detailed solution methodology is also reported. For MHHSD with ECT, 2-D and 3-D mathematical models developed for predicting the hydrogen absorption/desorption characteristics using COMSOL Multiphysics 4.3 and the detailed solution methodology are reported. Finally, the thermo-physical properties of MH alloys, hydrogen and constants used in the numerical analysis are listed in Tables 3.2 and 3.3. The detailed discretization of governing equations are reported in Appendix A.

Chapter 4

Experimental Set-up

In this chapter, schematic (assembled) and photographic views of the hydrogen storage reactors with 36 and 60 ECT, the detailed layout of the test set-up, and experimental procedure are discussed.

4.1 Details of experimental set-up and hydrogen storage reactors

The detailed schematic of the hydrogen storage reactor with 36 ECT is shown in Fig. 4.1. To withstand a high pressure (≈ 100 bar) during absorption/desorption of hydrogen to/from the reactor, the material used in its fabrication is SS–316L. The cylindrical reactor consists of a sintered SS–316 porous filter with pore size 2 μm and cooling tubes with outer and inner diameters 6.35 mm and 4.57 mm, respectively. The volume of the cooling tubes is 8.75×10^{-5} m^3

for the reactor with 36 ECT and 1.46×10^{-4} m^3 for the reactor with 60 ECT. The corresponding mass of the cooling tubes are 0.703 kg for 36 ECT and 1.172 kg for 60 ECT, respectively. The inner and the outer diameters, and the length of reactor body are 103.4 mm, 115.5 mm and 160 mm, respectively. In the sintered porous filter, one end is brazed with hydrogen supply line, and the other end is sealed to maintain the uniform supply of hydrogen axially during the absorption process and also to prevent the MH particles which come along with hydrogen gas during the desorption process.

Fig. 4.2(a) and (b) shows the pictorial views of the assembled reactors. Details of 36 and 60 ECTs are shown in Fig. 4.2(c) and (d). The ends of the cooling tubes are welded with flange 1 and flange 2 (Fig. 4.1) using TIG welding. These ECT is mainly used for enhancing the rate of heat transfer and improving the reaction kinetics. The HTF jackets are also welded at both ends of the reactor. With this, the HTF supplied at one (right) end passes through the ECT to heat/cool the reactor bed and then reaches other (left) end of the reactor (Fig. 4.1). The free space between the sintered porous filter and the reactor main body is filled with $LmNi_{4.91}Sn_{0.15}$. Top of the reactor has a provision to fill/remove MH alloy, and bottom of the reactor has the provisions for fixing the thermocouples.

The schematic of the experimental set-up is shown in Fig. 4.3. It consists of constant temperature oil circulating baths, hydrogen and argon supply cylinders, hydrogen receiver, Coriolis mass flow meter (sensitivity ±0.001 g), pressure transducers (sensitivity ±0.01 bar), pressure regulators, temperature sensors, rotary vacuum pump and data acquisition system. Oil circulating constant temperature bath provides the HTF at constant temperature in the range 10 – 100 °C.

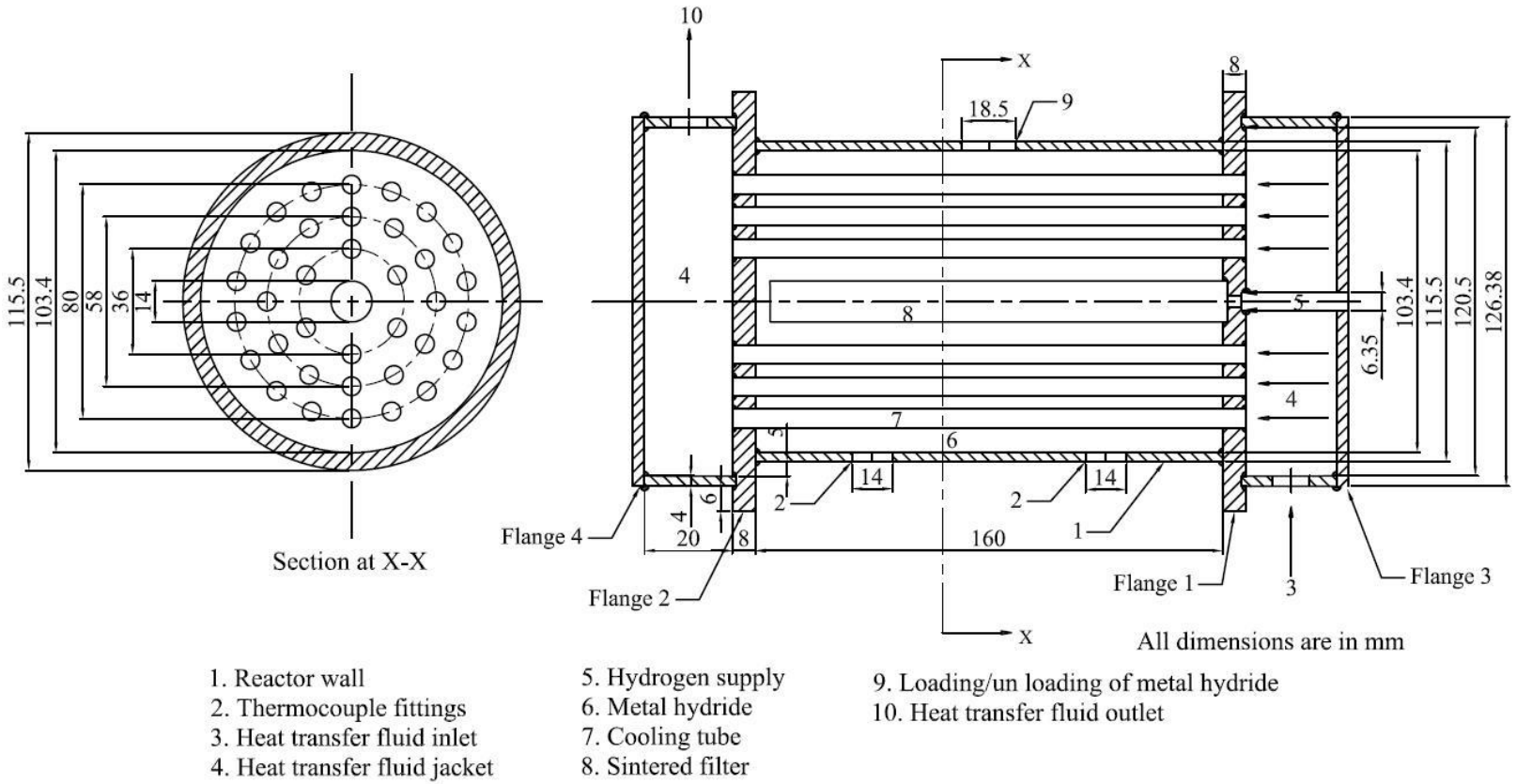

Fig. 4.1 - Schematic view of hydrogen storage device with 36 embedded cooling tubes.

(a) (b)

1. Reactor
2. Thermocouple
3. Hydrogen supply
4. Heat transfer fluid inlet
5. Alloy loading/unloading provision
6. Heat transfer fluid outlet

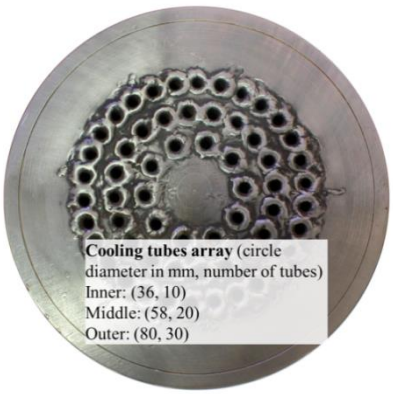

(c) (d)

Fig. 4.2 – Pictorial views of hydrogen storage device; assembled view with (a) 36 and (b) 60 embedded cooling tubes; arrangement of (c) 36 and (d) 60 embedded cooling tubes.

The HTF temperatures at the inlet and the outlet are measured using K–type metal sheathed thermocouples. As illustrated in Fig. 4.1, two high sensitivity K–type metal sheathed

thermocouples are fixed at an axial distance of 50 mm from flange 1 and also 50 mm from flange 2. The axial distance between these two thermocouple is 60 mm. The hydride bed temperature is measured at a regular interval of 2 s during both absorption and desorption processes. Average values of these two temperature readings are calculated. The gas pressures inside the hydride bed and hydrogen receiver are measured using Piezo–resistive transducers (pressure range 0 – 120 bar). The supplies of hydrogen and argon gases are controlled using the pressure regulators. The amount of hydrogen absorbed and desorbed to/from the MH reactor and the rate of absorption/desorption are measured directly from the Coriolis mass flow meter. These observations are monitored using a data acquisition system. Before the start of the activation process, the reactor and all the supply lines are evacuated down to $\approx 10^{-4}$ mbar using a vacuum pump. High–pressure bellow valves (120 bar) and Swagelok tubes are used for the fabrication of the test set-up. Pressure leak was tested up to 100 bar with argon gas, and the vacuum test was done up to 10^{-4} mbar.

In all the desorption studies, the preferred absorption conditions (both temperature and pressure) are maintained. After completing the absorption process, the bellow valves V_1, V_2 and V_3 are closed and then the hydride bed is heated using HTF at preferred desorption temperature. During the desorption process, the valves V_1, V_2, V_5 and V_7 are set at open position and all the other valves remain closed. The desorbed hydrogen from the MH reactor is collected in the hydrogen receiver. The amount and rate of hydrogen desorbed are observed from the Coriolis mass flow meter and the same values are also recorded using the data acquisition system. The valves V_1, V_2, V_5 and V_7 are closed when there is no significant change in hydrogen flow from the reactor.

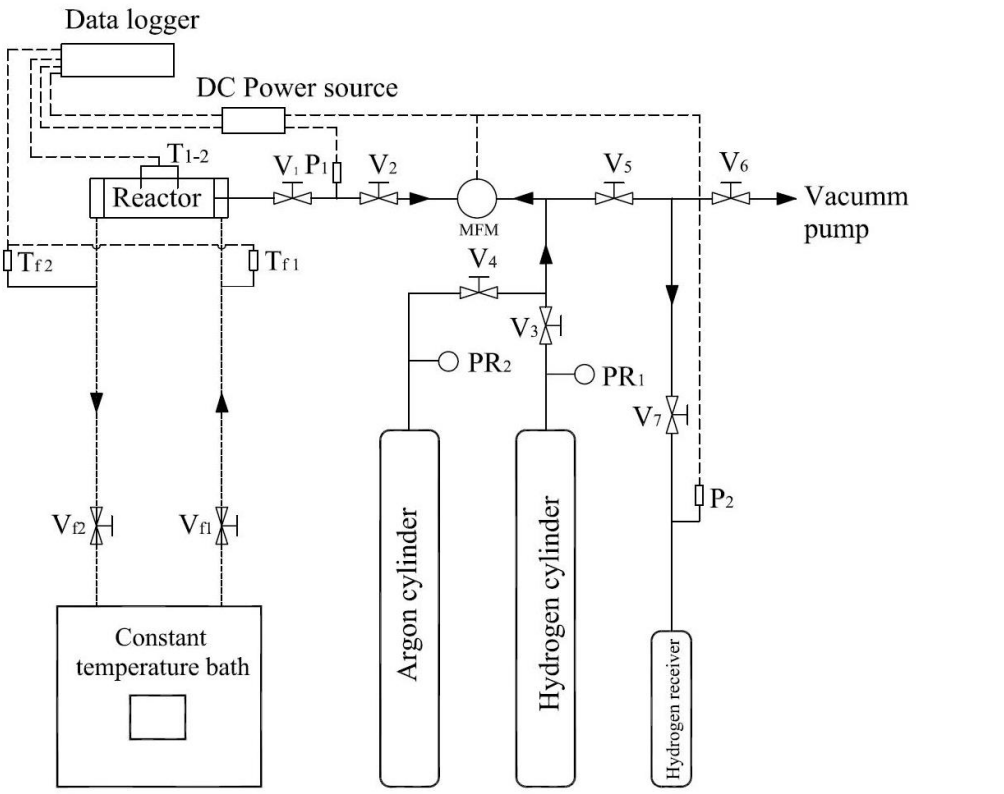

MFM	Coriolis mass flow meter	$T_{f1\text{-}f2}$	Heat transfer fluid inlet and outlet temperatures
P_1	Pressure transducer	$V_{1\text{-}7}$	Bellow sealed valve
$PR_{1\text{-}2}$	Pressure regulators	$V_{f1\text{-}f2}$	Ball valve
$T_{1\text{-}2}$	Metal Sheathed K type thermocouples		

Fig. 4.3 – Experimental test setup of hydrogen storage device.

4.2 Activation of alloy and experimental procedure for absorption/desorption process

Both the reactors are filled with 2.75 kg of $LmNi_{4.91}Sn_{0.15}$ (procured from M/s. Labtech Ltd., Bulgaria) in argon atmosphere using a glove box. Initially, the moisture is removed from the hydride bed by heating it to about 120 °C and then the reactors are continuously evacuated till vacuum pressure reaches down to 10^{-3} mbar. Activation of the MH involves about 10 – 14 times charging and discharging of highly pure hydrogen (99.999%) at 80 bar supply pressure, 30 °C

absorption temperature and 80 °C desorption temperature. The above said cycle has been repeated till hydrogen storage capacity of MHHSD's reach its maximum value (~ 1.18 wt %).

After activating the MH alloy, HTF at constant temperature is circulated to the reactor bed till the thermal equilibrium between the HFT and the hydride bed is reached. The valves V_1, V_2 and V_3 are opened and then, the hydrogen is admitted into the MH reactor at a desired supply conditions (e.g. 30 bar pressure and 30 °C absorption temperature). The flow of hydrogen into the reactor is observed using a Coriolis mass flow meter till the steady–state is reached. Once the absorption process is completed, the valves are closed. Later, the HTF temperature is set to a desired desorption temperature (e.g. 30 °C) in the constant oil circulating temperature bath. The HTF is circulated to the reactor through ECT till desorption process gets over. The bellow valves V_1, V_2, V_5 and V_7 are in open position during the desorption process. The rate of hydrogen absorption/desorption and the total amount of hydrogen absorbed and desorbed to/from the reactor are monitored with help of a Coriolis mass flow meter through a data acquisition system. Finally, all the valves are closed and the reactor is brought down to the ambient condition.

Fig. 4.4 shows the pictorial view of the MHHSD experimental setup developed at Thermal Science Lab, Mechanical Engineering Department, IIT Guwahati. The experimental setup consists of two reactors with different ECT arrangements, constant temperature oil circulating baths, hydrogen and argon cylinder, rotary vacuum pump, Coriolis mass flow meter, K-type metal sheathed thermocouples, constant DC power source, piezo resistive pressure sensors and data acquisition system connected to a desktop system. In hydrogen supply line, SS 316L ($1/4^{th}$ inch) tubes and bellow valves are used to direct the gas to/from the reactor. All valves and

the tubing are connected using Swagelok ferrule joints to avoid leak in the experimental setup. The thermocouples (K–type metal sheathed thermocouple with an accuracy ±0.5 °C) at different locations are placed to measure the temperature and also the pressure sensors (piezo resistive transducer with an accuracy ±0.1 bar) are used to measure pressure at different locations and these arrangements are shown in Fig. 4.4. Both hydrogen and argon gas with high purity (99.999%) are used in the experiment. The constant temperature oil circulating thermostatic bath (range 10 – 150 ºC) is used for supplying the HTF to the MHHSD during the hydriding and dehydriding processes. The rotary vacuum pump is used to create the vacuum in the experimental setup and also in the MHHSD. This has measured using Pirani and Penning gauge fixed with the pump. Tests were performed over 200 absorption and desorption cycles and no significant change in the absorption and desorption capacities was reported. In each case (parametric studies), experiments have been conducted twice, and the average values were reported. All the tests were carried out using high pure hydrogen (99.999%).

4.3 Summary

Based on the numerical investigations, the reactors with 36 and 60 ECT are chosen for the experimental study. Employing 2.75 kg of $LmNi_{4.91}Sn_{0.15}$, two reactors with different ECT arrangements are built. The schematic (assembled) and photographic views of the hydrogen storage reactor with 36 and 60 ECT, the detailed layout of the test set-up, and the experimental procedure are discussed in this chapter.

The details of various instruments and sensors used in this experimental study are listed in Appendix C.

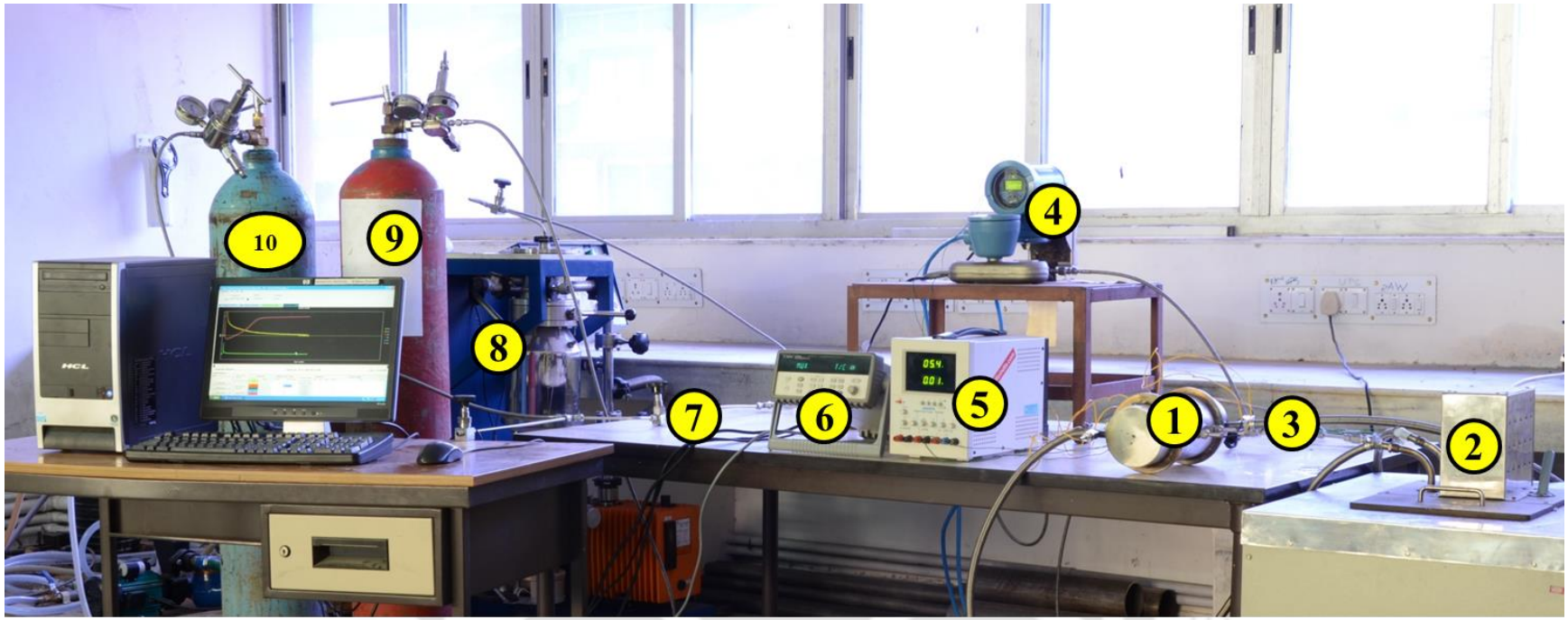

1. Reactor
2. Constant temperature bath
3. Pressure transducer
4. Coriolis mass flow meter
5. DC power source
6. Data acquisition system
7. Bellow sealed valve
8. Rotary vacuum pump
9. Hydrogen supply cylinder
10. Argon cylinder

Fig. 4.4 – Pictorial view of the metal hydride based hydrogen storage device experimental set-up.

Chapter 5

Results and Discussion

In this chapter, the results obtained from the numerical investigations on lab-scale metal hydride based hydrogen storage device (MHHSD) and MHHSD with embedded cooling tubes (ECT) and experimental studies on MHHSD with 36 and 60 ECTs are discussed.

5.1 Numerical results of lab-scale MHHSD: absorption process

The governing equations are discretized by using the finite volume method. The effect of sizes of the control volume $(\Delta r \times \Delta z)$ on the variation of average bed temperature is studied. No change in results is observed beyond 64×90 control volumes. Hence, in the following, all analyses are carried out employing 64×90 control volumes. In this section, the effects of hydride bed parameters (bed thickness and effective thermal conductivity of the hydride bed) and the effects of operating parameters (supply pressure and absorption temperature) on the absorption characteristics of lab-scale MHHSD are discussed.

5.1.1 Validation of numerical model

Employing Mg_2Ni, for 10, 15 and 20 bar supply pressures, the temporal variation of hydrogen storage capacity are shown in Fig. 5.1. Results are compared with the experimental results reported by Muthukumar *et al*. (2008). In following the references Muthukumar and Ramana (2009) and Muthukumar *et al*. (2009a), numerical results are obtained for the void fraction $\varepsilon = 0.5$. It is observed from Fig. 5.1 that the numerical results are close to the experimental values. For 10 bar supply pressure, at all times, the match is good. With 10, 15 and 20 bar supply pressures, the maximum deviations at t = 300 s are 9.09%, 7.14% and 11.76%, respectively. It is to be noted that in about 25 minutes, the steady-state condition is reached, and at that state, both the numerical and experimental values are found to be closer.

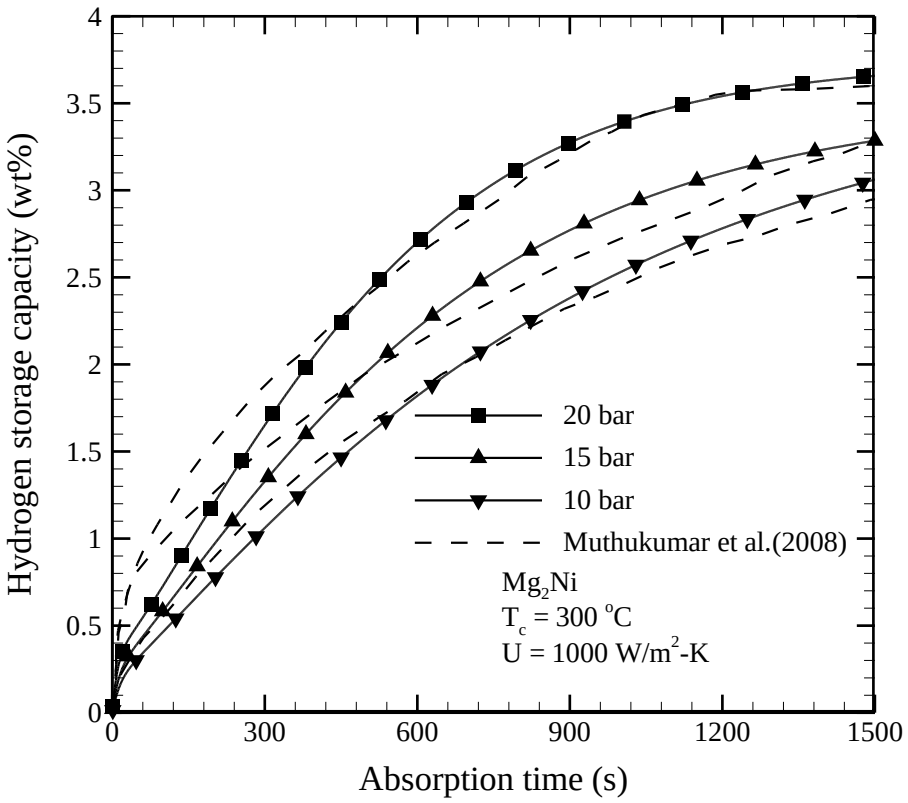

Fig. 5.1 – Comparison of the variation of hydrogen storage capacity with time.

5.1.2 Effect of supply pressure

Figs. 5.2(a) and (b) illustrate the effect of supply pressure on the variation of hydrogen storage capacity and the average hydride bed temperature, respectively. It is observed that the driving force is the difference between supply and hydride equilibrium pressures [Eq. 3.7]. Initially, the large pressure difference results in rapid exothermic reaction (hydrogen absorption), and it results in sudden rise in bed temperature. The rise in bed temperature increases the hydride equilibrium pressure [Eq. 3.9] and thereby reduces the rate of absorption (Fig. 5.2(a)). Due to decrease in driving force with time, the rate of reaction decreases, and as shown in the Fig. 5.2(a), the hydrogen storage capacity is also decreases. At any time, the absorption is higher for higher supply pressure. With the consideration of the volumetric radiation, the hydrogen absorption rate is higher. This is for the reason, with the consideration of radiation, heat transfer will increase, and this increased heat transfer reduces the bed temperature significantly, resulting in increasing the pressure difference between the supply pressure and hydride equilibrium pressure. Higher pressure difference leads to the higher hydrogen absorption rate. At the supply pressure of 20 bar, the maximum amount of hydrogen absorbed is 36.7 g of H_2/kg of Mg_2Ni. In the following pages, all results are obtained with the consideration of the volumetric radiation.

The temporal variation of the average bed temperature (Fig. 5.2(b)) follows the trend opposite to that of the hydrogen storage capacity. Due to the rapid reaction, initially there is a sudden rise of temperature, and afterwards, it keeps on decreasing with time. The sudden rise, over a very short period of time, is owing to the poor thermal conductivity of the MH bed which is unable to transfer the generated heat (exothermic reaction) promptly to the cooling fluid.

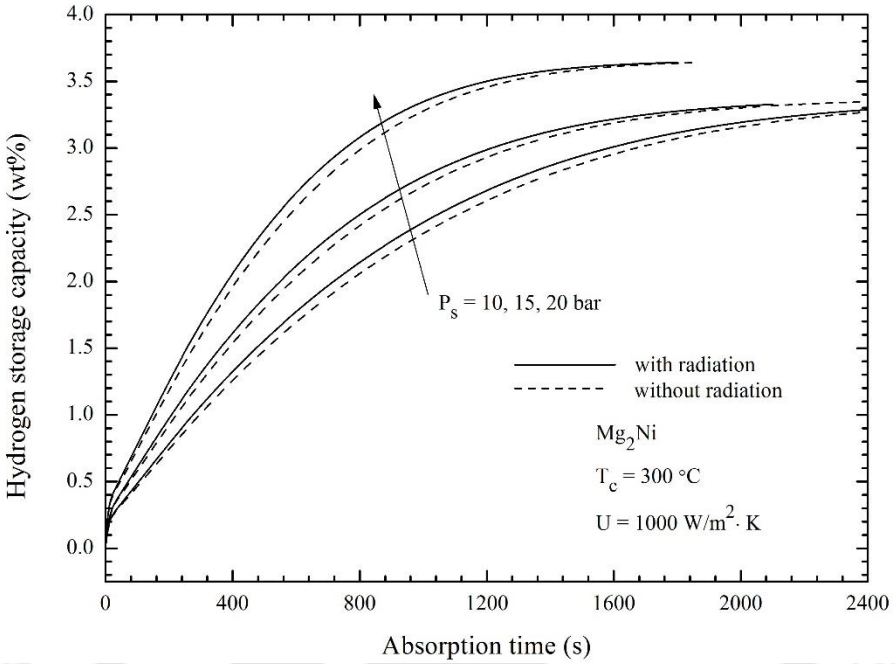

(a)

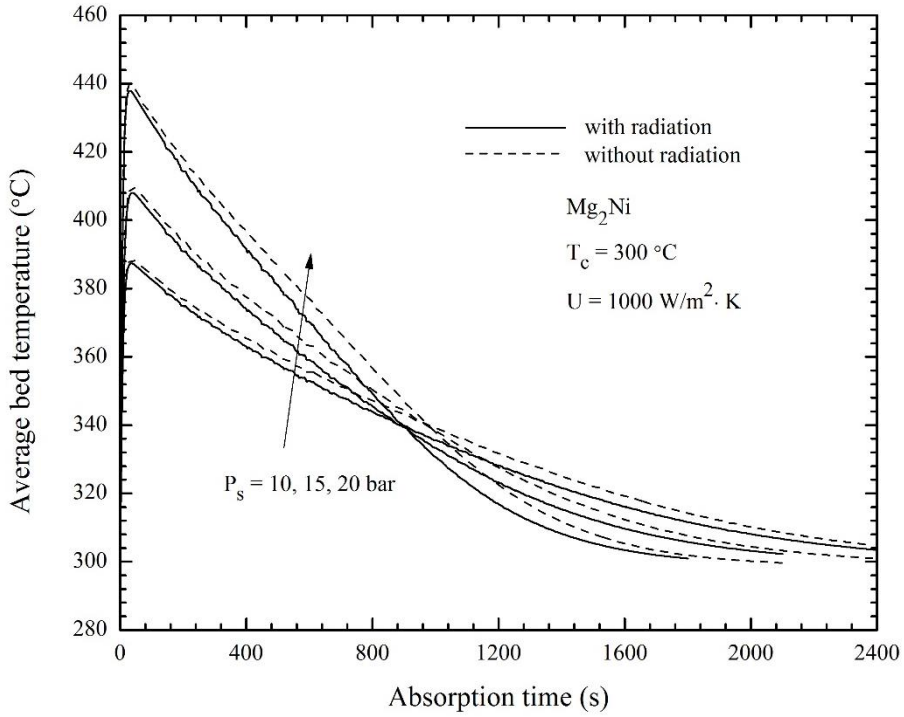

(b)

Fig. 5.2 – Effect of supply pressure on variations of (a) hydrogen storage capacity and (b) average bed temperature with and without radiation.

The maximum temperatures for 10, 15 and 20 bars are 387 °C, 407 °C and 440 °C, respectively. With the passage of time, the reaction rate decreases. This causes drop in the average bed temperature. Up to 800 s from the start, it is observed that higher the supply pressure, higher is the average bed temperature. After 800 s, this trend is reversed. With the passage of time, say 1500 s, hydrogen storage capacity (Fig. 5.2(a)) and average bed temperature (Fig. 5.2(b)) become almost steady. Opposite to the hydrogen storage capacity (Fig. 5.2(a)), with the consideration of the volumetric radiation, average bed temperature is less. As illustrated in Fig.5.2, at higher supply pressures (above 20 bar), Mg_2Ni completes the about 90% absorption process well before 800 s. Therefore, the bed temperature drops quickly (following the trend of sensible heat cooling) as the internal heat generation does not play a significant role beyond 800 s. At lower supply pressure, bed temperature takes more time to reach the heat transfer fluid temperature due to continuous generation of heat till about 2000 s.

5.1.3 Effect of radial locations

Hydrogen concentration and bed temperature at different locations are not the same. With Mg_2Ni, for the bed with 6 mm and 13.5 mm inner and outer radii (Fig. 3.1), respectively, for the 20 bar supply pressure and cooling fluid temperature of 300 °C, the variations of bed temperature and hydrogen concentration at different radial positions are shown in Figs. 5.3(a) and (b), respectively. It is observed that the temperature of the bed decreases from porous filter to the convective wall along radial direction. During the start of the hydriding process, the region close to the filter experiences rapid hydriding and hence, large amount of heat is released in this region. Compared to region close to the outer convective wall which is in contact with the cooling fluid, due to poor heat transfer rate, the region near to the porous filter experiences high

temperature. Owing to the higher heat transfer rate, the region close to the outer wall completes the absorption process well before the other regions of the MH bed.

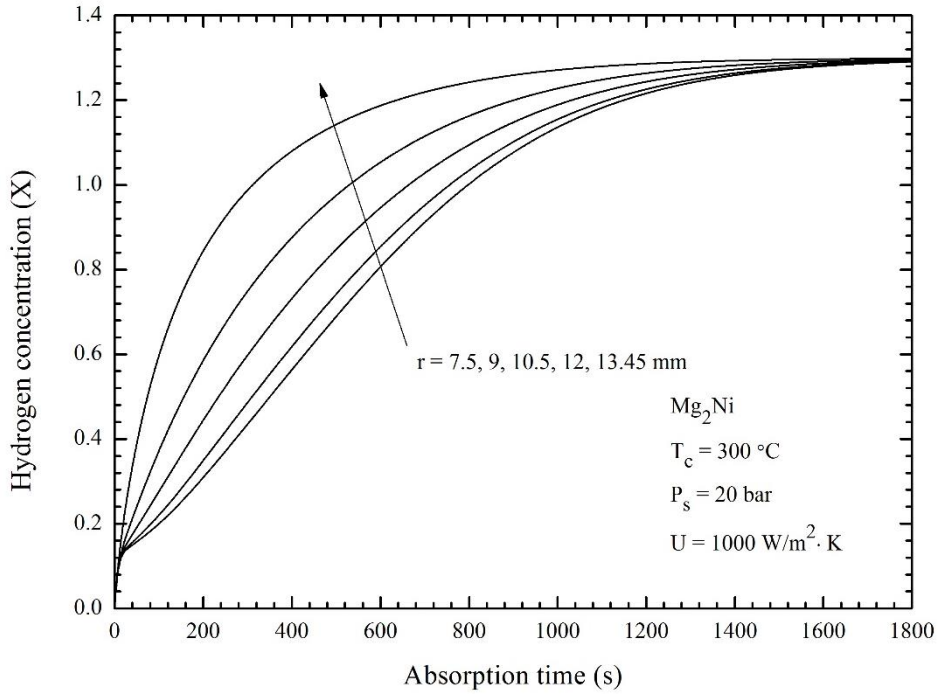

(a)

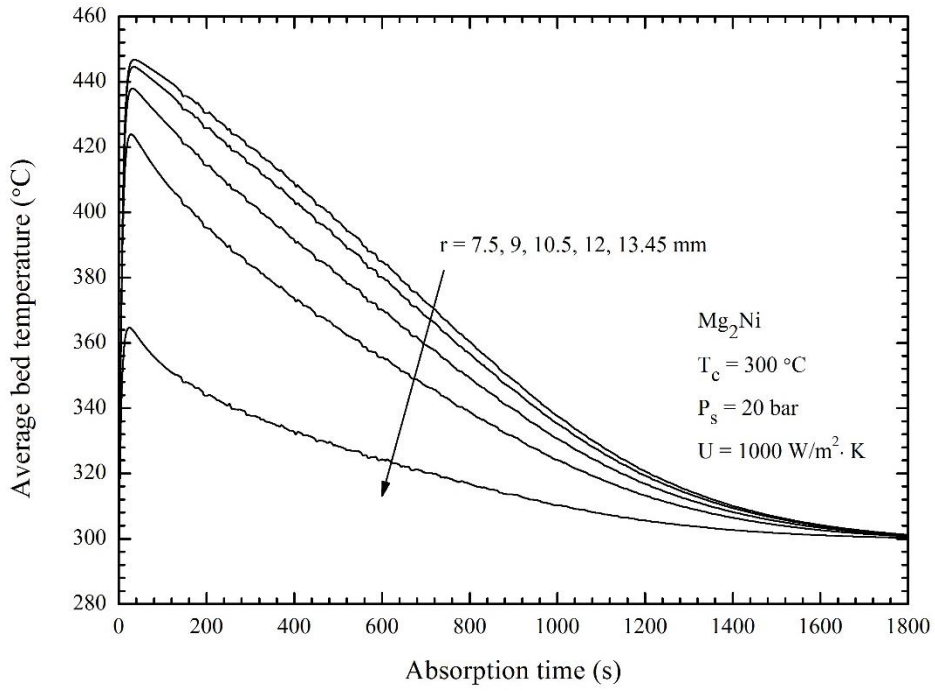

(b)

Fig. 5.3 – Variations at radial locations of (a) hydrogen concentration and (b) average bed temperature.

5.1.4 Effect of bed thickness

With other parameters same as that for the previous case, the effects of the bed thickness on the variations of the hydrogen storage capacity and the average bed temperature are investigated. The thickness of the bed i.e., difference between the radii of the outer and inner cylinders, $(r_0 - r_i)$ is varied from 7.5 to 12.5 mm in steps of 2.5 mm by keeping the inner radius constant at 6 mm. It is observed that the hydrogen absorption rate decreases with increase in the thickness of the bed (Fig. 5.4(a)). An opposite trend is observed for the temporal variation of the average bed temperature (Fig. 5.4(b)). This observation is attributed to the fact that with a smaller bed thickness, the average bed temperature reaches the cooling fluid temperature fast and hydrogen percolates fast to the MH volume. With increase in the bed thickness, rate of hydrogen absorption will be slower and hence, resulting in longer absorption time.

5.1.5 Effect of bed thermal conductivity

The thermal conductivity of an unmodified MH bed is very low in the order of 0.2 – 0.4 W/m·K. This limits the rate of hydrogen absorption. In order to improve the effective thermal conductivity of the hydride bed, several heat transfer augmentation techniques were proposed in the literature [Groll, 1993; Muthukumar and Groll, 2010]. Hence, the (effective) thermal conductivity λ_e of the MH bed is varied over a range. Figs. 5.5(a) and (b) show the effect of thermal conductivity λ_e of MH bed on the variation of average bed temperature and hydrogen storage capacity, respectively. For Mg_2Ni, with bed thickness of 12.5 mm, initial bed temperature 300 °C and supply pressure 20 bar, these results are shown for three representative values of λ_e the bed, viz., 1.4, 2.5 and 5.0 W/m·K. It is observed that higher the λ_e, higher is the absorption rate (Fig. 5.5(a)). An opposite trend is observed for the average bed temperature.

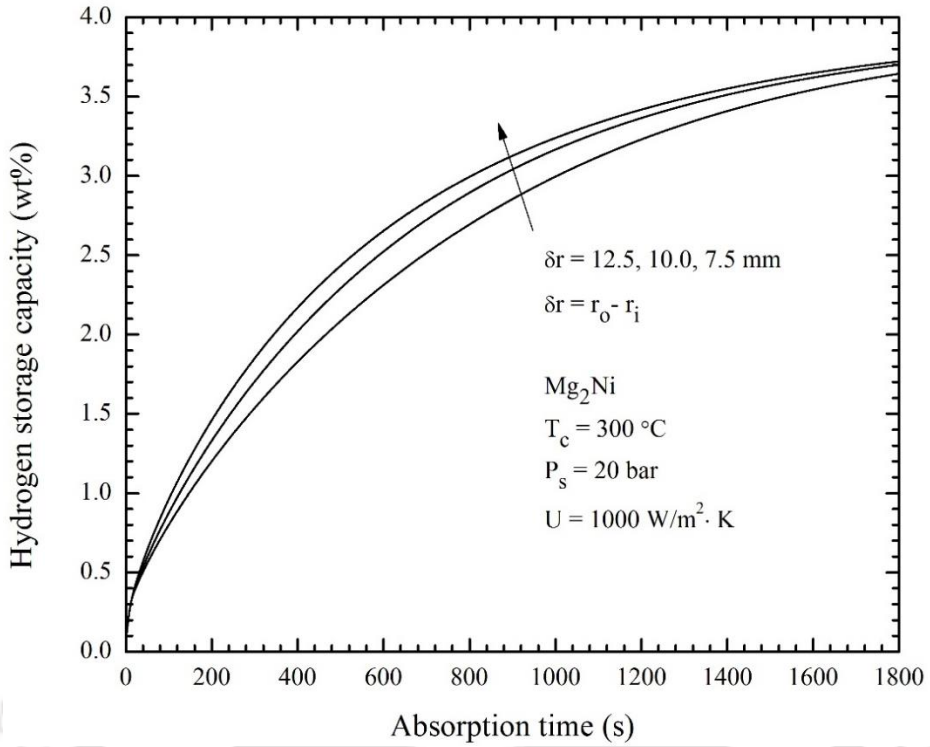

(a)

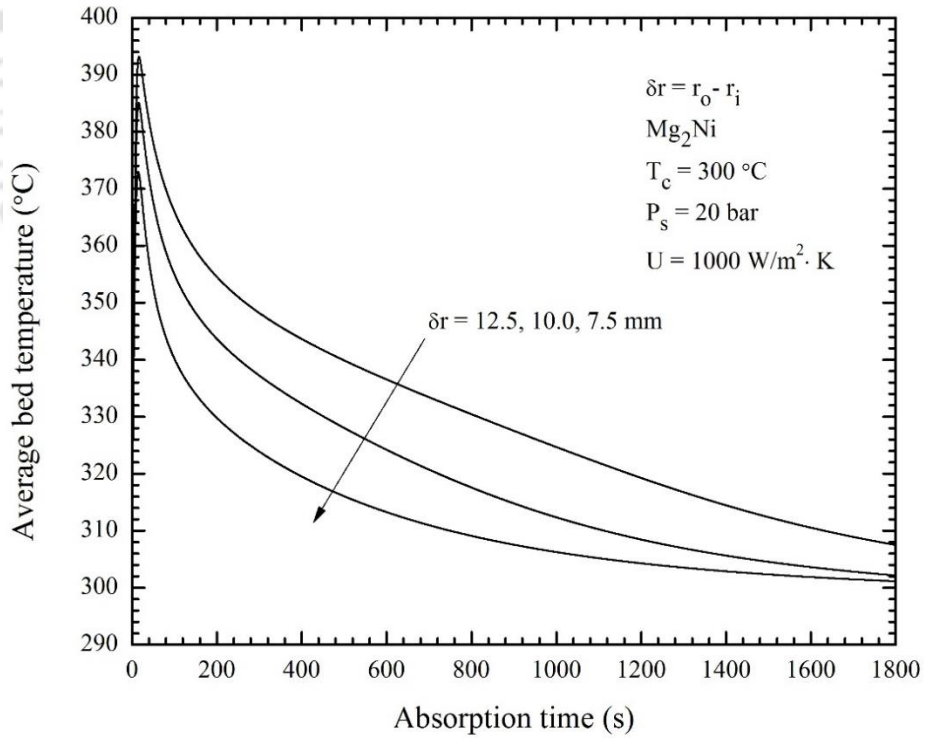

(b)

Fig. 5.4 – Effect of bed thickness on variations of (a) hydrogen storage capacity and (b) average bed temperature

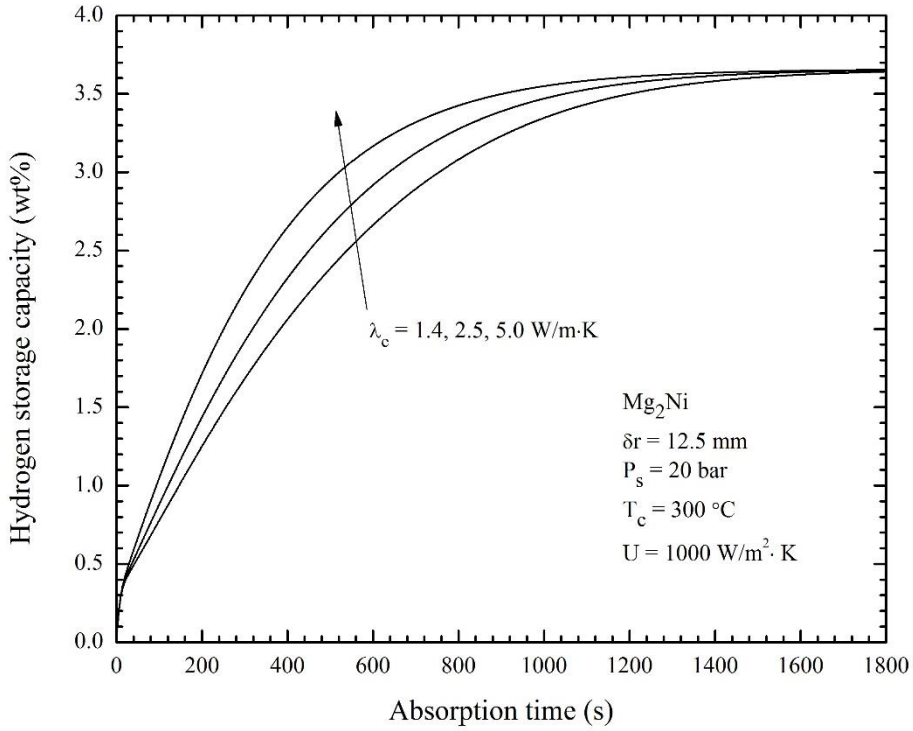

(a)

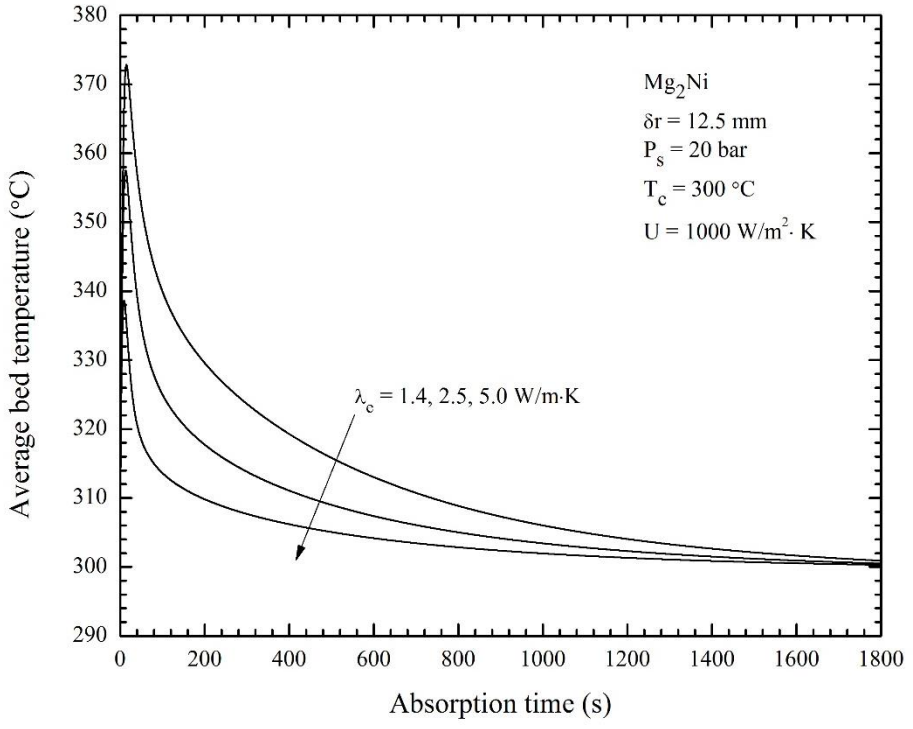

(b)

Fig. 5.5 – Effect of bed thermal conductivity on variations of (a) hydrogen storage capacity and (b) average bed temperature.

The observed trend is for the fact that higher is the thermal conductivity λ_e, higher is the heat transfer/removal from the MH reaction bed. The increased dissipation of heat from the MH volume induces higher absorption rate and lower average bed temperature. It is also observed that at a given supply pressure of 20 bar and absorption temperature of 300 °C, increasing the bed thermal conductivity beyond 2.5 W/m·K is not beneficial and hence, one can conclude that for a given reactor configuration and overall heat transfer coefficient, there exists an optimum value of bed thermal conductivity.

5.1.6 Effect of cooling fluid temperature

Mg_2Ni is a high temperature metal hydride alloy. Its absorption capacity is function of the initial bed temperature which is the cooling fluid temperature. The effect of the cooling fluid temperature on the hydrogen storage capacity and variation in average bed temperature are shown in Figs. 5.6(a) and (b), respectively. With supply pressure $P_s = 20\,\text{bar}$, effective thermal conductivity $\lambda_e = 2.5\,\text{W/m}\cdot\text{K}$, bed thickness 12.5 mm, the results are shown for $T_c = 300$ °C, 325 °C and 350 °C. It is observed from Fig. 5.6(a) that with an increase in the temperature of the cooling fluid, the rate of hydrogen decreases. An opposite trend is observed for the temporal variation of the average bed temperature. From these observations, at lower cooling fluid temperature of 300 °C, the average bed temperature is lowest, higher the rate of hydrogen and the MH bed is required minimum time to reach saturate.

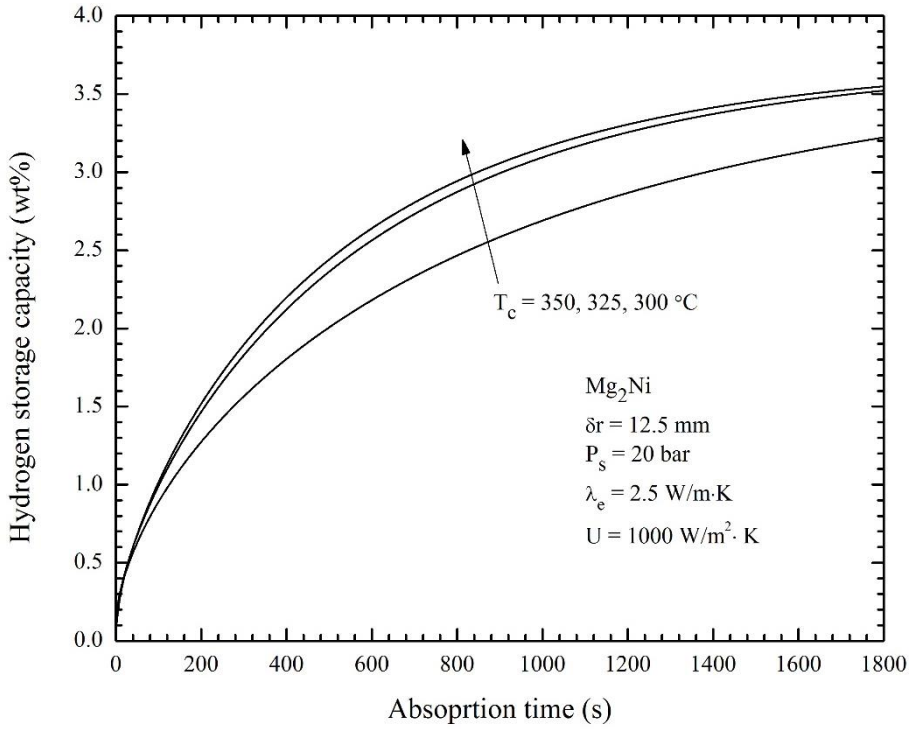

(a)

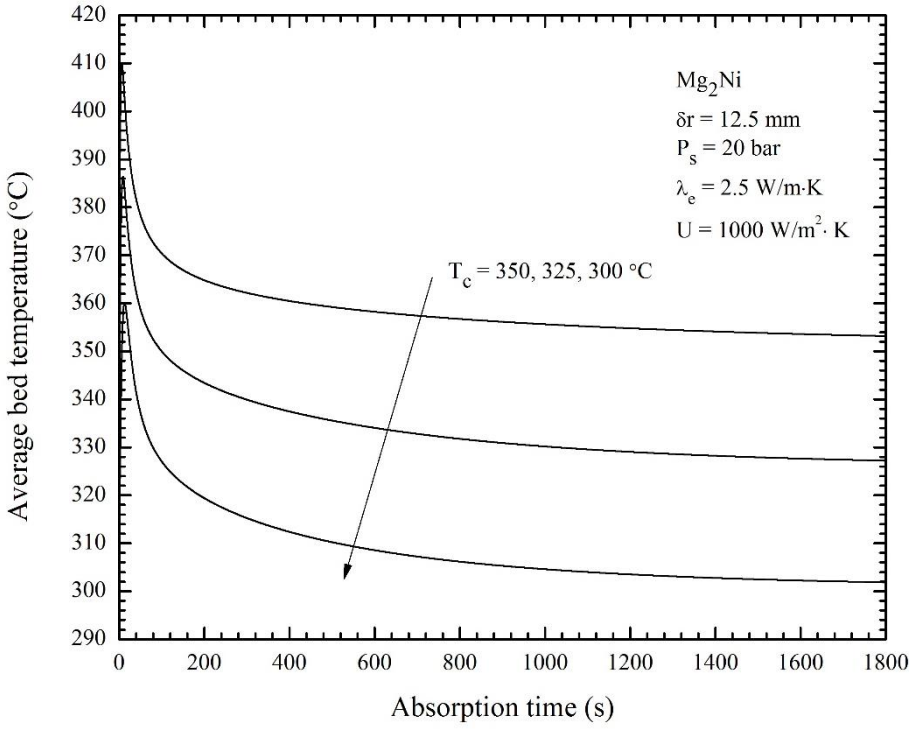

(b)

Fig. 5.6 – Effect of cooling fluid temperature on variations of (a) hydrogen storage capacity and (b) average bed temperature.

5.2 Numerical results of lab-scale MHHSD: desorption process

A 64×90 grid size is used in the desorption study. The present study has been carried out for desorption of hydrogen from the metal hydride bed with consideration of volumetric radiation. In this section, the effects of desorption temperature and overall heat transfer coefficient on the variations of the amount of hydrogen desorbed and average bed temperature are discussed.

5.2.1 Effect of radiation heat transfer

Figs. 5.7(a) and (b) illustrate the effect of radiation heat transfer on the variation in the average hydride bed temperature and amount of hydrogen desorbed. Initially, the reactor is fully hydride with hydrogen at 20 bar hydrogen supply pressure and 300 °C absorption temperature. Dehydriding process is initiated by supplying heat at 330 °C that creates higher pressure difference between dehydriding equilibrium pressure and desorption pressure. This pressure difference accelerates the desorption of hydrogen resulting to sudden drop in hydride bed temperature (due to rapid endothermic reaction) [Eq. 3.8], and so the MH bed temperature is reduced to 285 °C within 500 s. Later, the bed gains heat from heat transfer fluid for the further progress of desorption/dehydriding process. Due to lower thermal conductivity of MH bed, heat transfer from heat transfer fluid to MH bed is not enough to meet the initial rapid desorption process heating requirement and hence, the hydride bed takes heat from the bed itself resulting in sudden drop in temperature. This slows down the desorption process till about 500 s which is clearly observed from Fig. 5.7(a) and (b). Later, the heat transfer in the MH bed has improved and it accelerates the rate of desorption. In this present study, with consideration of effect of volumetric radiation, rate of desorption is rapid while comparing to the case without radiation effect. At the dehydriding conditions of desorption pressure 1 bar and initial bed temperature

330 °C, the maximum amount of hydride desorbed is 36.2 g of H_2/kg of Mg_2Ni. Considering, the case without volumetric radiation, the case with volumetric radiation improves the hydriding rate (near porous wall) by about 14.3%.

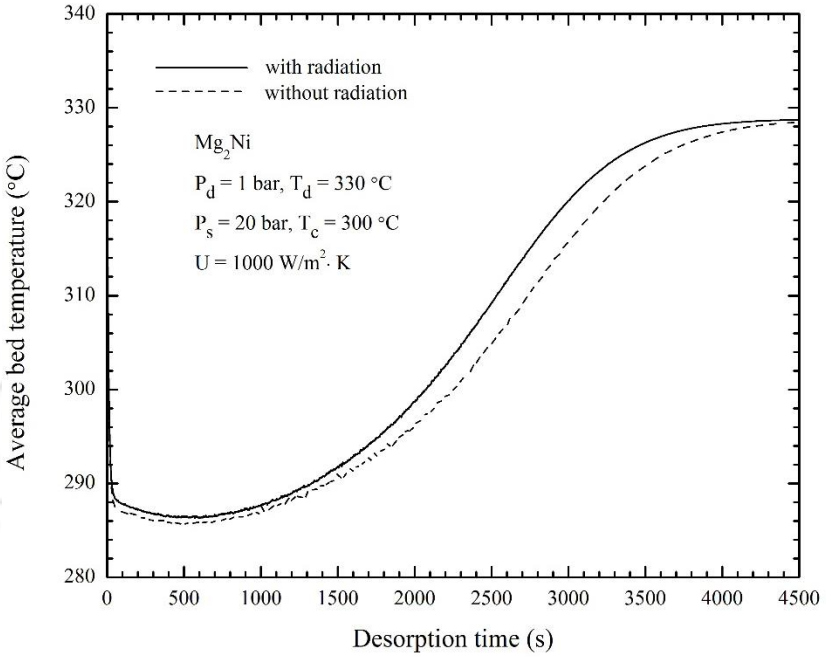

(a)

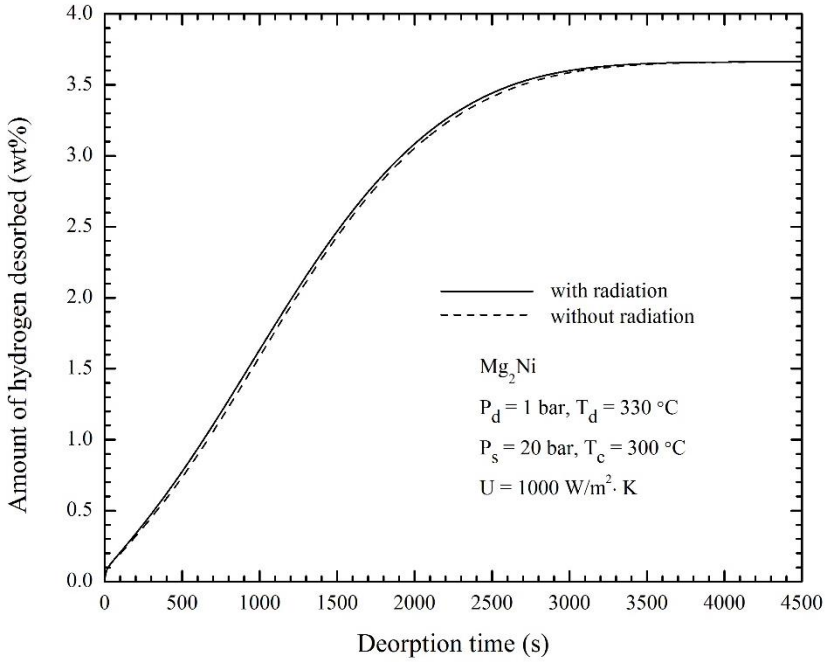

(b)

Fig. 5.7 – Effect of radiation heat transfer on variations of (a) average bed temperature with and without radiation and (b) amount of hydrogen desorbed.

5.2.2 Radial variations of bed temperature and hydrogen concentration

Figs. 5.8(a) and (b) show the temporal variations of hydride bed temperature and hydrogen concentration, respectively at different radial location, viz., $r = 7.5$, 9.0, 10.5, 12.0 and 13.45 mm. At all radial locations, initially temperature drops and then increases with time. At any instant, temperature is higher for a higher values of r. At the end of the desorption process, at all radial locations, temperature reaches close to the temperature of the heat transfer fluid. From Fig. 5.8(b), it is observed that unlike hydride bed temperature (Fig. 5.8(a)), hydride concentration decreases with time. The amount of hydrogen desorbed is found to be higher at higher values of r, i.e. the region closes the convective boundary. This is for the reason that the bed temperature is higher for a higher value of r. It is further observed from Fig. 5.8(b) that with the passage of desorption time, like temperature distribution, at all radial locations, concentration tend to the same value. Temperature and concentration both become radially uniform.

5.2.3 Effect of heat transfer fluid temperature

The effects of heat transfer fluid temperature (desorption temperature) on the temporal variations of the average bed temperature and the amount of hydrogen desorbed are shown in Figs. 5.9(a) and (b), respectively. With desorption pressure 1 bar, these variations are shown for the desorption temperature 330 °C, 340 °C and 350 °C. For any desorption temperature, initially bed temperature drops to low temperature and then rises slowly and finally it reaches its steady-state. The temporal variation of the amount of hydrogen desorbed rises with desorption time. The desorption rate is more for a higher value of desorption temperature. Irrespective of the desorption temperature, the maximum amount of hydrogen desorbed is about 3.62 wt%. This maximum is reached early for higher desorption temperatures. At given desorption time of

2000 s, the amount of hydrogen desorbed increases from 3 wt% at 330 °C to 3.5 wt% at 350 °C, i.e. 16.67% improvement in the desorption rate is observed for the increase in the desorption temperature from 330 °C to 350 °C.

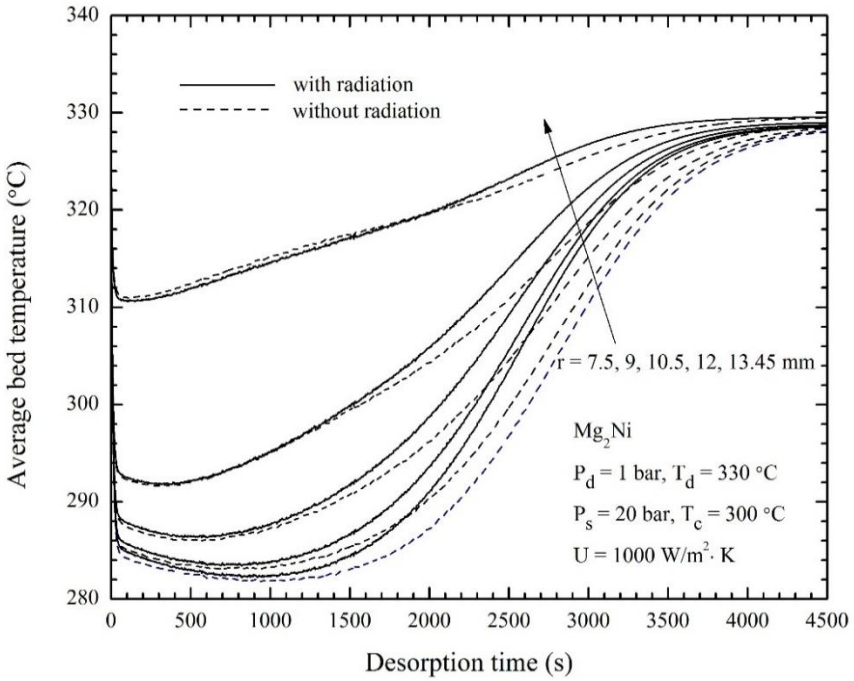

(a)

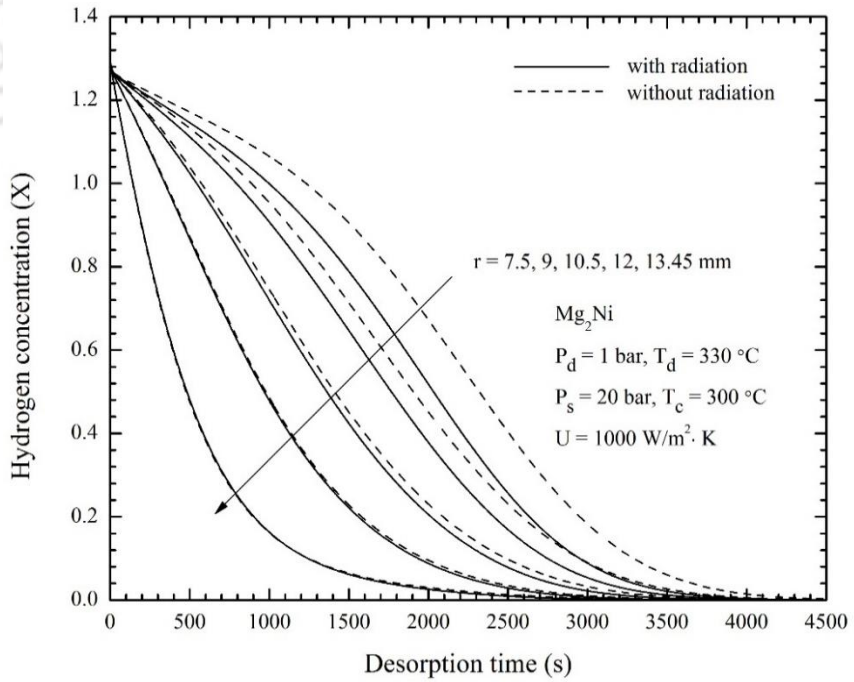

(b)

Fig. 5.8 – Radial variations of (a) average bed temperature and (b) hydrogen concentration.

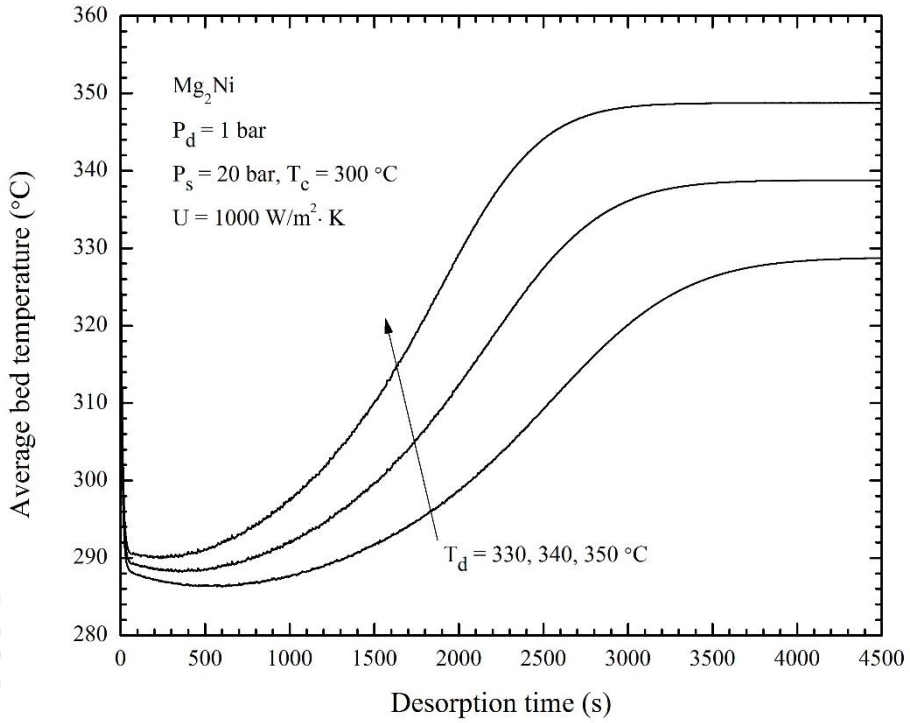

(a)

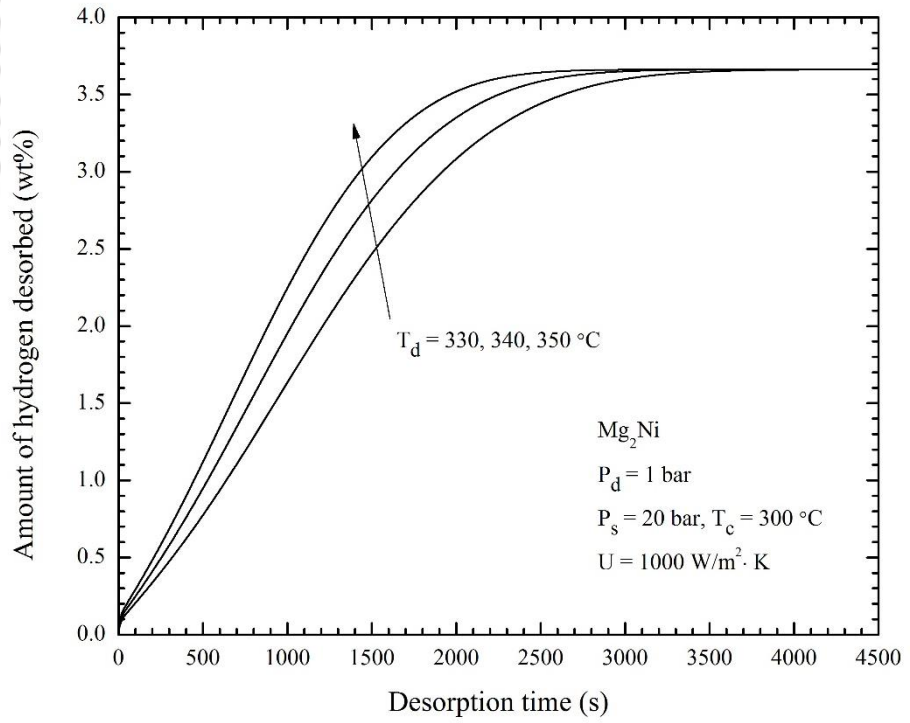

(b)

Fig. 5.9 – Effect of heat transfer fluid temperature on variations of (a) average bed temperature and (b) amount of hydrogen desorbed.

5.2.4 Effect of overall heat transfer coefficient

The effect of overall heat transfer coefficient (U) on the variation of average bed temperature and amount of hydrogen desorbed are illustrated in Figs. 5.10(a) and (b), respectively. By definition, U combines the external convective resistance, conducting resistance of the reactor wall and the contact resistance between the reactor wall and the MH particle. The overall heat transfer coefficient [Muthukumar *et al.*, 2005; 2007] plays significant role in absorption/desorption process. In the present study, the results are presented for overall heat transfer coefficient U = 500, 750, 1000 and 1250 W/m^2·K. It is observed from Fig. 5.10(a) that for a higher value U, the rate of desorption is higher. For any U, initially there is a drop in temperature and then it increases, and finally reaches the steady-state. From the temporal variation of the amount of hydrogen desorbed for different values of U shown in Fig. 5.10(b), it clear that for any U, with time, the desorption rate increases and for all values, the steady-state values are almost the same. In the transient state, desorption rate is more for a higher value of U. However, the difference in desorption rate decreases with increase in the value of U. Increase of U beyond 1000 W/m^2·K will not be beneficial because beyond this value, internal heat conductive resistance controls the dehydriding process. Hence, one can conclude that for a given MH reactor geometry there exists an optimum value of U.

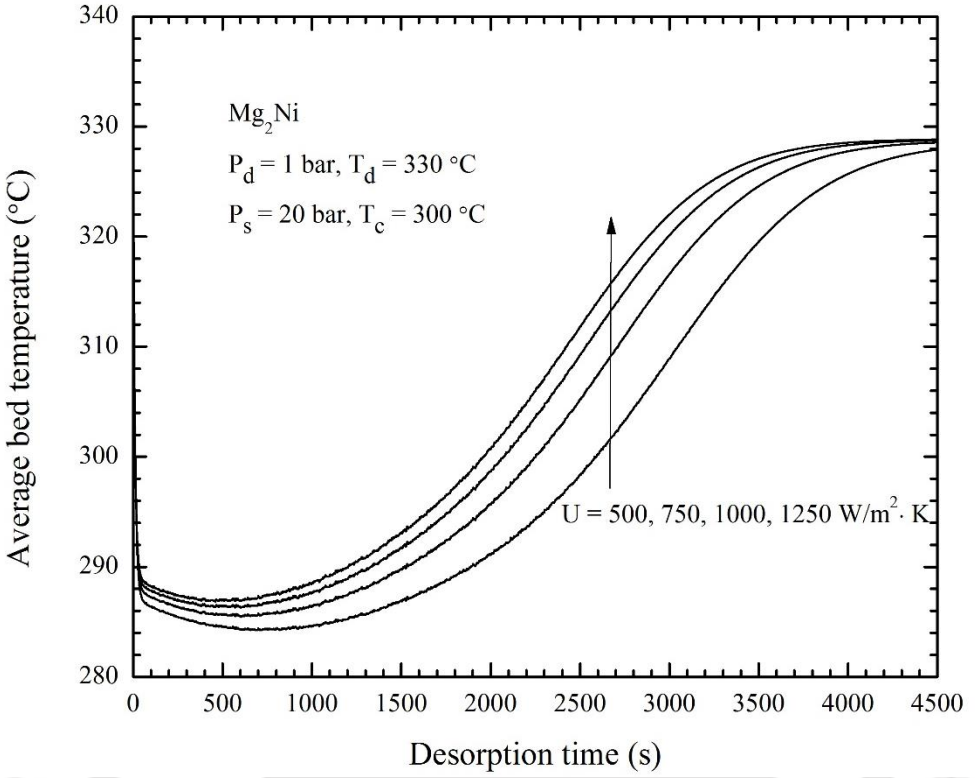

(a)

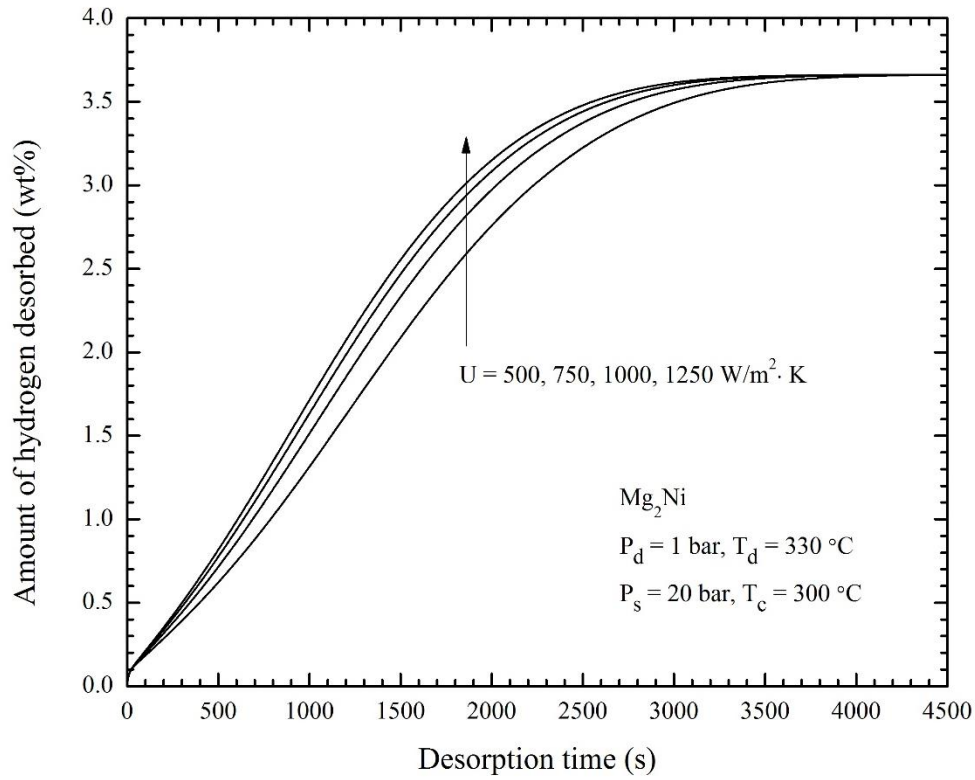

(b)

Fig. 5.10 – Effect of heat transfer coefficient on variations of (a) average bed temperature and (b) amount of hydrogen desorbed.

5.3 Numerical results of MHHSD with ECT

In this section, the influence of different arrangements of ECT on the hydriding and dehydriding characteristics of MHHSD employing 2.75 kg of $LmNi_{4.91}Sn_{0.15}$ and the effects of supply pressure, absorption and desorption temperatures and effective thermal conductivity of hydride bed on the performance of the MHHSD are discussed.

5.3.1 Effect of number of ECT

In order to find the optimum configuration of the MHHSD with ECT arrangement, a 2-D mathematical model is developed by keeping the outer and inner diameters of the storage container are same and by varying the number of ECT in radial and angular positions. The main objective of varying the number of ECT is to find the optimum configuration of the ECT which provides the minimum absorption and desorption times. The HTF is supplied through the ECT to the container. For a given geometry, the number of ECT has greater influence on the rate of hydrogen absorption/desorption. The thermal model is simulated for five different configurations of ECT viz., 24, 36, 48, 60 and 70 and the observations are given below. The detailed arrangement of different configurations is already presented in Table 3.1.

5.3.1.1 Absorption process

Effect of number of ECT on the variations of the average hydride bed (surface averaged) during absorption of hydrogen is shown in Fig. 5.11(a). At the supply conditions of 30 °C absorption temperature and 30 bar hydrogen supply pressure, it is observed from the Fig. 5.11(a) that the average bed temperature reaches the HTF temperature quickly for the reactors having higher ECT. The average hydride bed temperature initially increases due to rapid exothermic reaction in the MH bed and then starts decreasing slowly towards the temperature of the HTF. At the

beginning of hydriding process, the massive amount of heat released from the hydride bed that causes the rise in temperature. Later, the continuous supply of HTF removes the heat from the hydride bed. It is clearly evident from Fig. 5.11(a) that the reactors with 60 and 70 ECT have better heat removal rates than the reactors with 24 and 36 ECT. This is due to increase in effective heat transfer area with increase in the number of ECT.

Fig. 5.11(b) shows the influence of ECT arrangements on the variations of the hydrogen storage capacity (HSC) (wt%). With the same supply conditions, the HSC increases with increase in absorption time for all ECT. However, there is no variation in the total HSC (1.12 wt%). The maximum HSC reaches within 33 min for 24 ECT, 25 min for 36 ECT, 21 min for 48 ECT, 19 min for 60 ECT and 18 min for 70 ECT. The reactor with 60 ECT removes the liberated heat from the hydride bed much faster rate than the other configurations. It maintains a lower hydride bed temperature and accelerates the rate of hydrogen absorption.

5.3.1.2 Desorption process

To study the dehydriding characteristics at 50 °C desorption temperature and 1 bar desorption pressure, the absorption conditions of 30 bar hydrogen supply pressure and 30 °C absorption temperature is fixed. Fig. 5.12(a) illustrates the effect of number of ECT on the variations of average hydride bed temperature with desorption time. The average hydride bed temperature suddenly reduces to its low value owing to the rapid endothermic reaction of desorption/dehydriding process and then, the temperature starts increasing slowly to the temperature of HTF. The reactors with 60 and 70 ECT recover the heat from the HTF more

rapidly than other configurations. The reason is that more heat transfer surface area aids more heat recovery from the HTF.

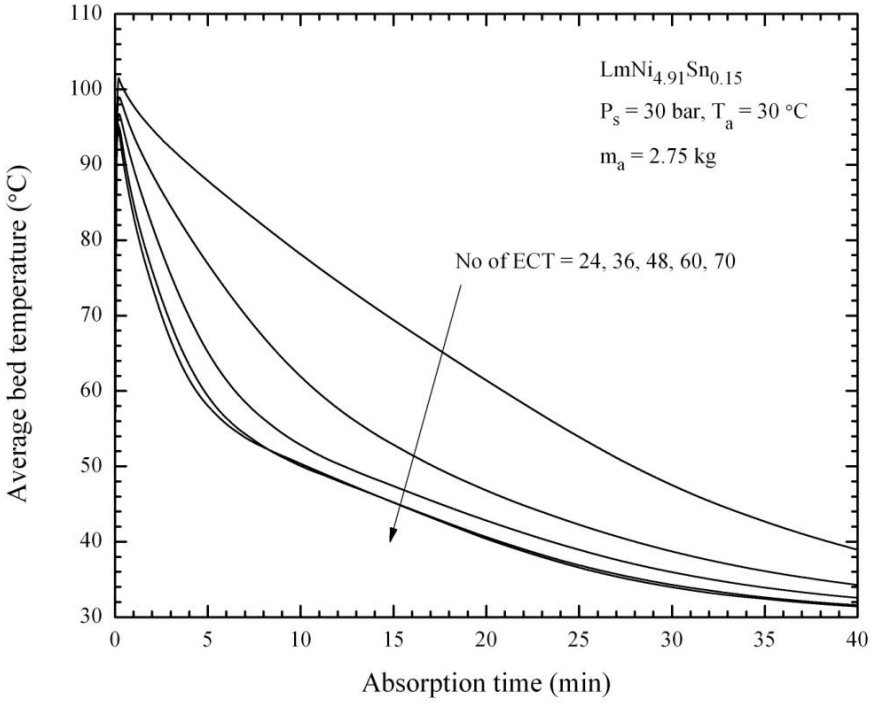

(a)

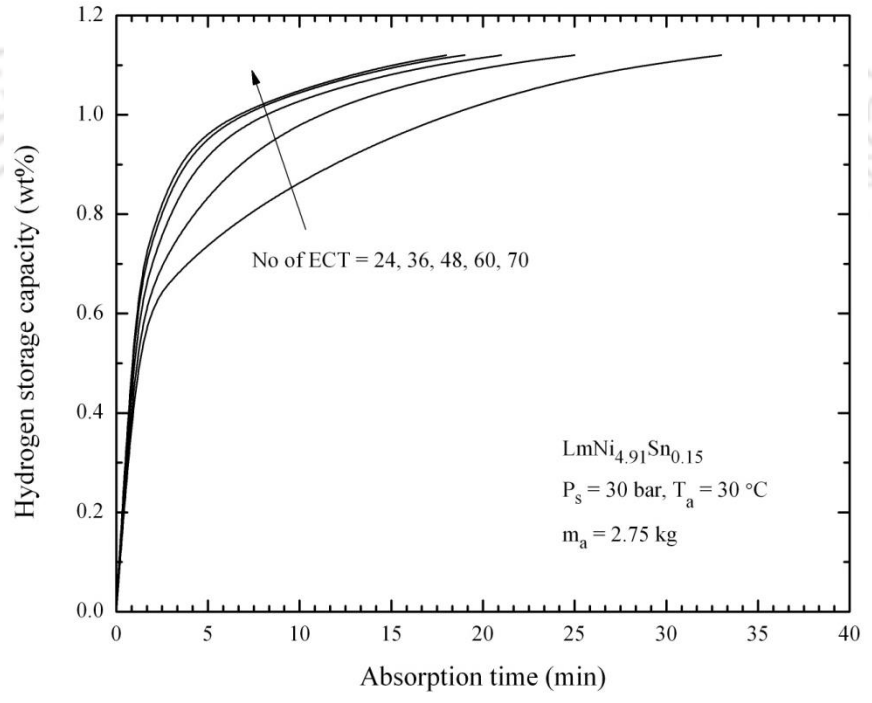

(b)

Fig. 5.11 – Effect of number of embedded cooling tubes on variations during hydriding process with time (a) average bed temperature and (b) hydrogen storage capacity.

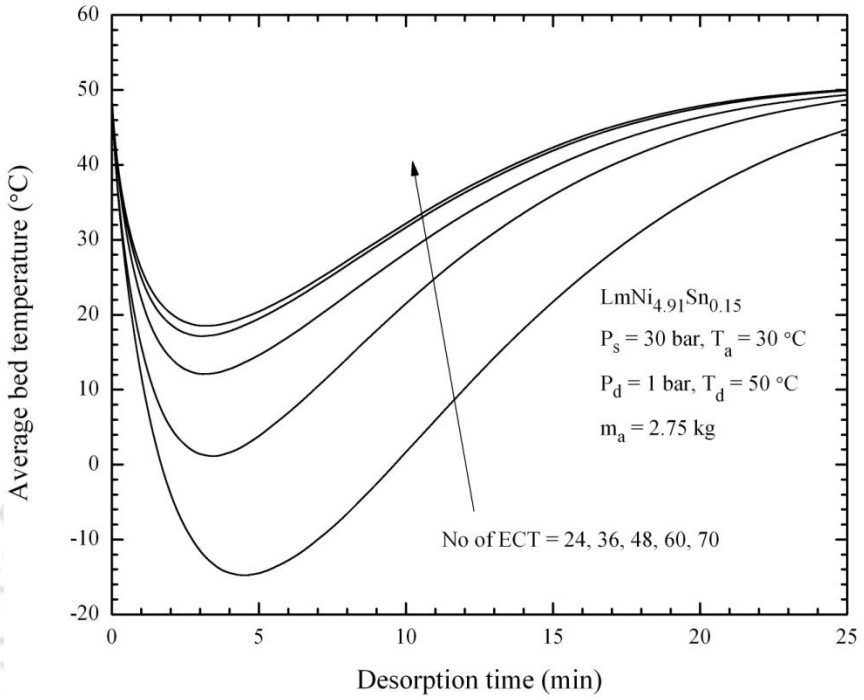

(a)

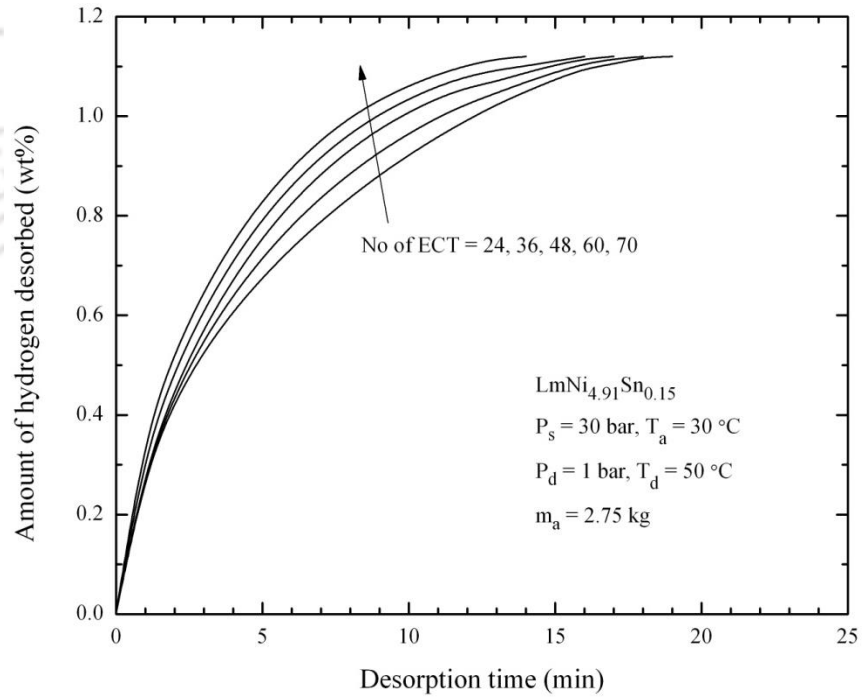

(b)

Fig. 5.12 – Effect of number of embedded cooling tubes on variations during dehydriding process with time (a) average bed temperature and (b) amount of hydrogen desorbed.

The effect of number of ECT on the variations of amount of hydrogen desorbed with time is shown in Fig. 5.12(b). The maximum amount of hydrogen desorbed (1.11 wt%) is same for all ECT configurations. The reactor with higher number of ECT (60 and 70 ECT) completes the desorption process more rapidly than other ECT configurations. This is mainly due to the enhancement in heat transfer with increase in ECT.

It is observed from Fig. 5.11(b) and Fig. 5.12(b) that the rector with 60 and 70 ECT have almost the same absorption/desorption times and by considering the complexity in the design and fabrication of the reactor bed, the reactor with 60 ECT is found to be optimum.

5.3.2 Grid independent test

From the 2-D analysis, a reactor with 60 ECT is considered for the detailed 3-D numerical simulation. A grid independent test was carried out by evaluating the effect of different element sizes on the variation of average bed temperature during absorption process. The number of grid with element sizes is presented in Table 5.1. It is observed from Fig. 5.13 that at a given absorption condition, there is no significant variations in the hydride bed temperature with increase in the grid element sizes (total elements) from 97,438 to 111,840. Therefore, for saving the computational time, 97,438 elements is selected for the present study.

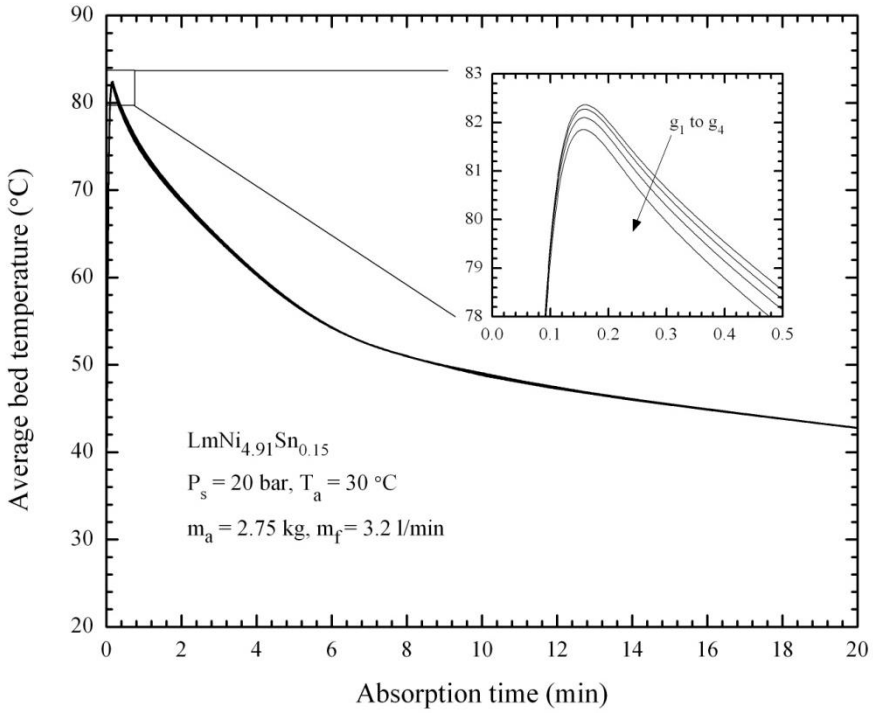

Fig. 5.13 – Grid independent test.

Table 5.1 – The number of grid with element sizes

Grid name	Minimum element size (mm)	Maximum element size (mm)	Number of elements
g1	0.201	6.72	97,438
g2	0.134	5.4	102,242
g3	0.0687	3.95	107,052
g4	0.0024	1.18	111,840

5.3.3 Comparison between 2-D and 3-D thermal models

The effect of hydrogen supply pressure on the variations of the average hydride bed temperature is shown in Fig. 5.14. The evaluated average hydride bed temperature from 2-D model with surface averaged and from 3-D model with volume averaged are compared for different hydrogen supply pressures i.e. 10 bar, 20 bar, 30 bar at 30 °C absorption temperature. It is

observed that the volume averaged hydride bed temperature is higher than the surface averaged hydride bed temperature. Therefore, for the large scale reactor with ECT, the numerical results obtained from the 3-D model will be closer to the realistic values.

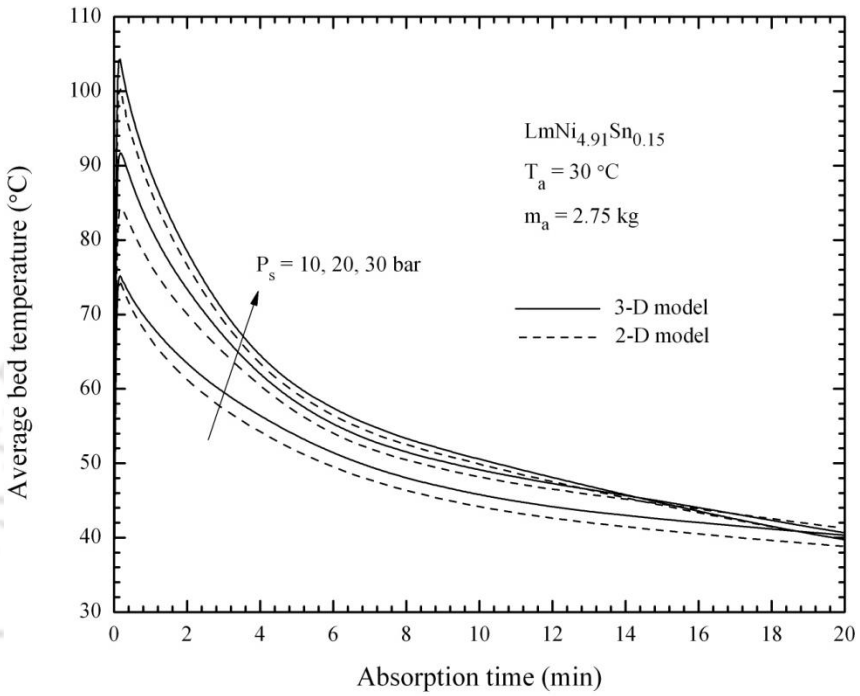

Fig. 5.14 – Comparison between 2-D and 3-D models.

5.3.4 Validation of numerical simulation

In order to validate the numerical results, the reactor with 60 ECT filled $LmNi_{4.91}Sn_{0.15}$ is chosen. This configuration is similar to the one reported in the experimental studies [section 5.4]. Employing 3-D mathematical model, the hydriding and dehydriding characteristics of MHHSD are predicted at the supply pressures of 10 and 20 bar at 30 °C absorption temperature. It is observed from Fig. 5.15(a) that the numerically predicted HSC are in good agreement with the experimental data. The maximum deviances between them are 6.59% at 10 bar and 8.18% at 20 bar. Initially the computed results of HSC is higher than the experimental data, due to rapid rate of hydrogen absorption and the trend is reverse after 11 min for 10 bar and 6 min for 20 bar.

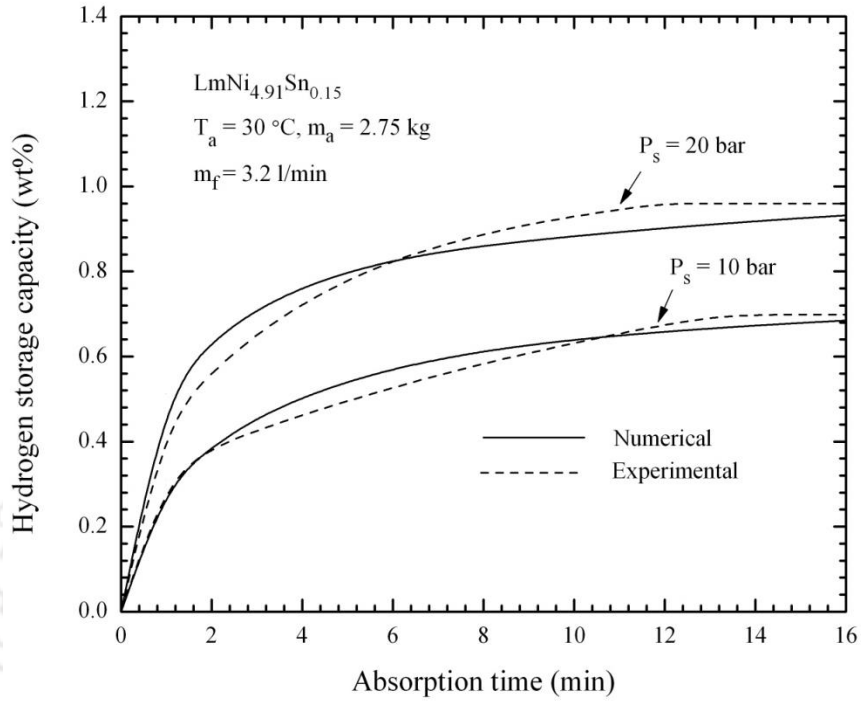

(a)

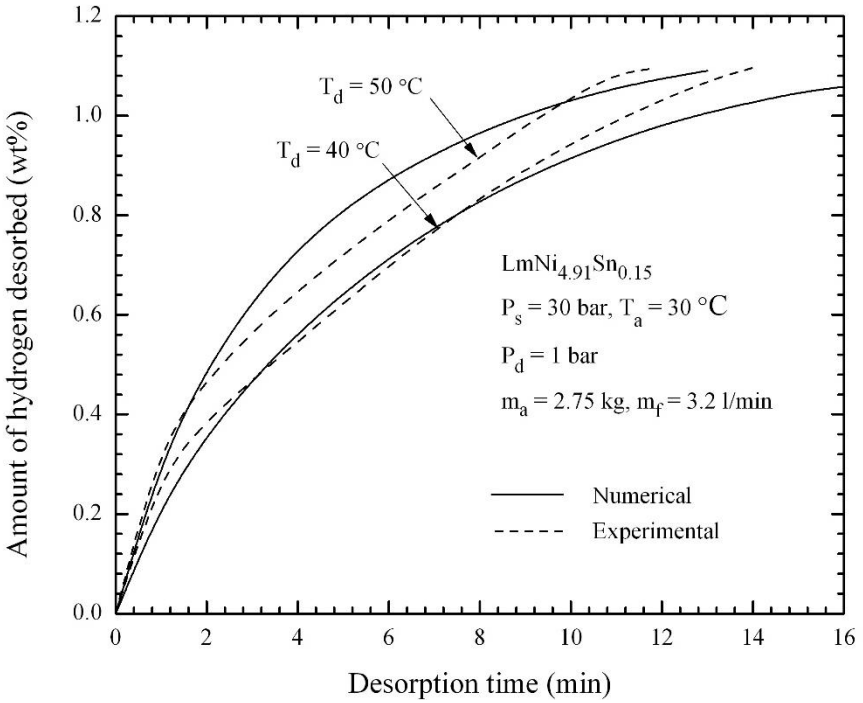

(b)

Fig. 5.15 – Validation of numerical results of the reactor with 60 embedded cooling tubes during (a) absorption process and (b) desorption process.

The experimental condition of hydriding process i.e. 30 bar at 30 °C is same for the dehydriding process performed with two hot fluid temperatures viz., 40 °C and 50 °C and at 1 bar desorption pressure. Fig. 5.15(b) illustrates the validation of amount of hydrogen desorbed for two desorption temperatures. The maximum deviations between the numerically estimated the amount of desorption and the experimental data are 3.57% at 40 °C and 9.52% at 50 °C. During the beginning of desorption process, the rate of hydrogen desorption is rapid owing to higher driving potential [Muthukumar *et al*., 2005; Muthukumar and Ramana, 2010; Sekhar *et al*., 2013] and the deviation between them is also less till 8 min for 40 °C and 2 min for 50 °C. These deviations are mainly due to the assumptions of uniform void fraction of MH and the uncertainties in the estimated values of thermo – physical properties of the hydride alloy.

5.3.5 Absorption characteristics

5.3.5.1 Effect of supply pressure

Fig. 5.16(a) illustrates the effect of hydrogen supply pressure on variations of the hydrogen storage capacity (HSC) with absorption time. In the present study, the absorption temperature is maintained at 30 °C and the hydrogen supply pressure is varied from 10 to 35 bar in steps of 5 bar. The observed HSC (wt%) are 0.7, 0.8, 0.96, 1.04, 1.12 and 1.19 respectively for the hydrogen supply pressures of 10, 15, 20, 25, 30 and 35 bar. The heat being released during the hydride formation process is carried away by the HTF continuously. There is a delay in removing the heat liberated by container owing to the lesser thermal conductivity of hydride bed and it slows down the hydride formation process. Higher supply pressure provides higher driving potential for hydride formation and takes lesser time to reach the maximum HSC. For the lower supply pressure, the trend is reverse. The hydriding process is completed within 11 min for

35 bar and 20 min for 10 bar hydrogen supply pressure. The HSC varies for different supply pressure because of Pressure – Concentration isotherms characteristics of $LmNi_{4.91}Si_{0.15}$.

5.3.5.2 Effect of (effective) thermal conductivity

Fig. 5.16(b) shows the effect of effective thermal conductivity of the hydride bed on the variation of HSC with absorption time. As the effective thermal conductance or conductivity of hydride bed is very low, many heat transfer enrichment techniques have been proposed in the literatures [Groll, 1993; Muthukumar and Groll, 2010] to improve the heat transfer within the hydride bed. For a given reactor geometry, at a hydriding condition of 30 bar hydrogen supply pressure at 30 °C, the variation of HSC is studied for different values of effective thermal conductivities viz. 0.2, 0.5, 1, 2 and 2.5 W/m·K. In general, the average hydride bed temperature decreases with increase in effective thermal conductivity of the hydride bed. Apparently the HSC does not increase for the given initial conditions. It remains the same as 1.11 wt%. The rate of hydrogen absorption is high for higher thermal conductivity of hydride bed. For the higher effective thermal conductivity of hydride bed, the faster rate of heat removal from the container enhances the hydriding process and the hydriding time is also lesser than the low thermal conductivity bed. The hydriding time is reduced by about 68.2% (from 22 to 7 min) when the effective thermal conductivity is varied from 0.2 to 2.5 W/m·K.

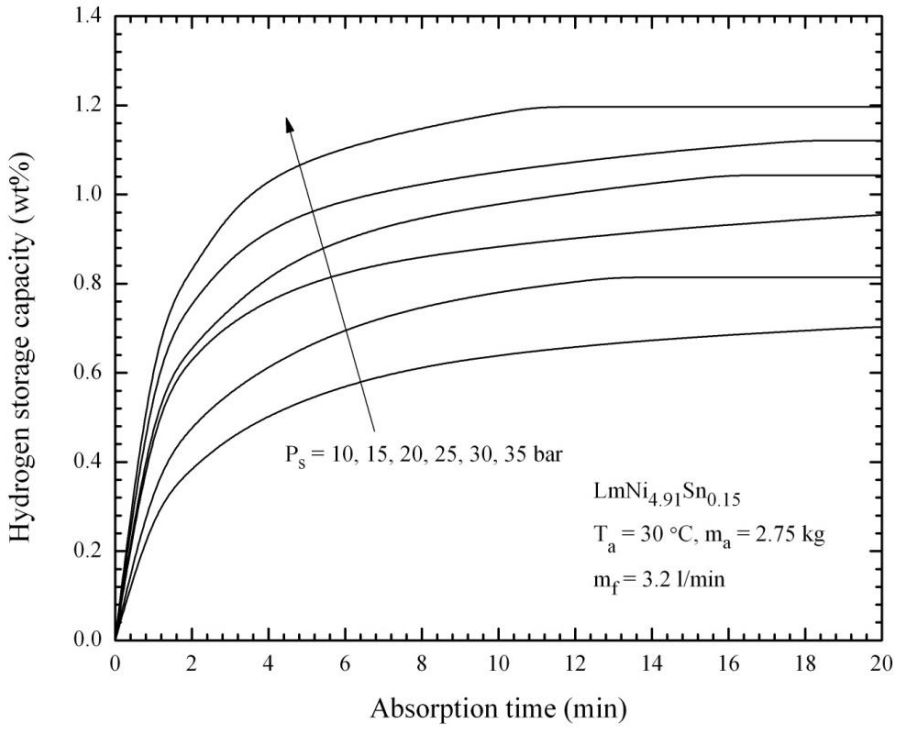

(a)

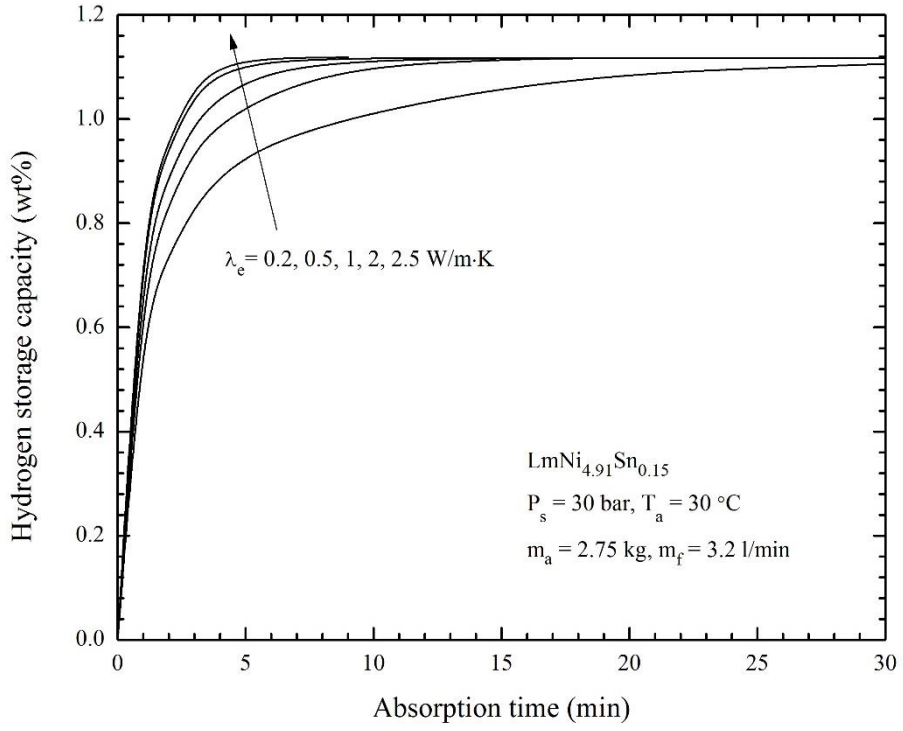

(b)

Fig. 5.16 – Effect of (a) supply pressure and (b) effective thermal conductivity of the hydride bed on the hydriding rate.

5.3.5.3 Pictorial representation of hydride bed temperature during absorption process

With the absorption condition of 30 bar at 30 °C, the transient behavior of hydride bed temperature during absorption process at different time intervals of 12, 100, 175, 250, 750 and 1200 s in the form of sliced view is presented in Fig. 5.17. As the hydride formation starts, the heat being released rises the hydride bed temperature to maximum at 12 s of absorption time. Poor effective thermal conductivity of hydride bed retards the process of heat removal from the container to the HTF. Hence, after 12 s of absorption time, the hydride bed temperature starts decreasing to its initial absorption temperature. The heat is removed much faster near the cooling tubes than the other region (near porous filter). The region of the hydride bed where the HTF enters experiences lower temperature than the region where the HTF leaves. The region with lower hydride bed temperature enhances the hydriding rate and attains saturation rapidly [Muthukumar *et al*., 2012]. This is clearly observed at all absorption time. It should be noted that a significant temperature change is observed between first and last slices. Initially the value of temperature variation between the first slice and last slice is about 10 °C (nearer at outer region) and this value is gradually reduced to zero at end of the absorption process. The time taken to reach the entire hydride bed to 30 °C (absorption temperature) is about 1200 s.

5.3.5.4 HTF variations along ECT at different axial locations: absorption process

Figs. 5.18(a) and 5.18(b) illustrate the co-ordinates at different axial and radial distances of MHHSD with 60 ECT respectively. Fig. 5.18 (c) shows the variations in HTF temperature along embedded cooling tubes at different axial distances (5, 50, 100 and 150 mm from the left end) [Fig. 5.18(a)]. The absorption condition of 30 bar supply pressure and 30 °C is maintained. Two rows of ECT i.e. inner row nearer to porous filter and outer row of MHHSD are considered for

the present study. Initially, from Figs. 5.18(c), it is observed that the difference between the inlet and outlet temperature of HTF is comparatively high due to rapid hydriding rate. As the hydriding reaction progress, the temperature difference is gradually decreased and finally becomes zero at the end of hydriding process. The heat is progressively transferred from the hydride bed to HTF temperature. The trend observed from both rows (inner and outer) are same. The temperature of HTF at inner row takes more time to reach initial supply temperature than outer row. The temperature of HTF at outer row attains the supply temperature within 6 min of absorption time. A maximum temperature difference between the HTF inlet and outlet is observed to be 4 °C for inner row and 12 °C for the outer row at the beginning of the hydriding process.

5.3.5.5 Variation in HTF at different radial locations: absorption process

With same absorption conditions, the variations in HTF temperature at different radial locations with time are illustrated in Figs. 5.19(a) and (b). HTF temperature profiles are plotted for fixed axial distances (50 and 100 mm) and at different radial locations of embedded cooling tubes (inner, middle and outer rows) [Fig. 5.18(b)]. The coordinates of the locations are mentioned in the Figs. 5.19(a) and (b). In the beginning of hydriding process, the HTF temperature increases quickly due to rapid exothermic reaction in the hydride bed and then it slowly reduces to initial temperature. The HTF temperature at middle row reaches the maximum temperature among other rows. The temperature of HTF at middle and outer row reaches the supply temperature of HTF well before the inner row within 8 min. This is due to presence of more no of ECTs and minimum angular distance between two ECTs in middle and outer rows than the inner row. For both axial distances, the observed trend is same.

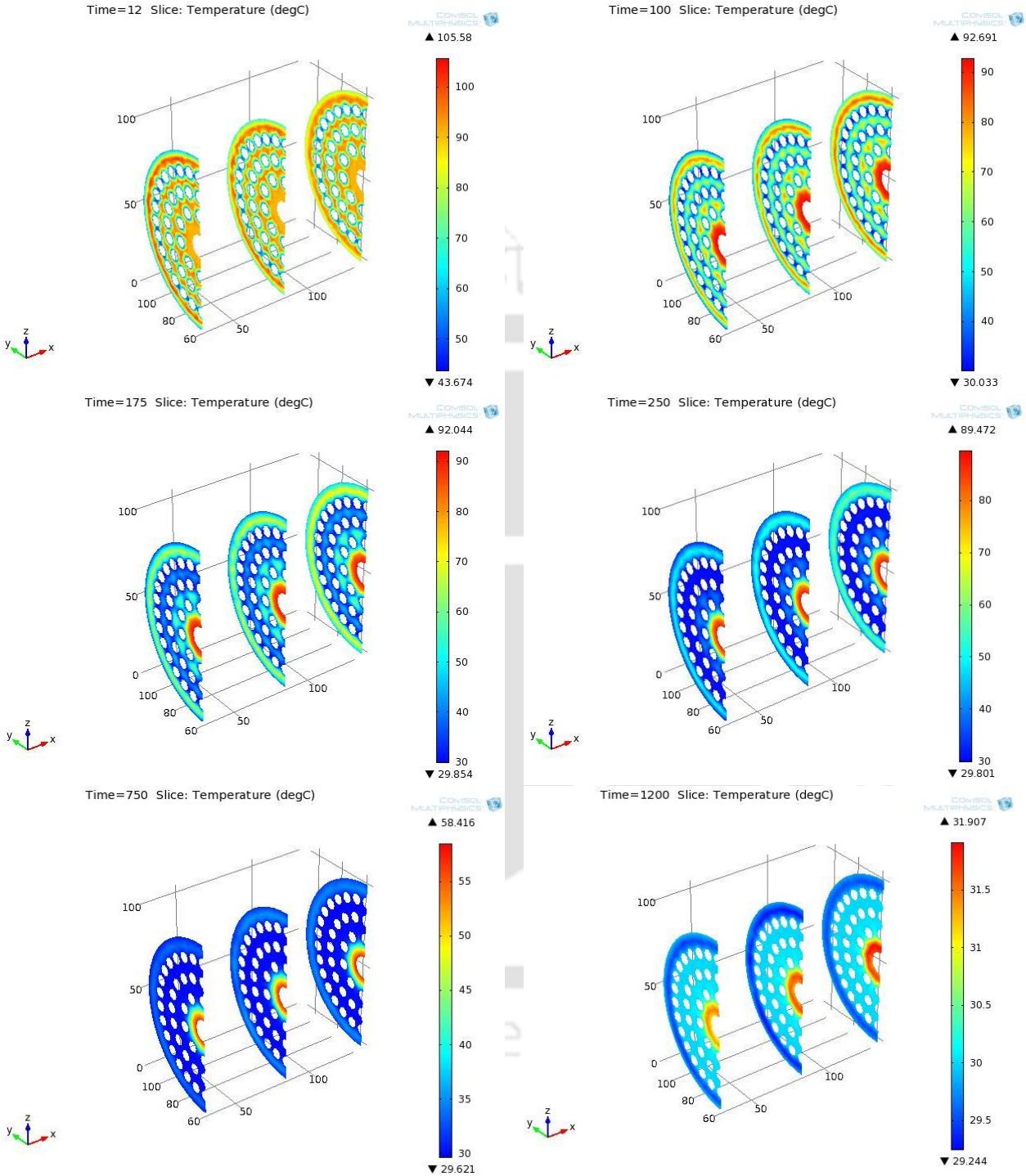

Fig. 5.17 – Pictorial sliced view of hydride bed temperature at different time intervals during absorption process.

A **B**

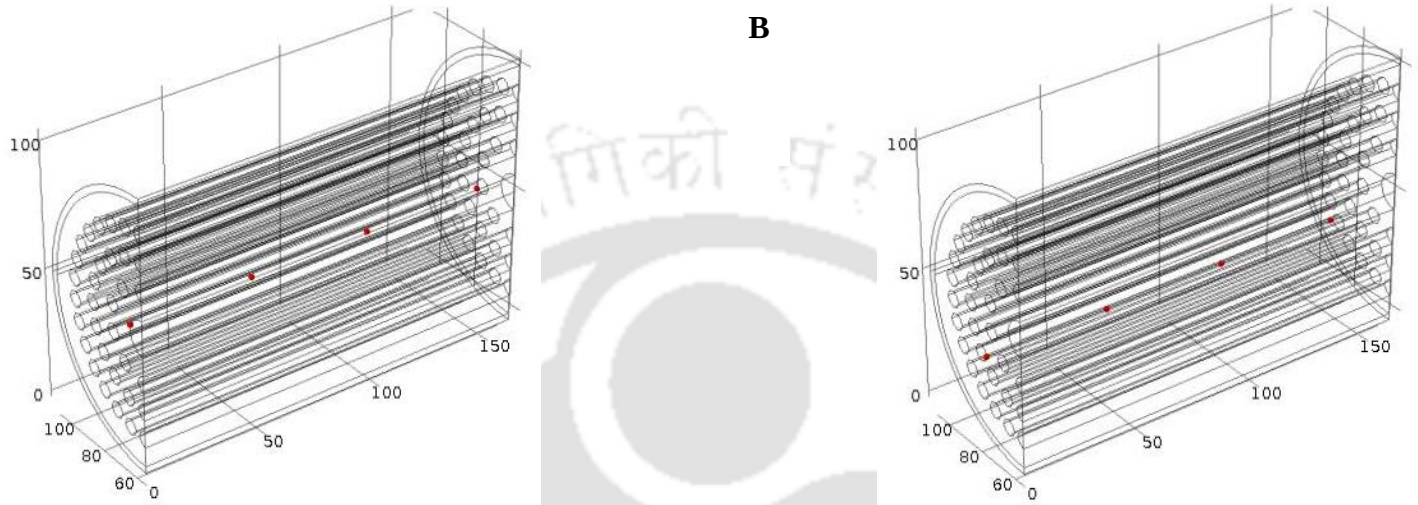

Fig. 5.18(a) – The co-ordinates at different axial locations of MHHSD with 60 ECT; (A) [(5, 50, 100, 150):69:48] and (B) [(5, 50, 100, 150):83:28]

A **B** **C**

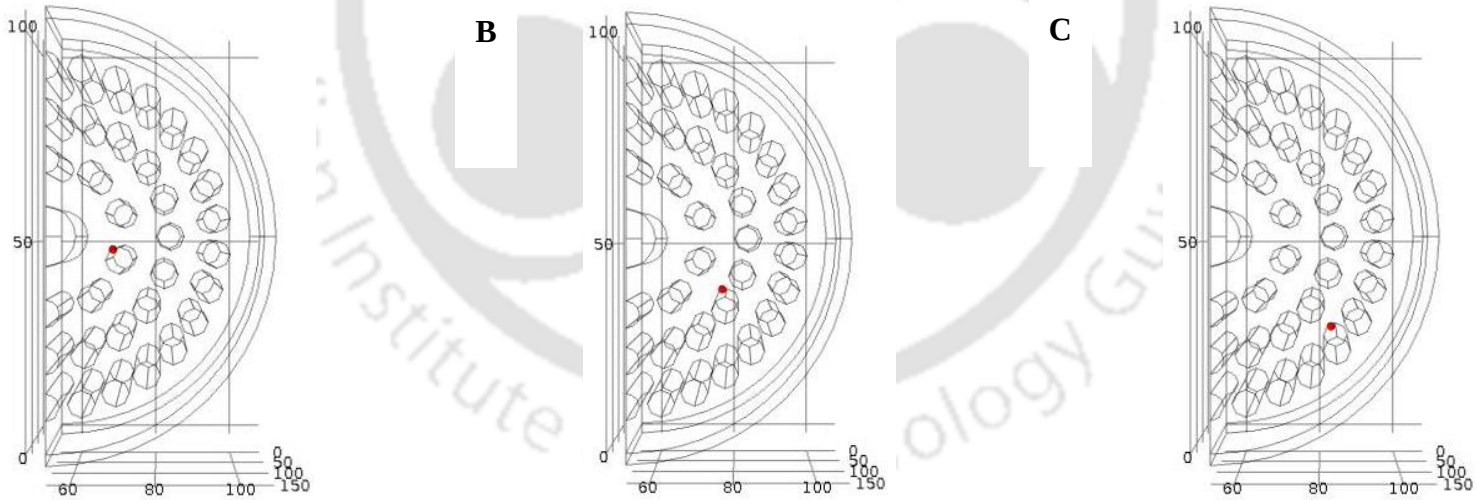

Fig. 5.18(b) – The co-ordinates at different radial locations of MHHSD with 60 ECT; (A) 50:69:48, (B) 50:77:38 and (C) 50:83:28

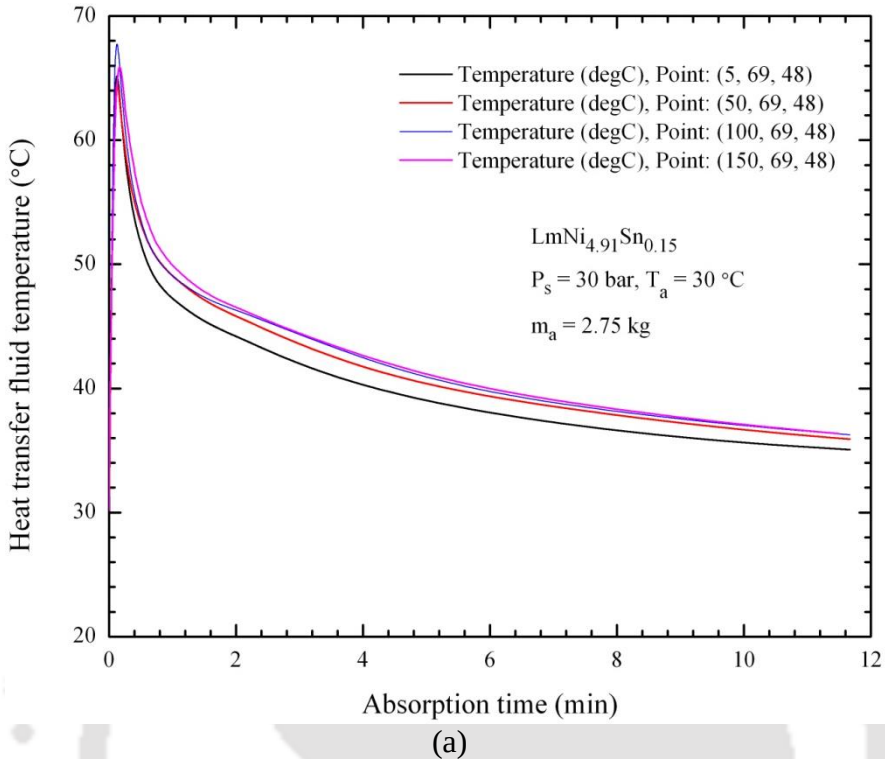

(a)

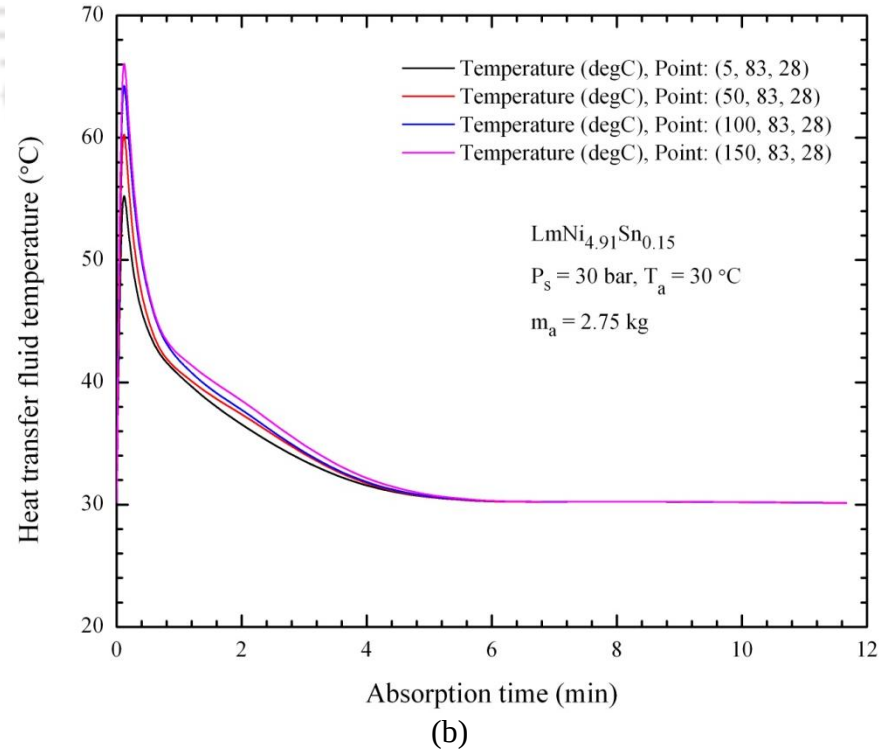

(b)

Fig. 5.18(c) – Variations in heat transfer fluid temperature along embedded cooling tubes at different axial distances with time (a) inner row and (b) outer row.

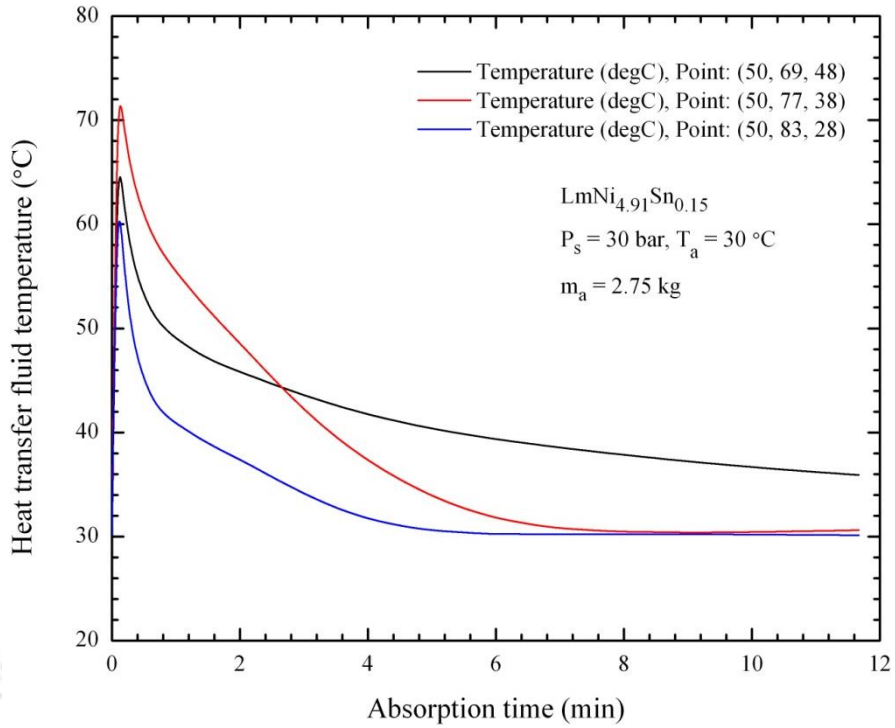

(a)

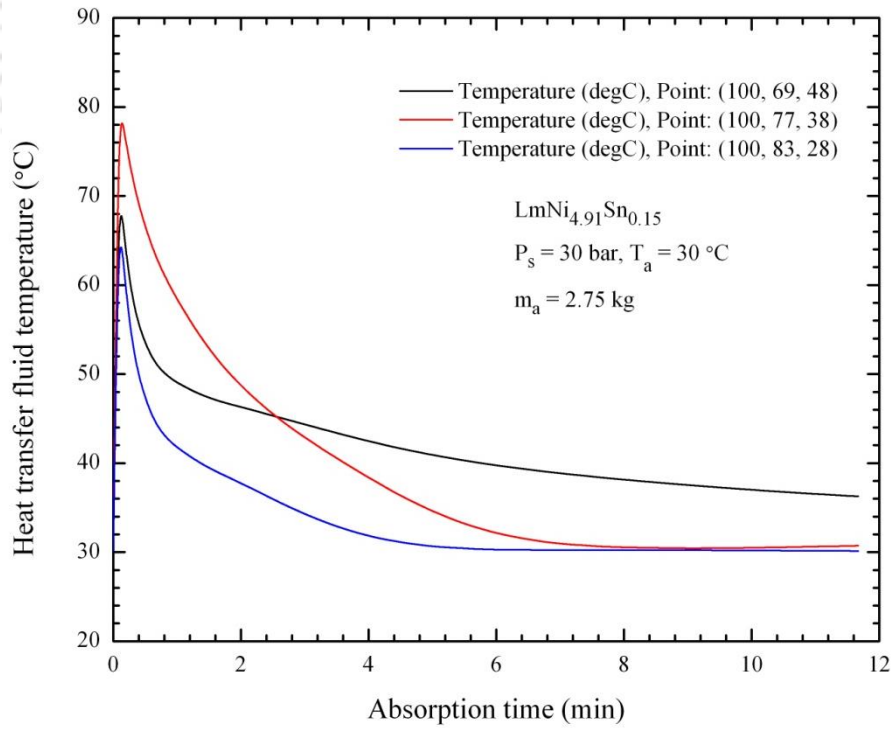

(b)

Fig. 5.19 – Variations in heat transfer fluid at different radial locations with time (a) at axial distance of 50 mm and (b) axial distance of 100 mm.

5.3.6 Desorption characteristics

5.3.6.1 Effect of hot fluid temperature

Fig. 5.20(a) illustrates the effect of hot fluid temperature (HFT) on the variation of the amount of hydrogen desorbed (wt%) with desorption time. The simulation for hydriding process is carried out at 30 bar supply pressure and 30 °C absorption temperature and simulation for desorption process is performed at different HFT viz., 30, 40, 50 and 60 °C by keeping the desorption pressure at 1 bar. Once the dehydriding process is initiated, the hydride bed temperature drops suddenly to a lower temperature owing to the endothermic reaction which happens during the discharge of hydrogen. Therefore, lower hydride bed temperature is observed at the beginning of dehydriding process and so excess heat required for promoting the dehydriding process is taken from the hydride bed. The hydride bed recovers the temperature slowly and reaches to the initial HFT at the end of the desorption process. At any given desorption time, the amount of hydrogen desorbed from the container is high for higher HFT. At higher HFT, larger pressure variance between the dehydriding equilibrium pressure and the desorption pressure accelerates the rate of dehydriding process [Muthukumar *et al*., 2005; Sekhar *et al*., 2013; Muthukumar and Ramana 2010]. Fig. 5.20(a) shows that the maximum amount of hydrogen (≈ 1.11 wt%) is desorbed within 30 min for 30 °C, 22 min for 40 °C, 13 min for 50 °C and 11 min for 60 °C. From this, it is clearly observed that the rate of desorption is rapid at higher HFT.

5.3.6.2 Effect of effective thermal conductivity of the hydride bed during desorption process

With the similar hydriding conditions of 30 bar supply pressure at 30 °C and the desorption/dehydriding condition of 1 bar dehydriding pressure and 40 °C desorption temperature, the simulation is carried out for different values of effective thermal conductivities of the hydride bed viz., 0.2, 0.5, 1.0, 2.0 and 2.5 W/m·K. The effect of variation of bed thermal conductivity on the amount of hydrogen desorbed is shown in Fig. 5.20(b). With different λ_e, the observed maximum amount of hydrogen desorbed is same as 1.11 wt%. However, the dehydriding time is eventually decreased by about 33.3% (from 24 to 16 min) when the effective thermal conductivity is varied from 0.2 to 2.5 W/m·K.

5.3.6.3 Pictorial representation of hydride bed temperature during desorption process

At different time intervals of 30, 100, 175, 300, 500 and 1000 s, the pictorial representation (sliced view) of hydride bed temperature during the dehydriding process at the hydriding condition of 30 bar hydrogen supply pressure and 30 °C and dehydriding condition of 1 bar and 50 °C is illustrated in Fig. 5.21. As soon as the desorption is started, the hydride bed temperature decreases suddenly near the porous wall which can be observed from the time intervals of 30, 100 and 175 s in Fig. 5.21. As the effective thermal conductivity of hydride bed is very low, the hydride particles are not able to fascinate the heat from the HFT temperature and this reduces the rate of dehydriding. Later, there is an improvement in hydride bed temperature and it starts increasing with desorption time. This trend is observed from the pictorial representation at 300 and 500 s and finally the hydride bed reaches to supply temperature of 50 °C at about 1000 s.

It is also observed from Fig. 5.21 that the temperature difference between the first and last slices is about 4 °C at the beginning and zero at the end of the desorption process.

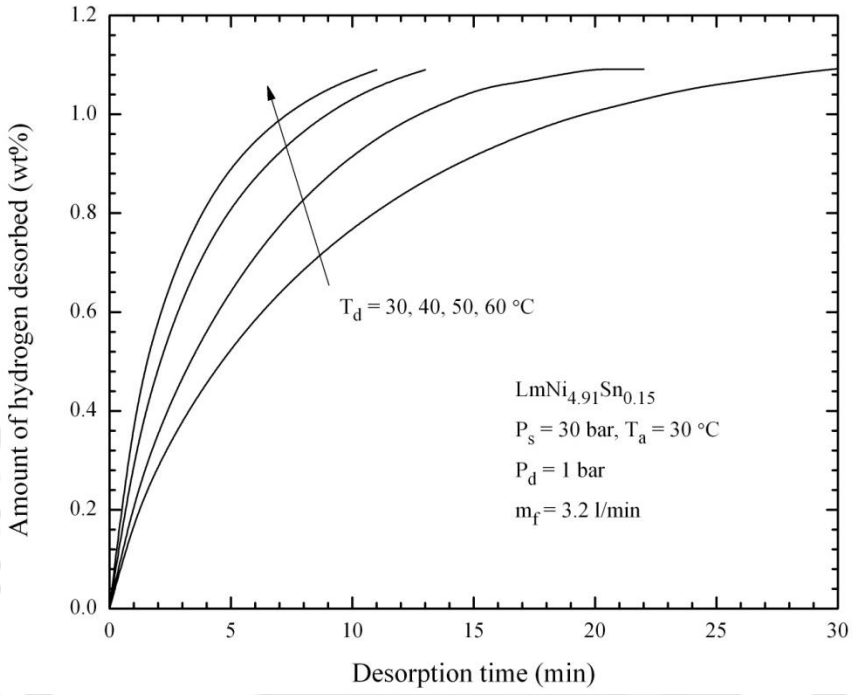

(a)

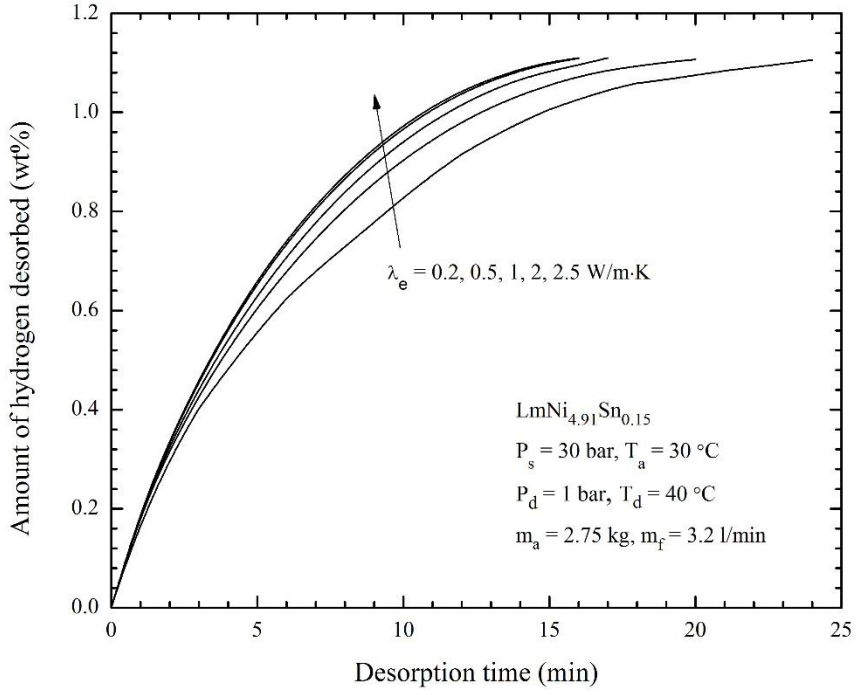

(b)

Fig. 5.20 – Effect of (a) hot fluid temperature and (b) effective thermal conductivity on hydrogen desorption rate.

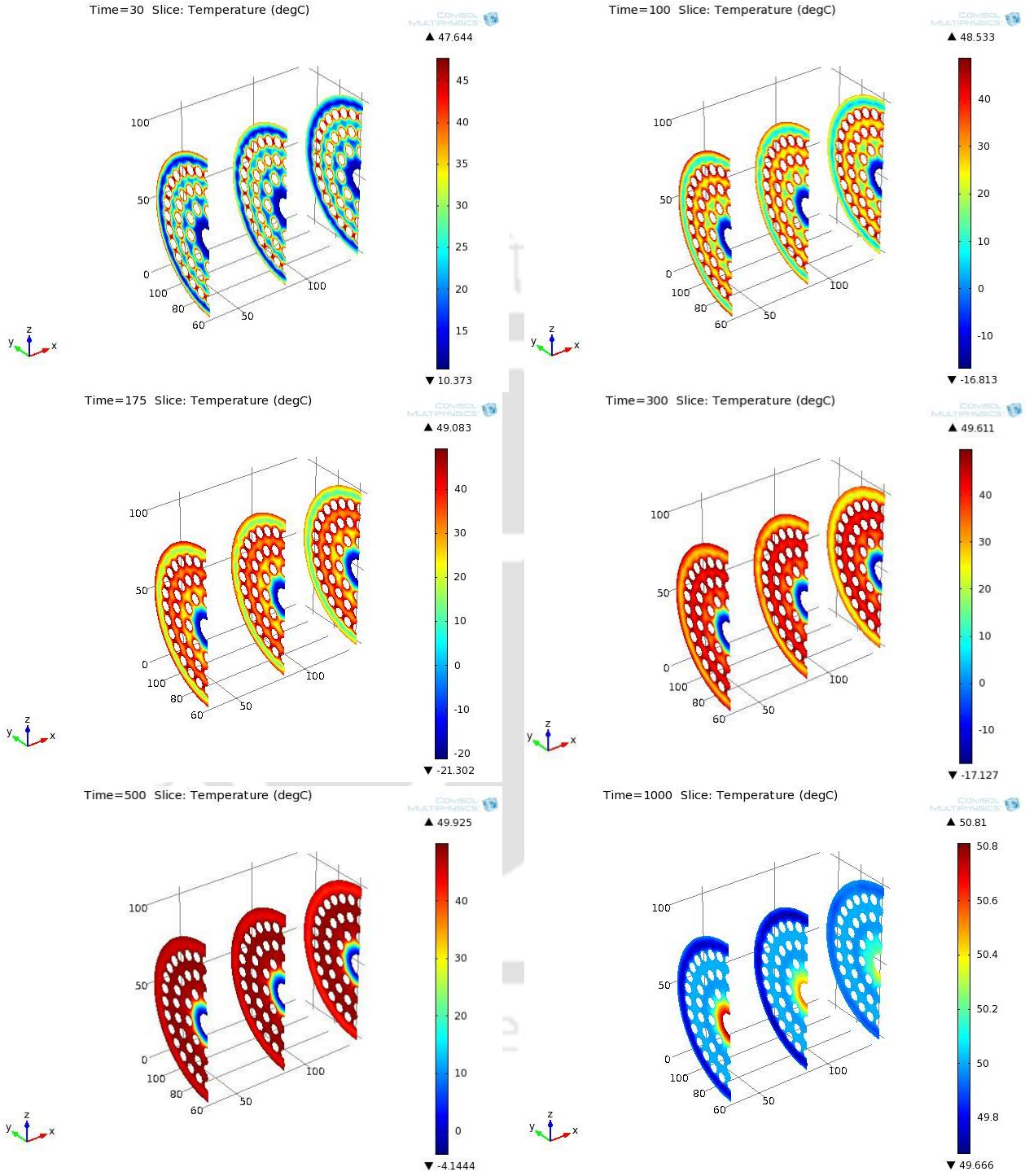

Fig. 5.21 – Pictorial sliced view of hydride bed temperature at different time intervals during dehydriding process.

5.3.6.4 Variation in HFT along the ECT at different axial locations: desorption process

The variations in HFT along the ECT at different axial distances with time are illustrated in Fig. 5.22. Temperatures at axial distances of 5, 50, 100 and 150 mm from the left end are shown for the supply conditions of absorption process of 30 bar supply pressure at 30 °C and the desorption conditions of 1 bar desorption pressure at 50 °C. Temperature profiles for two different rows of ECT are plotted (Fig. 5.18(a)). Initially, the temperature of hot fluid decreases suddenly due to rapid endothermic reaction and slowly increases to initial supply temperature. Temperature difference between inlet and outlet of hot fluid is high at the beginning of the dehydriding process and it tends to zero at the end of dehydriding process. A similar trend is observed form both rows (inner and outer). Temperature at outer row of ECT attains the initial temperature within 10 min (Fig. 5.22(b)). Temperature at inner row takes more than 12 min to reach initial hot fluid temperature and it is clearly observed from Fig. 5.22(a).

5.3.6.5 Variation in HFT at different radial locations: desorption process

With same absorption and desorption conditions, the variation in HFT at different radial locations with time is shown in Figs. 5.23(a) and (b). HFT profiles are plotted for fixed axial distances (50 and 100 mm) and at different radial locations of embedded cooling tubes (inner, middle and outer rows). The coordinates of the locations are mentioned in the Figs. 5.18(b). At the start of dehydriding process, the HFT decreases rapidly due to prompt endothermic reaction in the hydride bed and then it slowly increase to initial HFT. It is observed that the variation in HFT also follows the trend similar to the absorption process (Fig. 5.19(a) and (b)). The HFTs at middle and outer row attain the initial temperature about 12 min of desorption time. The reason

for rapid retrieval of HFT is the enhancement of heat transfer in the regions closer to middle and outer row. The observed trend is same for both axial distances.

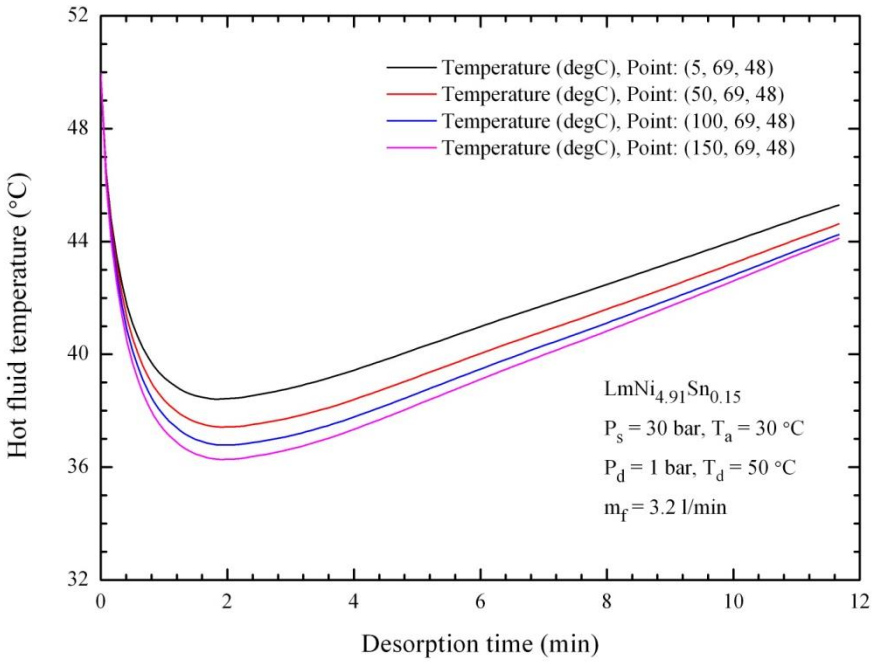

(a)

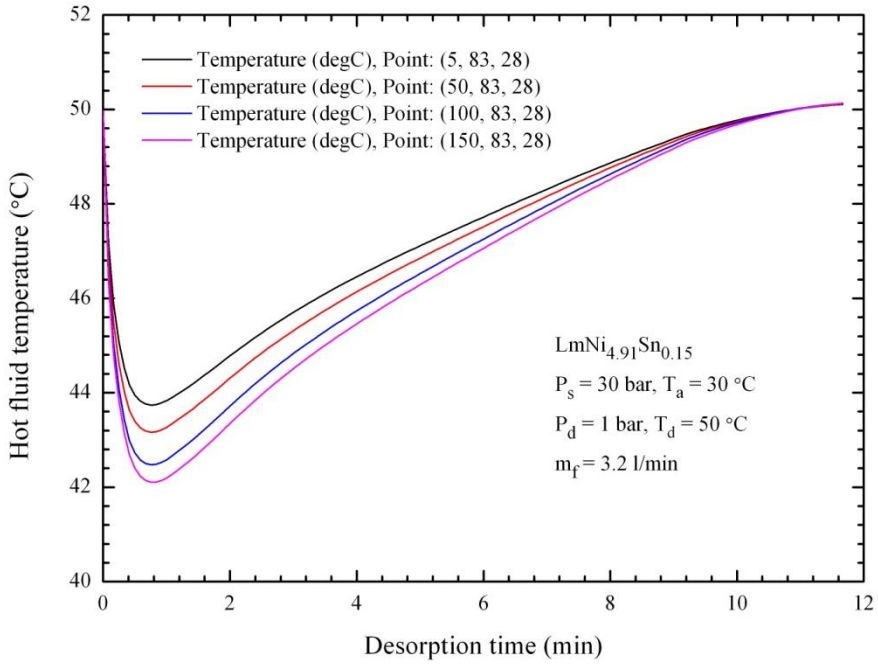

(b)

Fig. 5.22 – Variations in hot fluid temperature along embedded cooling tubes at different axial distances with time (a) inner row and (b) outer row.

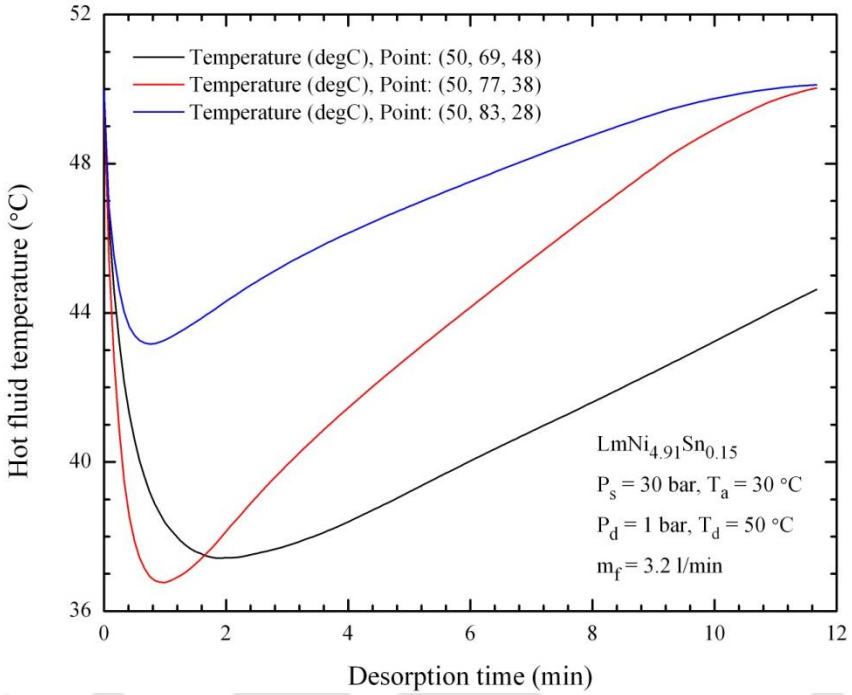

(a)

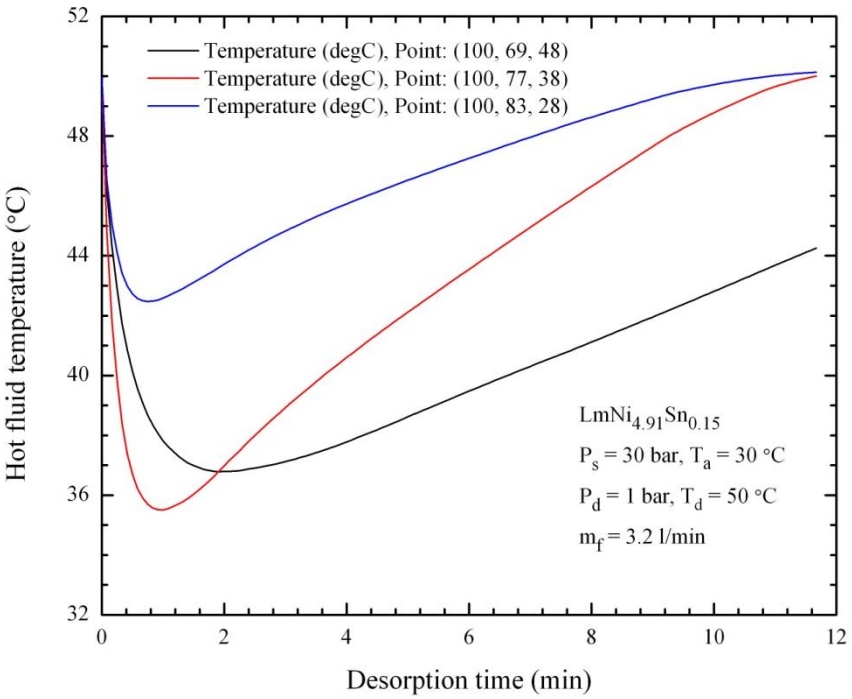

(b)

Fig. 5.23 – Variations in hot fluid temperature at different radial locations with time (a) at axial distance of 50 mm and (b) at axial distance of 100 mm.

5.4 Experimental results of MHHSD: absorption process

The experimental studies have been carried out for both the reactors (with 36 and 60 ECT) at different supply pressures (10 – 35 bar), absorption temperatures (20 – 30 °C) and cooling fluid flow rates (2.2 – 30 l/min). For the present experimental study, oil has been used as the HTF. Its maximum flow rate has been limited to 3.2 l/min (constrain imposed by the pressure pump of the oil circulating bath), and so to achieve the higher flow rate, experiment was also performed with water. Its flow rate varied from 5 l/min to 30 l/min using a centrifugal pump.

5.4.1 Effect of supply pressure

Effect of supply pressure on the variations of rate of hydrogen absorption and average bed temperature with time for the reactors with 36 and 60 ECTs are shown in Figs. 5.24(a) and (b). Throughout the absorption process, the supply condition of absorption temperature 30 °C and cooling fluid (oil) flow rate 3.2 l/min are maintained. The hydrogen storage performances of both the reactors are tested at 10, 15, 20, 25, 30 and 35 bar supply pressures. It is observed from Figs. 5.24(a) and (b) that the rate of absorption and average bed temperature increase with increase in hydrogen supply pressure. In the beginning of absorption process, the difference between the supply pressure and hydride equilibrium pressure is high, resulting in rapid hydriding and hence, liberation of more amount of heat. The increase in the hydride equilibrium pressure due to rise in hydride bed temperature, slows down the rate of hydrogen absorption. With increase in the absorption time, the hydride equilibrium pressure decreases gradually, and hence, the pressure difference drops to zero at the end of absorption process. At higher supply pressures, the pressure difference is higher, and this leads to faster rate of hydrogen absorption and lower absorption time.

It is also observed from Figs. 5.24(a) and (b) that the hydride bed temperature increases with increase in the supply pressures. The HTF is supplied continuously to take away the heat liberated from the reactor due to exothermic reaction during the absorption process. As the hydride particles have lesser thermal conductivity, the rate of heat removal from the hydride bed is low. Due to this reason, the temperature increases rapidly during the initial stage of absorption process, then decreases slowly with time, and finally reaches its initial absorption temperature at the end of the absorption process. At 6 min of the absorption, the average bed temperatures for 36 ECT are 55.99 °C, 60.86 °C, 68.41 °C, 73.70 °C, 74.58 °C and 73.57 °C, corresponding to the supply pressures of 10, 15, 20, 25, 30 and 35 bar, respectively. And, for 60 ECT, the respective values are 50.33 °C, 55.15 °C, 59.94 °C, 62.6 °C, 64.29 °C and 63.73 °C. From the above temperature variations, it is concluded that the rate of heat transfer is significantly faster in the reactor with 60 ECT.

Figs. 5.25(a) and (b) illustrate the effect of supply pressure on the amount of hydrogen absorbed for 36 and 60 ECT. For any supply pressure, the amount of hydrogen absorbed increases with the absorption time. In these reactors, the amount of hydrogen absorbed is found to increase from 19.19 g to 32.52 g, and the corresponding increase in wt% is 0.69 to 1.18, when the hydrogen supply pressure is varied from 10 to 35 bar. The reason for absorbing more amount of hydrogen at higher supply pressure is attributed to pressure - concentration isotherms. For the same increment in supply pressure, the reactor with 36 ECT, the absorption time decreases from 19 min to 10 min, while with 60 ECT, the corresponding reduction in the absorption time is from 14 min to 8 min. It is also clearly seen from Figs. 5.25(a) and (b) that the absorption time is significantly reduced for 60 ECT. At given supply conditions of 30 °C absorption temperature

and 35 bar supply pressure, the maximum amount of hydrogen absorbed is ≈ 1.18 wt% in 10 min for 36 ECT and 8 min for 60 ECT.

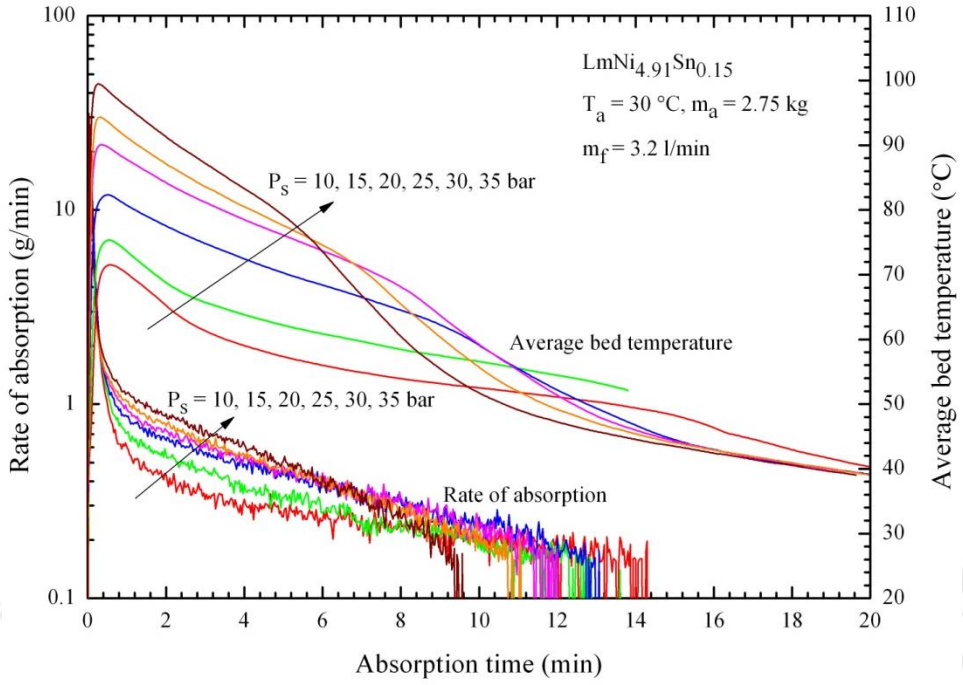

(a)

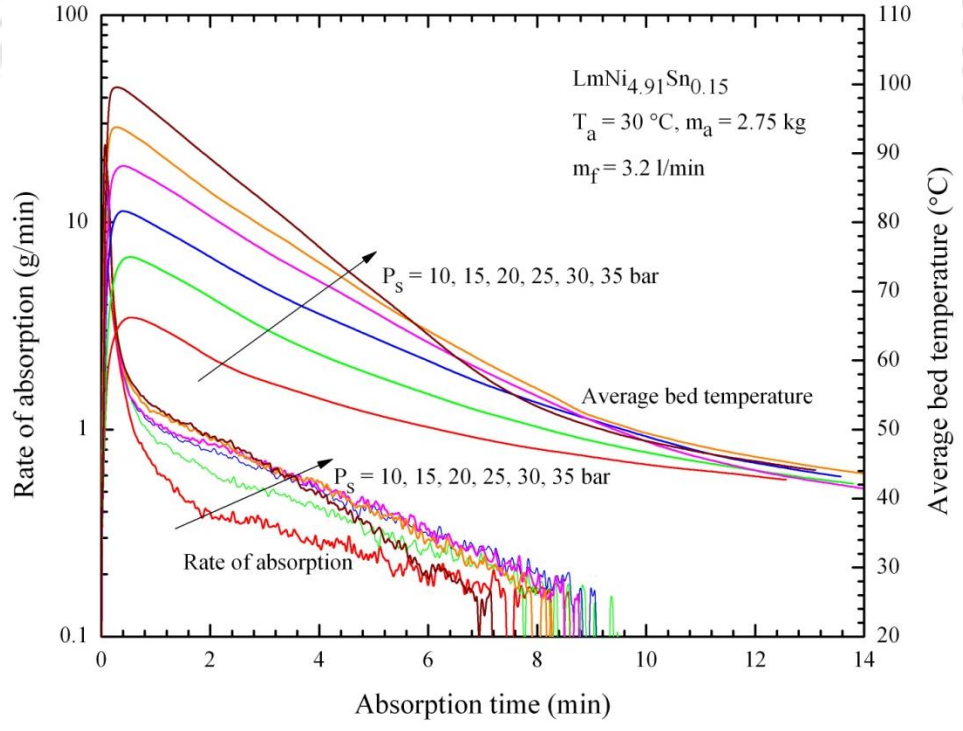

(b)

Fig. 5.24 – Effect of supply pressure on variations of rate of absorption and average bed temperature with time for (a) 36 and (b) 60 embedded cooling tubes.

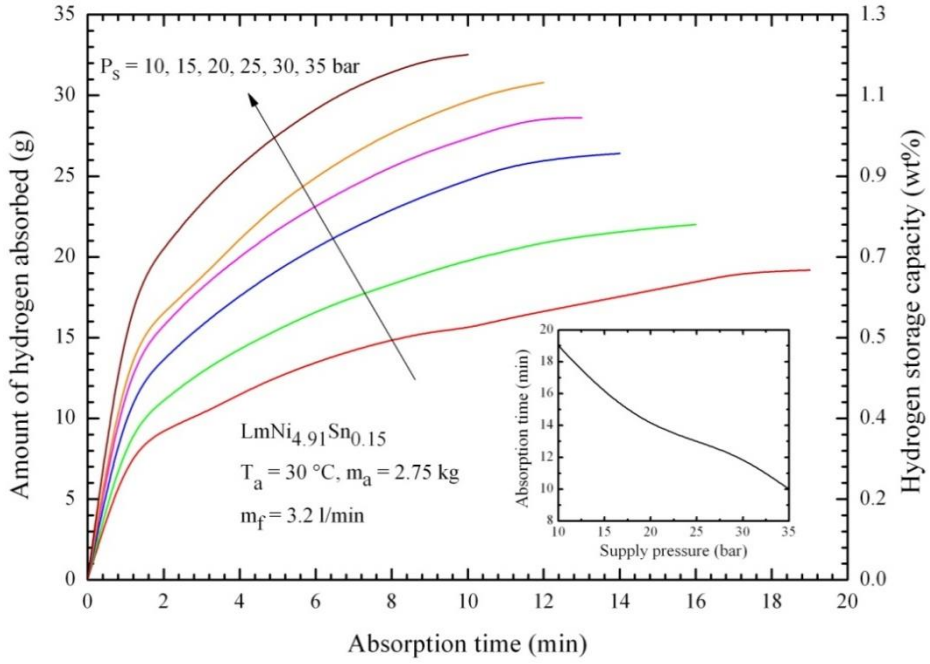

(a)

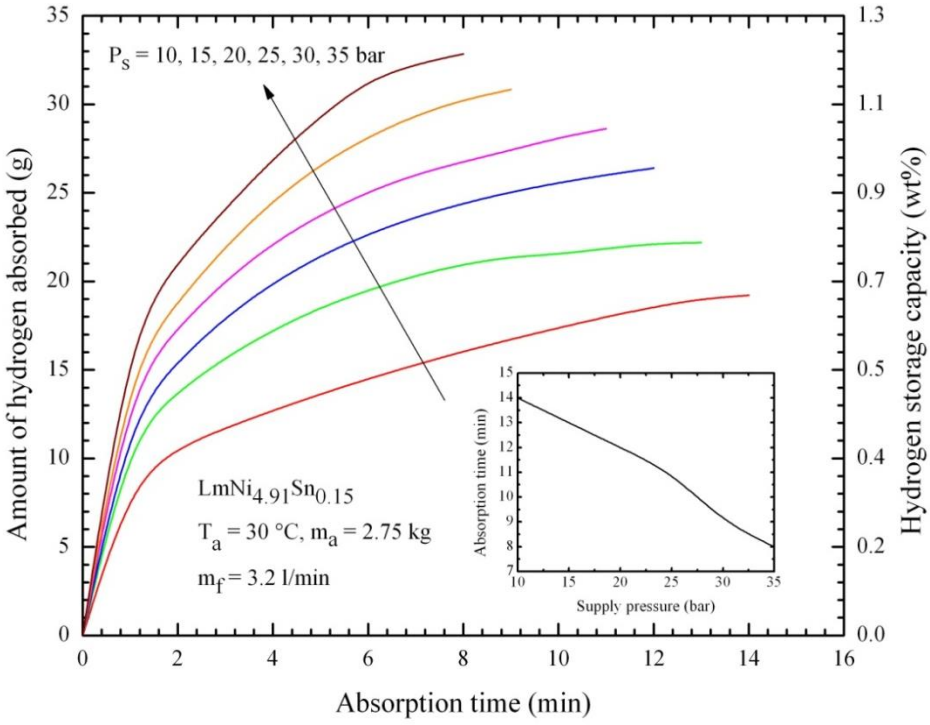

(b)

Fig. 5.25 – Effect of supply pressure on variations of amount of hydrogen absorbed and hydrogen storage capacity with time for (a) 36 and (b) 60 embedded cooling tubes.

5.4.2 Effect of absorption temperature

The effect of absorption temperature on the variations of rate of hydrogen absorption and average bed temperature with time for 36 and 60 ECT is shown in Figs. 5.26(a) and (b). At 30 bar supply pressure, the absorption temperature has been varied by supplying the HTF at 20 °C, 25 °C and 30 °C. It is observed from Figs. 5.26(a) and (b) that at lower the absorption temperature, the rate of hydrogen absorption is fast. Lower absorption temperature creates a lower hydride bed temperature, and this leads to low hydride equilibrium pressure. Hence, the higher pressure difference (difference between hydrogen supply pressure and hydride equilibrium pressure) at lower absorption temperature leads to rapid absorption of hydrogen and the lower absorption temperatures also reduce the absorption time significantly.

Figs. 5.26(a) and (b) also show the variations of the average hydride bed temperature with time for 36 and 60 ECT. The hydride bed temperature increases initially, and in short span of time after reaching the peak, it starts decreasing to the HTF supply temperature. The same trend is observed for both the reactors. In the reactor with 60 ECT, the hydride bed temperature reaches the initial absorption temperature well before the reactor with 36 ECT. More number of ECT provides more heat transfer surface area, and hence more heat is transferred from MH bed to the HTF.

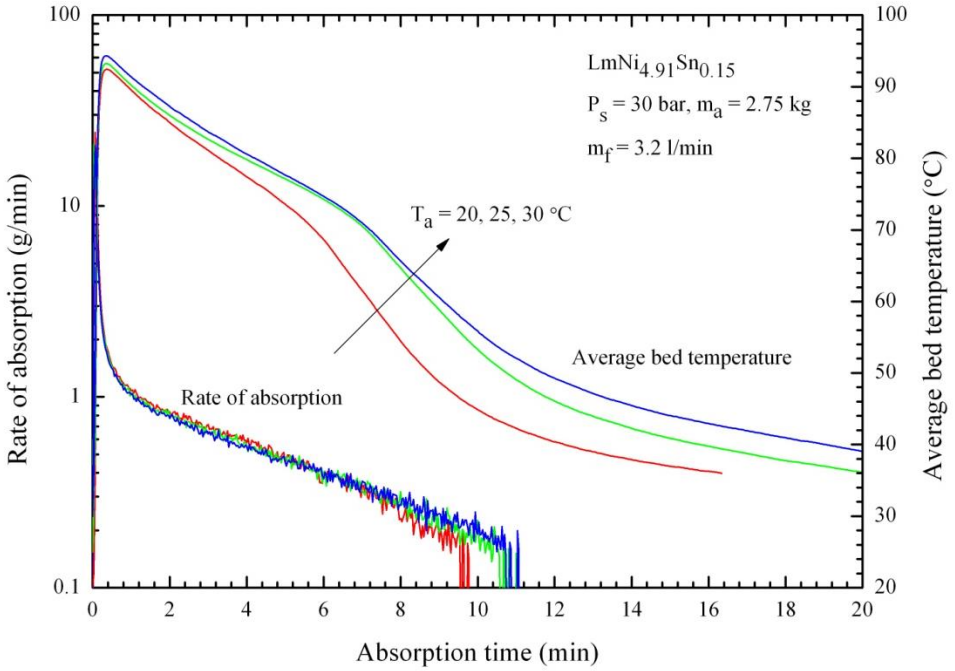

(a)

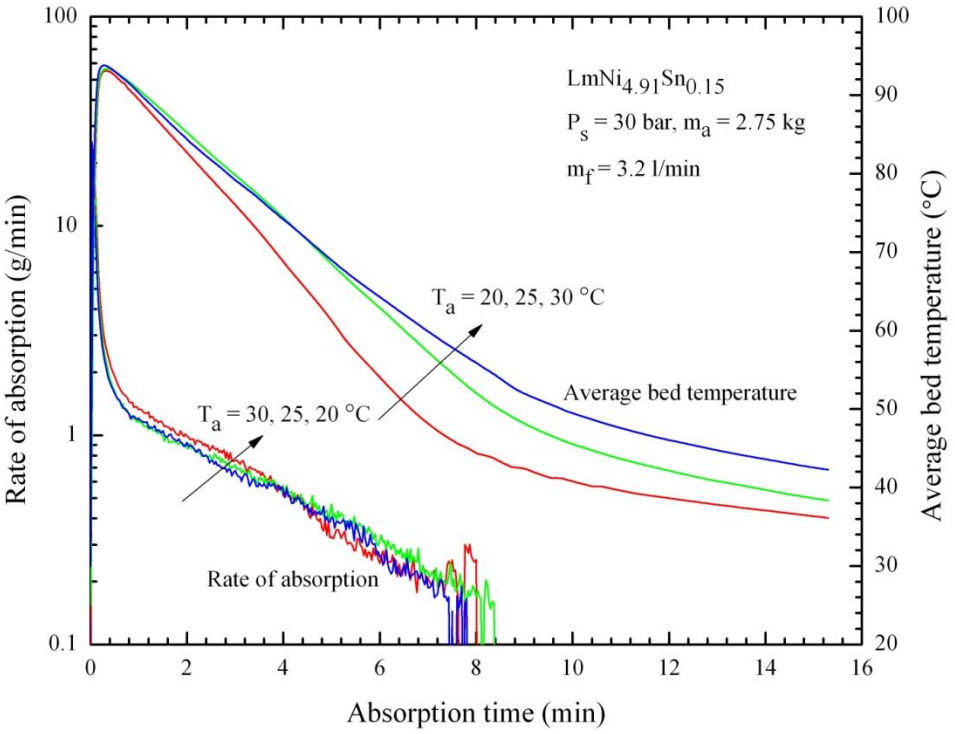

(b)

Fig. 5.26 – Effect of absorption temperature on variations of rate of absorption and average bed temperature with time for (a) 36 and (b) 60 embedded cooling tubes.

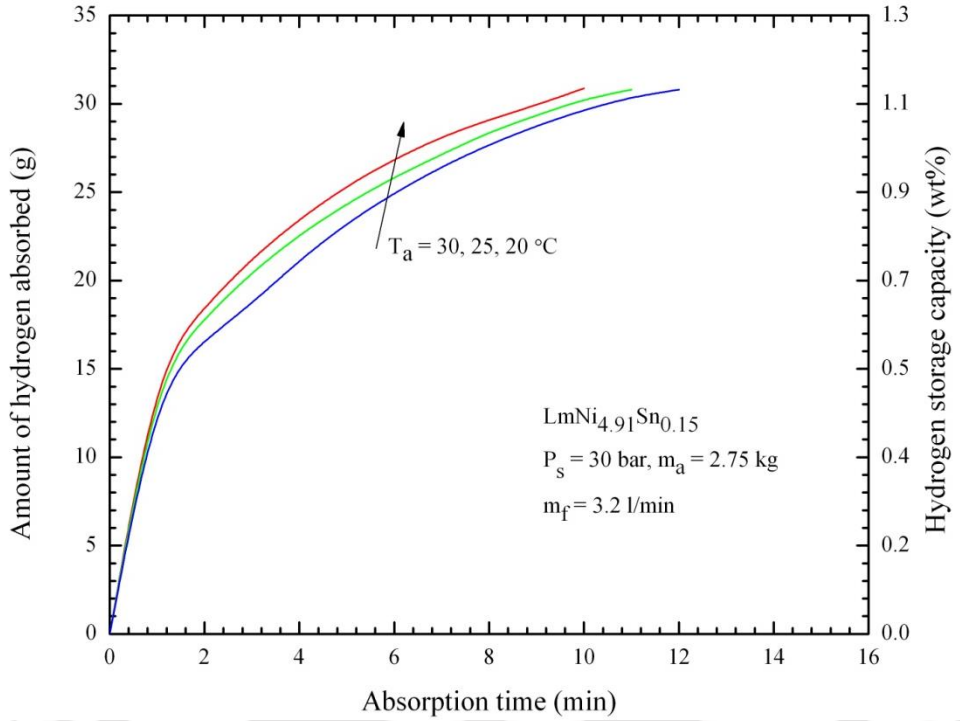

(a)

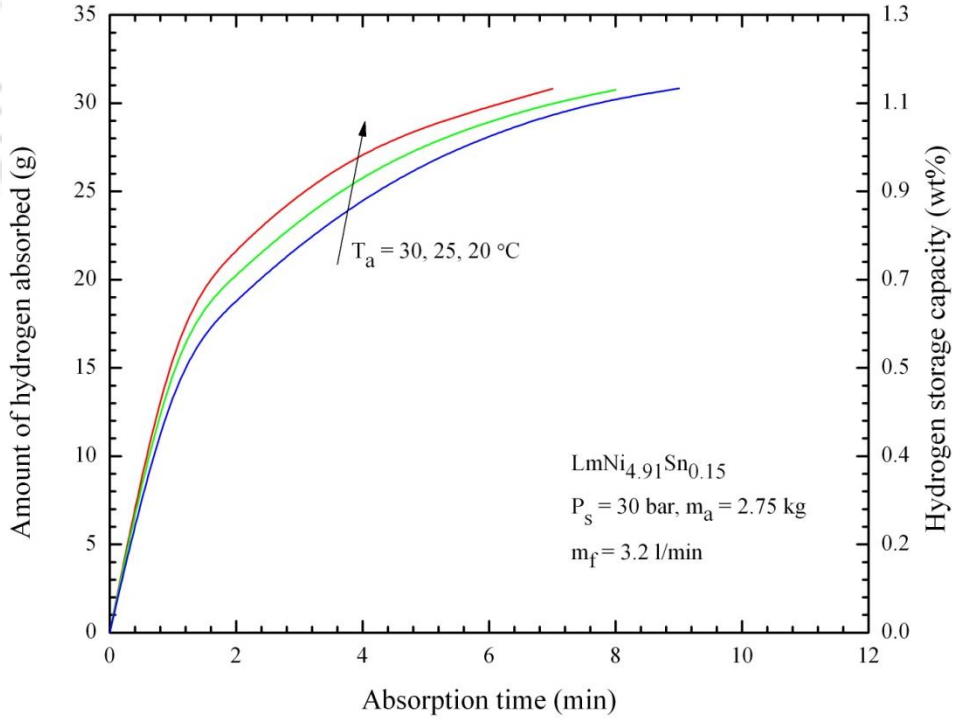

(b)

Fig. 5.27 – Effect of absorption temperature on variations of amount of hydrogen absorbed and hydrogen storage capacity with time for (a) 36 and (b) 60 embedded cooling tubes.

The variations in the amount of hydrogen absorbed (g) and the storage capacity (wt%) with time for reactors with 36 and 60 ECT are shown in Figs. 5.27(a) and (b). In both the reactors, the maximum amount of hydrogen absorbed is 30.82 g (1.12 wt%) for all the absorption temperatures at 30 bar supply pressure. The amount of hydrogen absorbed increases with increase in absorption time. The absorption time is found to decrease with decrease in the absorption temperature from 30 °C to 20 °C. The reduction in absorption time is attributed to having larger driving potential for hydrogen transfer at lower absorption temperature. For the reactor with 36 ECT, with 30 °C, 25 °C and 20 °C, the maximum storage capacity is attained at 12, 11 and 10 min, respectively. The same for the reactor with 60 ECT is attained at 9, 8 and 7 min, respectively.

5.4.3 Effects of cooling fluid (oil) flow rate

With oil as the HTF, the effect of its flow rate on the variations of rate of hydrogen absorption and average hydride bed temperature are presented in Figs. 5.28 (a) and (b). At 25 bar supply pressure and 30 °C absorption temperature, the variations are shown for the cooling fluid flow rates 2.2 l/min, 2.7 l/min and 3.2 l/min. It is observed that the rate of hydrogen absorption is found to increase with fluid flow rate. With increased flow rate of the HTF, more heat is removed from MH bed. The rate of hydrogen absorption/desorption was measured directly using Coriolis mass flow meter of having sensitivity ±0.001 g. At the beginning of absorption process, the rate of absorption is more due to rapid exothermic reaction. Hence, the fluctuations are higher and as the absorption time progress, the fluctuations are very low (less than 1%). In order to magnify the lower flow rates observed at the end of the process, logarithmic scale is used. Because lower flow rates are expressed in logarithmic scale, they are appeared to be in the form

of disturbances. But actually those values of are less than 1% of the full scale reading, which can be omitted also.

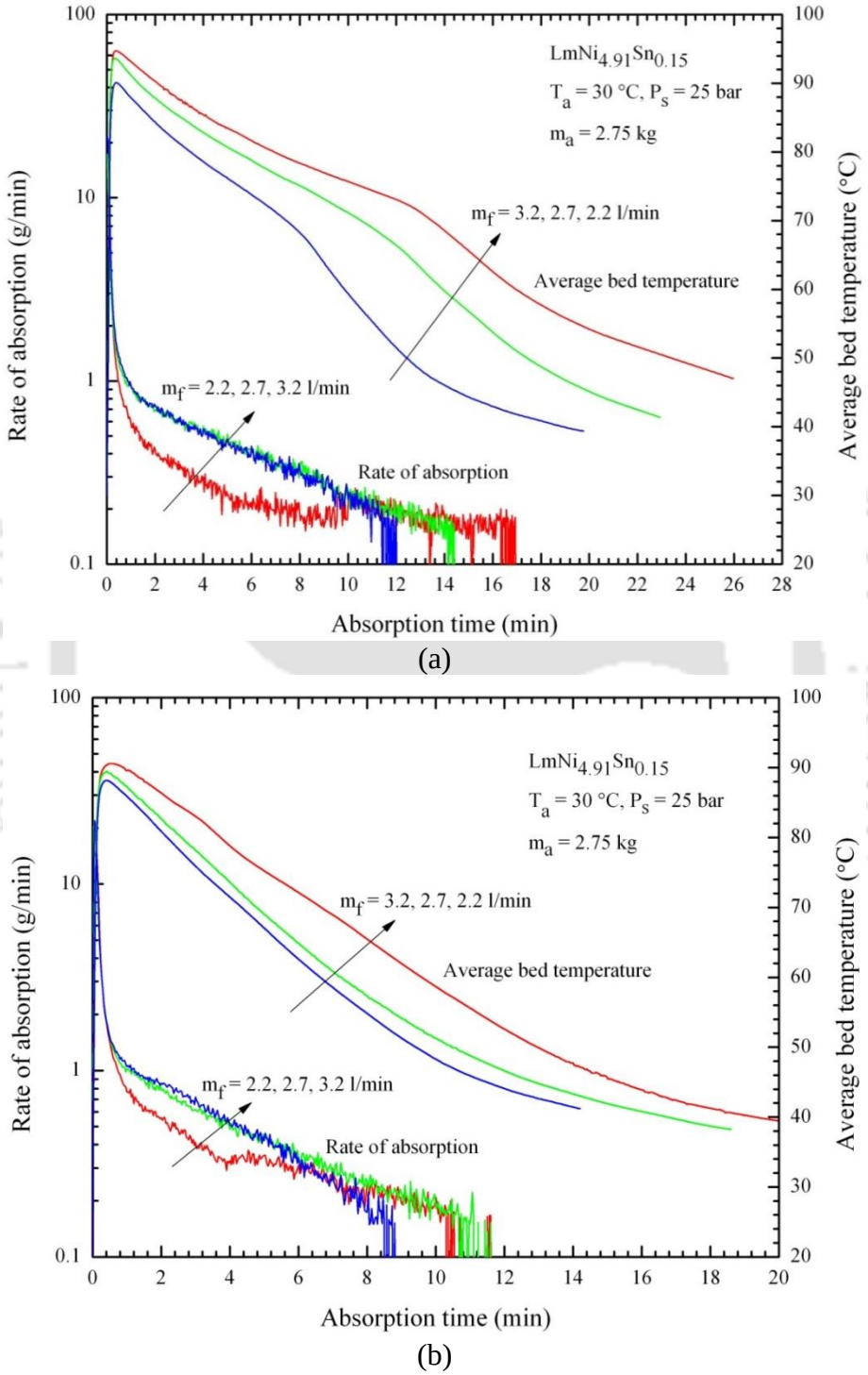

Fig. 5.28 – Effect of cooling fluid (oil) flow rate on variations of rate of absorption and average bed temperature with time for (a) 36 and (b) 60 embedded cooling tubes.

For 36 and 60 ECT reactors, the variations of the average hydride bed temperature with time are shown in Figs. 5.28 (a) and (b). Observed trend is similar to that of rate of absorption. At 12 min of the absorption time, the average hydride bed temperatures for 36 ECT are 73.08 °C for 2.2 l/min, 66.42 °C for 2.7 l/min and 51.51 °C for 3.2 l/min. The respective values for 60 ECT are 52.58 °C, 46.61 °C and 44.10 °C. For a given reactor design, the hydride bed temperature decreases with increase in the flow rate of the HTF. Higher flow rate (the lower temperature) of the HTF augments the removal of heat from the MH bed and thus helps in enhanced absorption rate. The reactor with 60 ECT removes heat faster, and thus as observed, the rate of hydrogen absorption is also high.

Figs. 5.29(a) and (b) illustrate the effect of cooling fluid flow rate on the variations of the amount of hydrogen absorbed with time for 36 and 60 ECT reactors. With increase in flow rate of the HTF, the rate of hydrogen absorbed is found to increase. For all three flow rates (2.2 l/min, 2.7 l/min and 3.2 l/min), the maximum amount of hydrogen absorbed is the same as 28.62 g (1.04 wt%). For the reactor with 36 ECT, when the flow rate is increased from 2.2 l/min to 3.2 l/min, the absorption time reduces by ≈ 47.8% (from 23 min to 12 min). The same for the reactor with 60 ECT is ≈ 47.05% (from 17 min to 9 min).

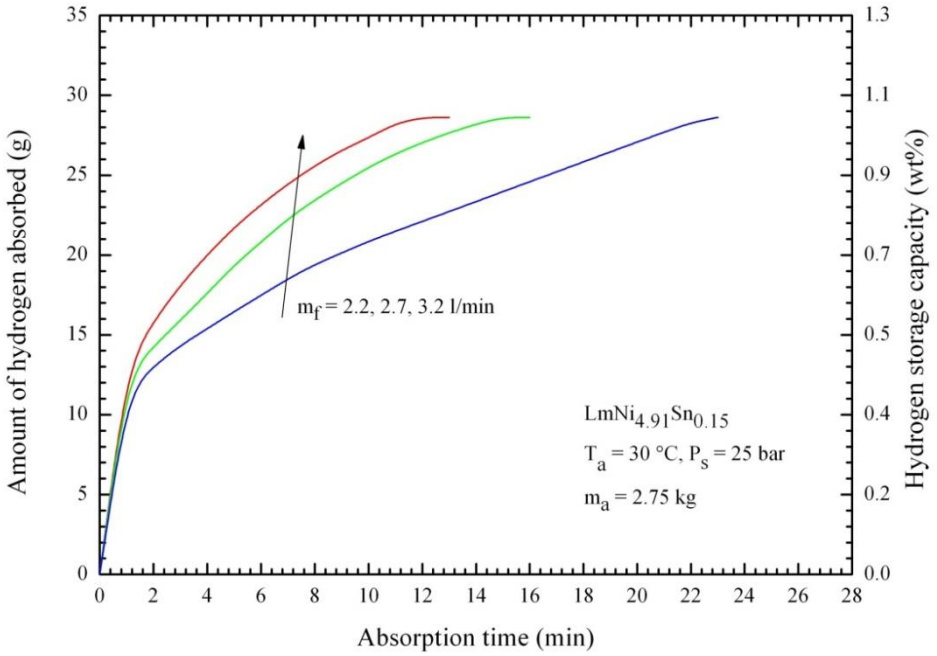

(a)

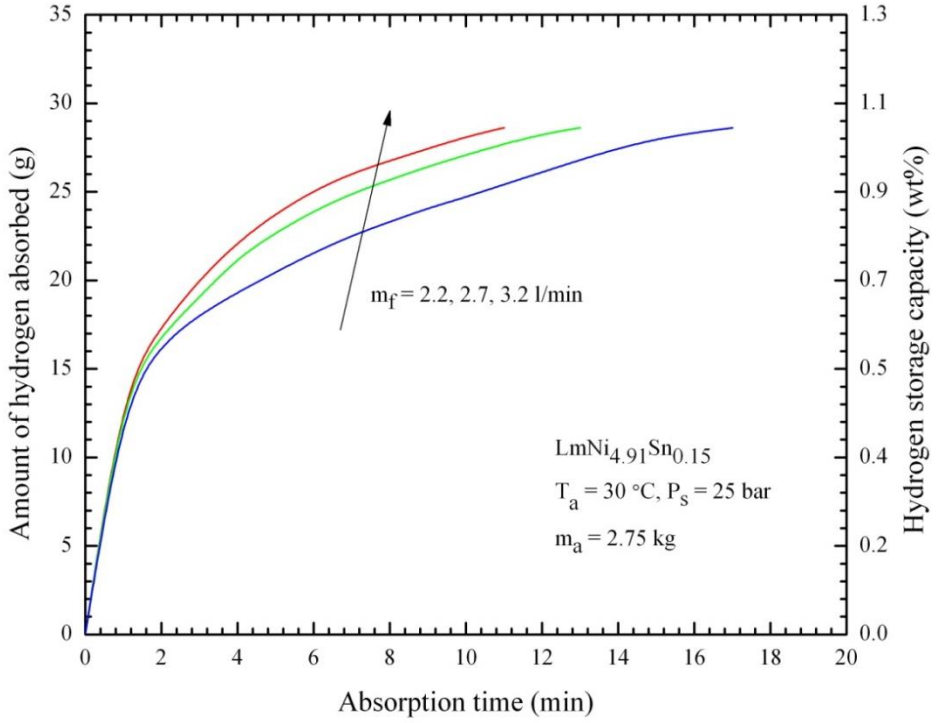

(b)

Fig. 5.29 – Effect of cooling fluid (oil) flow rate on variations of amount of hydrogen absorbed and hydrogen storage capacity with time for (a) 36 and (b) 60 embedded cooling tubes.

In the present work, due to the operating constrain of the constant temperature oil circulating bath, the flow rate of oil is restricted within 3.2 l/min. Thus, too see the effect of higher flow rates on the hydriding rate; the study is extended with water as the HTF. In the following, results are presented with water as the HTF.

5.4.4 Effect of number of embedded cooling tubes

The effect of number of ECT plays a significant role on the rate of hydrogen absorption and absorption time. This has been reported in literature [Mohan *et al*., 2007; Freni *et al*., 2009; Linder *et al*., 2010; Muthukumar *et al*., 2012]. In order to study the effect of number of ECT on the rate of hydrogen absorption, velocity of the HTF has been fixed at 0.33 m/s. The corresponding values of HTF flow rate for 36 ECT and 60 ECT are 12 l/min and 20 l/min respectively. Figs. 5.30(a) and (b) illustrate the effect of number ECT on the variations of hydrogen absorption rate, average bed temperature and amount of hydrogen absorbed. With 25 bar supply pressure, 30 °C absorption temperature and 0.33 m/s cooling fluid (water) velocity, the rate of hydrogen absorption is found to be much higher for the reactor with 60 ECT. This trend is for the mere fact that with inner and outer diameters of the ECT same, the surface area for the heat transfer from the hydride bed to the HTF is more when the number of ECT is more. At the same supply condition, Fig. 5.30(a) also shows variations of average bed temperature. In both the reactors, the hydride bed temperature first increases and then it decreases to initial absorption temperature. It is observed that the rate of heat rejection from the hydride bed increases by ≈ 38.5% when the number of ECT is increased from 36 to 60. With same amount (2.75 kg) of MH alloy in both the reactors, in the reactor with 36 ECT, MH alloy is loosely packed than the reactor with 60 ECT. Thus, the void space is more in the reactor with 36 ECT.

Convection is more when the void space is more, whereas opposite is the case for conduction. This explains the observed trend of the rate of absorption.

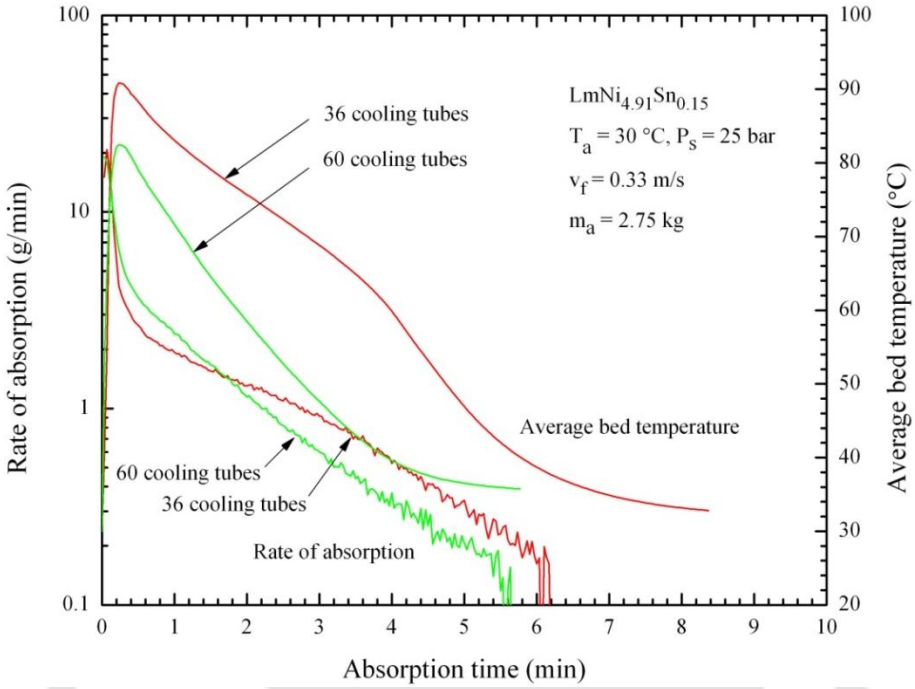

(a)

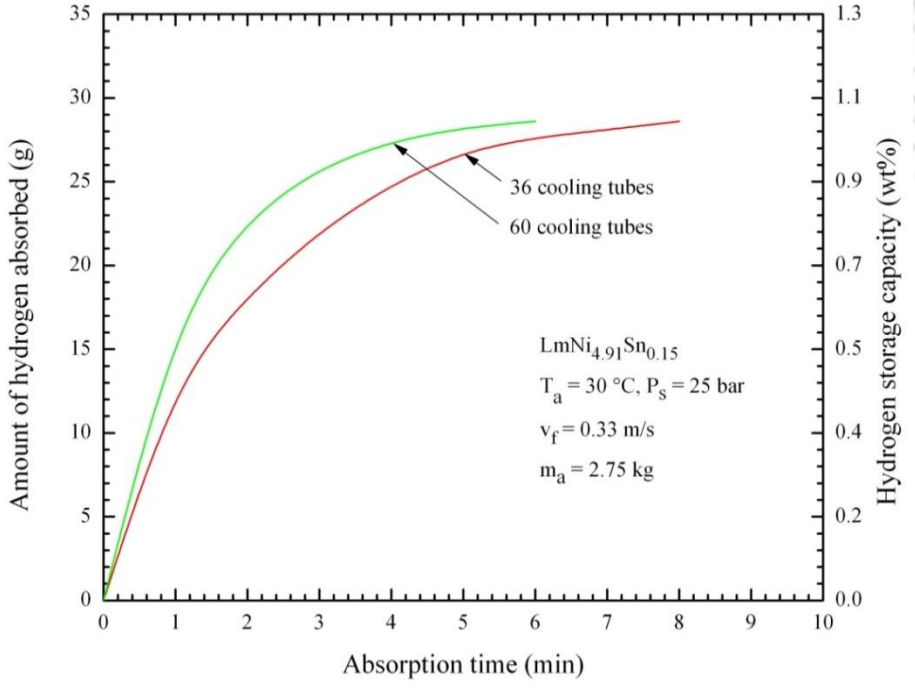

(b)

Fig. 5.30 – Effect of number of embedded cooling tubes on variations of with time (a) rate of absorption and average bed temperature and (b) amount of hydrogen absorbed and hydrogen storage capacity.

For the same supply condition as that for the results in Fig. 5.30(a), Fig. 5.30(b) shows the effect of number of ECTs on the variations of the amount of hydrogen absorbed with time. In 8 min, the amount of hydrogen stored is 28.62 g (1.04 wt%) for 36 ECT, while the same amount is absorbed in 6 min by the reactor with 60 ECT. The reduction in the absorption time of the reactor with 60 ECT is quite significant (≈ 37.5%).

5.4.5 Effect of cooling fluid (water) flow rate

Water as the HTF, the effect of its flow rate on the variations of rate of absorption and average hydride bed temperature are shown in Fig. 5.31(a). Fig. 5.31(b) shows the variation of the amount of hydrogen absorbed with time. For this study, only the reactor with 60 ECT is considered. At the absorption condition of 30 °C HTF temperature and 25 bar supply pressure, the observation has been carried out for four flow rates of HTF, viz., 5 l/min, 10 l/min, 20 l/min and 30 l/min. It is obvious that the rate of absorption increases with increase in the flow rate of the HTF. With increase in the flow rate of the HTF, more heat is removed from the hydride bed, and as observed from Fig. 5.31(a), this improves the rate of absorption and lowers the rise in average hydride bed temperature. At any flow rate, initially, the exothermic reaction of absorption process causes the sudden increase in the hydride bed temperature, and then as the heat extraction starts, the temperature starts reducing with the passage of time. When the flow rate is increased, the hydride bed temperature attains the initial absorption temperature much faster.

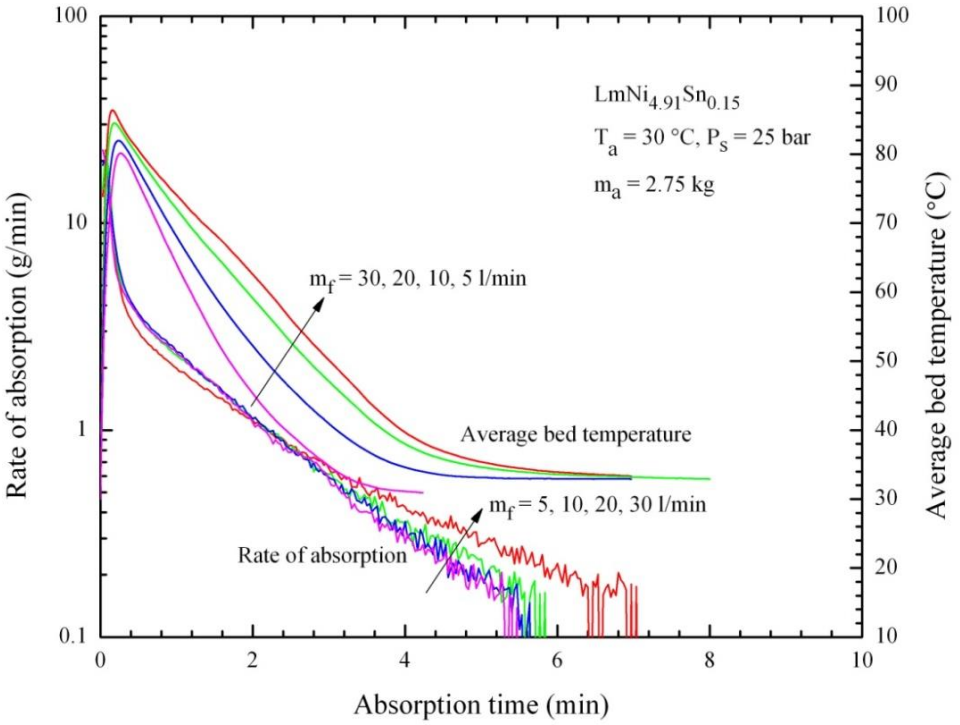

(a)

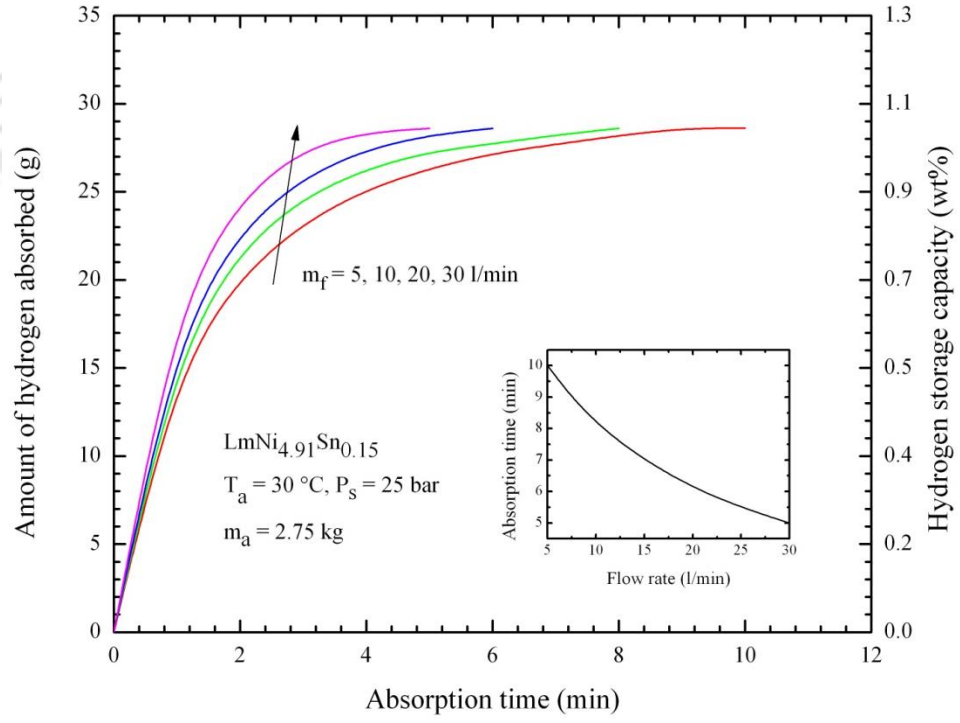

(b)

Fig. 5.31 – Effect of cooling fluid (water) flow rate on variations with time of (a) rate of absorption and average bed temperature and (b) amount of hydrogen absorbed and hydrogen storage capacity.

Fig. 5.31(b) illustrates the effect of HTF flow rate on the variations of the amount of hydrogen absorbed. Though the maximum amount of hydrogen absorbed remains unaffected, the absorption time is significantly reduced with increase in HTF flow rate. For 5, 10, 20 and 30 l/min of flow rates, the absorption time for the maximum amount of hydrogen absorbed are 10, 8, 6 and 5 min, respectively. It is also observed that increasing the water flow rate from 20 to 30 l/min reduces the absorption time marginally in comparison with it's from 10 to 20 l/min. Considering the amount of pumping power required and the absorption time, HTF flow rate in the range of 20 l/min may be the optimum value.

5.5 Experimental results of MHHSD: desorption process

In this section, experimental studies on desorption characteristics are discussed. Experiments are conducted at different desorption temperatures (30 °C – 60 °C) and hot fluid flow rates (2.2 l/min – 30 l/min). Both the cases, the desorption pressure is maintained at 1 atm. (absolute).

5.5.1 Effect of desorption temperature

With oil as the HTF, the same absorption conditions of supply pressure 30 bar and absorption temperature 30 °C are maintained and there by the total amount of hydrogen absorbed is also maintained constant at 30.83 g (≈ 1.12 wt%). The oil flow rate is kept constant at 3.2 l/min. Figs. 5.32(a) and (b) show the variations of desorption rate and average bed temperature with time for both the reactors. These variations are shown for the hot fluid temperatures of 30 °C, 40 °C, 50 °C and 60 °C. It is observed from Fig. 5.32(a) that for the reactor with 36 ECT, for about 11 min, the desorption rate is higher for the higher desorption temperature. Opposite is the trend beyond that. For the desorption temperatures of 30 °C, 40 °C, 50 °C and 60 °C, the peak

values of the desorption rate are 14.33 g/min, 15.5 g/min, 18.25 g/min and 20.05 g/min, respectively. When the desorption temperature is high, desorption process is completed fast. With increase in desorption temperature, the reason for higher rate of hydrogen desorption is attributed to the higher pressure difference between the hydride equilibrium pressure and the desorption pressure. At lower desorption temperature, low hydride equilibrium pressure results in the reduction in pressure difference, and hence, the rate of desorption is slow. With 60 ECT, at all the desorption temperatures, a similar trend is observed in Fig. 5.32(b).

The variations of the average hydride bed temperature with time for the reactor with 36 ECT and 60 ECT are also shown in Figs. 5.32(a) and (b), respectively. In the reactor with 36 ECT, at the beginning of desorption process, the drop in hydride bed temperatures within 1 min of desorption time are 5.5 °C, 10.4 °C, 13.3 °C and 15.5 °C, respectively at desorption temperatures 30 °C, 40 °C, 50 °C and 60 °C. After that the hydride bed temperature starts increasing slowly to its corresponding desorption temperature. Initially, the sudden drop in average hydride bed temperature is owing to the inability of the metal hydride bed to receive heat from the HTF. During this period, hydride bed utilizes its own heat for the desorption process to continue. Initially, the low thermal conductivity of the hydride alloy hinders the heat transfer between the metal hydride and the HTF. Shortly, when it starts receiving the heat from the HTF its bed temperature starts rising. The average hydride bed temperature reaches to the initial pre–set values 60 °C, 50 °C, 40 °C and 30 °C within a time interval of about 21 min, 23 min, 28 min and more than 30 min, respectively (Fig.5.32(a)). With 60 ECT, the corresponding time intervals are 12 min, 15 min, 18 min and 25 min, respectively (Fig. 5.32(b)). From Figs. 5.32(a) and (b), it is

observed that for any desorption temperature, the retrieval of heat from heat transfer fluid is more in the reactor with 60 ECT.

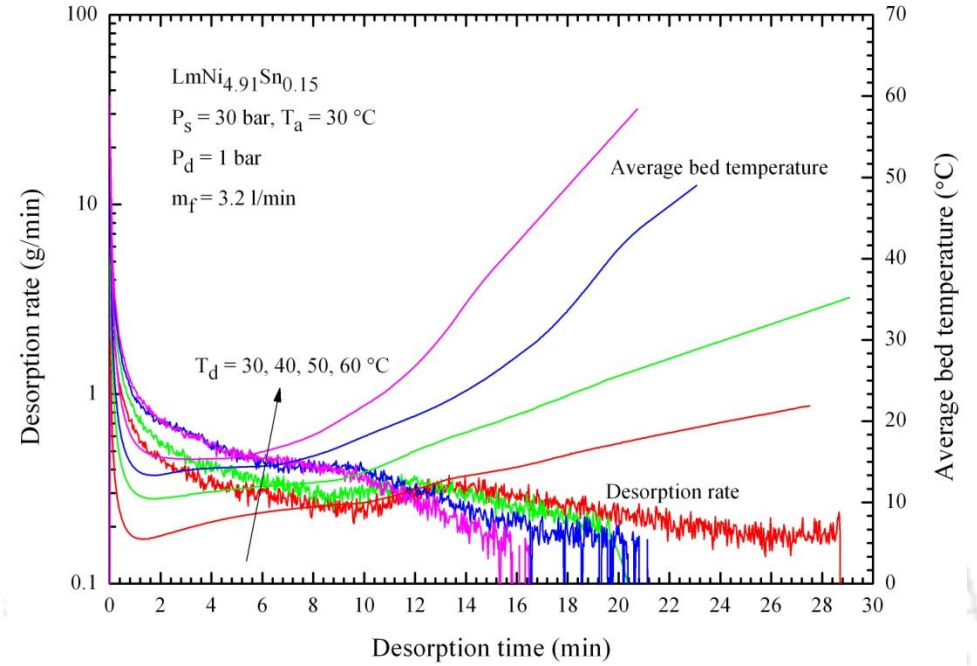

(a)

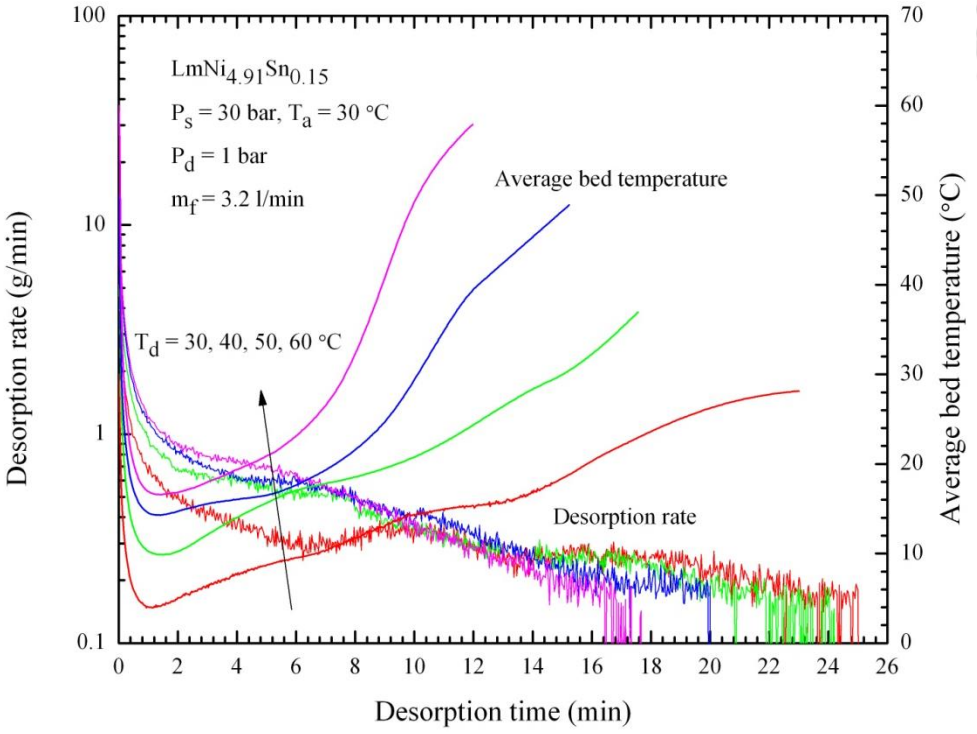

(b)

Fig. 5.32 – Effect of desorption temperature on the variations of desorption rate and average bed temperature with time (a) 36 and (b) 60 embedded cooling tubes.

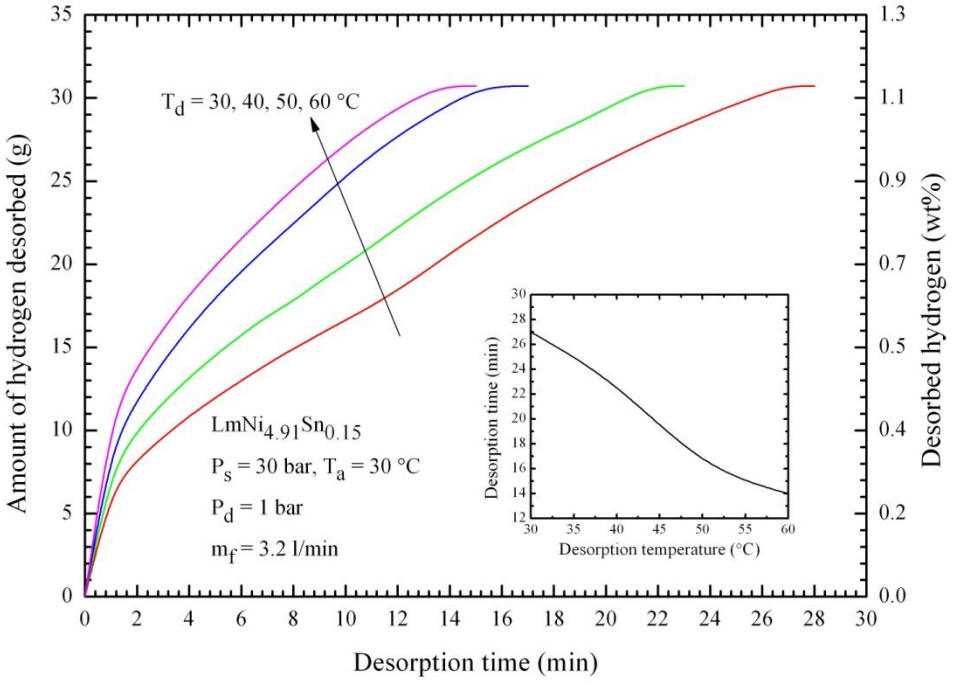

(a)

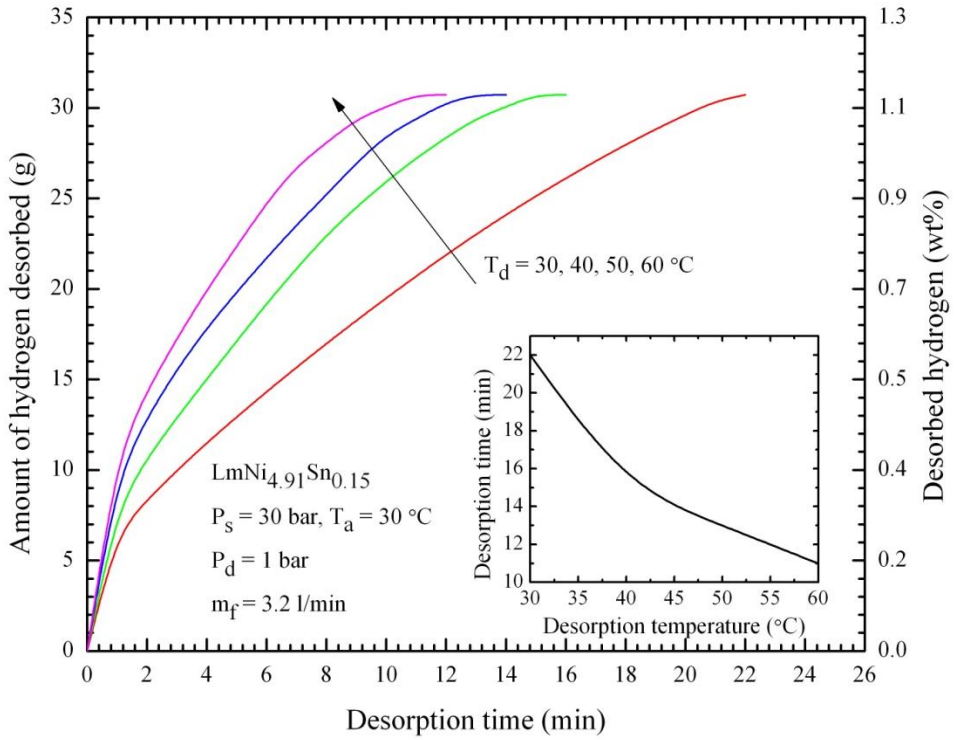

(b)

Fig. 5.33 – Effect of desorption temperature on the variations of amount of hydrogen desorbed with time for (a) 36 and (b) 60 embedded cooling tubes.

Effect of desorption temperature on the variations of amount of hydrogen desorbed with time is illustrated in Figs. 5.33(a) and (b) for the reactors with 36 ECT and 60 ECT, respectively. For the both reactors, the amount of hydrogen desorbed increases with an increase in desorption time. The desorption time is reduced from 27 min to 13 min (≈ 48%) for the reactor with 36 ECT, and from 22 min to 11 min (≈ 50%) for the reactor with 60 ECT, when the desorption temperature is increased from 30 °C to 60 °C. The maximum amount of hydrogen desorbed in both the reactors is about 30.72 g (1.1 wt%).

5.5.2 Effect of hot fluid (oil) flow rate

For the supply conditions of 30 bar supply pressure and 30 °C absorption temperature, the effect of hot fluid flow rate on the variations of desorption rate and average hydride bed temperature with time are shown in Figs. 5.34(a) and (b). Desorption pressure of 1 bar and desorption temperature of 50 °C are kept constant. With oil as the HTF, these results are shown for the three flow rates, viz., 2.2 l/min, 2.7 l/min and 3.2 l/min. The rate of desorption is significantly faster at higher flow rate, and this is mainly due to rapid heat transfer from the HTF to the hydride bed.

With the same absorption and desorption conditions, Figs. 5.34(a) and (b) shows the effect of the hot fluid/heat transfer fluid flow rate on variations of average hydride bed temperature for the reactor with 36 ECT and 60 ECT. In the reactor with 36 ECT, in 14 min of the desorption time, the hydride bed temperature are 18 °C, 20.9 °C and 23.7 °C, respectively, while for the reactor with 60 ECT, the same are 27.1 °C, 36.2 °C and 45.3 °C at hot fluid flow rates 2.2 l/min,

2.7 l/min and 3.2 l/min, respectively. When the flow rate of HTF is more, more heat is transferred to the hydride bed, and as a result, average bed temperature goes up.

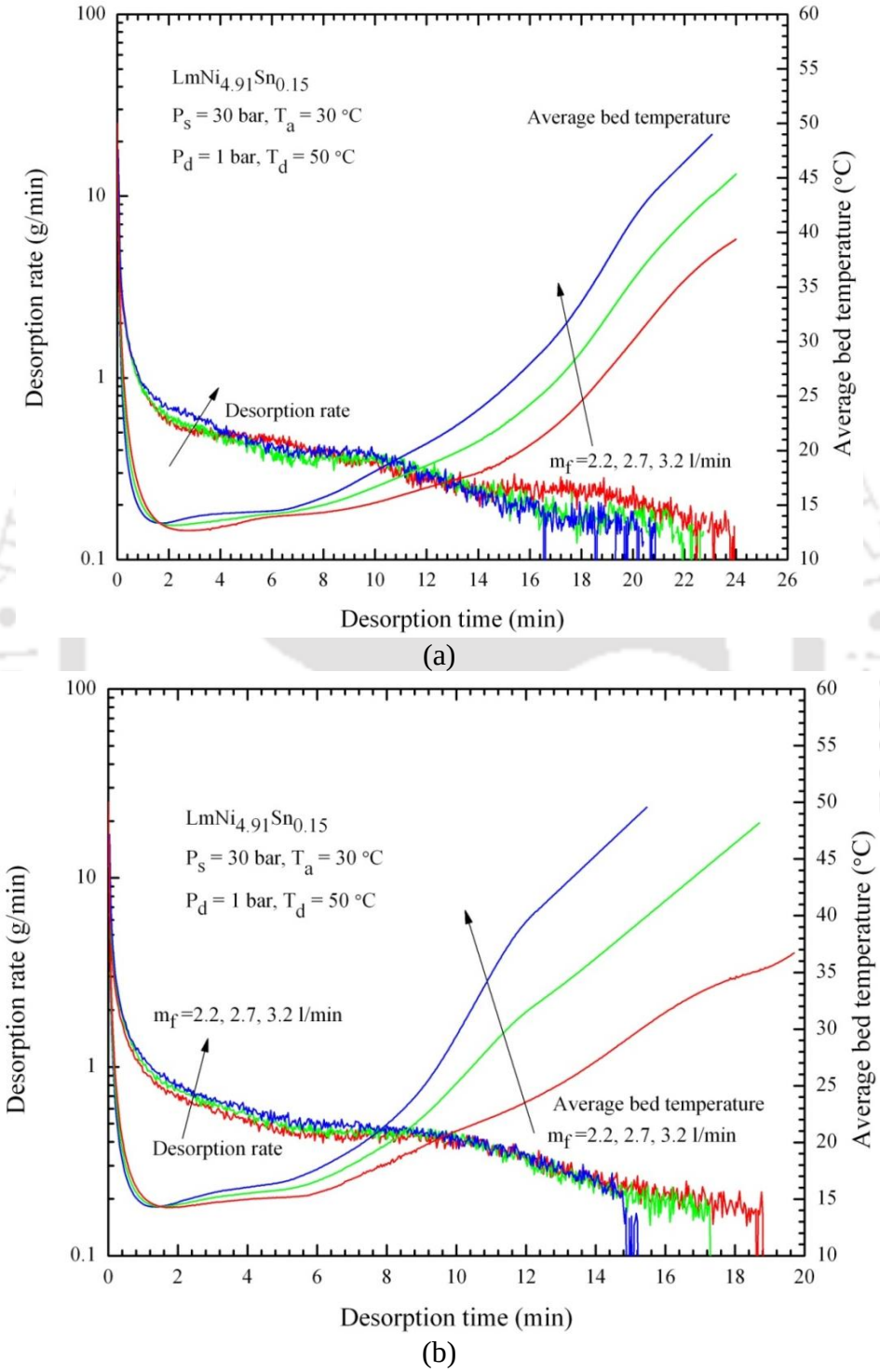

Fig. 5.34 – Effect of hot fluid (oil) flow rate on the variations of desorption rate and average bed temperature with time for (a) 36 and (b) 60 embedded cooling tubes.

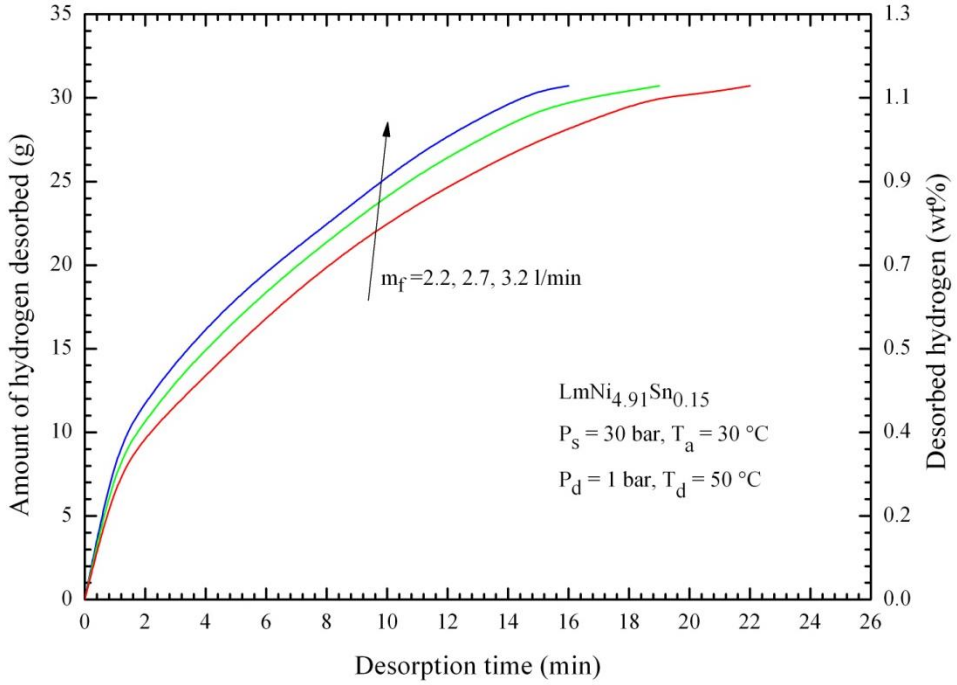

(a)

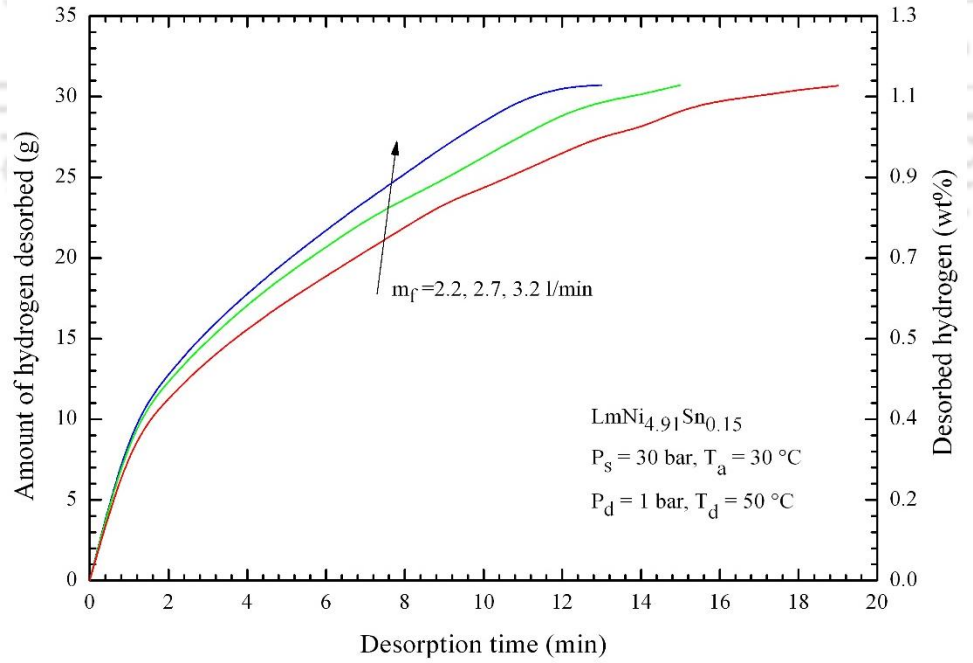

(b)

Fig. 5.35 – Effect of hot fluid (oil) flow rate on the variations of amount of hydrogen desorbed with time for (a) 36 and (b) 60 embedded cooling tubes.

Effect of HTF flow rate on variations of amount of hydrogen desorbed is shown in Figs. 5.35(a) and (b) for the reactors with 36 ECT and 60 ECT. For all flow rates (2.2 l/min, 2.7 l/min and 3.2 l/min), the total amount of hydrogen desorbed is 30.72 g (1.11 wt%). In the reactor with 36 ECT, it is observed that desorption time decreases by about 27% (from 22 min to 16 min) when the flow rate is increased from 2.2 l/min to 3.2 l/min. The same for the reactor with 60 ECT is ≈ 31.6% (from 19 min to 13 min). Hence, the desorption time is significantly faster in the reactor with 60 ECT.

5.5.3 Effect of number of embedded cooling tubes

With oil as the HTF, in the present study, its maximum flow rate was limited to 3.2 l/min. To see the effect of enhanced flow rate of the HTF on the desorption rate and the variation in average bed temperature, the study was extended with water as a HTF with flow rate ranged between 5 l/min and 30 l/min. The absorption condition of 25 bar supply pressure and 30 °C absorption temperature was maintained during these experiments and the corresponding maximum amount of hydrogen absorbed was 28.62 g. For both the reactors, the desorption pressure and temperature are 1 bar and 50 °C, respectively. With the fixed flow velocity of the HTF at 0.33 m/s, the flow rates in the reactors with 36 and 60 ECT are 12 l/min and 20 l/min, respectively.

The effects of number of ECT on variation of desorption rate of hydrogen, average hydride bed temperature and amount of hydrogen desorbed are illustrated in Figs. 5.36(a) and (b), respectively. The rate of hydrogen desorption (Fig. 5.36(a)) is comparatively higher for the reactor with 60 ECT due to higher hydride equilibrium pressure (associated with better heat

transfer) than the reactor with 36 ECT. This gives a larger pressure difference and it possess higher desorption rate. Fig. 5.36(a) also shows the temporal variation of the average hydride bed temperature for the reactors with 36 ECT and 60 ECT.

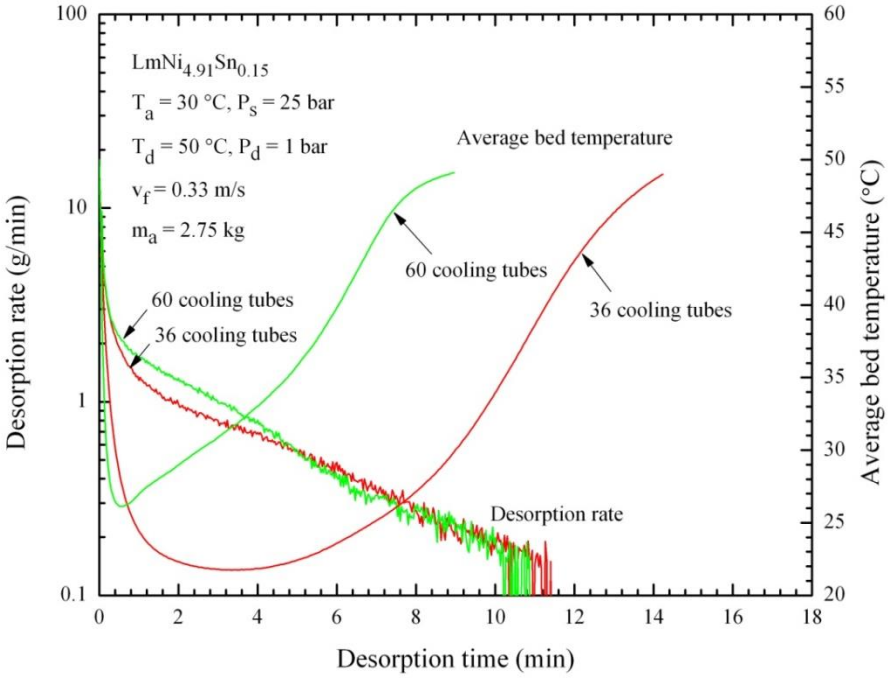

(a)

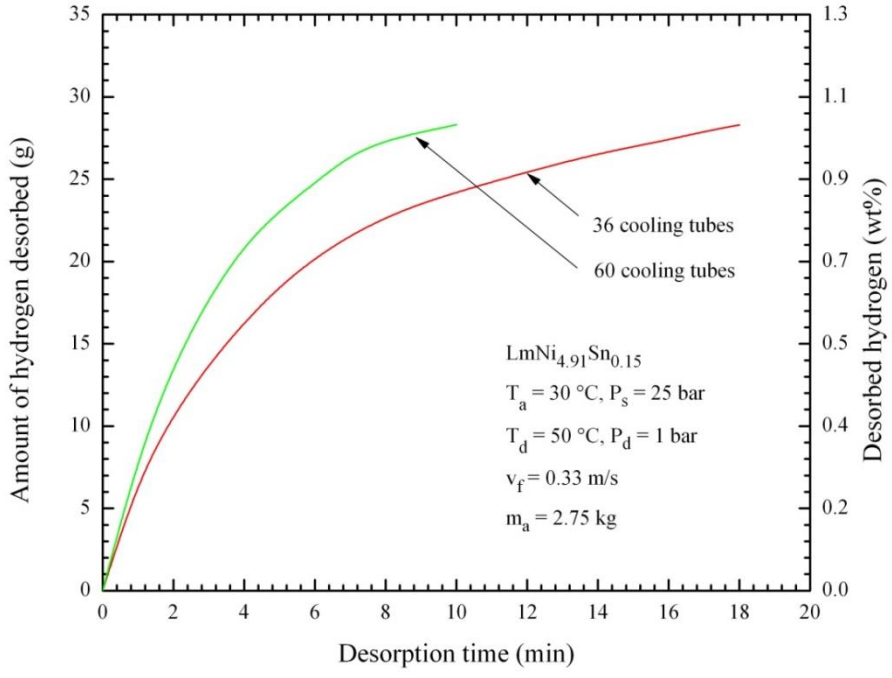

(b)

Fig. 5.36 - Effect of number of embedded cooling tubes on the variations of (a) desorption rate and average bed temperature and (b) amount of hydrogen desorbed.

5.5.4 Effect of hot fluid (water) flow rate

As reported in Fig. 5.36 that the minimum desorption time is obtained for the reactor with 60 ECT, and thus, the reactor with 60 ECT is considered for studying the effects of flow rate of water (HTF) on variations of the desorption rate of hydrogen, the average hydride bed temperature and the amount of hydrogen desorbed. Results are shown in Figs. 5.37(a) and (b). The supply conditions 25 bar and 30 °C are the same as the previous tests. Flow rates of hot fluid considered are 5, 10, 20 and 30 l/min. From Fig. 5.37(a), it is seen that at the commencement of desorption process, the desorption rate steadily increases, it reaches the maximum and then it starts decreasing towards zero with increase in desorption time. At 30 l/min, desorption rate of hydrogen is rapid, and thus the desorption time is the minimum.

Fig. 5.37(a) also shows the variations of average hydride bed temperature with time. It is observed that initially up to 30 s, the hydride bed temperature decreases and then it continuously increases till it reaches the desorption temperature 50 °C. For flow rates of 5, 10, 20 and 30 l/min, the corresponding values of minimum average bed temperatures are 23.9 °C, 25.2 °C, 27.9 °C and 29 °C, respectively. For the four different flow rates, viz., 5, 10, 20 and 30 l/min, Fig. 5.37(b) shows the effect of variations of the amount of hydrogen desorbed with time. From Fig. 5.37(a), it is observed that the desorption time decreases with increase in flow rate of the HTF. The reduction in desorption time is ≈ 46.7% (from 15 min to 8 min) when the flow rate is increased from 5 l/min to 30 l/min. This is owing to the better heat transfer rate from HTF to the hydride bed. No significant change in desorption time was found when the rate of the HTF was increased beyond 30 l/min. Thus, for the given reactor with 60 ECT, the MH bed cannot absorb more heat than that supplied with 30 l/min.

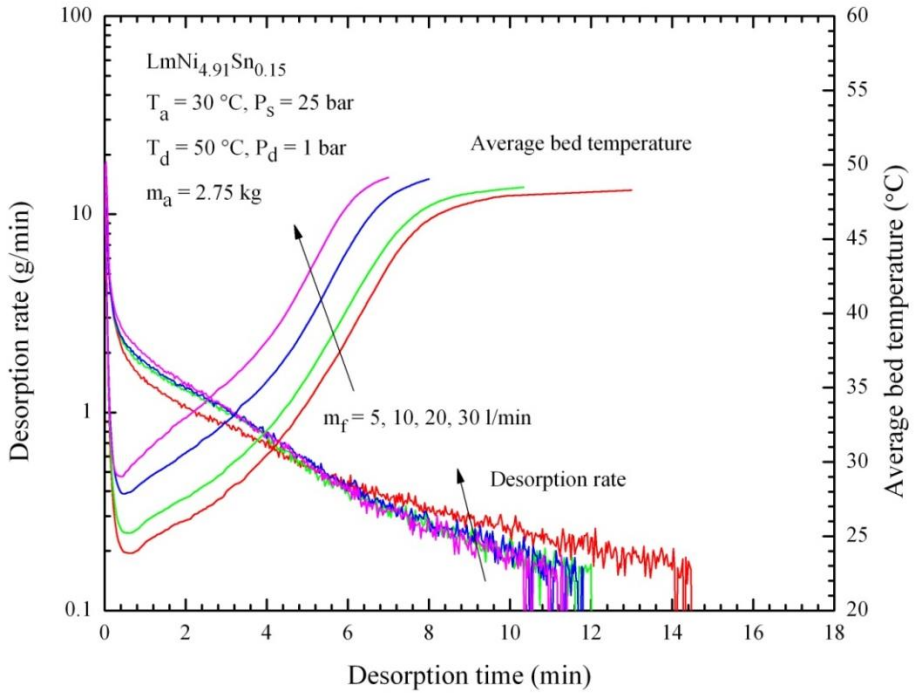

(a)

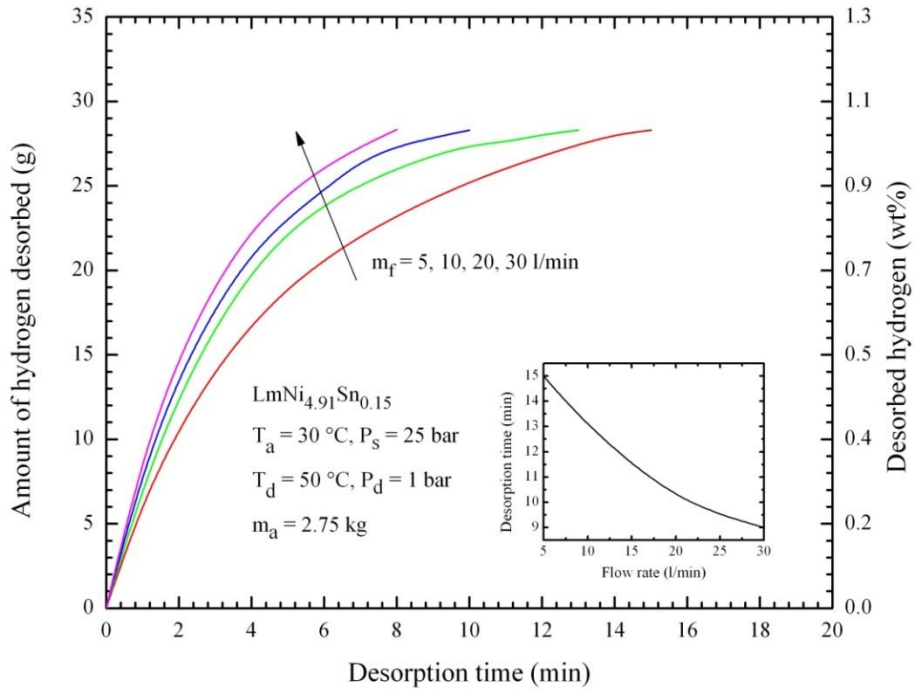

(b)

Fig. 5.37 – Effect of hot fluid (water) flow rates on the variations of (a) desorption rate and average bed temperature and (b) amount of hydrogen desorbed.

5.5.5 Pressure drop across the reactors

Fig. 5.38 shows the pressure drop across the reactors with 36 ECT and 60 ECT. The pressure drop tests have been performed with water by varying its flow rate from 5 l/min – 30 l/min. Pressure drop tests have been carried out by isolating the reactor from the hydrogen supply line. The pressure drop was measured using "U" tube Mercury manometer. The observed pressure drop for 36 ECT reactor are 24 mbar for 5 l/min, 76 mbar for 10 l/min, 357.3 mbar for 20 l/min and 544 mbar for 30 l/min, respectively. The respective values for 60 ECT are 14.7 mbar for 5 l/min, 50.6 mbar for 10 l/min, 158.7 mbar for 20 l/min and 264 mbar for 30 l/min, respectively. For a given flow rate, the reactor with 36 ECT is having more pressure drop in comparison with 60 ECT reactor. The reason for higher pressure drop in the reactor with 36 ECT is more flow resistance and higher flow velocity.

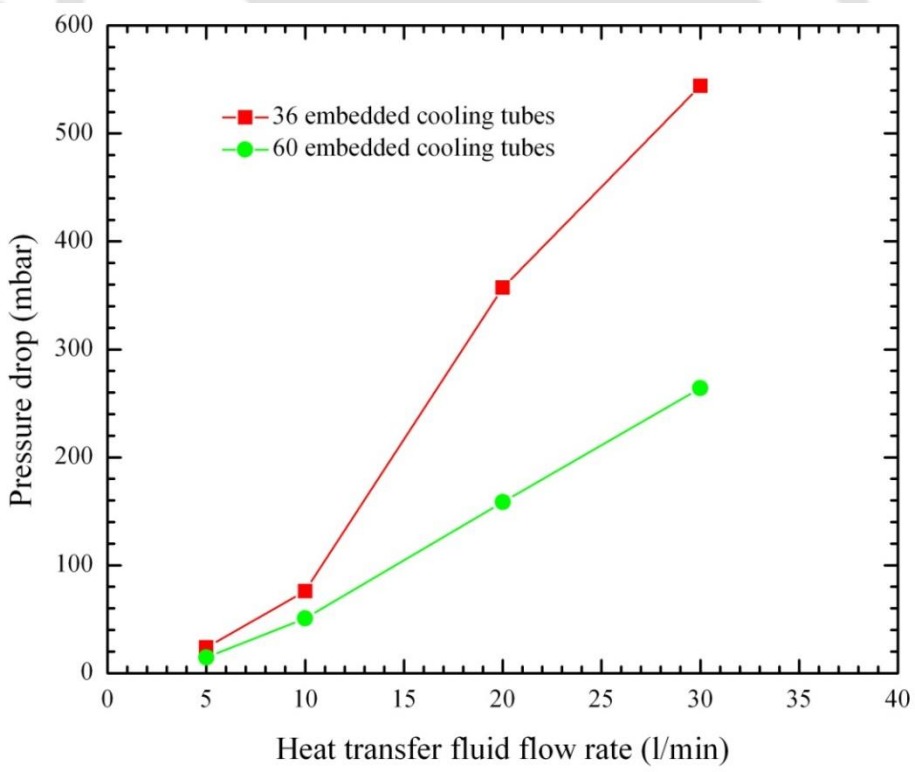

Fig. 5.38 – Pressure drop across the reactors.

5.6 Summary

The results obtained from the numerical investigations on lab-scale MHHSD and MHHSD with ECT and experimental studies on MHHSD with 36 and 60 ECT are reported in this chapter. In the first study, a 2-D mathematical model is developed for predicting the hydriding/dehydriding characteristics of lab-scale Mg_2Ni based hydrogen storage device during hydriding/dehydriding process at different operating parameters. Effects of supply pressure, bed thickness, bed thermal conductivity and cooling fluid temperature on the variations of hydrogen storage capacity and average bed temperature are reported. During dehydriding process, effects of desorption temperature and overall heat transfer coefficient on the variations of the amount of hydrogen desorbed and the average bed temperature are also reported. It is observed that at higher hydrogen supply pressure of 20 bar, lower bed thickness of 7.5 mm, higher effective thermal conductivity of 5 W/m·K and lower cooling fluid temperature of 300 °C, the maximum hydrogen storage capacity is found to 36.7 g of H_2/kg of Mg_2Ni. From the desorption study, it is observed that at higher desorption temperature (350 °C) significantly improves the rate of desorption.

In the second study, to optimize the number of ECT in MHHSD, a 2-D mathematical model is developed to predict the transient behaviour of hydriding/dehydriding characteristics of 2.75 kg $LmNi_{4.91}Sn_{0.15}$ based hydrogen storage device during hydrogen absorption/desorption process. After optimizing the number of ECT, the study is extended by developing a 3-D mathematical model to predict the hydriding/dehydriding characteristics of MHHSD with 60 ECT during absorption/desorption process at different operating conditions. Effects of supply pressure and effective thermal conductivity on the variation of the hydrogen storage capacity are reported. Effects of desorption temperature and effective thermal conductivity on the variations of the

amount of hydrogen desorbed are also reported. In addition the pictorial representation of hydride bed temperature during hydriding/dehydriding process is also reported in this chapter. The HTF variations along ECT at different axial and radial locations during both hydriding and dehydriding process are also discussed.

Finally, the results obtained from the experimental studies on hydriding/dehydriding characteristics of MHHSD with 36 and 60 ECT are reported for both absorption and desorption processes at different operating parameters. Effects of supply pressure, absorption temperature, and HTF flow rates (oil and water) on the variations of the rate of hydrogen absorption, the amount of hydrogen absorbed, the hydrogen storage capacity and the average bed temperature are reported. From the absorption study, it is observed that at higher supply pressure 35 bar, absorption temperature 30 °C and HTF flow rate 3.2 l/min, the maximum hydrogen storage capacity is reached about 1.18 wt% for both the reactors. The dehydriding characteristics are also reported for different desorption temperatures, hot fluid temperatures and hot fluid flow rates. From this experimental study, it is observed that at a given operating conditions, the rate of hydrogen absorption/desorption is rapid for the reactor with 60 ECT. The detailed conclusions obtained from both numerical and experimental investigations are reported in chapter 6.

Chapter 6

Conclusions and Future Scope

The major conclusions drawn from the numerical studies on lab-scale MHHSD and MHHSD with ECT and the experimental studies on MHHSD with 36 and 60 ECT are presented in this chapter.

6.1 Numerical studies

6.1.1 Lab-scale metal hydride based hydrogen storage device (MHHSD)

The performances of Mg_2Ni based solid state hydrogen storage device during absorption and desorption processes were studied. The numerical study was performed for the 2-D cylindrical reactor. Volumetric radiation was accounted in the energy equation. With the divergence of

radiative heat flux calculated using the FVM, the energy equation too was solved using the FVM. Effects of the supply pressure, the bed thickness, the effective thermal conductivity of the bed and the cooling fluid on the hydrogen storage capacity and the average bed temperature were studied. At different supply pressures, hydrogen storage capacities were compared with the experimental results available in the literature. A good agreement was found. Effects of desorption temperature and overall heat transfer coefficient on the variation of the amount of hydrogen desorbed and the average bed temperature were also investigated. The important conclusions are as follows:

- With the presence of volumetric radiative heat transfer, rate of hydrogen absorption was found to be rapid.
- With higher supply pressure (20 bar), lower bed thickness (7.5 mm), higher effective thermal conductivity (5.0 W/m·K), and lower temperature of the cooling fluid (300 °C), the hydrogen storage capacity was found to be maximum at 36.7 g of H_2 / kg of Mg_2Ni.
- It was observed that in the region close to the porous filter, the effect of volumetric radiation was more dominant than in the region nearer to convective wall. Hence, the absorption/desorption rate was low at the region close to porous wall.
- The maximum amount of hydrogen desorbed was 36.2 g of hydrogen per kg of alloy. At the given operating conditions of dehydriding temperature 350 °C and dehydriding pressure 1 bar, the optimum value of heat transfer coefficient for lab-scale solid stage hydrogen storage device was 1000 $W/m^2 \cdot K$.
- Higher desorption temperature significantly improves the rate of desorption and hence, the amount of hydrogen desorbed was rapid.

6.1.2 Metal hydride based hydrogen storage device (MHHSD) with embedded cooling tubes (ECT)

The transient behavior of heat and hydrogen transfer characteristics of $LmNi_{4.91}Sn_{0.15}$ based hydrogen storage container was studied using COMSOL Multiphysics 4.3. A 2-D mathematical model was developed for a cylindrical reactor by varying the arrangements of embedded cooling tubes (24 – 70 ECT) configurations and the hydrogen charging and discharging characteristics at different operating conditions were studied. This study was extended to 3-D mathematical model employing 2.75 kg of $LmNi_{4.91}Sn_{0.15}$ based hydrogen storage container with 60 ECT and their hydriding and dehydriding characteristics were predicted at different hydrogen supply pressure (10 – 35 bar), different hot fluid temperature (30 – 60 °C) and effective thermal conductivity of hydride bed (0.2 – 2.5 W/m·K). The variations in hydrogen storage capacity (wt%) and the amount of hydrogen desorbed (wt%) were reported for different supply pressures and hot fluid temperatures. The conclusions from this study are presented as follows:

- For the given absorption/desorption conditions, the hydriding and dehydriding times were reduced about ≈ 45.5% (33 min to 18 min) for hydriding process and ≈ 26.3% (19 min to 14 min) for dehydriding process, when the number of ECT was increased from 24 to 70.
- The number of ECT was optimized on the basis of hydriding/dehydriding time and found to be 60 ECT.
- The hydriding characteristics were influenced by the hydrogen supply pressure and the effective thermal conductivity, while the dehydriding characteristics were mainly influenced by the hot fluid temperature and the effective thermal conductivity.

- For the reactor with 60 ECT, the rate of hydriding was rapid for the supply condition of 35 bar hydrogen supply pressure and 30 °C heat transfer fluid temperature. The rate of dehydriding was prompt at higher hot fluid temperature of above 60 °C.
- For both hydriding and dehydriding processes, the increase in the effective thermal conductivity of hydride bed up to about 2 W/m·K provides significant reduction in the hydriding and dehydriding times.
- The numerical results were validated with experimental data and found a good concurrence between them.

Using the developed thermal models, one can predict the performances of MHHSD filled with any hydrogen absorbing alloys without performing the expensive experimental studies. One can also obtain the optimum operating parameters such as absorption/desorption temperatures and pressures, and bed parameter such as thermal conductivity of the hydride bed and thickness etc.

6.2 Experimental studies of hydrogen storage performance of MHHSD with ECT

The following conclusions are drawn from the performance tests on $LmNi_{4.91}Sn_{0.15}$ based MHHSD with 36 and 60 ECT.

6.2.1 Absorption process

Experiments were performed on two MHHSD with 36 and 60 ECT employing 2.75 kg of $LmNi_{4.91}Sn_{0.15}$. Performances of the storage devices in terms of hydrogen absorption rate and hydrogen storage capacity were studied for different supply pressures (10 – 35 bar), absorption temperatures (20 – 30 °C) and heat transfer fluid flow rates (2.2 – 30 l/min). The important conclusions are as follows:

- For the absorption temperature of 30 °C, the amount of hydrogen absorbed was found to increase from 19.19 g (0.69 wt%) to 32.52 g (1.18 wt%), when the hydrogen supply pressure was varied from 10 bar to 35 bar.
- At given supply conditions of absorption temperature 30 °C and hydrogen supply pressure 35 bar, the maximum amount of hydrogen absorbed was ≈ 1.18 wt% in 10 min for 36 ECT and 8 min for 60 ECT.
- With oil as the heat transfer fluid, when the flow rate was increased from 2.2 l/min to 3.2 l/min, in both the reactors, about 47% reduction in the absorption time was reported.
- When water was used as the heat transfer fluid, and its flow rate was more than that of oil, the absorption time was further reduced.
- At 25 bar supply pressure and 30 °C absorption temperature, water flow rate of 30 l/min, the absorption process was ended within 5 min for the reactor with 60 ECT.

6.2.2 Desorption process

The desorption characteristics on $LmNi_{4.91}Sn_{0.15}$ based hydrogen storage containers with 36 and 60 ECT were studied. The effect of desorption temperatures (30 – 60 °C) and hot fluid (oil and water) flow rates (2.2 – 30 l/min) on the variations of the dehydriding rate, the average hydride bed temperature and amount of hydrogen desorbed are reported. The important conclusions are as follows:

- For both the reactor, the desorption time was reduced about ≈ 48%, when the desorption temperature was increased from 30 °C to 60 °C and the maximum amount of hydrogen desorbed was about 30.72 g (1.1wt%).

- In the reactor with 60 ECT, at 60 °C desorption temperature and 3.2 l/min oil flow rate, the desorption rate of hydrogen was found to be rapid.
- With the same reactor configuration (60 ECT), water as heat transfer fluid at a flow rate of 30 l/min and at 50 °C, the maximum amount of hydrogen desorbed was ≈ 1.08 wt% within 8 min.
- The desorption time was decreased by 46.7% when the water flow rate was increased from 5 l/min to 30 l/min.
- For a given flow rate, the reactor with 36 ECT had more pressure drop in comparison with 60 ECT reactor. The reason for higher pressure drop in the reactor with 36 ECT was more flow resistance and higher flow velocity.

These experimental studies will provide some guidelines for the development of a commercial metal hydride based hydrogen storage device.

6.3 Scope of future work

The work presented in this thesis offers several opportunities to widen the research work on MHHSD. Some of the scopes of future work are listed below:

- The development of MHHSD with ECT equipped with fins and external cooling/heating jackets may be considered.
- This device may be upgraded to other metal hydride based thermal machines.
- The development of MHHSD with automatic control and monitoring system.

References

Aldas K, Mat MD, Kaplan Y (2002). A three-dimensional mathematical model for absorption in a metal hydride bed. Int J Hydrogen Energy, 27:1049-1056.

Askri F, Jemni A, Nasrallah SB (2003). Study of two-dimensional and dynamic heat and mass transfer in a metal–hydrogen reactor. Int J Hydrogen Energy, 28:537-557.

Askri F, Jemni A, Nasrallah SB (2004a). Prediction of transient heat and mass transfer in a closed metal–hydrogen reactor. Int J Hydrogen Energy, 29:195-208.

Askri F, Jemni A, Nasrallah SB (2004b). Dynamic behavior of metal-hydrogen reactor during hydriding process. Int J Hydrogen Energy, 29:635-647.

Askri F, Salah MB, Jemni A, Nasrallah SB (2009). Heat and mass transfer studies on metal-hydrogen reactor filled with $MmNi_{4.6}Fe_{0.4}$. Int J Hydrogen Energy, 34:6705-6711.

Bilgili M, Ataer OE (2005). Numerical analysis of hydrogen absorption in a P/M metal bed. Powder Technology, 160:141-148.

Chung CA, Ho CJ (2009). Thermal-fluid behavior of the hydriding and dehydriding processes in a metal hydride hydrogen storage canister. Int J Hydrogen Energy, 34:4351-4364.

Chung CA, Lin CS (2009). Prediction of hydrogen desorption performance of Mg2Ni hydride reactors. Int J Hydrogen Energy, 34:9409-9423.

Demircan A, Demiralp M, Kaplan Y, Mat MD, Veziroglu TN (2005). Experimental and theoretical analysis of hydrogen absorption in $LaNi_5$–H_2 reactors. Int. J. Hydrogen Energy, 30:1437-1446.

Dhaou H, Mellouli S, Askri F, Jemni A, Nasrallah SB (2007). Experimental and numerical study of discharge process of metal–hydrogen tank. Int J Hydrogen Energy, 32:1922-1927.

Dhaou H, Souahlia H, Mellouli S, Askri F, Jemni A, Nasrallah SB (2010). Experimental study of a metal hydride vessel based on a finned spiral heat exchanger. Int J Hydrogen Energy, 35:1674-1680.

Dhaou H, Khedher NB, Mellouli S, Souahlia A, Askri F, Jemni A, Nasrallah SB (2011). Improvement of thermal performance of spiral heat exchanger on hydrogen storage by adding copper fins. Int J Thermal Science, 50:2536-2542.

Dogan A, Kaplan Y, Veziroglu TN (2004). Numerical investigation of heat and mass transfer in a metal hydride bed. Applied Mathematics and Computations, 150:169-180.

Donald MBD, Rowe AM (2006a). A thermally coupled metal hydride hydrogen storage and fuel cell system. J Power Sources, 161:346-355.

Donald MBD, Rowe AM (2006b). Impacts of external heat transfer enhancements on metal hydride storage tanks. Int J Hydrogen Energy, 31:1721-1731.

Freni A, Cipiti F, Cacciola G (2009). Finite element-based simulation of a metal hydride-based hydrogen storage tank. Int J Hydrogen Energy, 34:8574-8482.

Gambini M (1994). Metal hydride energy systems performance evaluation. Part A: Dynamic analysis model of heat and mass transfer. Int J Hydrogen Energy, 19:67-80.

Gambini M, Manno M, Vellini M (2008). Numerical analysis and performance assessment of metal hydride-based hydrogen storage systems. Int J Hydrogen Energy, 33:6178-6187.

Goodell PD, Sandrock GD, Huston EL (1980). Kinetic and dynamic aspects of rechargeable metal hydrides. J Less-Common Metals, 73:135-142.

Goodell PD, Rudman PS (1983). Hydriding And dehydriding rates of the $LaNi_5$-H System. J Less-Common Metals, 89:117-125.

Gopal MR, Murthy SS (1992). Prediction of heat and mass transfer in annular cylindrical metal hydride beds. Int J Hydrogen Energy, 17:795-805.

Gopal MR, Murthy SS (1993). Parametric studies on heat and mass transfer in metal hydride beds. Chemical Engineering and processing, 32:217-223.

Gopal MR, Murthy SS (1995). Studies on heat and mass transfer in metal hydride beds. Int J Hydrogen Energy, 20:911-917.

Gopal MR, Murthy SS (1999). Predication of heat and mass transfer in annular cylindrical metal hydride bed. Int J Hydrogen Energy, 17:795-805.

Groll M (1993). Reaction beds for dry sorption machines. Heat Recovery System CHP, 13: 41-46.

Groll M, Supper W, Mayer U, Brost O (1987). Heat and mass transfer limitations in metal hydride reaction beds. Int J Hydrogen Energy, 12:89-97.

Guo Z, Sung HJ (1999). Technical Note Conjugate heat and mass transfer in metal hydride beds in the hydriding process. Int J Heat and Mass Transfer, 42:379-382.

Ha MY, Kim IK, Song HD, Sung S, Lee DH (2004). A numerical study of thermo-fluid phenomena in metal hydride beds in the hydriding process. Int J Heat and Mass Transfer, 47:2901-2912.

Han JS, Lee JY (1987). A study of the hydriding kinetics of Mg_2Ni. J Less-Common Metals, 131:109-116.

Hirata T, Matsumoto T, Amano M, Sasaki Y (1983). Dehydriding reaction kinetics in the improved intermetallic Mg_2Ni–H system. J Less-Common Metals, 89:85-91.

Huston EL, Sandrock GD (1980). Engineering properties of metal hydrides. J Less-Common Metals, 74:435-443.

Inomata A, Aoki H, Miura T (1998). Measurement and modelling of hydriding and dehydriding kinetics. J Alloys and Compound, 278:103-109.

Jemni A, Nasrallah SB (1995a). Study of two dimensional heat and mass transfer during absorption in a metal-hydrogen reactor. Int J Hydrogen Energy, 20:43-52.

Jemni A, Nasrallah SB (1995b). Study of two-dimensional heat and mass transfer during desorption in a metal-hydrogen reactor. Int J Hydrogen Energy, 20:881-891.

Jemni A, Nasrallah SB, Lamloumi J (1999). Experimental and theoretical study of a metal-hydrogen reactor. Int J Hydrogen Energy, 24:631-644.

Lucas GG, Richards WL (1984). Mathematical modelling of hydrogen storage systems. Int J Hydrogen Energy, 9:225-231.

Johnson TA, Kanouff MP, Dedrick DE, Evans GH, Jorgensen SW (2012). Model-based design of an automotive-scale, metal hydride hydrogen storage system. Int J Hydrogen Energy, 37:2835-2849.

Jung WB, Nahm KS, Lee WY (1990). The reaction kinetics of hydrogen storage in Mg_2Ni. Int J Hydrogen Energy, 15:641-648.

Kapischke J, Hapke J (1998). Measurement of the pressure-composition isotherms of high-temperature and low-temperature metal hydrides. Experimental Thermal and Fluid Science, 18:70-81.

Kaplan Y (2009). Effect of design parameters on enhancement of hydrogen charging in metal hydride reactors. Int J Hydrogen Energy, 34:2288-2294.

Kikkinides ES, Georgiadis MC, Stubos AK (2006). On the optimization of hydrogen storage in metal hydride beds. Int J Hydrogen Energy, 31:737-751.

Kim MY (2008). Assessment of the axisymmetric radiative heat transfer in a cylindrical enclosure with the finite volume method. Int J Heat Mass Transfer, 51:5144-5153.

Koh JT, Goudy AJ, Huang P, Zhou G (1989). A comparison of the hydriding and dehydriding kinetics of $LaNi_5$ hydride. J Less-Common Metals, 153:89-100.

Krokos CA, Nikolic D, Kikkinides ES, Georgiadis MC, Stubos AK (2009). Modelling and optimization of multi-tubular metal hydride beds for efficient hydrogen storage. Int J Hydrogen Energy, 34:9128-9140.

Kumar S, Raju M, Senthil Kumar V (2012). System simulation models for on-board hydrogen storage systems. Int J Hydrogen Energy, 37:2862-2873.

Linder M, Mertz R, Laurien E (2010). Experimental analysis of fast metal hydride reaction bed dynamics. Int J Hydrogen Energy, 35:8755-8761.

Lucas, G.G and W.L. Richards (1984). Mathematical modeling of hydrogen storage systems, Int. J. Hydrogen Energy, 9:225–231.

Martin M, Gommel C, Borkhart C, Fromm E (1996). Absorption and desorption kinetics of hydrogen storage alloys. J Alloys and Compounds, 238:193-201.

Marty P, Fourmigue JF, Rango PD, Fruchart D, Charbonnier J (2006). Numerical simulation of heat and mass transfer during the absorption of hydrogen in a magnesium hydride. Energy Conversion Management, 47:3632-3643.

Mat MD, Kaplan Y (2001). Numerical study of hydrogen absorption in an Lm-Ni_5 hydride reactor. Int J Hydrogen Energy, 26:957-963.

Mayer U, Groll M, Supper W (1987). Heat and mass transfer in metal hydride reaction beds: Experimental and theoretical results. J Less-Common Metals, 131:235-244.

Mellouli S, Dhaou H, Askri F, Jemni A, Nasrallah SB (2009). Hydrogen storage in metal hydride tanks equipped with metal foam heat exchanger. Int J Hydrogen Energy, 34:9393-9401.

Mellouli S, Askri F, Dhaou H, Jemni A, Nasrallah SB (2010). Numerical simulation of heat and mass transfer in metal hydride hydrogen storage tanks for fuel cell vehicles, Int J Hydrogen Energy, 35:1693-1705.

Melnichuk M, Silin N, Andreasen G, Corso HL, Visintin A, Peretti HA (2010). Hydrogen discharge simulation and testing of a metal-hydride container. Int J Hydrogen Energy, 35:5855-5859.

Melnichuk M, Silin N, Peretti HA (2009). Optimized heat transfer fin design for a metal-hydride hydrogen storage container. Int J Hydrogen Energy, 34:3417-3424.

Melnichuk M, Silin N (2012). Guidelines for thermal management design of hydride containers. Int J Hydrogen Energy, 37:18080-18094.

Mishra SC, Roy HK (2007). Solving transient conduction and radiation heat transfer problem using the Lattice Boltzmann method and the finite volume method. J Computational Physics, 223:89-107**.**

Miyamoto M, Yamaji K, Nakata Y (1983). Reaction kinetics of $LaNi_5$. J Less-Common Metals, 89:111-116.

Mohan G, Maiya MP, Murthy SS (2007). Performance simulation of metal hydride hydrogen storage device with embedded filters and heat exchanger tubes. Int J Hydrogen Energy, 32:4978-4987.

Mungole MN, Balasubramaniam R (1998). Hydrogen desorption kinetics in $MmNi_{4.2}Al_{0.8}$-H systems. Int J Hydrogen Energy, 23:349-353.

Muthukumar P, Abraham K, Prasad UAR, Maiya MP, Murthy SS (2003). Screening of metal hydride for engineering applications. Proceedings of ECOS (2003), Copenhagen, Denmark.

Muthukumar P, Maiya MP, Murthy SS (2005). Experiments on a metal hydride-based hydrogen storage device. Int J Hydrogen Energy, 30:1569-1581.

Muthukumar P, Madhavakrishna U, Dewan A (2007). Parametric studies on a metal hydride based hydrogen storage device. Int J Hydrogen Energy, 32:4988-4997.

Muthukumar P, Maiya MP, Murthy SS, Vijay R, Sundaresan R (2008). Tests on mechanically alloyed Mg_2Ni for hydrogen storage. J Alloys and Compounds, 452:456-461.

Muthukumar P, Satheesh A, Madhavakrishna U, Dewan A (2009a). Numerical investigation of coupled heat and mass transfer during desorption of hydrogen in metal hydride beds. Energy Conversion and Management, 50:69-75.

Muthukumar P, Satheesh A, Linder M, Mertz R, Groll M (2009b). Studies on hydriding kinetics of some La-based metal hydride alloys. Int J Hydrogen Energy, 34:7253-7262.

Muthukumar P, Linder M, Mertz R, Laurien E (2009c). Measurement of thermodynamic properties of some hydrogen absorbing alloys. Int J Hydrogen Energy, 34:1873-1879.

Muthukumar P, Ramana SV (2009). Numerical simulation of coupled heat and mass transfer in metal hydride-based hydrogen storage reactor. J Alloys and Compounds, 472:466-472.

Muthukumar P, Ramana SV (2010). Study of heat and mass transfer in $MmNi_{4.6}Al_{0.4}$ during desorption of hydrogen. Int J Hydrogen Energy, 35:10811-10818.

Muthukumar P, Groll M (2010). Metal Hydride based heating and cooling systems: A Review. Int J Hydrogen Energy, 35:3817-3831.

Muthukumar P, Singhal A, Bansal GK (2012). Thermal modeling and performance analysis of industrial-scale metal hydride based hydrogen storage container. Int J Hydrogen Energy, 37:14351-14364.

Nahm KS, Kim WY, Hong SP, Lee WY (1992). The reaction kinetics of hydrogen storage in $LaNi_5$. Int J Hydrogen Energy, 17:333-338.

Nakagawa T, Inomata A, Aoki H, Miura T (2000). Numerical analysis of heat and mass transfer characteristics in the metal hydride bed. Int J Hydrogen Energy, 25:339-350.

Nam J, Ko J, Ju H (2012). Three-dimensional modelling and simulation of hydrogen absorption in metal hydride hydrogen storage vessels. Applied Energy, 89:164-175.

Nasrallah SB, Jemni A (1997). Heat and mass transfer in metal-hydrogen reactor. Int J Hydrogen Energy, 22:67-76.

Nishizki T, Miyamoto K, Yoshida K (1983). Coefficient performance of hydride heat pumps. J Less-Common Metals, 89:559-566.

Paya J, Linder M, Laurien E, Corberan JM (2009). Mathematical models for the P-C-T characterization of hydrogen absorbing alloys. J Alloys and Compounds, 484:190-195.

Phate AK, Maiya MP, Murthy SS (2007). Simulation of transient heat and mass transfer during hydrogen sorption in cylindrical metal hydride beds. Int J Hydrogen Energy, 32:1969-1981.

Reilly JJ, Wiswall RH (1973). Formation and properties Iron Titanium hydride. Inorganic Chemistry, 13:218-222.

Raju M, Kumar S (2012). Optimization of heat exchanger design in metal hydride based hydrogen storage systems. Int J Hydrogen Energy, 37:2767-2778.

Satheesh A, Muthukumar P (2010). Performance investigations of a single-stage metal hydride heat pump. Int J Hydrogen Energy, 35:6950-6958.

Selvam KP, Muthukumar P, Linder M, Mertz R, Kulenovic R (2013). Measurement of thermochemical properties of some metal hydrides – Titanium (Ti), misch metal (Mm) and lanthanum (La) based alloys. Int J Hydrogen Energy, 38:5288-5301.

Sekhar BS, Muthukumar P, Saikia R (2012). Test on a metal hydride based thermal energy storage system. Int J Hydrogen Energy, 37:3818-3824.

Sekhar BS, Suresh P, Muthukumar P (2013). Performance tests on metal hydride based hydrogen storage devices. Int J Hydrogen Energy, 38:9570-9577.

Souahlia A, Dhaou H, Askri F, Sofiene M, Jemni A, Nasrallah SB (2011). Experimental and comparative study of metal hydride hydrogen tanks. Int J Hydrogen Energy, 36:12918-12922.

Skripnyuk VM, Ron M (2003). Hydrogen desorption kinetics in intermetallic compounds C2, $C5_1$ and $C5_2$ with Laves phase structure. Int J Hydrogen Energy, 28:303-309.

Suda S, Kobayashi N, Yoshida K (1980). Reaction kinetics of metal hydrides and their mixtures. J Less-Common Metals, 73:119-126.

Suda S, Kobayashi N, Morishita E, Takemoto N (1983). Heat transmission analysis of metal hydride beds. J Less-Common Metals, 89:325-332.

Sun DW, Deng SJ (1988). Study of heat and mass transfer characteristics of metal hydride beds. J Less-Common Metals, 141:37-43.

Supper W, Groll M, Mayer U (1984). Reaction kinetics in metal hydride reaction beds with improved heat and mass transfer. J Less-Common Metals, 104:279-286.

Van Mal HH, Buschow KHJ, Miedema AR (1974). Hydrogen absorption in $LaNi_5$ and related compounds: Experimental observations and their explanation. J Less-Common Metals, 35:65-76.

Visaria M, Mudawar I, Pourpoint T, Kumar S (2010). Study of heat transfer and kinetics parameters influencing the design of heat exchangers for hydrogen storage in high-pressure metal hydrides. Int J Heat and Mass Transfer, 53:2229-2239.

Visaria M, Mudawar I, Pourpoint T (2011a). Enhanced heat exchanger design for hydrogen storage using high-pressure metal hydride: Part 1. Design methodology and computational results. Int J Heat and Mass Transfer, 54:413-423.

Visaria M, Mudawar I, Pourpoint T (2011b). Enhanced heat exchanger design for hydrogen storage using high-pressure metal – Part 2. Experimental results. Int J Heat and Mass Transfer, 54:424-432.

Visaria M, Mudawar I (2012a). Coiled-tube heat exchanger for high-pressure metal hydride hydrogen storage systems – Part 2. Computational model. Int J Heat and Mass Transfer, 55:1796-1806.

Visaria M, Mudawar I (2012b). Coiled-tube heat exchanger for high-pressure metal hydride hydrogen storage systems – Part 1. Experimental study. Int J Heat and Mass Transfer, 55:1782-1795.

Visaria M, Mudawar I (2012c). Experimental investigation and theoretical modelling of dehydriding process in high-pressure metal hydride hydrogen storage systems. Int J Hydrogen Energy, 37:5735-5749.

Wang XL, Suda S (1990a). Study of the hydriding kinetics of $LaNi_{4.7}Al_{0.3}$–H system by a step-wise method. J Less-Common Metals, 159:109-119.

Wang XL, Suda S (1990b). A dehydriding kinetic study of $LaNi_{4.7}Al_{0.3}$ hydride by a step-wise method. J Less-Common Metals, 159:83-90.

Wang XL, Suda S (1990c). Reaction kinetics of hydrogen-metal hydride systems. Int J Hydrogen Energy, 15:569-577.

Wang Y, Adroher XC, Chen J, Yang XG, Miller T (2009). Three-dimensional modelling of hydrogen sorption in metal hydride hydrogen storage beds. J Power Sources, 194:997-1006.

Ye J, Jiang L, Li Z, Liu X, Wang S, Li X (2010). Numerical analysis of heat and mass transfer during absorption of hydrogen in metal hydride based hydrogen storage tanks. Int J Hydrogen Energy, 35:8216-8224.

Appendix A

Discretization of Governing Equations

A 2-D mathematical model is developed for predicting the coupled heat and mass transfer characteristics of lab-scale metal hydride based hydrogen storage devices (MHHSD). This model is numerically solved using finite volume method (FVM). The physical models of the cylindrical reactors used for absorption/desorption of hydrogen to/from the metal hydride beds are illustrated in Figs.3.1 and 3.2, respectively. The MH reaction beds are assumed to axisymmetric. For the present numerical analysis, only half of the MH bed is considered. The first step of FVM, the computational domain is divided into many discrete control volumes. The boundaries of the control are positioned at mid of two adjacent nodes. At the near edge of the domain the physical boundaries coincide with the control volume boundaries. In general (2-D geometry), the nodal point is called as 'P' and the neighbour points are called as north (N), south (S), east (E) and west (W) respectively. The control volume faces for different direction are denoted as n, s, w and e for north, south, west and east respectively. The distance between the nodes W and nodal point

P, and between the nodal point P and E is represented by ΔZ. Similarly, the distance between the point P and N, and between P and S is represented by ΔR. The distance between the control volumes faces n, s, e and w are given as Δr and Δz, respectively.

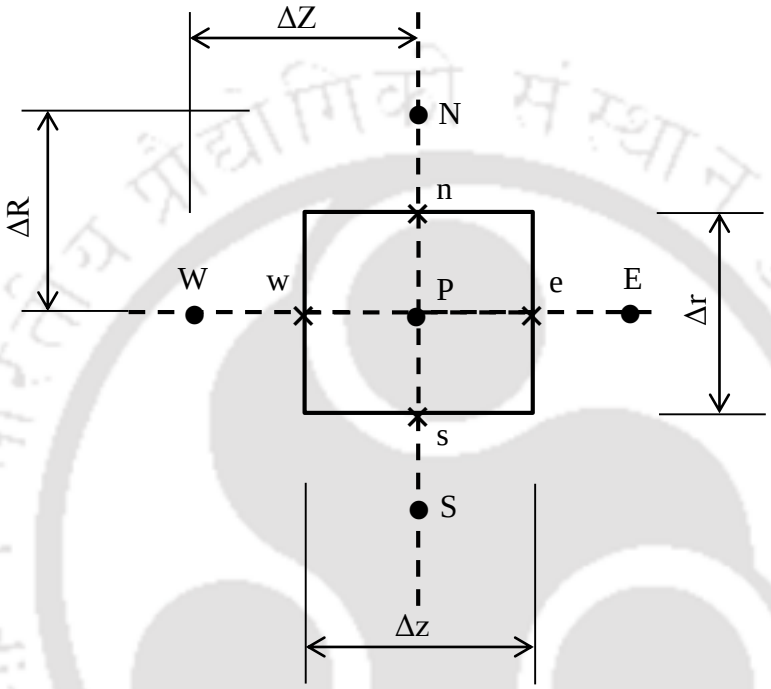

Fig. A. 1 – Two - dimensional grid generation technique

A. Energy equation

$$\left(\rho C_p\right)_e \frac{\partial T}{\partial t} = \frac{1}{r}\frac{\partial}{\partial r}\left(r\lambda_e \frac{\partial T}{\partial r}\right) + \frac{\partial}{\partial z}\left(\lambda_e \frac{\partial T}{\partial z}\right) - \left(\rho C_p V_{gr}\right)\frac{\partial T}{\partial r} - \left(\rho C_p V_{gz}\right)\frac{\partial T}{\partial z} - m\left[\frac{\Delta H}{M_g} - T\left(C_{pg} - C_{pm}\right)\right] - \nabla \cdot \vec{q}_R \quad \text{(A.1)}$$

The volumetric radiative heat flux term is discretized separately.

After integrating over control volume,

$$\begin{aligned}\left(\rho C_p\right)_e \frac{T-T_0}{\Delta t} = &\left(r\lambda_e \Delta z \frac{\partial T}{\partial r}\right)_n - \left(r\lambda_e \Delta z \frac{\partial T}{\partial r}\right)_s + \left(r\lambda_e \Delta r \frac{\partial T}{\partial z}\right)_e - \left(r\lambda_e \Delta r \frac{\partial T}{\partial z}\right)_w \\ &-\left(\rho C_p V_{gr} T\left(r\Delta z\right)\right)_n + \left(\rho C_p V_{gr} T\left(r\Delta z\right)\right)_s - \left(\rho C_p V_{gz} T\left(r\Delta r\right)\right)_e \\ &+\left(\rho C_p V_{gz} T\left(r\Delta r\right)\right)_w - \left(\rho C_p V_{gz}\right)\frac{\partial T}{\partial z} - m\frac{\Delta H}{M_g}\left(r_p \times \Delta r \times \Delta z\right) \\ &+ m\left(T\left(C_{pg} - C_{pm}\right)\right)\left(r_p \times \Delta r \times \Delta z\right)\end{aligned} \tag{A.2}$$

Let,

$$A_n = r_n \Delta z; A_s = r_s \Delta z; A_e = r_e \Delta r; A_w = r_w \Delta r \tag{A.3}$$

$$D_n = \frac{\lambda_e A_n}{\Delta r}; D_s = \frac{\lambda_e A_s}{\Delta r}; D_e = \frac{\lambda_e A_e}{\Delta z}; D_w = \frac{\lambda_e A_w}{\Delta z} \tag{A.4}$$

$$F_n = \left(\rho_g V_{gr}\right)_n A_n C_{pg}; F_s = \left(\rho_g V_{gr}\right)_s A_s C_{pg} \tag{A.5}$$

$$F_e = \left(\rho_g V_{gz}\right)_e A_e C_{pg}; F_w = \left(\rho_g V_{gz}\right)_w A_w C_{pg} \tag{A.6}$$

Then the Eq. (A.2) becomes

$$a_P T_P = a_N T_N + a_S T_S + a_E T_E + a_W T_W - b_1 + a_P{}^0 T_P{}^0 \tag{A.7}$$

where

$$a_P = a_N + a_S + a_E + a_W + a_P{}^0 + b \tag{A.8}$$

$$a_P{}^0 = \frac{\left(\rho C_p\right)\left(r_p \times \Delta r \times \Delta z\right)}{\Delta t} \tag{A.9}$$

$$a_E = D_e + \left[-F_e, 0\right]; a_W = D_w + \left[F_w, 0\right]; a_N = D_n + \left[-F_n, 0\right]; a_S = D_s + \left[-F_s, 0\right] \tag{A.10}$$

$$b = m\left(C_{pg} - C_{pm}\right)\left(r_p \times \Delta r \times \Delta z\right) \tag{A.11}$$

$$b_1 = m\left(\frac{\Delta H}{M_g}\right)\left(r_p \times \Delta r \times \Delta z\right) \tag{A.12}$$

B. Continuity equations

The MH bed is assumed as a sink. The amount of hydrogen absorbed/desorbed is calculated using the continuity equation which includes the density (ideal gas equation) and velocity (Darcy's law) of hydrogen inside the container. The continuity equation is written as

$$\varepsilon \frac{\partial \rho_g}{\partial t} + \nabla \cdot \left(\rho_g \vec{V}_g \right) = -\zeta \tag{A.13}$$

$$\rho_g = \frac{P_g M_{H_2}}{R_u T} \tag{A.14}$$

$$V_g = -\frac{K}{\mu_g} \nabla P_g \tag{A.15}$$

By substituting Eq. (A.14) and (A.15) in Eq. (A.13), then it becomes;

$$\left(\frac{\varepsilon M_g}{R_u T_g} \right) \frac{\partial P_g}{\partial t} + \left(\frac{\varepsilon M_g P_g}{R_u} \right) \frac{\partial}{\partial t} \left(\frac{1}{T_g} \right) - \left(\frac{K}{v_g r} \right) \frac{\partial}{\partial r} \left(r \frac{\partial P_g}{\partial r} \right) - \left(\frac{K}{v_g} \right) \frac{\partial}{\partial z} \left(\frac{\partial P_g}{\partial z} \right) = -\zeta \tag{A.16}$$

Integrating over control volume,

$$\begin{aligned} &\left(\frac{\varepsilon M_g}{R_u T_P} \right) \left(\frac{P_P - P_P{}^0}{\Delta t} \right) \left(r \times \Delta r \times \Delta z \right) + \left(\frac{\varepsilon M_g P_P}{R_u} \right) \left(\frac{1}{T_P} - \frac{1}{T_P{}^0} \right) \left(r \times \Delta r \times \Delta z \right) \\ &- \left(\frac{K}{v_g} r \Delta z \frac{\partial P_g}{\partial r} \right)_n + \left(\frac{K}{v_g} r \Delta z \frac{\partial P_g}{\partial r} \right)_s - \left(\frac{K}{v_g} r \Delta r \frac{\partial P_g}{\partial z} \right)_e \\ &+ \left(\frac{K}{v_g} r \Delta r \frac{\partial P_g}{\partial z} \right)_w = -\zeta \left(r_p \times \Delta r \times \Delta z \right) \end{aligned} \tag{A.17}$$

$$\begin{aligned} &\left(\frac{\varepsilon M_g}{R_u T_P} \right) \left(\frac{P_P - P_P{}^0}{\Delta t} \right) \Delta V + \left(\frac{\varepsilon M_g P_P}{R_u} \right) \left(\frac{1}{T_P} - \frac{1}{T_P{}^0} \right) \Delta V - \left(\frac{K}{v_g} r \Delta z \frac{P_N - P_P}{\Delta r} \right) \\ &+ \left(\frac{K}{v_g} r \Delta z \frac{P_P - P_S}{\Delta r} \right) - \left(\frac{K}{v_g} r \Delta r \frac{P_E - P_P}{\Delta z} \right) + \left(\frac{K}{v_g} r \Delta r \frac{P_P - P_W}{\Delta z} \right) = -\zeta \times \Delta V \end{aligned} \tag{A.18}$$

Let

$$A_n = r_n \Delta z; A_s = r_s \Delta z; A_e = r_e \Delta r; A_w = r_w \Delta r \tag{A.19}$$

$$a_N = \frac{KA_n}{v_g \Delta r}; a_S = \frac{KA_s}{v_g \Delta r}; a_E = \frac{KA_e}{v_g \Delta z}; a_W = \frac{KA_w}{v_g \Delta z} \tag{A.20}$$

Then Eq. (A.16) becomes,

$$a_P{}^0 \left(P_P - P_P{}^0\right) + bP_P = a_N \left(P_N - P_P\right) - a_S \left(P_P - P_S\right) + a_E \left(P_E - P_P\right) - a_W \left(P_P - P_W\right) - \zeta \times \Delta V \tag{A.21}$$

$$a_P P_P = a_N P_N + a_S P_S + a_E P_E + a_W P_W - \left(\zeta \times \Delta V\right) - a_P{}^0 P_P{}^0 \tag{A.22}$$

where

$$a_P = a_N + a_S + a_E + a_W + a_P{}^0 + b \tag{A.23}$$

$$a_P{}^0 = \frac{\varepsilon M_g \Delta V}{R_u T_p} \tag{A.24}$$

$$b = \frac{\varepsilon M_g}{R} \left(\frac{1}{T_P} - \frac{1}{T_P{}^0}\right) \Delta V \tag{A.25}$$

Super scripts '0' indicates the previous time step

C. Radiative transfer equation

In order to determine the divergence of radiative heat flux appearing the energy equation (A.26), the radiative transfer equation in any direction $\hat{s}$ identified by the solid angle Ω about an elemental solid angle is given by:

$$\frac{dI\left(\vec{r},\Omega\right)}{ds} = -\left(\kappa_a + \sigma_s\right) I\left(\vec{r},\Omega\right) + \kappa_a \left(\frac{\sigma T^4\left(\vec{r}\right)}{\pi}\right) + \frac{\sigma_s}{4\pi} \int_{\Omega'=4\pi} I\left(\vec{r},\Omega'\right) \phi\left(\Omega,\Omega'\right) d\Omega' \tag{A.26}$$

where κ_a is the absorption coefficient, σ_s is the scattering coefficient and ϕ is the scattering phase function.

Eq. (A.26) can be written as

$$\frac{dI}{ds} = -\beta I + S \tag{A.27}$$

where $\beta = \kappa_a + \sigma_s$ is the extinction coefficient and S is the source term given by

$$S = \kappa_a \left(\frac{\sigma T^4}{\pi} \right) + \frac{\sigma_s}{4\pi} \int_{\Omega'=4\pi} I(\vec{r}, \Omega') \phi(\Omega, \Omega') d\Omega' \tag{A.28}$$

Let $\vec{s} = (\sin\theta\cos\phi)\hat{i} + (\sin\theta\sin\phi)\hat{j} + (\cos\theta)\hat{k}$ and $\mu_r = \sin\theta\cos\phi; \mu_z = \cos\theta$

The directional weight, D_i^{mn}, denotes the inflow or outflow of radiant energy across the control volume face depending on its sign as defined in the form:

$$D_i^{mn} = \int_{\phi^{n-1/2}}^{\phi^{n+1/2}} \int_{\theta^{m+}}^{\theta^{m+}} (\vec{s}.\vec{n}_i) \sin\theta d\theta d\phi \tag{A.29}$$

To obtain the finite volume discretized form of the RTE, Eq. (A.27) is integrated over a control volume ΔV and a control angle $\Delta\Omega^{mn}$ thereby; the following equation can be obtained:

$$\sum_{i=n,s,t,b} I_i^{mn} \Delta A_i D_i^{mn} + \left[\Delta A_e D_e^{mn+1/2} I_e^{mn+1/2} + \Delta A_w D_w^{mn-1/2} I_w^{mn-1/2} \right] + \beta I_P^{mn} \Delta V \Delta\Omega^{mn} = S_P^{mn} \Delta V \Delta\Omega^{mn} \tag{A.30}$$

where $\Delta A_n = r_n \Delta\phi\Delta z, \Delta A_s = r_s \Delta\phi\Delta z$ and $\Delta A_t = \Delta A_b = \pi\left(r_n^2 - r_s^2\right)/2N_\phi$ are the surface area of north, south, top and bottom faces, respectively. $\Delta V = \pi\left(r_n^2 - r_s^2\right)\Delta z / 2N_\phi$ is the volume of the control volume P and $\Delta\Omega^{mn} = \left(\cos\theta^{m-1/2} - \cos\theta^{m+1/2}\right)\left(\phi^{n+1/2} - \phi^{n-1/2}\right)$ is the discrete solid angle.

The discretization equation can be written as

$$a_P^{mn} I_P^{mn} = \sum_{i=N,S,W,E} a_i^{mn} I_i^{mn} + b_P^{mn} \tag{A.31}$$

where

$$a_P^{mn} = \sum_{i=n,s,w,e} \max\left(\Delta A_i D_i^{mn}, 0\right) + \beta\Delta V \Delta\Omega^{mn} + \Delta A_e D_e^{mn+1/2} \tag{A.32}$$

$$a_i^m = \max\left(-\Delta A_i D_i^{mn}, 0\right) \tag{A.33}$$

$$b_P^{mn} = S_P{}^{mn}\Delta V \Delta\Omega^{mn} - \Delta A_w D_w{}^{mn-1/2} I_P{}^{mn+1/2} \tag{A.34}$$

To relate the facial intensity, I_i^{mn}, and the angular edge intensity, $I_i^{mn\pm1/2}$, to the nodal intensity , I_I^{mn}, FVM is introduced to ensure positive intensity:

$$\begin{aligned} I_I^{mn} D_I^{mn} &= I_P^{mn} \max\left(D_i^{mn}, 0\right) - I_I^{mn} \max\left(-D_i^{mn}, 0\right) \\ I_e^{mn+1/2} &= I_P^{mn} \\ I_w^{mn-1/2} &= I_W^{mn-1/2} = I_P^{mn-1/2} \end{aligned} \tag{A.35}$$

The boundary condition for a diffusively reflecting and emitting wall can be written as:

$$I_w^{mn} = \varepsilon_w I_{b,w} + \frac{1-\varepsilon_w}{\pi} \sum_{m',n',D_w^{m'n'}} I_w^{m'n'} \left|D_w^{m'n'}\right| \; for \; D_w^{mn} > 0 \tag{A.36}$$

where $D_w^{mn} = \int_{\Delta\Omega^{mn}} \left(\vec{s}.\vec{n}_w\right) d\Omega$ is the directional weight at wall.

The radiative heat flux in the radial and axial directions can be estimated by

$$\begin{aligned} q_r^R &= 2\sum_{m=1}^{N_\theta}\sum_{n=1}^{N_\phi} I^{mn} D_n^{mn} \\ q_z^R &= 2\sum_{m=1}^{N_\theta}\sum_{n=1}^{N_\phi} I^{mn} D_t^{mn} \end{aligned} \tag{A.37}$$

Once the intensity distributions are known, the radiative information $\nabla\cdot\vec{q}_R$ required for the energy equation is computed from,

$$\nabla\cdot\vec{q}_R = \beta\left(1-\omega\right)\left(4\pi\frac{\sigma T^4}{\pi} - G\right) \tag{A.38}$$

where, $\omega = \sigma_s / \beta$ is the scattering albedo, β is extinction coefficient, $\left(\beta = \sigma_a + \sigma_s\right)$

Appendix B

Error Analysis

Kline and McClintock (1953) have proposed a procedure for estimating the uncertainty of any measure quantity in experimental studies. The principle is given as:

If a measure quantity, R depends on independent variables like V_1, V_2, V_3,……V_n then,

$$R = R(V_1, V_2, V_3 ..... V_n) \tag{B.1}$$

Let the uncertainty in the measured quantity be W_R and that for the independent variables are W_1, W_2, W_3, …… W_n. Then the uncertainty in the measured quantity, W_R is given by:

$$W_R = \left[\left(\frac{\partial R}{\partial V_1} \right)^2 W_1^{\,2} + \left(\frac{\partial R}{\partial V_2} \right)^2 W_2^{\,2} + ... \left(\frac{\partial R}{\partial V_n} \right)^2 W_n^{\,2} \right]^{\frac{1}{2}} \tag{B.2}$$

where $W_R = \frac{\partial R}{R}; \pm \partial R$ is the error in R

The important quantities that estimated in the experimental studies are temperature, pressure, the amount of hydrogen absorbed/desorbed and mass flow rate of heat transfer fluid during absorption and desorption processes.

1. Temperature measurement

The temperature at different locations of the system is measured using 'K' type metal sheathed thermocouples (Chromel – Alumel). Hence the error in the measurement of temperature is owing to the error in the voltage output from the thermocouple. The outputs from the 'K' type thermocouples are measured by the data acquisition system as mentioned in Chapter 4. The maximum possible uncertainty in the case of temperature measurement is estimated from the minimum value of the measured quantity and the accuracy of the instrument.

The minimum bed temperature measured is 5.5 °C and the accuracy is 0.2 °C, hence the maximum uncertainty in the case of temperature measurement with data acquisition system is:

$$\frac{\partial T}{T} = \pm \frac{0.2}{5.5} = \pm 0.036 = \pm 3.6\% \tag{B.3}$$

2. Pressure measurement

Hydrogen inside the storage container/device during absorption/desorption process are measured by piezo-resistive transducers as discussed in Chapter 4. The minimum pressure measured is 10.0 bar and the accuracy is 0.1 bar, hence:

$$\frac{\partial P}{P} = \pm \frac{0.1}{10} = \pm 0.01 = \pm 1.0\% \tag{B.4}$$

3. Measurement of hydrogen transferred

Hydrogen transferred during absorption/desorption is obtained from the Coriolis mass flow meter as mentioned in Chapter 4. The minimum value of hydrogen absorbed/desorbed is 6.51 g within 60 s and the accuracy of the mass flow meter is 0.001 g. The accuracy of the time measurement by stop watch is 0.1 s. Hence the maximum uncertainty in the measurement of hydrogen is given by:

$$\frac{\partial m_{H_2}}{m_{H_2}} = \pm\left[\left(\frac{0.001}{6.51}\right)^2 + \left(\frac{0.1}{60}\right)^2\right]^{0.5} = \pm 0.00167 = \pm 0.167\% \quad \text{(B.5)}$$

4. Measurement of heat transfer fluid flow rate

The flow rate of heat transfer fluid is measured using standard measuring jar and stop watch. The maximum possible uncertainty in the case of measurement of heat transfer fluid flow rate is calculated from the volume and time measurement:

$$\frac{\partial m_{HTF}}{m_{HTF}} = \pm\left[\left(\frac{10}{1000}\right)^2 + \left(\frac{0.1}{60}\right)^2\right]^{0.5} = \pm 0.0101 = \pm 1.01\% \quad \text{(B.6)}$$

5. Measurement of hydrogen storage capacity/amount of hydrogen desorbed

Hydrogen storage capacity (wt%) is given by ratio of the amount of hydrogen absorbed to per kg of hydride alloy. The minimum value of hydrogen absorbed is 7.68 g within 60 s and the accuracy of the mass flow meter is 0.001 g. The accuracy of the time measurement by stop watch is 0.1 s. The accuracy of the weighing balance is 0.5 g per kg of alloy (during measurement of alloy). Hence the maximum uncertainty in estimating the hydrogen storage capacity is given by:

$$\frac{\partial(wt\%)}{(wt\%)} = \pm\left[\left(\frac{0.001}{7.68}\right)^2 + \left(\frac{0.1}{60}\right)^2 + \left(\frac{0.0005}{2.75}\right)^2\right]^{0.5} = \pm 0.00168 = \pm 0.168\% \quad \text{(B.7)}$$

The maximum uncertainty in estimating the amount of hydrogen desorbed (wt%) is given by:

$$\frac{\partial(wt\%)}{(wt\%)} = \pm\left[\left(\frac{0.001}{6.51}\right)^2 + \left(\frac{0.1}{60}\right)^2 + \left(\frac{0.0005}{2.75}\right)^2\right]^{0.5} = \pm 0.00175 = \pm 0.175\% \quad \text{(B.8)}$$

Appendix C

Specifications of Instruments

The specifications of instruments used for the experimental investigations are listed below:

C.1 Data Acquisition System

Make	:	Agilent Technologies
Model	:	Agilent 34972A
Scan rate	:	60 to 250 channels/second
Scan intervals	:	0 to 99 hours; 1 ms time step
Accuracy	:	6 digits of resolution with 0.004%

C.2 Mass flow meter

Type	:	Coriolis mass flow meter
Make	:	Emerson Process Management Pvt. Ltd.
Model	:	CMF010P323NQB2E222
Fluid	:	Hydrogen
Flow range	:	0 to 50 g/min

Flow accuracy	:	± 0.35% of full scale
Sensitivity	:	0.001g
Temperature range	:	-10 to 100 °C
Operating pressure range	:	0 to 150 bar
Output type	:	4-20 mA signal

C.3 Pressure transducer

Type	:	Piezo – resistive
Model	:	PT series
Operating range	:	0 to120 bar
Operating temperature	:	0 to 100 °C
Output	:	0 to 10 V DC
Accuracy	:	± 0.1 bar

C.4 DC power supply

Make	:	Scientific
Model	:	PSD3304
DC output	:	30V/2A; 0 to ± 15V; 5V/5A
Input supply	:	230 AC ± 10%
Operating temperature	:	0 to 40 °C

C.5 Thermocouple

Type	:	K type metal sheathed
Make	:	Industrial Heators
Range	:	0 to 1400 °C
Sensitivity	:	± 0.5 °C

C.6 Thermostatic bath

Make	:	NR Enterprises Pvt. Ltd.
Model	:	Microprocessor based
Temperature range	:	-30 °C to 200 °C
Cooling capacity	:	1.5 kW at 0 °C
Heating capacity	:	3.0 kW
Accuracy	:	± 0.1 °C

C.7 Vacuum pump

Make	:	Vacuum Technologies
Model	:	VT – 2305
Pump-1	:	Rotary vacuum pump
Pumping speed	:	0 to 200 l/min
Pump speed	:	1440 rpm
Vacuum pressure range	:	1 to 10^{-3} mbar
Pump-2	:	Diffusion pump
Pumping speed	:	280 l/s
Heating rating	:	500 W
Ultimate vacuum	:	10^{-3} mbar to 10^{-7} mbar

C.8 weighing balance

Make	:	Sartorious
Model	:	CP8201
Capacity	:	0 to 20 kg
Accuracy	:	± 0.5 g

C.9 Valves

Make	:	Swagelok, USA
Type	:	Pack less metallic bellow type needle
Model	:	SS-4UW
Fluid	:	Hydrogen
Pressure range	:	0 to 120 bar
Temperature range	:	0 to 450 °C
End fittings	:	1/4 inch NPT

C.10 Filter

Make	:	Finix filters Pvt. Ltd.
Material	:	Sintered SS 316L
Pore size	:	2 micron
Outer diameter	:	14 mm
Operating pressure range	:	0 to 150 bar

C.11 Stopwatch

Make	:	Pacer
Model	:	Sports timer (SW – 101)
Accuracy	:	± 0.1 s

List of Publications

In Peer-reviewed Journals

1. Anbarasu S, Muthukumar P, Mishra SC. Thermal model on $LmNi_{4.91}Sn_{0.15}$ based solid state hydrogen storage device embedded cooling tubes. Int J Hydrogen Energy 2014; 39:15549-15562.
2. Anbarasu S, Muthukumar P, Mishra SC. Tests on $LmNi_{4.91}Sn_{0.15}$ based solid state hydrogen storage device with embedded cooling tubes – Part B: Desorption process. Int J Hydrogen Energy 2014;39(10):4966–4972.
3. Anbarasu S, Muthukumar P, Mishra SC. Tests on $LmNi_{4.91}Sn_{0.15}$ based solid state hydrogen storage device with embedded cooling tubes – Part A: Absorption process. Int J Hydrogen Energy 2014; 39(7):3342-3351.
4. Anbarasu S, Muthukumar P, Mishra SC. Thermal modeling on Mg_2Ni based solid state hydrogen storage hydrogen reactor. Heat Transfer Eng. 2014;35(14–15):1354–1362.

International Conferences:

1. Anbarasu S, Muthukumar P, Mishra SC. Thermal Modeling of Mg_2Ni based Solid State Hydrogen Storage Reactor During Desorption of Hydrogen, 22st National & 11th ISHMT-ASME Heat and Mass Transfer Conference, IIT Kharagpur, Kharagpur, West Bengal, India, 28-31 December 2013.

2. Anbarasu S, Muthukumar P, Mishra SC. Tests on $LmNi_5$ Based Solid-State Hydrogen Storage Container, International Conference on Recent Advances in Material Science, Tumkur University, Bangalore, Karnataka, India, 6-8 November 2012.

3. Anbarasu S, Muthukumar P, Mishra SC. Numerical heat and mass transfer analysis of a hydriding process in Mg_2Ni based hydrogen storage reactor with volumetric radiation, 21st National & 10^{th} ISHMT-ASME Heat and Mass Transfer Conference, IIT Madras, Chennai, Tamil Nadu, India, 27-30 December 2011.

4. Anbarasu S, Muthukumar P, Mishra SC. Parametric studies on an Mg_2Ni based hydrogen storage reactor, International Conference on Thermal Energy and Environment, Kalasalingam, Tamil Nadu, India, 24-26 March 2011.

5. Anbarasu S, Muthukumar P, Mishra SC. Numerical investigation of coupled heat and mass transfer in Mg_2Ni based hydrogen storage reactor, 7^{th} International Conference on Flow Dynamics, Sendai, Japan, 1-3 November 2010.